United States
Environmental Protection
Agency

EPA 600/R-09/096 | September 2009 | www.epa.gov/ada

Impacts of DNAPL Source Treatment: Experimental and Modeling Assessment of the Benefits of Partial DNAPL Source Removal

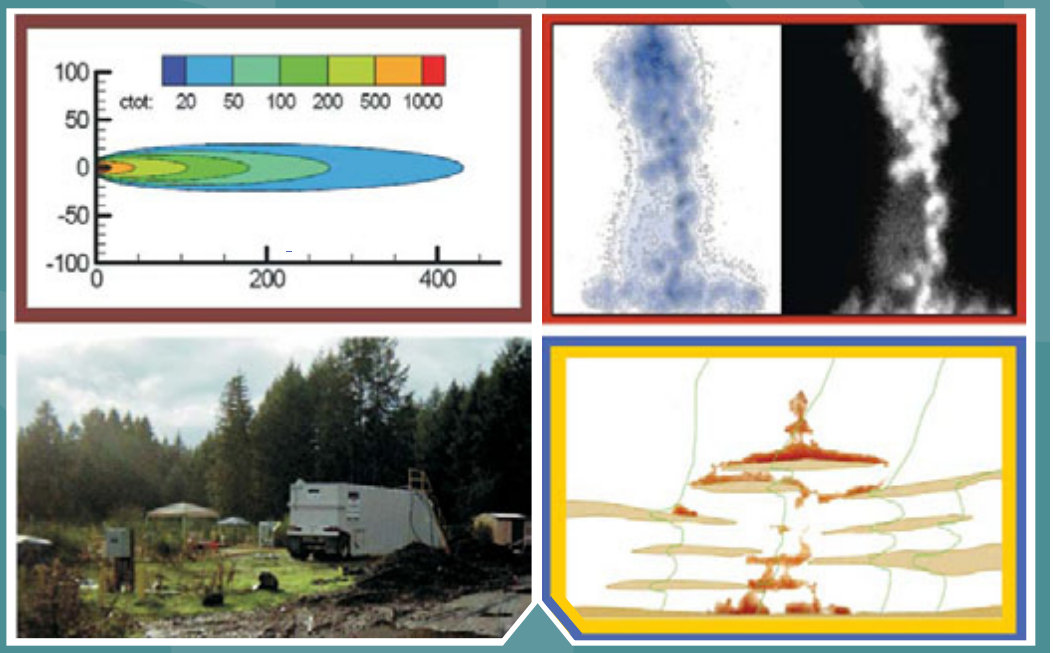

Office of Research and Development
National Risk Management Research Laboratory, Ada, Oklahoma 74820

Impacts of DNAPL Source Treatment: Experimental and Modeling Assessment of the Benefits of Partial DNAPL Source Removal

SERDP Project ER-1295

A. Lynn Wood, *Principal Investigator*
U.S. Environmental Protection Agency

Michael D. Annable
James W. Jawitz
University of Florida

Ronald W. Falta
Clemson University

Michael C. Brooks
Carl G. Enfield
U.S. Environmental Protection Agency

P. Suresh C. Rao
Purdue University

Mark N. Goltz
Air Force Institute of Technology

Office of Research and Development
National Risk Management Research Laboratory, Ada, Oklahoma 74820

Notice

The work on which this report is based was supported by the U.S. Environmental Protection Agency through its Office of Research and Development with funding provided by the Strategic Environmental Research and Development Program (SERDP), a collaborative effort involving the U.S. Department of Defense (DoD), the U.S. Department of Energy (DOE), and the U.S. Environmental Protection Agency (EPA). It has been subjected to EPA's peer and administrative review and has been approved for publication as an EPA document. Mention of trade names or commercial products does not constitute endorsement or recommendation for use.

All research projects making conclusions or recommendations based on environmentally related measurements and funded by the Environmental Protection Agency are required to participate in the Agency Quality Assurance Program. This project was conducted under an approved Quality Assurance Project Plan. The procedures specified in this plan were used without exception. Information on the plan and documentation of the quality assurance activities and results are available from the Principal Investigator.

Foreword

The U.S. Environmental Protection Agency is charged by Congress with protecting the Nation's land, air, and water resources. Under a mandate of national environmental laws, the Agency strives to formulate and implement actions leading to a compatible balance between human activities and the ability of natural systems to support and nurture life. To meet this mandate, EPA's research program is providing data and technical support for solving environmental problems today and building a science knowledge base necessary to manage our ecological resources wisely, understand how pollutants affect our health, and prevent or reduce environmental risks in the future.

The National Risk Management Research Laboratory (NRMRL) is the Agency's center for investigation of technological and management approaches for preventing and reducing risks from pollution that threatens human health and the environment. The focus of the Laboratory's research program is on methods and their cost-effectiveness for prevention and control of pollution to air, land, water, and subsurface resources; protection of water quality in public water systems; remediation of contaminated sites, sediments, and ground water; prevention and control of indoor air pollution; and restoration of ecosystems. NRMRL collaborates with both public and private sector partners to foster technologies that reduce the cost of compliance and to anticipate emerging problems. NRMRL's research provides solutions to environmental problems by: developing and promoting technologies that protect and improve the environment; advancing scientific and engineering information to support regulatory and policy decisions; and providing the technical support and information transfer to ensure implementation of environmental regulations and strategies at the national, state, and community levels.

This report has been prepared as part of the Laboratory's strategic long-term research plan. At many hazardous waste sites contaminants reside in the subsurface as separate dense non-aqueous phase liquids (DNAPL). These DNAPL serve as persistent sources of dissolved phase contamination and are a major impediment to successful and cost-effective site cleanup. Although substantial progress has been made in the development of source zone remediation technologies, total DNAPL removal remains problematic and the benefits of partial removal have been questioned. The research reported here was undertaken to evaluate these benefits and to provide information and tools to support the development of technically and economically responsible strategies for mitigating the impact of DNAPL contaminated sites on human health and the environment.

Robert W. Puls, Acting Director
Ground Water and Ecosystems Restoration Division
National Risk Management Research Laboratory

Contents

List of Figures . . . vii
List of Tables . . . xi
List of Acronyms . . . xii
Acknowledgments . . . xiii
Executive Summary . . . xv
1.0 Objectives . . . 1
2.0 Background . . . 1
3.0 Materials and Methods . . . 5
3.1 Data Quality . . . 6
3.2 Field Studies . . . 7
3.3 Laboratory Studies . . . 7
3.4 Modeling Studies . . . 8
4.0 Results and Accomplishments . . . 9
4.1 Field Research . . . 9
4.1.1 Flux Measurement Methods . . . 9
4.1.2 Hill Air Force Base Operable Unit 2 . . . 12
4.1.3 Fort Lewis East Gate Disposal Yard Site . . . 17
4.1.4 Former Sages Dry Cleaner Site, Jacksonville, Florida . . . 22
4.1.5 Borden CFB Site . . . 30
4.1.6 MIPT Uncertainty Analysis . . . 34
4.2 Laboratory Research . . . 45
4.2.1 Light Transmission Visualization Methods . . . 45
4.2.2 Relationship between Source Mass and Source Strength . . . 50
4.2.2.1 DNAPL source depletion: Linking architecture and flux response . . . 50
4.2.2.2 Fluid and porous media property effects on dense non-aqueous phase liquid migration and contaminant mass flux . . . 54
4.2.2.3 Reactive tracer tests to predict dense non-aqueous phase liquid dissolution dynamics in laboratory flow chambers . . . 58
4.2.2.4 Laboratory investigation of flux reduction from dense non-aqueous phase liquid (DNAPL) partial source zone remediation by enhanced dissolution . . . 62
4.2.2.5 The impacts of partial remediation by sparging on down-gradient DNAPL mass discharge . . . 68
4.3 Theoretical and Modeling Research . . . 73
4.3.1 Lagrangian Models . . . 74
4.3.2 Coupled Source Zone and Plume Models . . . 78
4.3.2.1 Analytical expressions of source flux and mass . . . 80
4.3.2.2 Analytical approaches including plume remediation and natural attenuation . . . 83
4.3.2.3 REMChlor model . . . 85
4.3.2.4 Cancer risk assessment . . . 91
4.3.2.5 Analytical/numerical approach including plume remediation and natural attenuation . . . 92

4.3.3 Model Assessments and Applications 96
4.3.3.1 Simulation of laboratory and field air sparging 96
4.3.3.2 Simulations of cosolvent flushing 102
4.3.3.3 Dissolved chemical discharge from fractured clay 110
4.3.3.4 Monte Carlo simulations of source behavior with remediation 113
4.3.3.5 Simplified contaminant source depletion models as analogs of multiphase simulators 117
4.3.3.6 Temporal evolution of DNAPL source and contaminant flux architecture 123
4.3.3.7 Predicting DNAPL dissolution using a simplified source depletion model parameterized with partitioning tracers 127

5.0 Conclusions 131

6.0 References 133

7.0 Appendix A - List of Technical Publications 143
Peer-Reviewed Papers 143
Technical Reports 144
Conference Proceedings 145
Published Technical Abstracts 145
Book Chapters 149

Figures

Figure ES-1. Impacts of Source Remediation: Conceptual Model. xv

Figure 2.0-1. Plan view of DNAPL source and dissolved plume. 2

Figure 2.0-2. Impacts of source remediation: conceptual model. 3

Figure 2.0-3. Contaminant mass flux leaving the source zone. 4

Figure 3.0-1. Integrated research approach. 5

Figure 3.0-2. Project organizational chart. 6

Figure 3.3-1. Coupled modeling approach used in the project. 8

Figure 4.1-1. Plan view of Panel 5 area at Hill AFB. 13

Figure 4.1-2. Hydrographs from Hill AFB OU2 wells U2-214 and U2-117, along with the average clay elevation (dashed line) across the transect. 14

Figure 4.1-3. Contaminant flux distribution from selected wells with the largest fluxes as measured prior to remediation at Hill AFB. 14

Figure 4.1-4. Average mass discharge (g/day) for each well at Hill AFB OU2, as measured by PFMs for a) May 2002 (pre-remedial), b) June 2003 (first post-remedial), and c) October 2004 (second post-remedial) tests; and as measured by MIPTs for d) May 2002 (pre-remedial), e) June 2003 (first post-remedial), and f) October 2004 (second post-remedial) MIPTs. 15

Figure 4.1-5. Plan view of the NA1 source area at the East Gate Disposal Yard site at Fort Lewis and the downgradient flux well transect. 18

Figure 4.1-6. Mass flux profiles measured in selected wells with the largest fluxes as measured prior to remediation using the PFMs. 20

Figure 4.1-7. Average mass discharge (g/day) for each well at Fort Lewis. Measured by a) PFMs and b) MIPT for the pre-remedial tests; and by c) PFMs and d) MIPT for the post-remedial tests. TCE is shown in black, and cis-DCE is shown in white. 21

Figure 4.1-8. Multilevel sampler locations, flux well locations, and the general areas targeted during the first and second ethanol flushing events at the Sages site. 23

Figure 4.1-9. MLS source zone PCE/TCE and TCE/c-DCE ratios as a function of ethanol concentration in the groundwater up to four years after the 1998 pilot test (Sages site). . .24

Figure 4.1-10. Sages source zone transect natural gradient concentrations for the 6-year period after the August 1998 ethanol flood. Values are millimolar sums of chlorinated ethenes (mM). 25

Figure 4.1-11. Sages source zone mass discharge (mmol/day) before and following the August 1998 ethanol flood. 26

Figure 4.1-12. Sages downgradient concentration distribution for the 6-year period. 27

Figure 4.1-13. Sages downgradient transect mass discharge in mmol/day for the six-year period following the 1998 ethanol flushing event. 28

Figure 4.1-14. Pre- and post-cosolvent flood MLS mass discharge measurements in the downgradient transect at the Sages site. 28

Figure 4.1-15. Pre- and post-cosolvent flood passive flux meter mass discharge measurements in the down gradient well transect at the Sages site. 29

Figure 4.1-16. Pre- and post-cosolvent flood MIPT mass discharge measurements in the down gradient transect at the Sages site. 30
Figure 4.1-17. Borden controlled release DNAPL site instrumentation. 31
Figure 4.1-18. PCE mass flux from passive flux meters installed in wells down-gradient of row 6 at the Borden CFB site. 32
Figure 4.1-19. PCE mass flux from MIPT measurements at the Borden CFB site. 32
Figure 4.1-20. Example breakthrough curve for the pre-remediation partitioning tracer test at the Borden CFB site. 33
Figure 4.1-21. Pre- and post-remedial mass flux distribution of PCE in the row 6 transect at the Borden CFB site. 34
Figure 4.1-22. Covariance of *J* plotted as a function of the covariance for *C* and *q* assuming *C* and *q* are independent random variables. 35
Figure 4.1-23. Standard deviation and the coefficient of variation for *q* as a function of uncertainty in head measurements.. 37
Figure 4.1-24. Covariance of *J* plotted as a function of the covariance for *C* and the standard deviation of head measurements.. 37
Figure 4.1-25. Layered (a) and block (b) macro-scale hydraulic conductivity patterns investigated with numeric modeling simulations. 39
Figure 4.1-26. Capture zones for an MIPT with seven concurrent pumping wells in an unconfined aquifer with $K = 10$ m/day and $q = 5$ cm/day. 40
Figure 4.1-27. Capture zones for an MIPT with seven concurrent pumping wells in an unconfined aquifer with a log-normally distributed random *K* field. 41
Figure 4.1-28. Comparison of capture zones with seven concurrent pumping wells for the homogeneous case (a) and heterogeneous cases: realization 1 (b) and realization 2 (c). . .42
Figure 4.1-29. a) Capture zones during an MIPT consisting of seven concurrently pumping wells, and b) the resulting concentration-time series for a mature contaminant plume centered at $y = 1.5$ m (midway between the third and fourth pumping wells), a maximum concentration of 20 mg/L, and a plume width described by a standard deviation of 0.4 m. 43
Figure 4.1-30. Results from Monte Carlo simulations where plume position is treated as a uniform random variable. 44
Figure 4.2-1. Distribution of PCE in porous media as determined by LTV. 49
Figure 4.2-2. PCE volume calculated from image analysis versus actual PCE volume present in the model. 49
Figure 4.2-3. Flux plane response to changes in NAPL architecture for experiment DCA-1. 51
Figure 4.2-4. Comparison of the rate-limited streamtube, equilibrium streamtube, and effective Damkohler approaches for modeling source depletion from experiments DCA-1, TCE-1, and DCA-2.. 53
Figure 4.2-5. Tracings of observed distributions of DNAPL injected 10 cm above the flow chamber bottom in 30/40 sand with a) PCE and untreated sand, b) PCE and 50% OTS treated hydrophobic sand mixture, c) PCE and 100% hydrophobic sand, d) untreated sand and DNAPL mixture of density 1.1 g/cm^3.. 56
Figure 4.2-6. Fractional flux increase versus DNAPL loading for each interfacial tension value in untreated 30/40 sand.. 57
Figure 4.2-7. Fractional flux increase versus PCE loading for varying density and media. 57
Figure 4.2-8. PCE spills before flushing. Images from experiments 1 and 2 are reflected light captured with standard digital camera and the NAPL is dyed red. 60

Figure 4.2-9. BTCs from surfactant flushing for Experiments I and II. 61
Figure 4.2-10. BTCs from surfactant flushing for Experiment III. 62
Figure 4.2-11. Displacement of resident water at different cosolvent injection volumes (PV). 64
Figure 4.2-12. BTCs for all Single Flush experiments with cosolvent mixtures. 65
Figure 4.2-13. Aqueous based mass reduction (R_M) versus flux reduction (R_J) of the single and multiple-flushing experiments with the solubility scaled approach (SSA) path estimation of the single-flushing experiment. 66
Figure 4.2-14. Digital photographs of the 2-D flow chamber: (a) and (b) show the initial distribution of PCE in Pack A and Pack B, respectively, and (c) and (d) show the sparging channels during the sparging experiments for Pack A and Pack B, respectively.. 69
Figure 4.2-15. The initial PCE saturation distribution in the flow chamber and the saturation distribution following each sparging event. 71
Figure 4.2-16. Relative effluent mass discharge as a function of PCE mass removed for the two experiments.. 72
Figure 4.3-1. Lagrangian conceptualization of DNAPL source zones.. 75
Figure 4.3-2. (a) Field dissolution data (from Jawitz et al., 1998) compared to equilibrium solution with a bimodal travel time distribution and homogeneous NAPL content (b) $R_J(R_M)$ based on model parameters.. 77
Figure 4.3-3. Measured and predicted remedial performance in a vertical circulation implementation of surfactant extraction (Wood et al., 2005). 78
Figure 4.3-4. Solid lines are reduction in contaminant flux as a function of reduction in source zone mass for $\sigma \ln \tau = \{0.05, 0.2, 0.6, 1.0, 1.5, 2, 3\}$. 78
Figure 4.3-5. Source zone dissolved concentrations as a function of source zone DNAPL mass (from Falta et al., 2005a). 79
Figure 4.3-6. Power function representation of source mass/source discharge relationship (Equation 4.3-6). 80
Figure 4.3-7. Conceptual model of source zone with time-dependent contaminant mass and discharge. 80
Figure 4.3-8. Source zone dissolved concentration with and without source remediation for $\Gamma = 0.5$ (from Falta et al., 2005a). 83
Figure 4.3-9. Source zone dissolved concentrations with and without source remediation for $\Gamma = 2.0$ (from Falta et al., 2005a). 83
Figure 4.3-10. Distance-time plot for advective transport with a single set of reaction rates. 86
Figure 4.3-11. Distance-time plot for advective transport with multiple sets of reaction rates. 87
Figure 4.3-12. Hypothetical design of an enhanced plume remediation scheme with an enhanced reductive dechlorination zone for destruction of PCE and TCE and an enhanced aerobic degradation zone for destruction of DCE and VC. 88
Figure 4.3-13. Comparison of the REMChlor reactive streamtube solution with BIOCHLOR for a two-zone case with steady state concentrations in the upstream zone (t = 20 years). 90
Figure 4.3-14. Steady-state TCE concentration at varying source mass reductions for a monitoring well 800 meters downgradient of the source. 95
Figure 4.3-15. Steady-state vinyl chloride (VC) concentrations at varying source mass reductions for a monitoring well 800 meters downgradient of the source.. 95
Figure 4.3-16. A simulated sparge zone in a single medium multiphase flow model versus realistic channeling that occurs in air sparging. 97

Figure 4.3-17. Schematic of connections in a dual media grid. Both media are globally connected and share a local connection. 98
Figure 4.3-18. Results from air sparging experiments (Heron et al. 2002). 99
Figure 4.3-19. Total experimental mass removal and simulated removal with TMVOC using a dual-media approach with A_{12}/d_2 ratio from the laboratory-scale air sparging simulation (75,000) and the adjusted A_{12}/d_2 ratio (75). 101
Figure 4.3-20. Modeled and measured ternary phase diagram for the system of water-ethanol-PCE. . . .104
Figure 4.3-21. Plan view of model domain with the site map of well and MLS locations within the approximated DNAPL source zone at Sages (adapted from Jawitz et al. 2000). 105
Figure 4.3-22. PCE effluent concentrations and ethanol effluent percentages for RW002, RW003, RW004, RW005, RW006, RW007, and total fluid (heterogeneous case).. 107
Figure 4.3-23. PCE effluent concentrations and ethanol effluent percentages for the calibrated heterogeneous case. 109
Figure 4.3-24. Conceptual view of a fractured clay aquitard. 111
Figure 4.3-25. Simulated TCE aqueous concentration in the fracture during the 20-year equilibrium period for a 30 μm fracture with no TCE decay and a clay f_{oc} of 0.01. 111
Figure 4.3-26. TCE concentration in the fracture effluent for the 30 μm and 100 μm fractures. 112
Figure 4.3-27. TCE concentration in the fracture effluent for the 30 μm and 100 μm fractures. 113
Figure 4.3-28. Two input probability distribution functions (without source remediation).. 114
Figure 4.3-29. Probability simulation output of source concentration (without source remediation). . . .115
Figure 4.3-30. Three input probability distribution functions (with source remediation). 116
Figure 4.3-31. Probability simulation output of source concentration (with source remediation).. 117
Figure 4.3-32. DNAPL spills for six representative cases. 120
Figure 4.3-33. UTCHEM-generated dissolution profiles (symbols) and corresponding model fits for simulation realizations 3-1 and 3-3 ($\sigma^2_{\ln\varepsilon} = 3$). 121
Figure 4.3-34. UTCHEM-generated mass reduction-flux reduction profiles (symbols) compared with DaM (Set 1-3), ESM (Set 2-3), ESM (Set 3-1),and PLM (Set 3-3) fits (lines) to the dissolution profile. 122
Figure 4.3-35. Relationship between the relative reductions in the mean and standard deviations of the contaminant flux. 125
Figure 4.3-36. Locus of the Centroid of the DNAPL and contaminant flux distributions (at the source control plane) in Domain 2 (white circles indicate the initial location of the centroid and black stars denote their final location). 125
Figure 4.3-37. Spatial variance of the DNAPL and contaminant flux distributions in (a) Domain 1, Case 1 (ISCO3D), and Domain 2, Cases 1 and 2 (T2VOC). 126
Figure 4.3-38. Non-partitioning and partitioning tracer data for simulation set 2-4. 127
Figure 4.3-39. ESM-predicted and UTCHEM-generated dissolution profiles for simulation sets 1-4, 2-4, and 3-2. 128
Figure 4.3-40. ESM-predicted and UTCHEM-generated mass reduction-flux reduction profiles for simulation set 1-4, 2-4, and 3-2. 128
Figure 4.3-41. Comparison between the ESM and the GTP models for prediction of source dissolution behavior. 130

Tables

Table ES-1. Summary of field demonstrations to assess DNAPL mass depletion flux reduction relationships . . . xvii

Table 3.1-1. Field study sites. . . . 7

Table 4.1-1. Summary of TCE and DCE mass discharge (g/day) and combined TCE and DCE molar discharge (moles/day) for Hill AFB OU2 using PFM and MIPT results, as well as estimates based on the Transect Method (TM). . . . 16

Table 4.1-2. Summary of TCE and DCE mass discharge (g/day) and combined TCE and DCE molar discharge (moles/day) for Fort Lewis EGDY site using PFM and MIPT results, as well as estimates based on the Transect Method (TM). . . . 22

Table 4.2-1. PCE distribution recovery, mean, and variance determined using the LTV models. . . . 47

Table 4.2-2. Summary of flow chamber experiments. . . . 48

Table 4.2-3. Summary of experimental conditions. . . . 50

Table 4.2-4. PCE/n-decane mixture densities, media sieve and grain sizes, and best fit β values for mass loading/flux generation relationships measured in these media. . . . 55

Table 4.2-5. Summary of the four experiments, equipment and truncated moment analysis results. . . . 59

Table 4.2-6. Fluid properties. . . . 63

Table 4.2-7. Numerical simulation input parameters. . . . 67

Table 4.2-8. Summary of PCE sparging test parameters. . . . 71

Table 4.2-9. Summary of PCE sparging test results. . . . 72

Table 4.3-1. Fraction of DNAPL source removal (X) required to reduce maximum plume length by a specified amount using Equation (4.3-19) (from Falta et al., 2005a). . . . 84

Table 4.3-2. California cancer risk slope factors for PCE and its degradation products (OEHHA, 2006). . . . 92

Table 4.3-3. Reaction zone degradation rates (Clement et al., 2000). . . . 93

Table 4.3-4. Percent mass reduction necessary to achieve remediation goals. . . . 96

Table 4.3-5. Constant input parameters used in probabilistic simulation applications. . . . 115

Table 4.3-6. Attributes of the simulated DNAPL source zones used in the numerical simulations. . . . 123

Table 4.3-7. Coefficient of variation (CV) of the Darcy flux (q), contaminant flux (J), and the DNAPL mass (S_N) distribution. . . . 124

Table 4.3-8. Tracer-derived ESM parameters. . . . 129

Acronyms

ADM	Advection Dispersion Model
API	American Petroleum Institute
BDI	Borden DNAPL Injection
BTC	Breakthrough Curve
CCD	Charge Coupled Device
CDI	Chronic Daily Intake
COV	Coefficient of Variation
CP	Control Plane
CV	Coefficient of Variation
CVOC	Chlorinated Volatile Organic Compounds
DaM	Damkohler number Model
DCE	Dichloroethylene
DLL	Dynamic-Link Library
DNAPL	Dense Non-Aqueous Phase Liquid
EGDY	East Gate Disposal Yard
EL	Ethyl-Lactate
EPA	Environmental Protection Agency
EPA/ORD	Environmental Protection Agency/ Office of Research and Development
ESM	Equilibrium Streamtube Model
GC/FID	Gas Chromatograph / Flame Ionization Detector
GC/MS	Gas Chromatograph/Mass Spectrometer
GMS	Groundwater Modeling System
GoldSim	Probabilistic Simulation Software
GTP	Ganglia To Pool ratio
IMPES	Implicit in Pressure
IFT	Interfacial Tension
IPT	Integral Pumping Test
ISCO	In-Situ Chemical Oxidation
LaSAR	Lagrangian Stochastic Advective Reactive
LTV	Light Transmission Visualization
MCL	Maximum Contaminant Level
MF	Multiple Flushing
MIBK	Methyl IsoButyl Ketone
MIPT	Modified Integral Pumping Test
MLS	Multi-Level Sampler
MODFLOW	MODular three-dimensional finite-difference ground-water FLOW model
NAPL	Non-Aqueous Phase Liquid
ND	Neutral Density
NDS	Neutral Density Surfactant
NRMSD	Normalized Root Mean Square Deviation
OEHHA	California Office of Environmental Health Hazard Assessment
OU2	Operable Unit 2
PCE	Tetrachloroethylene
PDF	Probability Density Function
PFM	Passive Flux Meter
PITT	Partitioning Inter-well Tracer Test
PLM	Power Law Model
PM	Point measurement
RA	Reagent Alcohol
REMChlor	Remediation Evaluation Model for Chlorinated Solvents
RMSE	Root Mean Square Error
RT3D	Three-dimensional, multispecies reactive transport in groundwater simulator
RW	Recovery Well
SERDP	Strategic Environmental Research and Development Program
SF	Single Flush
SI-GAC	Silver-Impregnated Granular Activated Carbon
SlF	Cancer risk Slope Factor
SSLE	Sum of Squares Logarithmic Error
T2VOC	Numerical simulator for three-phase, three-component, non-isothermal flow of water, air and a volatile organic compound in multidimensional heterogeneous porous media
TCE	Trichloroethylene
TE	Water to gas Transfer Efficiency
TM	Transect Method
TMVOC	A numerical simulator for three-phase non-isothermal flows of multicomponent hydrocarbon mixtures in saturated-unsaturated heterogeneous media
TVD	Total Variation Diminishing
USACE	U.S. Army Corps of Engineers
USGS	United States Geological Survey
UTCHEM	University of Texas Chemical Composition Simulator
VC	Vinyl Chloride
VOC	Volatile Organic Compound

Acknowledgments

The research upon which this report is based was a joint effort between the Strategic Environmental Research and Development Program (SERDP, project ER-1295), EPA's National Risk Management Research Laboratory, Air Force Institute of Technology (AFIT), Clemson University, University of Florida, and Purdue University. This report presents the collective work of the research team. Contributing authors and their affiliations are listed below:

Contributing Author	Affiliation
Michael D. Annable	University of Florida, Department of Environmental Engineering Sciences, Gainesville, FL 32611
Mustafa M. Bob	USEPA/ORD, National Risk Management Research Laboratory, Ada, OK 74820
Michael C. Brooks	USEPA/ORD, National Risk Management Research Laboratory, Ada, OK 74820
Carl G. Enfield	USEPA/ORD, National Risk Management Research Laboratory, Cincinnati, OH 45268 (retired)
Ronald W. Falta	Clemson University, Department of Environmental Engineering and Earth Sciences, Clemson, SC 29634
Mark N. Goltz	US Air Force Institute of Technology, Wright-Patterson Air Force Base, OH 45433
James W. Jawitz	University of Florida, Soil and Water Science Department, Gainesville, FL 32611
P. Suresh C. Rao	Purdue University, School of Engineering, West Lafayette, IN 47907
A. Lynn Wood	USEPA/ORD, National Risk Management Research Laboratory, Ada, OK 74820

Appreciation is extended to the following individuals who assisted with the many field, laboratory and modeling studies that contributed to this project: A. Noman M. Ahsanuzzaman, Steve Acree, Nandita Basu, Sten Berglund, Carol Bratt, Gordon Brown, Xaisong Chen, Jaehyun Cho, Pat Clark, Murray E. Close, Ravi Costa, Joseph J. Delfino, Erica DiFilippo, George G. Demmy, Rob Earle, Felipe P. Espinoza, Dennis Fine, Mark Flintoft, Adrian Fure, John Gierke, Erik Gonzales, Kirk Hatfield, John Hoggatt, Chuck Holbert, Junqi Huang , Ken Jewell, Andy Kaye, Robert Knox, Tony Lee, Hailian Liang, Bob Lien, Liping Pang, Kira Lynch, Susan Mravik, Russell Neill, Emile Pitre, Jeff Powell, Irene Poyer, Randall Ross, David Sabatini, Brad Scroggins, Randy Sillan, John Skender, Richard Smith, Mark Stacy, Chris Totten, Darby VanAntwerp, Jianlin Wang, Mingyu Wang, and Alex McKown.

Critical and constructive reviews were provided by Murray Einarson (AMEC Geomatrix), Mark Kram (Groundswell Technologies, Inc.), Scott Huling (USEPA/ORD National Risk Management Laboratory), John McCray (Colorado School of Mines), Jon Atkinson (Air Force Center for Engineering and the Environment), and Michelle Simon (USEPA/ORD National Risk Management Laboratory). Pat Bush (NCBA/SEE), Martha Williams and Kathy Tynsky (SRA International) are hereby acknowledged for their assistance with technical editing and formatting.

Executive Summary

Once released into the subsurface environment, dense nonaqueous phase liquids (DNAPLs) serve as long term sources of groundwater contamination, and are therefore a significant risk to water resources. Containment or removal, are the two basic strategies that can be used in the management or restoration, respectively, of a DNAPL contaminated site. Restoration can be pursued either through in-situ destruction or extraction, and a number of aggressive DNAPL remediation techniques (e.g., alcohol or surfactant flushing; thermal treatment; air sparging; chemical oxidation) have been developed for these purposes. Using the techniques, complete DNAPL removal may be possible at some sites, but because of technology limitations, such as the lack of reliable characterization and assessment approaches, and financial restrictions, partial mass depletion may be the most likely end result of aggressive source treatment at most DNAPL contaminated sites. When it is not practical or economically feasible to achieve complete DNAPL mass depletion, it must be determined if the aggregate benefits of partial DNAPL mass depletion are sufficient to reduce risks to an acceptable level, and if the costs associated with this partial depletion are justified by the benefits received.

This report summarizes research conducted to address these issues with the primary objective of the research being the development of a scientifically defensible approach for assessing the long-term environmental impacts (benefits) of DNAPL removal from source zones. The technical approach used to achieve this objective was to (1) characterize the relationships between DNAPL mass reduction, contaminant mass flux, and plume behavior, and (2) to use this information to develop a strategy for assessing the benefits of DNAPL source remediation. As discussed in Section 3, three lines of investigation were employed in our technical approach: field site demonstrations (Section 3.1), laboratory experiments (Section 3.2), and numerical and analytical modeling (Section 3.3). Using a combination of these applications allowed evaluation of varied hydrogeological settings and remediation scenarios. Specifically, field demonstrations and laboratory experiments were used to investigate the relationships between aggressive source treatment, mass removal, and flux response (Figure ES-1). Numerical and analytical modeling was likewise used to investigate specific linkages between the components in Figure ES-1, as well as develop an overall framework encompassing all conceptual model components.

The research project was primarily funded by the Strategic Environmental Research and Development Program, with substantial in-kind contributions from the participating organizations. The research team consisted of members from the Air Force Institute of Technology, Clemson University, the U.S. Environmental Protection Agency, the University of Florida, and Purdue University.

The Project Conceptual Model and Technical Approach

Sections 1 and 2 of the report discuss the project background, motivation and objectives. Two spatial domains of interest are defined: the *source zone,* and the *dissolved plume*. The source zone is defined as the groundwater region in which DNAPL is present, either as randomly distributed sub-zones at residual saturations or "pools" of DNAPL at higher saturations as accumulated above capillary barriers. The term *source-zone architecture* is used here to refer to both the form and function of the DNAPL sub-zones as they impact the evolution of the dissolved plume and the efficiency of remediation. The shape and extent of the dissolved plume is determined by mass flux [$ML^{-2}T^{-1}$] from the source-zone (which is a function of the source architecture), by hydrogeologic heterogeneity, and by natural attenuation processes occurring within the plume zone.

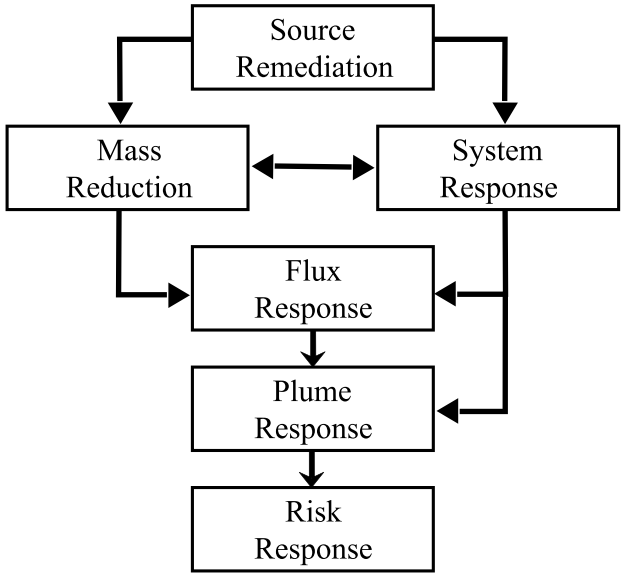

Figure ES-1. Impacts of Source Remediation: Conceptual Model.

The linkage between source zone remediation and risk reduction (i.e., benefits) is illustrated by the conceptual model shown in Figure ES-1. The first component of the conceptual model is the implementation of an aggressive remediation technology to achieve a rapid reduction in DNAPL mass. This in turn has an impact on the post-remediation contaminant flux leaving the source zone in response to groundwater flow under natural or induced gradients. Flux measurements are a critical link between changes in source-zone architecture and the resulting changes in the contaminant plume. The third component (Plume Response) of the conceptual model is the impacts of source-zone remediation on the dissolved plume. Because of their relatively large areal extent, dissolved contaminant plumes typically serve as the dominant exposure pathway and are the main focus for regulatory compliance. Consequently, changes in the contaminant plume due to source-zone treatment are important in an analysis of source-zone treatment benefits. Another element of the conceptual model is the System Response, and it accounts for secondary, long-term benefits in enhancing contaminant degradation within the source and plume due to certain source-zone treatment technologies. Thus, aggressive source-zone remediation technologies can be designed not only to remove substantial DNAPL mass, but also to promote contaminant attenuation in the plume.

The final component of the model is risk response. Risk is generally defined as the likelihood of the occurrence of adverse health or ecological effects as the result of hazard exposure and is characterized by evaluating the extent and effects of the exposure. In the case of groundwater contamination, risk is typically evaluated in terms of contaminant concentrations in the groundwater. However, because the dissolved plume is often the dominant exposure pathway, changes in groundwater concentrations in the source zone resulting from source treatment may not be the best metric for assessing the risk response. Instead, a mass balance approach can be used to estimate the impact of source-zone remediation on the dissolved plume. Thus, the endpoint for the risk assessment in our conceptual model is not based on a reduction of the resident contaminant concentrations in ground water within the entire source zone. Rather, the analysis is predicated on a reduction in the DNAPL content (total mass or average saturation), and, more importantly, the alteration in source zone architecture as a result of remediation. This in turn affects the dissolved plume where risk is defined in terms of two features of the dissolved plume: the spatial extent (defined by length or area or shape), and the average contaminant concentration or mass. Our metrics for risk reduction are then based on whether (1) the spatial extent of the existing dissolved plume is stable or decreases; (2) the total contaminant mass within the plume is constant or diminishing; and (3) contaminant fluxes decrease at succeeding control planes along the plume. Alternately, concentration-based risk responses at discrete receptors can be estimated. However, these estimates require detailed site information that is difficult to obtain and seldom available, and will likely be accompanied by greater uncertainty than mass balance-based estimates.

Field-scale Evaluation of Contaminant Flux Reduction

Changes in contaminant fluxes resulting from aggressive remediation of DNAPL source zones were investigated at four sites: Hill AFB, Layton, Utah (Section 4.1.2); Fort Lewis Army Base, Tacoma, Washington (Section 4.1.3); Former Sages Dry Cleaners, Jacksonville, Florida (Section 4.1.4); and Canadian Forces Base, Ontario, Canada (Section 4.1.5). These sites were selected primarily because they represented a range of hydrogeologic conditions and applied remedial treatments (see Table ES-1 for remedial treatments). Groundwater and contaminant fluxes were measured before and after the source-zone treatment, and the measured contaminant fluxes were integrated across the well transect to estimate contaminant mass discharge (M_D; MT^{-1}) from the source zone. Results were primarily used to investigate changes in flux due to DNAPL mass depletion at the field scale. Passive Flux Meters (PFM) and a variation of the Integral Pumping Test (herein referred to as the modified IPT, or MIPT) were primarily used to measure fluxes in wells installed along a transect down-gradient of the DNAPL source zones, and perpendicular to the mean groundwater flow direction (see Section 4.1.1 for flux measurement methods). The MIPT was developed as part of this study, and the theoretical development is presented in Section 4.1.1, and a method uncertainty analysis is presented in Section 4.1.6. Uncertainty associated with passive flux meter measurements was completed independently of this project, and results are discussed elsewhere.

Table ES-1. Summary of field demonstrations to assess DNAPL mass depletion flux reduction relationships

Site	Hill AFB		Fort Lewis NA1		CFB Borden		Sages Dry Cleaner	
Primary Contaminant	TCE		TCE		PCE		PCE/DCE	
Treatment	Surfactant		In Situ Heating		ISCO		Cosolvent	
Estimated Mass Reduction	>60%		>68%		Unknown		>100%[a]	
Flux Method	PFM	MIPT	PFM	MIPT	PFM	MIPT	PFM	MIPT
Pre-Remedial M_D (g/day)	76	76	743	536	2.2	2.2	5.8	1.0
Post-Remedial M_D (g/day)	6.0	3.9	3.4	2.2	0.54	2.4	2.0	1.1
M_D Reduction	92%	95%	99.5%	99.6%	75%	-9%	66%	-10.0%

[a]The estimated mass removed was greater than that initially estimated.

A summary of M_D measurements is presented in Table ES-1. Pre-remediation M_D ranged three orders of magnitude, from values as low as 1.0 g/day at the Sages site based on MIPT results, to values as high as 743 g/day at the Fort Lewis site based on PFM results. Significant reductions in M_D were observed at Hill AFB and Fort Lewis following source mass depletion. Results at these sites also indicate similarity between the different flux-measurement methods employed. However, results from PFM and MIPT as deployed at the Former Sages Dry Cleaner site and CFB Borden were not as similar. Differences between measurement results were noted, and while the PFM results indicated flux reductions due to source treatment, the MIPT results did not (Table ES-1). One trait common to all sites was the observation that the majority of the mass flux occurred over a fraction of the control plane area, which suggests flux measurements may be useful to improve treatment efficiency by targeting treatment to locations of elevated flux.

Laboratory-scale Evaluation of Contaminant Flux Reduction

The laboratory component of the project (Section 4.2) focused on controlled fluid-displacement experiments conducted in two-dimensional laboratory aquifer models. With respect to Figure ES-1, laboratory experiments were used to investigate the interrelation between source treatment, mass depletion and flux reduction. Accounting for spatial heterogeneity of both media and DNAPL saturation is critical to the study of source-zone removal. Two-dimensional flow chamber experiments allowed for the emplacement of heterogeneous distributions of porous media and contaminants, and more closely approached the three-dimensional complexity of the field-scale processes compared to one-dimensional column studies. Experiments were conducted in glass-sided, two-dimensional flow chambers to promote characterization through visualization techniques.

Innovative Techniques for Source-Zone Visualization. The architecture of the DNAPL source zone is an important component in the relationship between DNAPL source mass depletion and flux reduction, and Light Transmission Visualization (LTV) techniques were used to characterize the DNAPL architecture in the physical aquifer models (Section 4.2.1). Three general types of systems were explored: undyed water/dyed DNAPL, dyed water/undyed DNAPL, and undyed water/undyed DNAPL. Since light adsorption characteristics of dyed DNAPL may change as DNAPL mass is removed through dissolution or volatilization, the latter two approaches offer an advantage over the first. Moreover, the last system has the added advantage of eliminating concerns associated with dye induced changes in interfacial tension properties. The LTV methods developed were expansions of earlier LTV methods and took into account both absorption and refraction light theories. Results indicated that the LTV methods developed were capable of measuring DNAPL content with minimal calibration procedures.

Relationships between DNAPL source architecture and flux response. Section 4.2.2.1 summarizes laboratory experiments conducted to investigate the relationship between DNAPL mass depletion and contaminant mass flux in four heterogeneous model source zones. Flux information was coupled with image analysis to investigate the relationship between flux and DNAPL architecture. Once emplaced, the DNAPL was removed by aqueous dissolution, and results indicated that in the systems studied, the relationship between DNAPL mass reduction and contaminant mass flux was primarily controlled by the DNAPL architecture. For three of the experiments, the relationship between reductions in mass and flux for the integrated response of the whole flow cell was found to be approximately 1:1. Responses from individual well segments however deviated from the 1:1 behavior. Results from the fourth experiment and from a theoretical scenario were used to illustrate cases where mass depletion/flux reduction would deviate significantly from the 1:1 behavior observed in the other three experiments. Two simplified models, a streamtube model and an effective Damkohler model, were investigated for their ability to simulate experimental dissolution dynamics, and both modeling approaches were able to adequately simulate the experimental results.

Another experimental study was conducted to investigate the benefits of partial removal of DNAPL source zones using enhanced dissolution (Section 4.2.2.4). Four flushing agents with a range of densities were evaluated in eight controlled laboratory experiments to examine the effects of displacement fluid property contrasts and associated override and underride on contaminant flux reduction vs. mass reduction relationships. Source zone dissolution experiments using either a single flushing event or multiple shorter-duration floods were used to deplete DNAPL mass. All of the single-flushing experiments exhibited similar mass depletion-flux reduction relationships, indicating that override and underride effects associated with cosolvent densities did not significantly affect the remediation performance. However, for the flushing solutions with densities different from water, the mass depletion-flux reduction relationship of the multiple injection experiments tended to be less desirable in the sense that there was less flux reduction as mass was depleted. UTCHEM simulations supported the observations from the laboratory experiments and demonstrated the capability of this model to predict mass depletion-flux reduction relationships for non-uniformly distributed DNAPL sources.

The effects of fluid density and interfacial tension (IFT), and porous media grain size and wettability on contaminant flux were evaluated in flow chambers in which DNAPL mass was incrementally injected (Section 4.2.2.2). Contaminant mass flux was found to increase as grain size decreased, and increased slightly as the DNAPL approached neutral buoyancy. DNAPL spatial distribution and contaminant mass flux were only minimally affected by IFT and by intermediate-level wettability changes, but were dramatically affected by wettability reversal. The relationship between DNAPL loading and flux generation became more linear as grain size decreased and density contrast between fluids decreased. These results imply that capillary flow characteristics of the porous media and fluid properties will control mass flux generation from source zones.

Reactive tracer tests to predict DNAPL flux responses. Section 4.2.2.3 summarizes reactive tracer tests that were conducted to evaluate the relationship between contaminant mass depletion and flux reduction. The reduction in contaminant flux resulting from partial mass removal was obtained from continuous and pulsed cosolvent and surfactant flushing dissolution tests in laboratory flow chambers packed with heterogeneous porous media. Using the streamtube concept, a Lagrangian analytical solution was used to predict contaminant dissolution. The analytical solution was independently parameterized using nonreactive and reactive tracer tests, and the predicted dissolution was compared to the observed data. Reactive travel time variance, derived from this combination of nonreactive and reactive tracers, was used to predict the mass depletion/flux reduction relationship. Predictions based on the tracer tests closely matched measured dissolution data, suggesting that tracers can be used to characterize the DNAPL spatial distribution, which controls the dissolution behavior.

Modeling Evaluations of DNAPL Source-Zone Remediation

Numerical and analytical models, based on both Eulerian and Lagrangian frameworks, were used to investigate linkages between the conceptual model components illustrated in Figure ES-1. Numerical models with an Eulerian framework were used in this project to investigate DNAPL dissolution from source zones, DNAPL mass depletion due to aggressive treatment techniques, temporal characteristics of mass flux crossing the source control plane, DNAPL mass depletion/flux reduction relationships, and plume responses to flux reduction brought about by DNAPL mass depletion. Lagrangian-based analytical models were used to investigate DNAPL dissolution from source

zones and DNAPL mass depletion/flux reduction relationships. Moreover, research was conducted on the field-scale parameterization of Lagrangian models using tracer tests, and on the development of a holistic source-plume model using a semi-analytical approach within an Eulerian framework.

Numerical models. DNAPL remediation by air sparging at both laboratory and field scales was examined using TMVOC (Section 4.3.3.1). Results successfully matched mass removal data for both laboratory and field-scale experiments. Moreover, a dual-domain mass transfer technique accurately predicted concentration tailing following pulsed sparging, but simulations using this technique did not match concentration profiles observed during sparging. Mass transfer rates used to simulate the laboratory experiments were much larger than those used to simulate the field experiment, suggesting that mass transfer rates measured at a bench scale may not be applicable to field-scale processes. A drawback noted to this modeling approach for air sparging was the relatively large amount of site parameter data needed. However, this study showed a moderate amount of site information can still produce reasonable results if data are available for model calibration.

Section 4.3.3.2. presents simulations using UTCHEM of DNAPL remediation associated with the first cosolvent flooding pilot test conducted at the former Sages Dry Cleaner site in Jacksonville, Florida. The field simulations were carried out in three steps. At the first level, a simple uncalibrated two-layered permeability model was developed, which was capable of roughly reproducing the production well concentrations of alcohol, but not of PCE. At the second level, a more refined permeability distribution was used, and this model was able to more accurately simulate the recovery of injected alcohol from the production wells, but was still unable to accurately predict the PCE removal. The final model used the refined permeability distribution of the second model, but also included a calibration process where observed PCE breakthrough curves from extraction wells were used to adjust the initial DNAPL distribution. The results of these simulations suggest that the effectiveness of DNAPL source zone remediation was mainly affected by characteristics of the spatial heterogeneity of porous media and the variable (and unknown) DNAPL distribution.

Numerical models were also used to investigate changes in mass flux due to DNAPL mass depletion (Section 4.3.3.6). Using numerical models ISCO3D and T2VOC, changes in the distribution of DNAPL mass within a heterogeneous aquifer during dissolution, and the resulting changes in the contaminant flux distribution at a source control plane were investigated. As DNAPL mass was depleted, the mean and standard deviation of the flux distribution at the source control plane decreased proportionally (i.e., constant coefficient of variation). However, as DNAPL mass was depleted, the mean of the DNAPL mass distribution decreased faster than the standard deviation (i.e., increasing coefficient of variation). Also, the spatial moments of the contaminant flux distribution remained essentially constant over time, suggesting that – for DNAPL source zones cleaned up through in-situ flushing – the contaminant flux distribution remains stable throughout the DNAPL depletion process while the flux magnitude gradually decreases over time. These observations appeared to be independent of the permeability heterogeneity, correlation structure, and the DNAPL dissolution model, for the cases studied. Analysis of flux data from the Hill AFB site also revealed temporal invariance of the contaminant flux distribution.

Section 4.3.3.3 summarizes a modeling study using T2VOC, conducted to explore the matrix diffusion process in a fractured aquitard, and assesses the potential impact to an underlying potable water aquifer. It was assumed that a DNAPL spill has occurred on top of a fractured clay aquitard, and that a small, finite amount of the DNAPL had penetrated the fractures, but no DNAPL had reached the aquifer itself. Results indicated that DNAPL disappeared from the fractures relatively quickly due to forward diffusion processes (i.e., from the fracture to the clay). However, in the absence of degradation in the clay matrix, back diffusion from the clay to the fractures served as a contaminant source for hundreds to thousands of years based on the size of the fractures. Moderate degradation in the clay resulted in reduced time scales for the back diffusion source, ranging from tens to hundreds of years. It should be noted that an estimate of the actual impact of this source to the underlying aquifer and potential downgradient receptors can only be made in a mass discharge framework. For example, the impact may be negligible if the contaminant mass discharge from the fractured clay aquitard is small relative to groundwater flow in the aquifer.

Also investigated was the combined use of numerical and analytical models (Section 4.3.2.5). In this approach, an analytical power law model (PLM) was used to describe the relationship between DNAPL source mass depletion and flux reduction. This was used as a boundary condition to a numeric transport model (MODFLOW/RT3D) to investigate the plume response to source-zone DNAPL mass depletion. The model was based on a previous biodegradation modeling study conducted at a Dover AFB site. Results were used to investigate the extent of source mass depletion required to reach maximum contaminant level (MCL) goals for TCE and vinyl chloride at the receptor located 800 m

downgradient of the source. When the exponent of the power function (Γ) was set to 2.0, approximately 92% of the mass in the source zone needed to be removed to reduce vinyl chloride concentrations to the MCL at the receptor. However, as Γ was decreased, the required mass removal to reach MCL goals increased.

Analytical Models in a Lagrangian framework. The use of Lagrangian models to simulate DNAPL source dissolution, and the flux response to changes in source mass under dissolution processes is discussed in Section 4.3.1. Lagrangian models describe the source zone as a collection of non-interacting streamtubes, with hydrodynamic and DNAPL heterogeneity represented by the variations in the travel time and trajectory-integrated DNAPL saturation within the streamtubes. The properties of the hydrodynamic field and the DNAPL saturation distribution are described by the mean and standard deviation of the non-reactive travel time and the trajectory integrated DNAPL content, which are estimated by performing non-reactive and reactive tracer tests. Two techniques were investigated for estimating the characteristics of the travel time and the trajectory integrated DNAPL saturation distribution based on tracer test results: the method of moments where measured moments from tracer breakthrough curves are equated with derived moment equations to calculate the required parameters, and an inverse modeling approach where tracer breakthrough curves were fitted to a transport model and the parameters estimated by a genetic optimization algorithm.

A DNAPL source depletion model was also formulated based on the Lagrangian concept of the reactive travel time, defined as the time required to remove DNAPL from a streamtube under a given set of flushing conditions. This modeling approach was used to estimate contaminant elution curves from pilot-scale in-situ flushing tests, and results compared well to observed elution behavior. Parameters for the models were derived from tracer tests conducted prior to flushing. Furthermore, this approach was used to evaluate the relationship between contaminant mass depletion and contaminant flux reduction. The combined effects of aquifer and NAPL heterogeneities were shown to be captured in a single parameter, reactive travel time variability, which was determined to be the most important factor controlling the mass depletion/flux reduction relationship. It was shown that as heterogeneity in aquifer properties and NAPL spatial distribution increased, less mass depletion was required to achieve a given flux reduction, although the overall source longevity increased.

Section 4.3.3.7 summarizes additional investigation into the use of non-reactive and reactive tracer tests to parameterize the streamtube model. The spill and subsequent dissolution of DNAPLs was simulated in two-dimensional domains having different hydraulic conductivity distributions using the UTCHEM numerical model. Non-reactive and reactive tracers were used to characterize the Lagrangian properties (travel time and trajectory-integrated DNAPL content statistics) of the DNAPL source zones, which were in turn shown to be sufficient for accurate prediction of source dissolution behavior using the streamtube model over the relatively broad range of hydraulic conductivity distributions tested. The results were found to be relatively insensitive to travel time variability, suggesting that dissolution could be accurately predicted even if the travel time variance was only coarsely estimated. Estimation of the streamtube model parameters was also demonstrated using an approximate technique based on Eulerian data, as may be required in the absence of tracer data.

Analytical Models in an Eulerian framework. In addition to the Lagrangian based approach, three other analytical DNAPL source depletion models based on an Eulerian framework were evaluated for the prediction of long-term effects of source depletion under natural gradient flow (Section 4.3.3.5). The spill and subsequent dissolution of DNAPLs was simulated in domains having different hydraulic conductivity distributions using the UTCHEM model. The four analytical models (i.e., the equilibrium streamtube model [ESM], the advection dispersion model [ADM], the PLM, and the Damkohler number model [DaM]) were then fit to the dissolution profiles obtained from the UTCHEM simulations. All four models, though very different in their conceptualization, included parameters that described the mean DNAPL mass and the joint variability in the velocity and DNAPL distributions. The variability parameter was observed to be strongly correlated with the variance of the log hydraulic conductivity field in the ESM and ADM, but weakly correlated in the PLM and DaM. All four models were able to emulate the characteristics of the dissolution profiles generated from the complex numerical simulator, but in general the PLM consisting of a single fitting parameter did not match the UTCHEM results as well as the other models consisting of two fitting parameters.

Nonetheless, the PLM provides a convenient means to develop a screening level model useful in the evaluation of DNAPL remediation. Analytical solutions were developed for approximating the time-dependent contaminant discharge from DNAPL source zones undergoing dissolution and other decay processes (Section 4.3.2.1). The source functions assumed the PLM described the relationship between source mass and contaminant discharge, and accounted for partial DNAPL source remediation (depletion) at any time after the initial DNAPL release. The empirical exponent (Γ) of the PLM is a function of the flow field heterogeneity, DNAPL architecture, and the correlation between them. The source function was used as a time-dependent boundary condition in an idealized chemical transport model to

develop leading order approximations of the plume response to DNAPL source removal. Moreover, the source function was also used as a time-dependent flux-boundary condition in a semi-analytical contaminant transport model (Section 4.3.2.2). The semi-analytical transport model considered advection, retardation, three-dimensional dispersion, and sequential first-order decay/production of several species. A separate solution was used to compute the time-dependent mass of each contaminant in the plume. This approach allowed for flexible simulation of natural attenuation or remediation efforts that enhance plume degradation. The plume remediation effort may be applied to limited regions of the plume, for limited durations, and it may have different chemical effects on different contaminant species in the decay chain. A series of examples using different values of Γ illustrated the benefits of partial DNAPL source remediation for various site conditions. In general, when $\Gamma > 1$, relatively large short-term reductions in the plume concentrations and mass occur, but the source longevity is not strongly affected. Conversely, when $\Gamma < 1$, the short-term reductions in the plume concentrations and mass are smaller, but the source longevity can be greatly reduced. In addition, the model was used in a Monte Carlo analysis to investigate the impact of uncertainty in site conditions on remedial performance (Section 4.3.3.4).

It is often difficult at contaminated sites to decide whether remediation efforts should be focused on the contaminant source, the dissolved plume, or on both zones. The decision process at these sites is hampered by a lack of quantitative tools for comparing remediation alternatives. Consequently, the source function model coupled with the semi-analytical model as described in the previous paragraph is viewed as a screening-level mass balance approach to assess the transient effects of simultaneous DNAPL source and plume remediation. A graphical user interface was developed for the model, and the complete package, referred to as REMChlor, is publicly available on the internet. Many of the regulated groundwater contaminants and their degradation products are considered to be known or probable carcinogens by the U.S. EPA, and cancer risk from exposure to carcinogens was also incorporated into the model. This modeling approach essentially captures all of the conceptual model elements shown in Figure ES-1, and provides a screening level protocol with which to assess benefits obtained from DNAPL source remediation.

1.0 Objectives

There is currently no consensus in the academic, technical, and regulatory communities on the ecological or environmental impacts of dense non-aqueous phase liquid (DNAPL) source-zone treatment. The cost of source-zone treatment is high, and the anticipated benefits need to be understood before significant resources are committed to source-zone removal. The primary objective of this project was to develop a scientifically defensible approach for assessing the long-term environmental benefits of DNAPL removal from source zones. The technical focus of the project was to: (1) characterize the relationship between DNAPL mass reduction and contaminant mass flux (used as a measure of source "strength"), and (2) to use this information to develop a strategy for assessing the benefits of DNAPL source remediation. Project objectives were accomplished through a comprehensive approach that included coordinated and integrated field, laboratory, and modeling studies. This approach allowed the evaluation of several hydrogeologic settings with varied contaminant and remediation scenarios. Specific objectives of the project were:

- Characterize the functional relationship between DNAPL architecture, mass removal and contaminant mass flux in laboratory aquifer models under well-defined conditions,
- Assess the response to DNAPL mass removal through mass flux and plume behavior at several field sites,
- Conduct numerical simulations to describe the relationship between DNAPL removal, mass flux and subsequent plume response for the laboratory and field sites, and
- Compile statistics on the general relationship between partial DNAPL removal and contaminant flux reduction for simulations of several hydrogeologic templates of actual field sites

2.0 Background

Through field-scale research funded by SERDP and other agencies, it has been demonstrated that a high percentage (~70 to 90+%) of the NAPL mass can be removed from source zones by implementing several aggressive *in-situ* technologies, such as alcohol or surfactant flushing or steam flooding (Wood and Enfield, 1999). These studies and others (Lowe et al., 1999) have shown that while a significant fraction of the NAPL mass can be efficiently removed in a short period, the efficiency of NAPL mass extraction often decays exponentially with increasing mass removed. Thus, it may be neither practical nor economically feasible to remove all of the NAPL mass from the source zone. With finite resources, one needs to know the maximum amount of NAPL mass that can be left in the source zone while being protective of human health and the environment.

A reduction in the DNAPL source zone mass is expected to provide the following explicit benefits: a reduction in human health risks and adverse ecological impacts; a decrease in source and plume longevity; and lower life-cycle cost of site cleanup (Sale and McWhorter, 2001; EPA, 2003). However, there is disagreement in the technical and regulatory communities as to whether the aggregate benefits of partial DNAPL mass removal are sufficient to reduce risks to an acceptable level, and if the costs associated with partial DNAPL mass removal are justified by the benefits received. Furthermore, there is no consensus on appropriate risk metrics that should be used to evaluate the derived benefits from partial mass removal from DNAPL source zones, especially if ecological receptors are included in such evaluations. These types of considerations provided the motivation for this project, with the following primary research question to be answered: What are the impacts of partial NAPL source removal in heterogeneous aquifers with respect to

the extent of migration and the longevity of the contaminant plume compared to no source removal? Thus, the goal was to provide a scientific analysis and decision framework for exposure assessment as an element of risk-cost-benefit analysis.

Two spatial domains of interest were defined: the *source zone,* and the *dissolved plume* (Figure 2.0-1). The source zone is defined as the groundwater region in which DNAPL is present as a separate phase, either as randomly distributed sub-zones at residual saturations or "pools" of accumulation above confining units (Mackay and Cherry, 1989; Feenstra et al., 1996). The DNAPL sub-zones are usually thin, discontinuous DNAPL accumulations where subtle changes in either texture or permeability occur (e.g., Schwille, 1988; Feenstra et al., 1996). Thus, a significant volume fraction of the source zone may contain no DNAPL. Following Sale and McWhorter (2001), the term *source-zone architecture* is used to collectively refer to the geometry (shapes, sizes, inter-connections), spatial distribution, and DNAPL content of the sub-zones. Thus, the term architecture implies both the form and function of the sub-zones as they impact efficiency of remediation, and the evolution of the dissolved plume. At a given site, the DNAPL source-zone architecture depends on the following primary factors: (1) the nature of the DNAPL spill scenario (i.e., locations, rate, volume); (2) the spatial structure of the hydrogeologic properties of the aquifer (i.e, capillary retention and hydraulic conductivity functions); and (3) the DNAPL fluid properties (i.e., density, viscosity, wettability). Small DNAPL source zones can generate extensive dissolved plumes (Mackay and Cherry, 1989). The shape and extent of the dissolved plume are determined by several factors including: source-zone architecture; hydrogeologic heterogeneity; time since NAPL release; groundwater velocity; and the magnitude and coupling of several natural attenuation processes (e.g., retardation, dispersion, reductive dechlorination) occurring within the plume zone. Thus, information regarding the spatial extent and architecture of the existing (pre-remediation) source zone and the plume characteristics (spatial extent, concentration distribution, and attenuation processes) will facilitate the design of effective site remediation strategies.

Figure 2.0-1. Plan view of DNAPL source and dissolved plume.

The linkage between source zone remediation and potential system response benefits are considered according to the conceptual model shown in Figure 2.0-2. The first component of this model is the implementation of an aggressive remediation technology to achieve a rapid reduction in DNAPL mass within the source zone, via either *in-situ* extraction or destruction. The endpoint for our risk assessment is not based on a reduction of the resident contaminant concentrations in ground water within the entire source zone. Rather, the analysis is predicated on a reduction in the DNAPL content (total mass or average saturation), and, more importantly, the alteration in source zone architecture as a result of remediation. The nature of the expected changes in the source-zone architecture depends on the processes underlying the remediation technology and how it is implemented at a site.

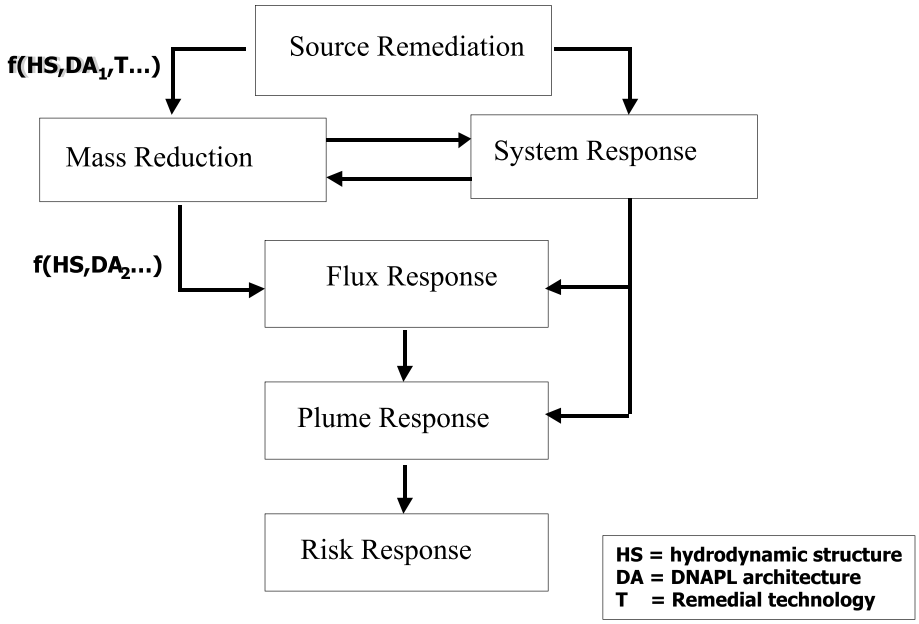

Figure 2.0-2. Impacts of source remediation: conceptual model.

The second model component relates post-remediation conditions (e.g., modified hydrodynamic contact with the remaining DNAPL mass) to contaminant flux leaving the source zone in response to groundwater flow under induced gradients (as in pump-and-treat) or natural gradients. Contaminant flux is defined as the rate of contaminant mass per unit area leaving the source zone across a control plane orthogonal to the mean groundwater flow, and may vary widely over the control plane (Figure 2.0-3; Guilbeault, et al., 2005). Contaminant mass discharge, M_D, is the total contaminant mass per unit time from the source and is a direct measure of the source strength. Feenstra et al. (1996) discussed the use of contaminant flux as a metric for risk assessment at DNAPL sites. Einarson and Mackay (2001) used this concept more recently to evaluate the impacts of source zones on down-gradient water-supply wells. They provide a simple approach for estimating likely contaminant concentrations in down-gradient supply wells given the contaminant flux from a source within the capture zone, and demonstrate the method's utility at several sites.

The third model component is an analysis of the impacts of source-zone remediation on the dissolved plume. Risk is defined in terms of two features of the dissolved plume: the spatial extent (defined by length or area or shape), and the average contaminant concentration. The metrics for risk reduction are then based on whether (1) the spatial extent of the existing dissolved plume is stable or decreases; (2) the total contaminant mass within the plume is constant or diminishing; and (3) contaminant fluxes decrease at succeeding control planes along the plume. The linkage between source-zone and plume assessments is that to achieve a stable or shrinking plume, the contaminant fluxes leaving the source zone must be equal to or less than the intrinsic potential within the plume zone to attenuate the contaminants of interest. In this project, existing protocols were used, as well as, newly developed approaches to estimate the effects of contaminant mass-flux reductions from partial source removal on changes in plume geometry and concentration. Source remediation technologies often have secondary long-term impacts within the source zone and the dissolved plume (System Response in Figure 2.0-2). For example, long-term monitoring data collected subsequent to *in-situ* ethanol flushing of the DNAPL source zone at the Sages site (Jacksonville, FL) indicate that the residual ethanol in the source zone serves as an electron donor in promoting reductive dechlorination of PCE (Mravik et al., 2000). Field tests conducted at the Hill and Dover AFB sites show that microbial activity was increased after *in-situ* alcohol or surfactant flushing. Thus, aggressive source-zone remediation technologies can be designed not only to remove substantial DNAPL mass, but also to promote contaminant attenuation in the plume.

The final component of the model is risk response. It is recognized that risk assessment methodologies should be used to evaluate the benefits accrued from partial DNAPL mass removal in the source zone. It is possible to estimate the probabilities of contaminant concentrations exceeding some critical value (e.g., MCL) in groundwater to evaluate risks to human health, but similar analyses for ecosystem impacts are much more complex, in part because there are multiple receptors that have different sensitivities to type, magnitude and duration of exposure to contaminants (Suter et al., 1993). Here, we focus on exposure assessment as a component of more comprehensive risk assessment.

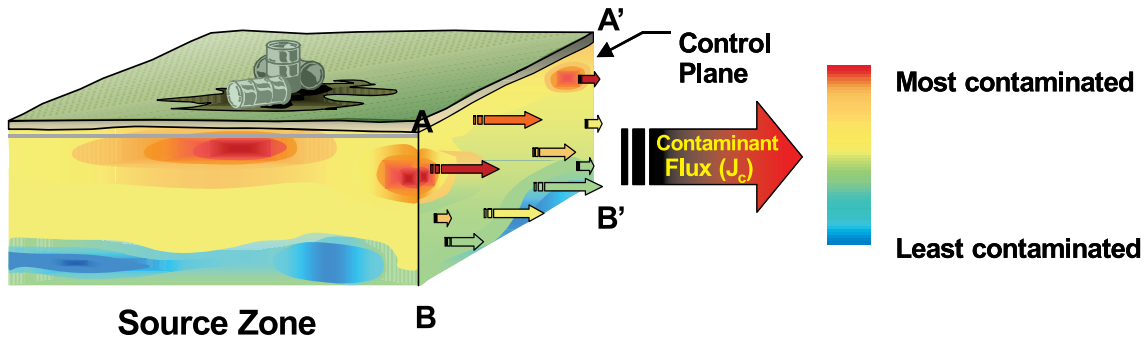

Figure 2.0-3. Contaminant mass flux leaving the source zone.

Remedial objectives and site conditions are primary determinants of the need for source treatment or control at a site. As illustrated in Figure 2.0-1, points of compliance are often located in the dissolved groundwater plume and the groundwater concentrations at these points (or more generally, compliance planes considering the entire cross section across the plume) are functions of contaminant discharge from the source (source strength) and the attenuation capacity within the plume. The integrated behavior of DNAPL sources and plumes must be evaluated when designing a remediation system (Chapelle and Bradley, 1998; Chapelle et al., 2004; Widdowson et al., 2005; Basu et al., 2006). The objective of flux-based remedial design is to reduce contaminant discharge at the down-gradient compliance plane to achieve appropriate risk reduction (Basu et al., 2006). Thus, the development of a site remediation strategy involves defining a target receptor loading based on the remedial objective similar to approaches used in surface water discharge permitting (Kovalic, 1987). For example, if the water at the receptor is to be used for drinking, the target receptor loading, $M_{D,r}$ would be (Einarson and Mackay, 2001):

$$M_{D,r} = (MCL) q_0 A_W \tag{2.0-1}$$

where q_0 is the groundwater or Darcy flux and A_w is a representative area that is a function of the capture zone of the supply well. The target loading can be achieved by (1) decreasing q_0, (2) decreasing the source strength through source treatment, (3) increasing plume degradation rates through plume treatment, or (4) a combination of source and plume treatment. Source strength can be reduced by removing contaminant mass from the source. It is very difficult to characterize the magnitude and distribution of the source mass, but it is easier to characterize the source strength (Basu et al., 2006). It has been shown that source mass can be related to source flux or source strength (Rao et al., 2001; Rao and Jawitz, 2003; Parker and Park, 2004; Jawitz et al., 2005; Falta et al., 2005a, b; Enfield et al., 2005; Wood et al., 2005) using a power function of the form:

$$\frac{M_D}{M_{D,0}} = \left(\frac{M_S}{M_{S,0}} \right)^{\Gamma} \tag{2.0-2}$$

where, M_D and $M_{D,0}$ are the present and initial source strength (mass discharge from the source), M_S and $M_{S,0}$ are present and initial source masses, and Γ is an empirical constant that is a function of the heterogeneity of the flow field and the NAPL architecture (Rao et al., 2001; Jawitz et al., 2005; Falta et al., 2005a, b).

3.0
Materials and Methods

The fundamental approach for this research was an integration of field, laboratory and modeling studies (Figure 3.0-1). Field data provided the foundation for the project, while laboratory investigations were used for in-depth evaluation of important processes, and modeling provided the framework for assessment and application of study results. Laboratory tests were designed to supplement field studies and focused primarily on the relationships between hydrodynamic structure, DNAPL architecture and contaminant mass discharge.

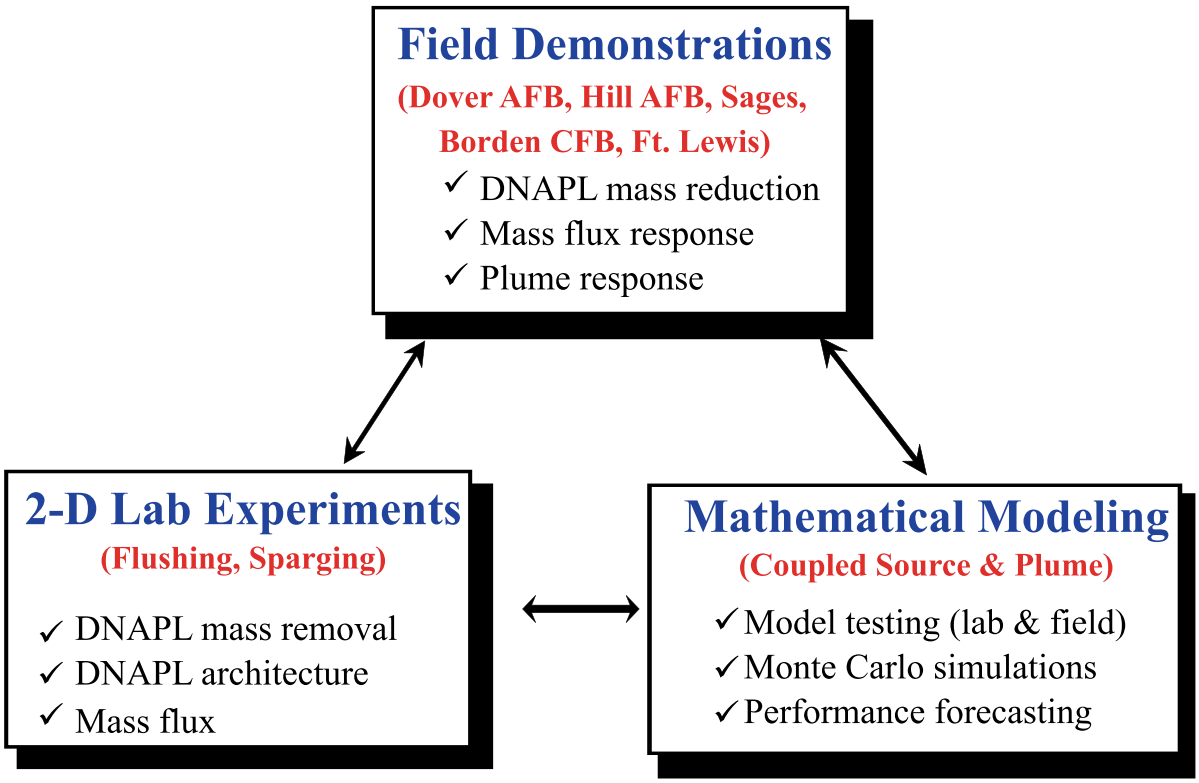

Figure 3.0-1. Integrated research approach.

The research was conducted by a team of scientists and engineers from the U.S. Environmental Protection Agency, U.S. Air Force, Clemson University, University of Florida and Purdue University. The project organizational chart is shown in Figure 3.0-2.

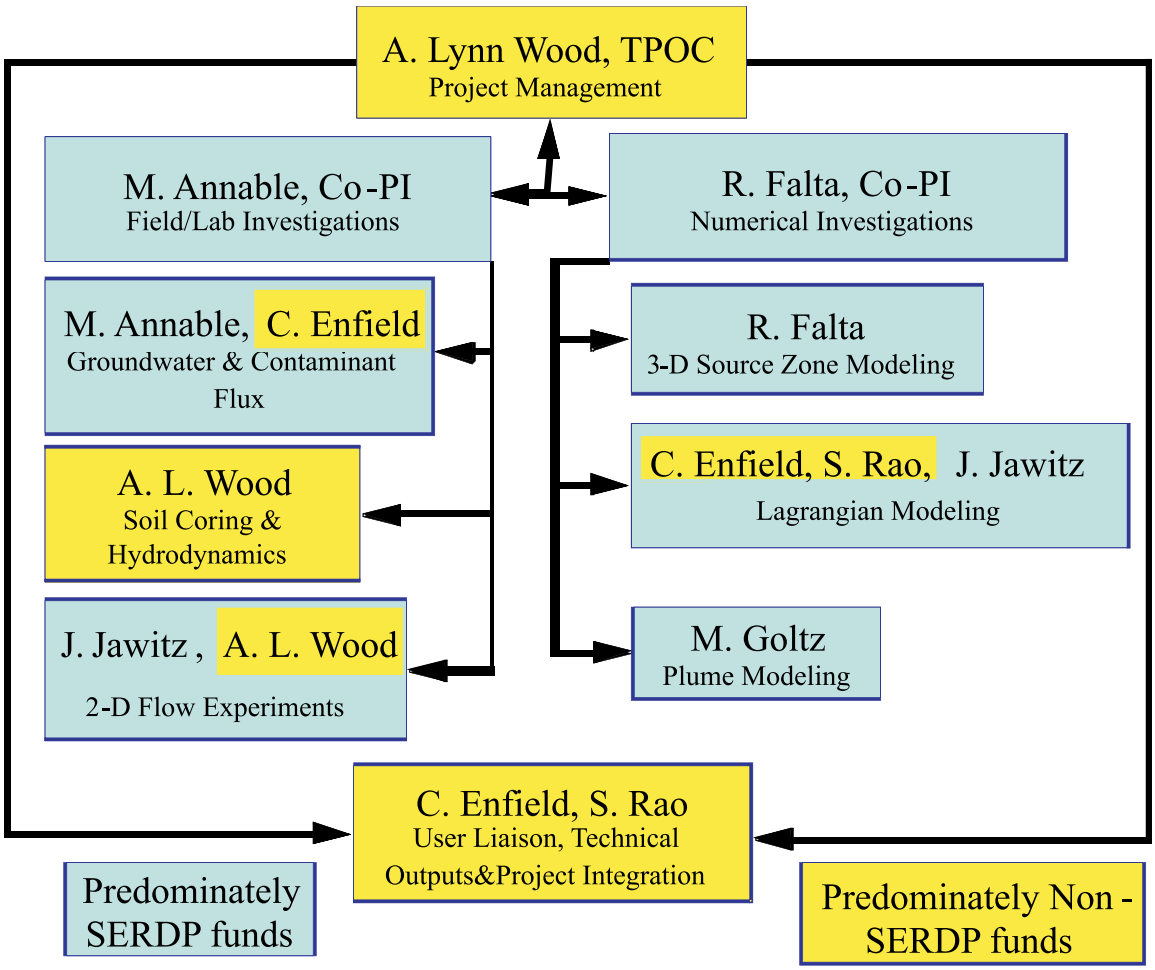

Figure 3.0-2. Project organizational chart.

3.1 Data Quality

The following quality assurance project plans (QAPPs) were prepared to encompass the laboratory, field, and numerical investigations that comprised the research project described in this report: Impacts of DNAPL Source Zone Treatment: Laboratory and Field Assessment of the Benefits of Partial Source Removal; Modeling Assessment of the Benefits of Partial DNAPL Source Removal; and Benefits of Partial Source Removal: An Experimental Assessment. These plans detail data quality assurance objectives, training, documentation and records, sampling, chain of custody, analytical methods requirements, quality control, instrumentation, calibration and frequency, inspection, data management, assessment and oversight, and data validation and usability. The QAPPs were reviewed and approved by EPA's quality management staff.

The data contained in this report were collected in accordance with provisions described in the quality assurance project plans. The quality of the data has been evaluated and determined to be sufficient for the intended applications unless otherwise noted in the report. A variety of experimental and analytical procedures were used in this project. These procedures are briefly described in Section 4 of this report. Additional information can be found in the peer-reviewed project publications that are cited throughout Section 4.

3.2 Field Studies

DNAPL source treatment effectiveness was evaluated at four sites: Hill Air Force Base Operable Unit 2, Layton, Utah; Fort Lewis East Gate Disposal Yard Site (EGDY), Tacoma, Washington; Borden Forces Base, Borden, Ontario, Canada; and Sages Dry Cleaner, Jacksonville, Florida (see Table 3.1-1). Contaminant discharge from the DNAPL source zone (source strength) was measured at each site before and after DNAPL source treatment. These data were collected using two innovative techniques: passive flux meters (PFM) and a modified version of the integrated pumping technique (MIPT). In addition, multiple-level sampler data were collected at the Sages site and these data along with independent estimates of groundwater flow velocities provided a third estimate of contaminant discharge. At each site, source strength was measured along a control plane established by installing a transect of wells immediately downgradient of the source and approximately perpendicular to the mean groundwater flow direction as determined from hydraulic head data.

The field sites represented a range of hydrogeological conditions and remediation technologies. Surfactant flooding was used to remove DNAPL mass at the Hill AFB site; thermal resistive heating was the technology of choice at the Fort Lewis EGDY; source mass reduction was accomplished by flushing the Sages site with ethanol; and in-situ oxidation was selected at the Borden site. Details of site conditions, contaminant properties and measurement techniques are provided in the project manuscripts that are identified and summarized in Section 4 of this report.

Table 3.1-1. Field study sites.

Field Site	Location	Primary Contaminants	Initial Mass Estimate	Treatment Technology
Hill AFB OU2	Hill AFB, Utah	TCE	1360 liters	Surfactant-Enhanced Aquifer Remediation
Fort Lewis	Tacoma, Washington	TCE	2600 to 8200 liters	Resistive Heating
Borden	Canadian Forces Base, Ontario, Canada	PCE	5 liters	In-situ Chemical Oxidation (permanganate)
Sages	Sages Dry Cleaner, Jacksonville, Florida	PCE, DCE	19 liters	Cosolvent Flood (ethanol)

3.3 Laboratory Studies

Laboratory experiments focused on controlled fluid-displacement experiments conducted in two-dimensional model heterogeneous aquifers. The goals of the experiments were to: (1) quantify the reduction in contaminant flux due to partial removal of DNAPL source zones, and (2) to provide high quality data sets for validating the deterministic process models and the stochastic stream tube models. The work included the development and application of methods for characterizing the source-zone architecture using partitioning tracer tests, and the application of innovative visualization techniques to observe source distribution and alterations.

Two types of extraction technologies were evaluated: in-situ flushing (surfactant or cosolvent), and volatilization (air sparging). DNAPL was emplaced within a range of model hydrogeologic settings and down-gradient contaminant concentrations and mass fluxes were measured both before and after source depletion. Experiments were conducted in two-dimensional flow chambers with tempered-glass side walls to facilitate the evaluation of media structure, contaminant distribution, fluid displacement and DNAPL removal dynamics using visualization techniques. Details of the flow chambers, measurement and visualization techniques, and experimental procedures are described in Section 4.

3.4 Modeling Studies

The basic modeling approach was to couple source-zone models with reactive solute transport models to estimate the benefits of contaminant source remediation (Figure 3.3-1). Three basic source zone modeling approaches were used for the project.

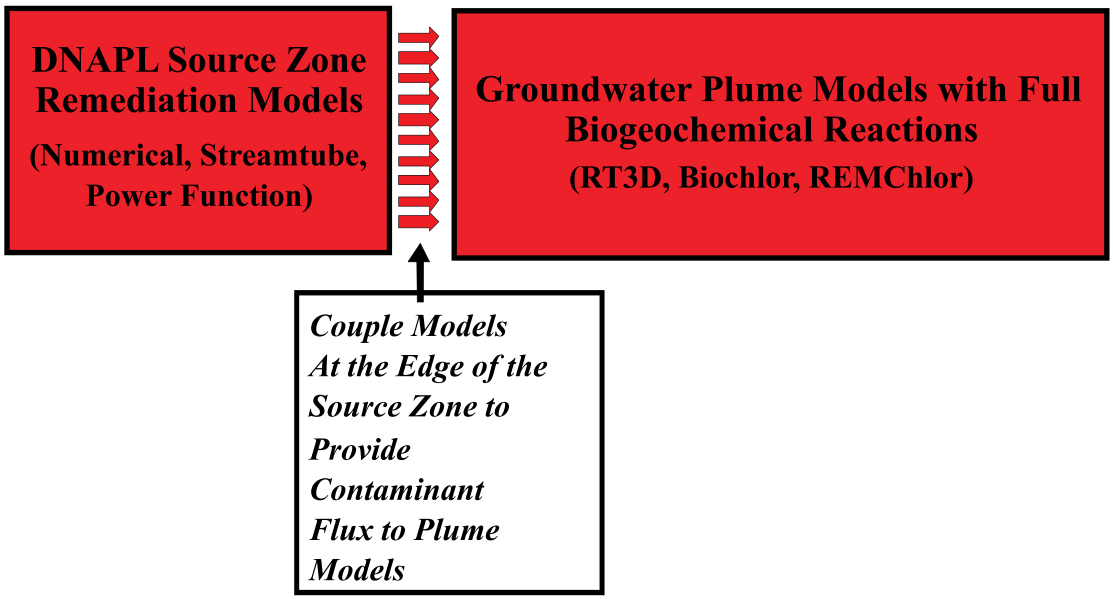

Figure 3.3-1. Coupled modeling approach used in the project.

The first was to apply existing deterministic codes, such as T2VOC and UTCHEM, to the DNAPL source zone to simulate the remediation processes during remediation and to predict the temporal and spatial distribution of contaminant fluxes leaving the source zone. The second approach utilized the Lagrangian Stochastic Advective-Reactive (LaSAR) streamtube technique to estimate mass flux across a control plane. With this method, the complexities of the medium are represented by the statistics and spatial correlation structure for the major parameters and the contaminant flux at the control plane is the ensemble average of all the stream tubes that contribute to the sampled flow. In the third approach, contaminant discharge from the source was estimated by a power function that quantifies the relationship between source mass and mass discharge. In this third approach a power function was used to describe the changes in source strength as a function of source mass reduction. Output from each of these approaches provided input boundary fluxes for dissolved-plume transport simulations. Modeling approaches and applications are described in Section 4.

4.0
Results and Accomplishments

Results of the research conducted through this project are described in a variety of products. A complete list of these products is presented in Appendix A. The following sections of the report provide an overview of the detailed information contained in these products.

4.1 Field Research

A primary objective of this project was to evaluate changes in contaminant flux and discharge resulting from source zone treatment. An extensive search was conducted to locate field sites with delineated DNAPL source zone and where aggressive source treatment was planned during the first two years of the project. Four field sites were selected: 1) Hill Air Force Base, UT, 2) Ft. Lewis, WA, 3) Sages Dry Cleaner site in Jacksonville, FL, and 4) Canadian Forces Base, Borden, ON, Canada. At each of these sites, contaminant flux and discharge were measured down-gradient of the source zone both before and after source remediation. Flux was measured using both passive flux meters and integral pump tests. Results of field-based experiments conducted as part of this project are described in detail in the following reports and journal articles:

Brooks, M.C., A.L. Wood, M.D. Annable, K. Hatfield, J. Cho, C. Holbert, P.S.C. Rao, C.G. Enfield, K. Lynch, and R.E. Smith (2008). Changes in contaminant mass discharge from DNAPL source mass depletion: evaluation at two field sites. *Journal Contaminant Hydrology* 102(1-2):140-153, doi:10.1016/j.jconhyd.2008.05.008.

Brown, G. (2006). Using Multilevel Samplers to Assess Ethanol Flushing and Enhanced Bioremediation at Former Sages Drycleaners. M.S. Thesis, University of Florida.

Goltz, M.N., J. Huang, M.E. Close, M.J. Flintoft, and L.Pang (2008). Use of tandem circulation wells to measure hydraulic conductivity without groundwater extraction. *Journal of Contaminant Hydrology* 100(3-4):127-136.

4.1.1 Flux Measurement Methods

Passive Flux Meters (PFM)

General experimental methods for deployment and recovery of PFMs are described by Annable et al. (2005) and Basu et al. (2006). Briefly, the approach to the measurement of groundwater and contaminant fluxes involves deployment of a permeable, sorbent pack (i.e., PFM) in the wells located along a transect of wells that are screened across the aquifer depth of interest. The PFM sorbent (e.g., silver-impregnated granular activated carbon [SI-GAC]) is pre-loaded with known amounts of tracers and these tracers are displaced from the sorbent at rates proportional to groundwater flux and the tracer retardation on the sorbent. The PFM sorbent material is selected to capture the target contaminants dissolved in the groundwater flowing through the device during the designated deployment period. Because these measurements are made under natural gradient groundwater flow conditions, this approach is referred to as “passive” in contrast to the MIPT method (see below) that requires pumping.

The PFMs may be packed on site and are constructed to match the saturated thickness in each well, and multiple PFMs may be deployed as needed in wells to cover well-screen intervals. Each PFM sock can be divided into segments separated by Norprene rubber washers to prevent vertical water flow in the PFM. A sample of the sorbent is collected for analysis of the initial tracer concentrations (analytical details are provided in Annable et al. (2005)). The completed PFM is inserted into the well to the desired screen interval.

Estimations of groundwater flux based on depletion of alcohol tracers, and contaminant fluxes based on contaminant accumulation, have been described by Hatfield et al. (2004) and Annable et al. (2005). After a specified period of exposure to groundwater flow, the PFM is removed from the well; the sorbent is carefully extracted to quantify the mass of contaminants intercepted and the residual masses of all resident tracers. Groundwater fluxes (seepage velocities) are calculated from the tracer mass depletion and sorbed contaminant mass is used to directly estimate contaminant fluxes. Retardation factors for tracer depletion from the PFM sorbent were reported by Annable et al. (2005). The depth profile of contaminant fluxes from each well is averaged to determine $\overline{J}$ for each well. These averages are calculated by weighting the *local* contaminant flux values (J_i) by the length of the vertical interval (b_i) as follows:

$$\overline{J} = \frac{\sum_{i=1}^{n-vert} J_i b_i}{\sum_{i=1}^{n} b_i} \tag{4.1-1}$$

where *n-vert* is the number of intervals in the well screen, b_i is the length of each interval [L], and J_i is the local contaminant flux [$ML^{-2}T^{-1}$]. The $\overline{J}$ values are integrated over the width of the control plane to determine a transect-wide contaminant mass discharge, $\overline{\overline{M}}_D$ (g/day):

$$\overline{\overline{M}}_D = \sum_{j=1}^{n-well} \left(\sum_{i=1}^{n-vert} \left(J_{i,j} A_{i,j} \right) \right) \tag{4.1-2}$$

where *n-well* is the number of wells and $A_{i,j}$ is the area [L^2] represented by the vertical sampling interval (b_i times the horizontal spacing between wells). Because this calculation is predicated on the assumption that contaminant fluxes measured in the wells are representative of the entire well spacing, reducing this spacing should improve mass discharge estimates. In addition, techniques used to interpolate between wells can impact these estimates.

Integral Pumping Test (IPT)

The IPT technique to measure $\overline{J}$ and $\overline{M}_D$ is primarily based on the measurement of the contaminant concentration-time series, $C(t)$, in the effluent of multiple pumping wells aligned perpendicular to the prevailing direction of groundwater flow. While the use of $C(t)$ data for groundwater investigations was introduced in the early 1980's (Keely, 1982; Keely and Wolf, 1983), estimation of J and M_D using the IPT method was first described by Schwarz et al. (1998), and IPT field applications were described by Bockelmann et al. (2001, 2003) and Bauer et al. (2004). Under steady-state conditions, the mass discharge entering the capture zone of the pumping wells is equal to the product of the pumping rate and pumping well effluent concentration (Holder et al., 1998; Einarson and Mackay, 2001). However, achieving this steady-state condition may not be a practical goal for short-term pumping tests. Alternatively, the transient concentration-time series from a pumping well may be used to estimate the average spatial concentration in the capture zone of the well (e.g., Bayer-Raich et al., 2004, 2006), which is combined with an estimate of the groundwater flux to give the contaminant flux.

For the MIPTs conducted as part of this study, all wells were pumped concurrently rather than sequentially as conducted in previous deployments of the IPT method. Wells were pumped concurrently to minimize the disturbance to the contaminant distribution that would result from pumping each well sequentially, and to avoid the uncertainty associated with double counting mass located between adjacent wells. However, the disadvantage to concurrent pumping is both the development of stagnation points between wells, and a more complex flow field which precludes the use of the Bayer-Raich et al. (2004) analytical solution. With respect to the former disadvantage, it is nonetheless possible to sample a large fraction of the space between wells, so that the general goal of the IPT (i.e., a measured response integrated over a large area) is maintained. With respect to the latter disadvantage, the average spatial concentration in the capture zone of the well was estimated using the average concentration of the concentration-time series. The mass discharge was then obtained from the product of the contaminant flux and the cross-sectional flow area associated with the wells in the transect.

Using an average of the concentration-time series is, however, only an approximation that should be evaluated on a case by case basis. For transient pumping tests, the only statement that can be made without simplifying assumptions is that the mass recovered in the pumping well effluent over a given duration is equal to the mass in the capture zone of the well corresponding to the pumping duration and pumping rate. Beyond this, simplifying assumptions are needed if the concentration-time series from the pumping well effluent is to be used to estimate an average spatial concentration crossing the control plane around the pumping well. Following Bayer-Raich et al (2004), two degrees of spatial freedom are eliminated by assuming the concentration in the pumping well effluent is depth-averaged, and that changes in concentration over the length of the capture zone parallel to the direction of groundwater can be neglected. Therefore, concentration is reduced to a one-dimensional function that varies only in the spatial dimension perpendicular to groundwater flow. A closed form analytical solution was presented in Bayer-Raich et al (2004) for the condition of small dimensionless pumping times (see Bear and Jacob (1965) for a definition of dimensionless pumping time), and uses the analytical travel-time solution provided by Bear and Jacob (1965) for a single pumping well in a uniform flow field. This solution was extended to the case of an aquifer with linear retardation by Bayer-Raich et al. (2006). Since there is no general solution to travel time in a uniform flow field with multiple pumping wells, however, a numerical technique would be required to calculate the travel time distribution for each well and subsequently estimate the average one-dimensional concentration. However, if the concentration-time series is uniform or varies mildly, then the spatial concentration in the capture zone is uniform (or approximately so), and an average of the concentration-time series provides a reasonable estimate of the average one-dimensional concentration distribution at the control plane. With a few exceptions, the concentration-time series information obtained during the MIPTs conducted in this project were relatively uniform (for example, see the discussion in Brooks et al 2008 for the Hill AFB and Fort Lewis sites). When the concentration-time series changes significantly with time, then an average is less accurate. Work is currently being conducted to quantify the inaccuracy of a straight average when the concentration-time series varies significantly with time.

The IPT method was further modified to allow the estimation of groundwater fluxes based on the hydraulic information collected during the MIPT. The basis for this new approach was the assumption that the aquifer in the vicinity of the well transect could be described as one with homogeneous and isotropic hydraulic conductivity, and a uniform saturated thickness. Consequently, the hydraulic head (h; L) can be described using superposition of uniform flow and sink terms (Bear, 1979):

$$h(x,y) = -\frac{qB}{T}x + \frac{-Q}{4\pi T}\ln\left[\left(x-x_w\right)^2 + \left(y-y_w\right)^2\right] + h_0 \qquad (4.1\text{-}3)$$

where; B is the saturated thickness [L]; T is the aquifer transmissivity [L^2T^{-1}], equal to the product of hydraulic conductivity K [LT^{-1}] and B; and Q is the pumping rate [L^3T^{-1}] for a well located at x_w, y_w. Assuming the origin of the coordinate system coincides with a pumping well of interest and that the well transect is aligned perpendicular to the groundwater flow direction, the difference in head between the pumping well and a down-gradient monitoring well is:

$$\Delta h = -\frac{qB}{T}\Delta x + \frac{-1}{4\pi T}\sum_{i=1}^{n} Q_i \ln\frac{r_{obs[i]}^2}{r_{w[i]}^2} \qquad (4.1\text{-}4)$$

where the summation term accounts for concurrent pumping from n other wells in the transect, and $r_{obs[i]}$ and $r_{w[i]}$ are the distances from the observation well to the ith pumping well and from the pumping well of interest to the other pumping wells, respectively. Note that $r_{w[i]}$ for the pumping well of interest itself refers to the well radius. Equation (4.1-4) is linear with a slope of $(4\pi T)^{-1}$ and an intercept of $-qB\Delta xT^{-1}$. By measuring the difference in hydraulic head under a series of pumping rates, the hydraulic conductivity and the groundwater flux can be estimated using linear regression techniques and an *a priori* estimate of the saturated thickness. Equation (4.1-4) is based on the assumption that the ambient flow direction is perpendicular to the well transect. If this condition is not met, equation (4.1-3) can be modified to account for non-perpendicular flow (Brooks, et al, 2008).

For this project, each of the MIPTs was conducted immediately following the retrieval of the PFMs from the wells, thus allowing for a comparison of measured fluxes with minimum time lag. During the MIPT, flow rates and water levels are measured periodically at the wells and the combined flow is recorded as it accumulates in a temporary storage tank. Water levels are also monitored in nearby observation wells. The pumping rates are selected to bracket the calculated specific discharge rate across the control plane area, while still yielding a sufficiently large volume of pumped water (and hence sampling space surrounding the well) over the duration of the test.

Groundwater samples from the effluent of each pumping well are collected for contaminant analysis approximately once every three to six hours throughout each MIPT. Once collected, the samples are immediately placed in coolers with frozen ice packs, and shipped overnight to the laboratory for refrigerated storage and analysis.

Transect Method

The "Transect Method" (TM), as described in API (2003), involves estimating contaminant discharge per well as the product of the average groundwater flux ($\overline{\overline{q}}$, where the double over bar indicates a spatial average over a region larger than the well), the well cross sectional area (A), and the flux-averaged contaminant concentration in the well ($\overline{C}_J$, where the subscript J indicates a flux-averaged value, and the over bar indicates a spatial scale associated with the well). In turn, $\overline{\overline{q}}$ is estimated as the product of the hydraulic gradient ($\overline{\overline{i}}$) and saturated hydraulic conductivity ($\overline{\overline{K}}$). Measured hydraulic gradients and previously reported values of $\overline{\overline{K}}$ were used to estimate $\overline{\overline{q}}$ whereas contaminant concentrations measured during the MIPTs were used to estimate $\overline{C}_J$. Note that the first value of the concentration-time series measured during the MIPTs most closely represents the concentration measured by traditional groundwater sampling (e.g., bailing or pumping), and was therefore used in this approach.

4.1.2 Hill Air Force Base Operable Unit 2

From 1967 to 1975, spent degreasing solvents, primarily TCE, were disposed into two unlined disposal pits dug into the sandy surface soil located along the northeast boundary of Hill AFB, near Layton, UT. As a result, the DNAPL contaminated the underlying alluvium (the Provo Formation), predominantly as a mobile phase, pooled in topographic depressions on top of a thick clay aquiclude (the Alpine Formation), but also as an immobile or "residual" phase retained as ganglia by capillary forces in the alluvium's pore spaces. Under the Installation Restoration Program that began at Hill AFB in 1981, significant work has been completed to characterize, remove, and contain the site contamination; the site is now called Operational Unit number 2 (OU2).

In 1996, a containment wall (Figure 4.1-1) was constructed around the known source prior to initiation of several actions for enhanced DNAPL mass extraction within the contained zone. Additional DNAPL was discovered outside of the containment well in a depression in the clay surface (see Figure 4.1-1) in 1997 during efforts to quantify the mass of DNAPL remaining in the formation. This area, referred to as the Panel 5 area, was the focus of the present study (Brooks et al., 2008). The paleo-channel aquifer at OU2 consists of the shallow, permeable Provo Formation underlain by the thick, clay and silt Alpine Formation. The hydrogeology and DNAPL distribution within the containment wall have been described by Meinardus et al. (2002).

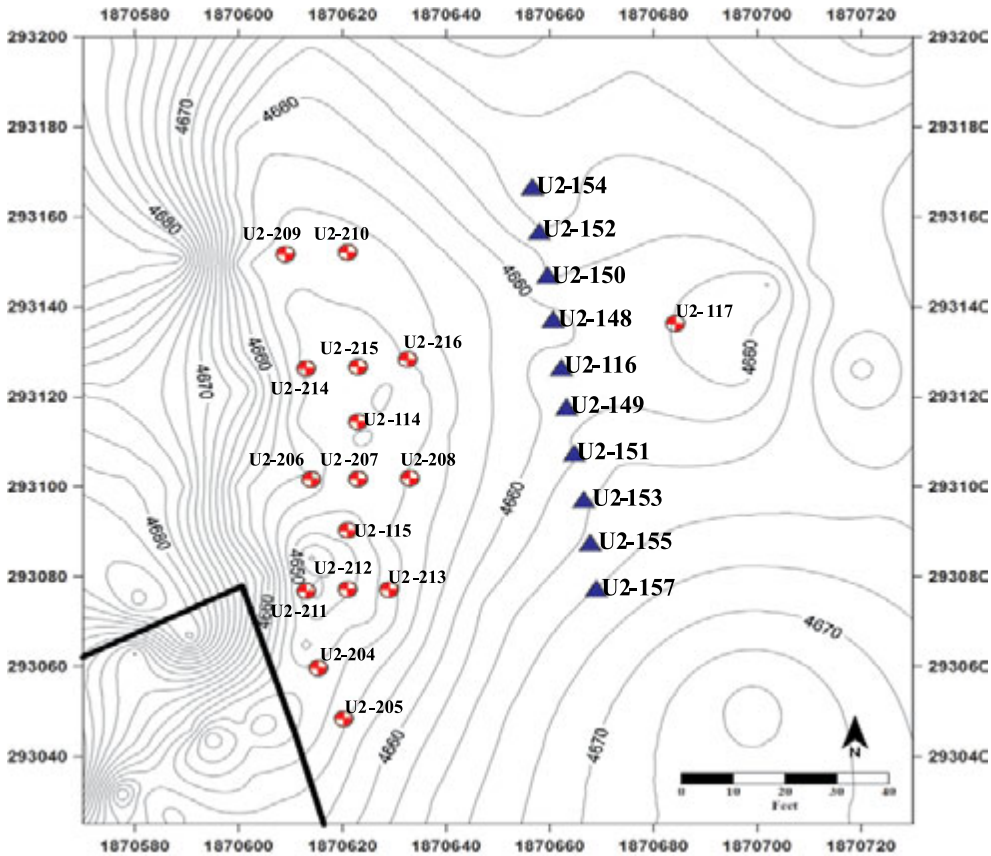

Figure 4.1-1. Plan view of Panel 5 area at Hill AFB. The thick black line in the lower left corner represents the containment wall installed around OU2. The triangular symbols represent wells used for mass flux measurements. Contour lines denote the elevation of the top of the Alpine Formation (Brooks et al., 2008).

To evaluate groundwater and contaminant fluxes, a control-plane transect of ten monitoring wells (wells U2-116 and U2-148 through U2-157) was installed in an approximate north-south direction, down-gradient from Panel 5 and just up-gradient from a natural spillway above the Weber River Valley (Figure 4.1-1). In October of 2001, with remediation of the DNAPL zone outside of the containment wall planned for the following summer, pumping used to contain the source area was discontinued. This allowed groundwater to flow over the sill area and through the transect of flux wells. A hydrograph from wells U2-214 and U2-117 is shown in Figure 4.1-2, and indicates the water elevation relative to the average clay elevation across the sill, as well as the water elevation during the remediation and flux measurement events.

In May 2002, groundwater and contaminant fluxes were measured, prior to the surfactant flood, using both innovative techniques described above. The PFM method allowed characterization of depth variations in *local* groundwater and contaminant fluxes along the well screen, while the MIPT provided flux values that were depth-averaged over the well-screen interval. The mass discharge estimates from PFM and MIPT were also compared with those from the Transect Method. The PFM measurements were performed prior to disturbing the groundwater flow field with the pumping tests. Surfactant-enhanced aquifer remediation was performed by URS and INTERA using the wells shown in Figure 4.1-1 (wells to the northeast of the containment wall) during June and July 2002 (URS and INTERA, 2003). Based on the results from a partitioning tracer test conducted in Panel 5, the pre-remedial estimate of DNAPL mass was 2,180 kg (360 gallons). Estimates of the DNAPL mass removed by the surfactant flood ranged from 1,340 kg (221 gallons), based on liquid-phase separation in the effluent treatment system, to 2,250 kg (371 gallons), based on effluent TCE breakthrough curves from the extraction wells.

Additional, post-remedial activities continued until February 2003, after which pumping stopped and groundwater levels increased, allowing groundwater to flow over the spillway (see Figure 4.1-2). Post-remedial characterizations indicated some DNAPL remained in the Panel 5 source zone. Post-remedial flux measurements were conducted at the transect in June 2003 and again in October 2004. Groundwater levels in the transect wells during the first post-remedial flux measurements were similar to those during pre-remedial measurements (Figure 4.1-2). Prior to the second, post-remediation flux measurement, however, groundwater levels rose approximately 107 cm (3.5 feet) above those during the first two measurements, presumably in response to above-average storm events that produced twice the amount of rainfall between December 2003 and February 2004 compared to the same period in the previous two years

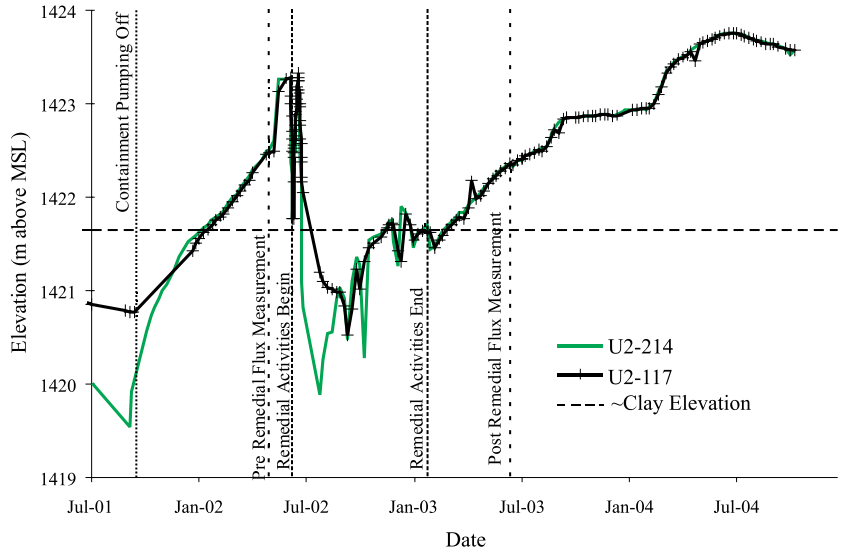

Figure 4.1-2. Hydrographs from Hill AFB OU2 wells U2-214 and U2-117, along with the average clay elevation (dashed line) across the transect. Also shown are selected events relative to the remedial and flux measurement activities.

Contaminant fluxes were measured before and twice after the surfactant flood by collecting 63, 48 and 106 SI-GAC samples from PFM deployments during each of the events. The TCE contaminant flux profiles from selected wells with the largest fluxes measured prior to remediation are provided in Figure 4.1-3. The contaminant flux profiles generally indicate that the higher contaminant flux zones were located near the aquifer clay interface prior to remediation. The primary contaminant mass flux is located between wells 152 and 149, with minimal flux outside this region. Following the surfactant flood, TCE levels were reduced significantly with only minimal local hot spots remaining in the transect (further details can be found in Brooks et al 2008).

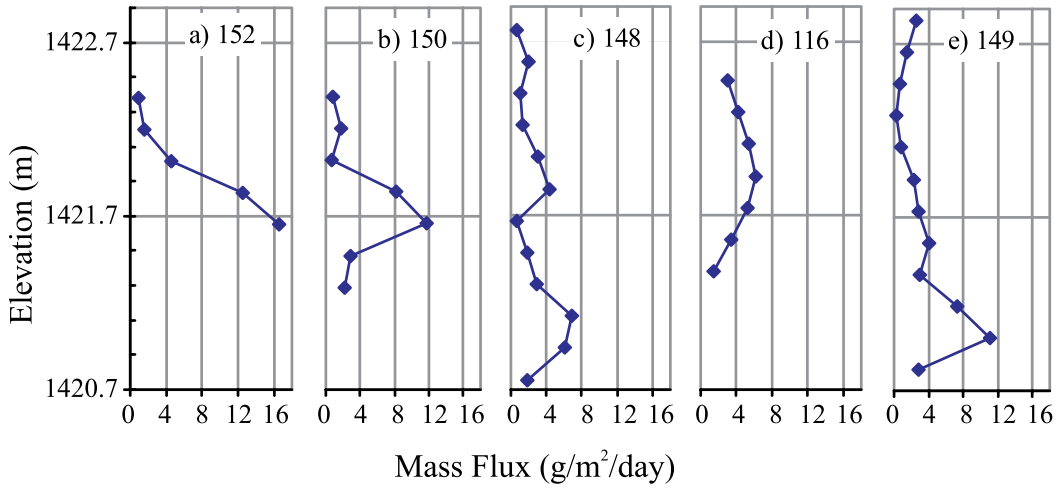

Figure 4.1-3. Contaminant flux distribution from selected wells with the largest fluxes as measured prior to remediation at Hill AFB (Brooks et al., 2008).

The depth profiles of contaminant fluxes from each well were averaged to determine a mean contaminant flux value for each well (Equation 4.1-1). These depth-averaged values are plotted in Figure 4.1-4 and can be later compared to the average contaminant flux for each well estimate based on the MIPTs. The data can also be integrated over the width of the control plane to determine a transect-wide contaminant mass discharge $\bar{\bar{M}}_D$ (g/day):

$$\bar{\bar{M}}_D = \sum_{j=1}^{n-well} \left(\sum_{i=1}^{n-vert} \left(J_{i,j} A_{i,j} \right) \right) \tag{4.1-5}$$

where *n-well* is the number of wells and $A_{i,j}$ is the area represented by the vertical sampling interval, b_i, and the horizontal spacing between wells. TCE mass discharge before source treatment was 76 g/day based on both PFM and MIPT methods (Table 4.1-1). Measurements one and two years after the source remediation ranged from 6.0 to 2.4 g/day (first and second measurements, respectively) based on the PFM approach, and 3.9 and 7.1 g/day based the MIPT method. Mass discharge, calculated using the TM approach, was 78, 7.2, and 1.3 g/day, for the pre-remedial, first and second post-remedial tests, respectively. These discharge measurement techniques provided comparable results, and show significant reduction (>90%) in TCE contaminant mass fluxes as a result of source treatment.

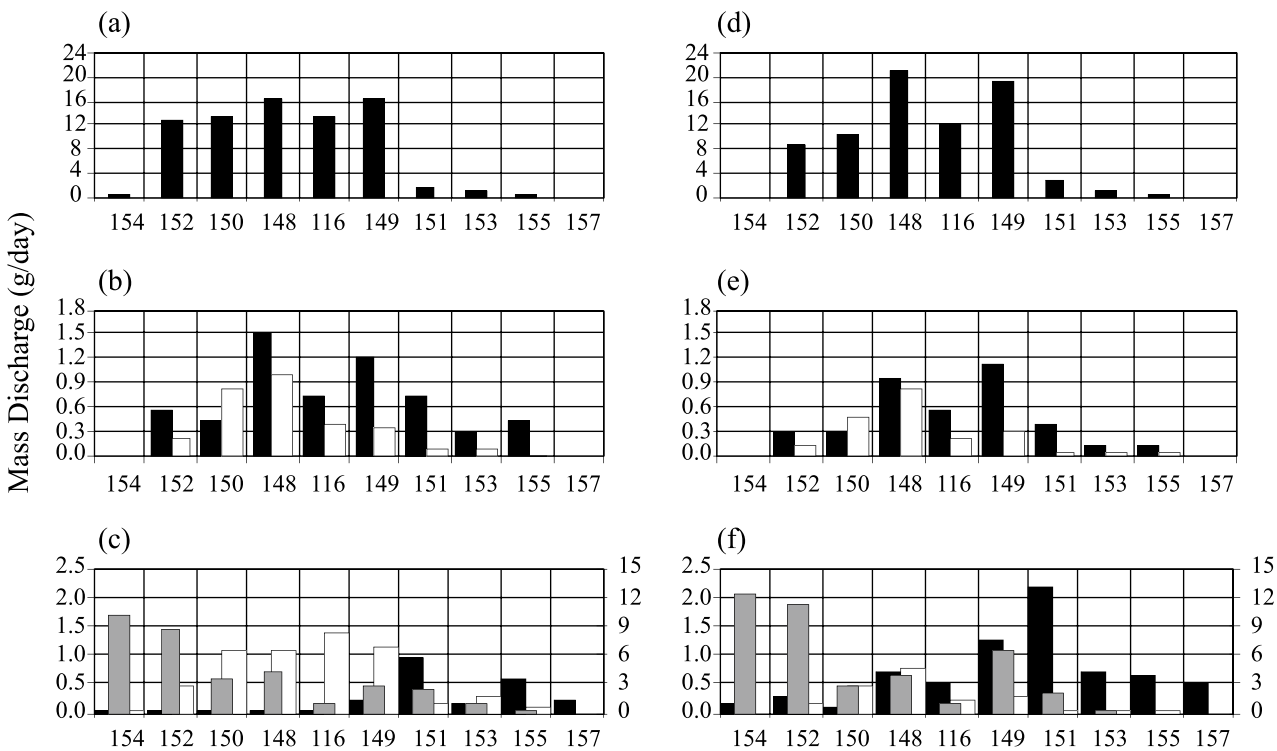

Figure 4.1-4. Average mass discharge (g/day) for each well at Hill AFB OU2, as measured by PFMs for a) May 2002 (pre-remedial), b) June 2003 (first post-remedial), and c) October 2004 (second post-remedial) tests; and as measured by MIPTs for d) May 2002 (pre-remedial), June 2003 (first post-remedial), and f) October 2004 (second post-remedial). TCE is shown in black, *cis*-DCE is shown in white, and MIBK is shown in grey. Note the change in scale on the y-axis to accommodate the data. In figures c) and f), the MIBK mass discharge is plotted on the second y-axis.

Table 4.1-1. Summary of TCE and DCE mass discharge (g/day) and combined TCE and DCE molar discharge (moles/day) for Hill AFB OU2 using PFM and MIPT results, as well as estimates based on the Transect Method (TM).

Discharge	Method	Pre-Remediation Test May 2002	First Post-Remediation Test Jun 2003	Second Post-Remediation Test Oct 2004
TCE (g/day)	PFM	76	6.0	2.4
	MIPT	76	3.9	7.1
	TM	78	7.2	1.3
DCE[1] (g/day)	PFM	a	3.0	5.8
	MIPT	b	2.0	20
	TM	b	3.8	4.2
TCE & DCE (mole/day)	PFM	0.58	0.077	0.078
	MIPT	0.58	0.051	0.26
	TM	0.59	0.094	0.054

[1]*Based on results from selected samples, DCE concentrations were an order of magnitude less than TCE concentrations during tests prior to source treatment. Therefore, DCE was not analyzed during the pre-remediation flux tests. More information is provided in Brooks et al. (2008).*

a - DCE concentrations were below the level of quantification.

b – DCE was not included in all sample analysis.

Under steady-state conditions, the contaminant mass discharge [M/T] entering the capture zone of a well during the MIPT is the product of the pumping rate [L^3/T] and contaminant concentration [M/L^3]. Achieving such steady-state conditions most likely did not occur within the test durations, consequently, the contaminant mass discharge was calculated as the product of the contaminant flux and the cross-sectional area assigned to each well. The cross-sectional area for each well was based on the well spacing (305 cm) and the depth between the water table and the clay interface. The contaminant flux was calculated as the product of the Darcy flux (the transect-wide average Darcy flux based on the MIPT hydraulic data as described in Section 4.1.1) and the average concentration of the concentration-time series. The mass discharge measured for each well in each test is shown in Figure 4.1-4. The mass discharge estimates based on the MIPT tests are similar to those measured by the PFM method with exceptions noted for the DCE mass discharge and combined TCE/DCE molar discharge measured during the second post-remediation test (Table 4.1-1). The difference in estimates is primarily attributed to the difference in estimated Darcy flux for the two methods, which differed by a factor of 2.

Results from the post-remediation tests indicate a significant increase in the concentration of DCE relative to the pre-remediation DCE concentrations (Figure 4.1-4). Since DCE was not present in significant concentrations prior to remediation, these results indicate that the surfactant used for in-situ flushing may have contributed to the reductive dechlorination of TCE, as suggested by the presence of Methyl Isobutyl Ketone (MIBK) in the second post-remedial test (Figure 4.1-4). The contaminant flux of TCE and DCE can be combined on a molar basis as shown in Table 4.1-1. The total pre-remediation molar flux was 0.58 to 0.59 moles/day, and with the exception of the second post-remediation results from the MIPT, the post-remediation total mass discharge (molar basis) TCE and DCE ranged from 0.051 to 0.094 moles/day. Based on these measures, total molar discharge reductions ranged from 84 to 91%. If groundwater flow continues as it has in the past, the contaminant discharge will likely continue to decline for the next several years before new, quasi steady-state conditions are achieved. At this site the wells were relatively close together (~300 cm spacing). Concentrations of TCE observed at the well remained relatively constant for all of the pumping rates used. This suggests that it was not possible using the MIPT method to delineate spatial variability within the well spacing using the flow steps implemented during these measurements. Considering the well spacing, finer delineation may not be necessary.

During remedial activities within Panel 5 at the OU2 site, the surfactant flood resulted in estimated DNAPL mass removal ranging from 1,340 kg (221 gallons) to 2,250 kg (371 gallons) (URS and INTERA, 2003). Based on the estimated DNAPL mass prior to the remedial activity [2,180 kg (360 gallons) based on a partitioning tracer test], 60% or more of the DNAPL was removed. Free phase DNAPL has since been detected in wells within Panel 5, indicating some DNAPL was not removed. Based on the PFM and MIPT contaminant flux measurements reported here, TCE flux reductions ranged from 92% to 97%, based on the PFM and MIPT measurements. Consequently, at this site partial DNAPL mass removal from the source did result in a reduction in the contaminant mass flux. It should be noted that, as shown by groundwater elevation data in Figure 4.1-2, groundwater flowed over the spillway for approximately four months prior to the first post-remediation flux measurements. This is insufficient time to establish steady-state contaminant transport conditions from the source area to the well transect. However, in light of the active pumping activity that occurred in the Panel 5 source area, the flux measurements cannot be viewed as those originating from a stagnant pool of water in contact with the DNAPL. Moreover, the first post-remediation measurements were conducted under very similar conditions to the pre-remediation measurements with respect to the duration in which groundwater flowed through the transect prior to the flux measurements.

4.1.3 Fort Lewis East Gate Disposal Yard Site

The EGDY site, located on the Fort Lewis Military Reservation near Tacoma, Washington, was used from 1946 to 1960 as a disposal area for drums of used solvents and oils that were placed in excavated trenches, and is the source for a large chlorinated solvent plume (predominantly TCE) which extends to the northwest for approximately 2.5 miles (USACE, 2002). The plume was discovered in the mid 1980's, and the primary source was identified as the EGDY site. The operation of a pump-and-treat system was started in 1995 for hydraulic control purposes, and drum excavation activities at the EGDY site were conducted between late 2000 and mid 2001. In 2001, thermal treatment was selected as a source removal method, and subsequent characterization work conducted in 2001 and 2002 identified three main areas of DNAPL contamination within the EGDY site. These areas were referred to as NAPL Areas 1, 2, and 3 (NA1, NA2, and NA3, respectively). The focus of work reported here was on the performance assessment associated with remedial activity conducted in NA1 (Brooks et al., 2008). While the source zone contained other petroleum-related contaminants, our focus herein is limited to an assessment of the changes in mass discharge of chlorinated solvents.

The surficial, unconfined aquifer at the site is composed of the Vashon Recessional Outwash/Steilacoom gravel unit (consisting of loose, well-graded sandy, cobbly gravel or gravelly sand). In the immediate vicinity of NA1, this unit is underlain by Vashon Till (consisting of loose to dense silty, sandy gravel with some clay), which is considered to be a generally continuous intermediate aquitard. This layer in turn is underlain by more Vashon Recessional Outwash/Steilacoom gravel or Vashon Advance Outwash (loose sandy gravel to gravelly sand with cobbles). The contamination is predominantly located in the surficial unconfined aquifer, although contamination has migrated into the aquifer below the Vashon Till layer (USACE, 2002). Regional groundwater flow is directed to the northwest towards American Lake, as indicated by the orientation of the TCE contaminant plume.

A control-plane transect of ten monitoring wells (LC-201 through LC-207, LC-211, LC-212 and LC-213) was installed in the surficial aquifer immediately downgradient of the source area (Figure 4.1-5) to measure groundwater and contaminant discharge from NA1. In November of 2003 the groundwater and contaminant discharge were measured prior to thermal treatment using PFMs and MIPTs. In-situ resistive heating thermal treatment was conducted by Thermal Remediation Services, Inc in NA1 from December 2003 until August 2004 (Beyke and Fleming, 2005; TRS, 2005; Powell et al., 2007). To ensure pre- and post-remedial mass discharge measurements were comparable, the post-remedial measurements were delayed until the groundwater temperatures had returned to ambient levels. Moreover, treatment of NA2 was initiated shortly after NA1 treatment, consequently NA1 post remedial discharge measurements were delayed until the completion of NA2 treatment (which occurred in August, 2005) because of the proximity of the flux well transect to NA2. Consequently, post-remedial discharge measurements for NA1 were collected in June 2006.

Shallow transect wells LC-201 though LC-207 (Figure 4.1-5) were installed at a nominal spacing of 6.1 m (20 feet) between August 23 and 25, 2003 using a rotosonic drilling method. Additional information on the design and installation of these wells are presented by Brooks et al., (2008). Initial samples collected from these wells indicated relatively high concentrations in LC-207 (data not shown), consequently the transect was extended to the north by three more wells (LC-211, LC-212, and LC-213). These additional wells were installed between October 16 and 17, 2003 using an air rotary drilling method, and similar construction materials as used for wells LC-201 through LC-207. All wells were screened from above the water table to the top of the till unit at a depth of approximately 10.1 m (33 ft). The wells were installed in a 15.2-cm diameter borehole, and were constructed using 5.08-cm diameter stainless steel casings, 2.44 m in length, and 5.08-cm diameter stainless steel well screens, 7.62 m in length. A 12/20 sand filter pack was installed in the annular space around the well screens, on top of which was placed a bentonite seal, and the remaining space to land surface was filled with grout.

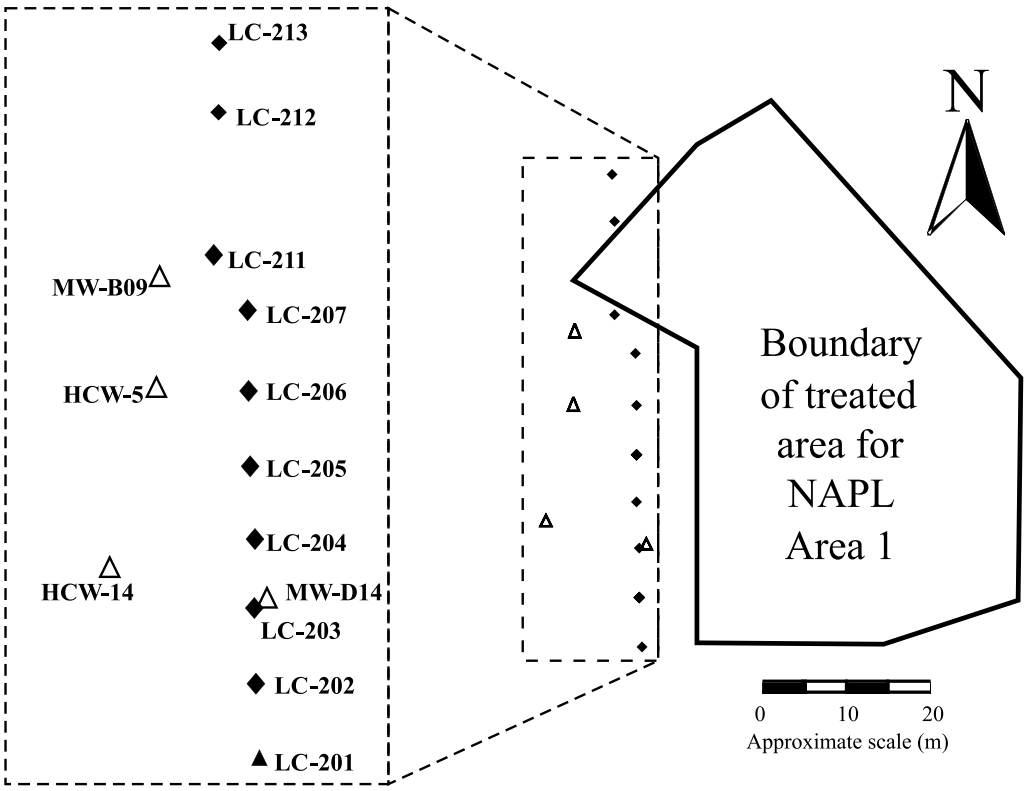

Figure 4.1-5. Plan view of the NA1 source area at the East Gate Disposal Yard site at Fort Lewis and the downgradient flux well transect. The diamonds represent flux wells and the triangles represent hydraulic monitoring points (Brooks et al., 2008).

The PFMs were deployed for a period of three days: October 22, 2003 through October 25, 2003 for pre-remedial measurements, and June 2, 2006 to June 5, 2006 for post-remedial measurements. After the designated deployment period, the PFMs were retrieved and sampled using similar methods to those described in Annable et al. (2005). Note that the PFM results reported below were not corrected for convergence associated with flow around the well screen (Hatfield et al., 2004; Klammer et al., 2007). The convergence factor (defined as the ratio of flux inside the PFM to that in the aquifer) can be estimated based on hydraulic conductivity estimates of the aquifer ($K_{aquifer}$), well-screen filter pack material ($K_{filter\ pack}$), well screen (K_{screen}) and PFM sorbent used (K_{PFM}). Often these properties are difficult to estimate or measure because fine materials are removed in the developed zone near the well, some of which may become trapped in the well screen, reducing its hydraulic conductivity. Best estimates of these properties for the NA1 site are $K_{aquifer}$ = 9,100 cm/d; $K_{filter\ pack}$ = 43,200 cm/d; K_{screen} = 3,540 cm/d and K_{PFM} = 33,000 cm/d. This produces an estimated convergence factor of 1.03. The PFM data presented here are uncorrected (i.e.,

the flux as measured inside the PFM is presented), and given the relative insignificance of 3%, it is assumed that the flux inside the PFM and that in the aquifer are the same. Also, it is noted that the convergence factor has no impact on the comparison of pre- to post-remediation PFM results.

The MIPTs were conducted as soon as possible following the retrieval of the PFMs from the wells to allow a comparison of measured fluxes with a minimum time lag. The pre-remedial MIPT was conducted between November 3, 2003 and November 7, 2003, and the post-remedial MIPT was conducted between June 12, 2006 and June 17, 2006. Flow rates and water levels were measured periodically at each of the wells and the combined flow was recorded as it accumulated in a temporary storage tank. Water levels during the pre-remedial shallow transect MIPT were also monitored in one well (D14) near well LC-203, and one down-gradient well (B09); and water levels in two additional down-gradient wells (HCW-5 and HCW-14) were also monitored during the shallow post-remedial MIPT.

For the pre-remedial MIPT, each well was pumped using a single peristaltic pump with dual heads. Once the MIPT was underway, it became evident however that the peristaltic pumps were inadequate to induce sufficient hydraulic stress based on the limited amount of drawdown observed in the pumping wells. Based on this experience, the pumping equipment used during the post-remedial MIPT included a centrifugal pump that provided for higher pumping rates.

Groundwater samples from the effluent of each pumping well were collected for contaminant analysis approximately once every four hours throughout each MIPT. Once collected, the samples were immediately placed in coolers with frozen ice packs, and the coolers were shipped overnight to the laboratory for refrigerated storage and analysis using a gas chromatograph/flame ionization detector (GC/FID). For the post-remedial test, initial results indicated that the contaminant concentrations were below method detection limits. Consequently, the samples were re-analyzed using a hexane extraction process to concentrate the contaminant in the samples prior to GC/FID analysis.

Based on 204 samples collected from the shallow flux well transect during the pre-remedial PFM deployment, the minimum, maximum, mean, and spatial standard deviation groundwater flux values were 0.8 cm/day, 68.8 cm/day, 26.9 cm/day, and 19.3 cm/day, respectively. Note that PFM data are integrated over the vertical sampling interval of approximately 30 cm. Based on 166 samples collected from the shallow flux well transect during the post-remedial PFM deployment, the minimum, maximum, mean, and spatial standard deviation groundwater flux values were 0.3 cm/day, 70.4 cm/day, 16.1 cm/day, and 11.7 cm/day, respectively. The mean post-remedial groundwater flux was less than the pre-remedial groundwater flux, apparently the result of changes in the local hydraulic gradients.

As discussed above, the pumping rates used during the pre-remedial MIPT were not large enough to induce sufficient changes in hydraulic head to estimate the groundwater flux directly from the test results, an issue that was compounded by interference from a series of precipitation events that occurred prior to and during the MIPT. As a result, the pre-remedial groundwater flux was estimated by scaling the Darcy flux estimates obtained during the post-remedial MIPT using the ratio of the pre- to post-remedial hydraulic gradients as measured in surrounding wells. Furthermore, an analysis of the hydraulic gradient in the vicinity of the transect indicated considerable temporal variation in the flow direction, and it was considered necessary to explicitly account for the flow direction relative to the transect.

The hydraulic gradient in the vicinity of the transect was estimated using hydraulic head measurements obtained from the US Army Corps of Engineers. For the pre-remedial test, an average of measurements collected on November 4 and November 20, 2003 were used, providing an average hydraulic gradient magnitude of 0.0037, directed at an azimuth of 294 degrees. For the post-remedial test, the average of measurements collected on June 6 and June 12, 2006 were used, which gave an average hydraulic gradient of 0.0021 directed at an azimuth of 219 degrees (see Brooks et al [2008] for a discussion of the groundwater flow direction and its impact on mass discharge estimates crossing the source control plane). While November 4, 2003 and June 12, 2006 corresponded to the start of the MIPTs, the rates used at the beginning of these tests were considered insufficient to affect the surrounding water elevations (i.e., the maximum drawdown in the wells was only 2 cm over the first six hours of the test, prior to or during which the surrounding water level measurements were collected).

The transect-wide average post-remedial groundwater flux based on the MIPT data was estimated at 18.0 cm/day. The pre-remedial groundwater flux was estimated by multiplying the post-remedial groundwater flux by the ratio of the pre-remedial to post-remedial hydraulic gradients. The pre-remedial transect-wide groundwater flux estimate was therefore 31.7 cm/day.

Contaminant flux measurements based on the accumulation of contaminant in PFMs were completed at each of the 204 pre-remedial sampling locations and 166 post-remedial sampling locations. The contaminant flux profiles from selected wells with the largest fluxes measured prior to remediation are provided in Figure 4.1-6. The depth profiles of contaminant flux from each well were averaged to determine a mean contaminant flux value for each well, which was then multiplied by the cross-sectional area associated with that well (equal to the product of the saturated thickness and well spacing) to provide a mass discharge estimate per well (Figure 4.1-7). The data were also integrated over the width of the control plane to determine a transect-wide contaminant mass discharge $\overline{\overline{M}}_D$ (g/day). The estimated total pre-remediation TCE contaminant mass discharge was 743 g/day, while the post-remediation value was 3.4 g/day (Table 4.1-2). This corresponds to a contaminant mass discharge reduction of approximately 99.5%. The pre and post remedial DCE mass discharge was 155 g/day and 5.7 g/day, respectively, corresponding to a mass discharge reduction of 96.4%.

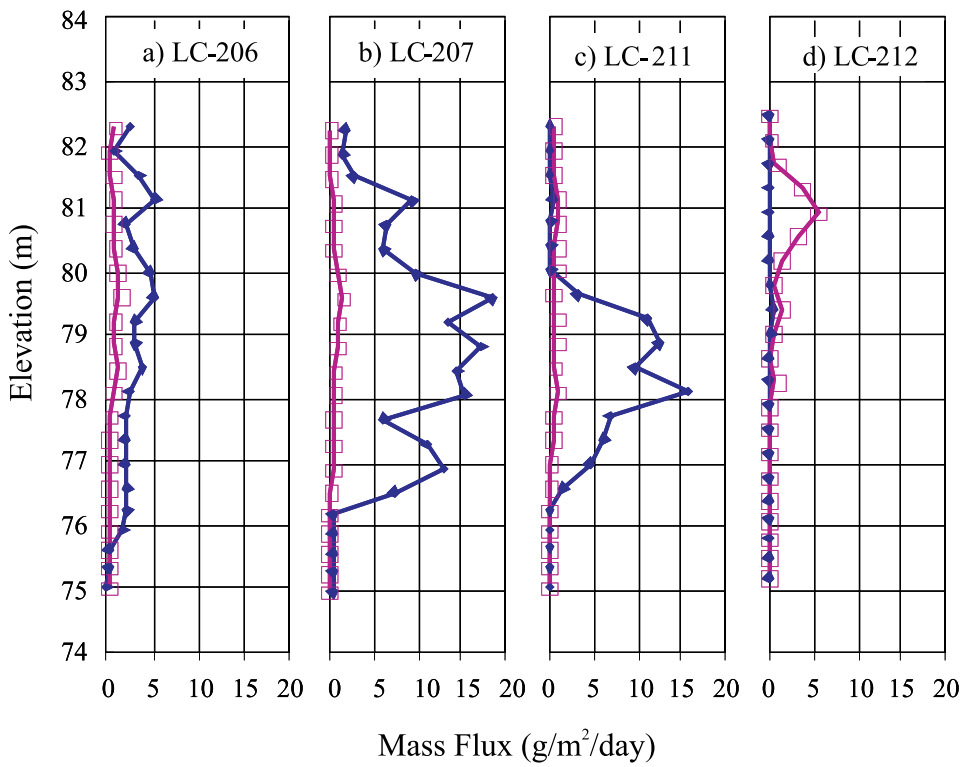

Figure 4.1-6. Mass flux profiles measured in selected wells with the largest fluxes as measured prior to remediation using the PFMs. The solid diamond represents TCE, and the open square represents DCE (Brooks et al., 2008).

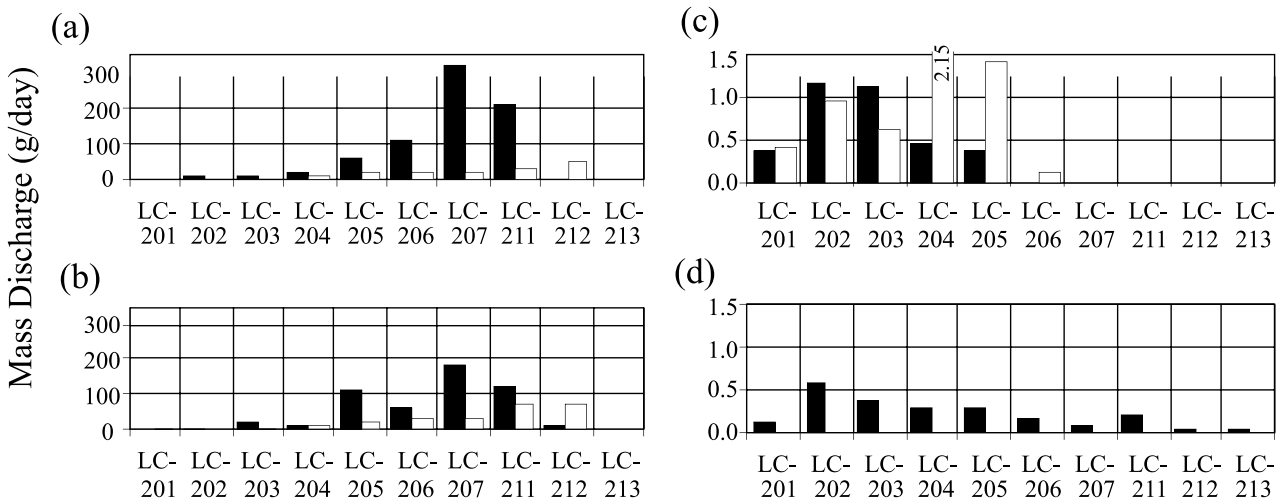

Figure 4.1-7. Average mass discharge (g/day) for each well at Fort Lewis. Measured by a) PFMs and b) MIPT for the pre-remedial tests; and by c) PFMs and d) MIPT for the post-remedial tests. TCE is shown in black, and *cis*-DCE is shown in white. Note the change in scale on the y-axis from the pre- to the post-remedial results to accommodate the data.

Using the MIPT, the total mass discharge across the transect was estimated as the sum of the contaminant mass discharge for each well, calculated as the product of the contaminant flux and the cross-sectional area assigned to each well. The cross-sectional area for each well was based on the well spacing (average spacing of 6.4 m) and the depth between the water table and the bottom of the well screen (approximately 7.6 m). The contaminant flux was calculated as the product of the groundwater flux and the average concentration measured in the pumping well effluents. For these calculations, sampling results reported as "not detected" were assigned a value of zero. The mass discharge measured for each well in each test is shown in Figure 4.1-7. The total TCE mass loading for each test and the DCE mass loading for the pre-remedial test is presented in Table 4.1-2, along with the combined TCE and DCE molar loading for each test.

The pre-remedial transect-wide TCE mass discharge estimates based on the MIPT test (536 g/day) was less than the estimate by the PFM method (743 g/day), while the DCE mass discharge estimate by the MIPT method (257 g/day) was higher than that estimated by the PFM method (155 g/day). For the post-remedial test, the TCE mass discharge by the MIPT method (2.2 g/day) was likewise less than the PFM estimate (3.4 g/day), but the DCE mass discharge by the PFM (5.7 g/day) was higher than the MIPT method (0 g/day, DCE was not detected in the pumping well effluent samples).

A mean vertical gradient in the Vashon aquifer was estimated to be directed upward at 0.019 near NAPL Areas 1 and 2 (USACE, 2002). Vertical gradients may create ambient flow and mixing in wells that are screened across heterogeneous contaminant distributions. However, once PFMs are deployed in the wells, the sorbent material and impermeable spacers minimize vertical flow in the well. Moreover, while deployed the PFM is measuring a temporally integrated response to groundwater that flows into the well, which predominantly occurs from up gradient, not down gradient. Any biases in the distribution of contaminants created by ambient flow in the well will be predominantly reflected down gradient of the well, not up gradient. Alternatively, if it is assumed that the PFMs or an aqueous sample (in the case of the MIPT for example), is impacted by ambient flow in the well, the critical issue is the potential dilution of concentration below detection limits as a result of vertical flow in the well. Otherwise, dilution of concentration (but still detectable) across the well depth should not affect the mass discharge estimates since the depth over which the dilution occurred is explicitly included in the estimate of the control plane area. Using an estimated pre-remedial detection limit of 0.1 mg/L, a pre-remedial groundwater flux of 30 cm/day, and a control plane area of ~418 m^2, then a rough estimate of the sensitivity of the pre-remedial mass discharge estimate is ~13 g/day, which is an order of magnitude lower than the pre-remedial mass discharge estimates. Likewise, using an estimated post-remedial detection limit of 0.005 mg/L, a post-

remedial groundwater flux of 16 cm/day, and a control plane area of ~418 m^2, then the estimated sensitivity of the post-remedial measurements is ~0.3 g/day, which is again an order of magnitude lower than the post-remedial mass discharge estimates. Consequently, it seems unlikely that dilution due to vertical flow would significantly change our conclusions about mass discharge reduction at Fort Lewis.

During remedial activities at NA1, the thermal treatment resulted in an estimated TCE mass removal of 2,576 kg (425 gallons) (Beyke and Fleming, 2005). Based on the estimated DNAPL mass prior to the remedial activity [3,800 kg (627 gallons) based on boring data], 68% of the TCE was removed. According to PFM and MIPT contaminant flux measurements, TCE flux reductions were 99% or higher. Consequently, at this site partial DNAPL mass removal from the source did result in a significant reduction in the contaminant mass flux.

Table 4.1-2. Summary of TCE and DCE mass discharge (g/day) and combined TCE and DCE molar discharge (moles/day) for Fort Lewis EGDY site using PFM and MIPT results, as well as estimates based on the Transect Method (TM).

Discharge	Method	Pre-Remediation Test Oct 2003	Post-Remediation Test Jun 2006	Percent Reduction in Mass or Molar Discharge
TCE (g/day)	PFM	743	3.4	99.5%
	MIPT	536	2.2	99.6%
	TM	688	2.8	99.6%
DCE (g/day)	PFM	155	5.7	96.4%
	MIPT	257	0	100%
	TM	288	0	100%
TCE & DCE (mole/day)	PFM	7.3	0.085	98.8%
	MIPT	6.7	0.017	99.8%
	TM	8.2	0.021	99.7%

4.1.4 Former Sages Dry Cleaner Site, Jacksonville, Florida

The former Sages Dry Cleaner site in Jacksonville, Florida, was operational from 1968 to 1973 and from 1979 to 1989, and the primary subsurface contaminant at the site is PCE. Although the PCE release history is unknown and PCE was not stored on site, PCE is presumed to have been released through operational activities associated with the dry cleaner business. Based on soil cores, the site-specific hydrogeology consists primarily of fine-grained sands with a discontinuous clay layer at approximately 10.7 m (35 ft) below ground surface (bgs). The water table ranges from approximately 2 to 2.6 m (6.5 to 8.5 feet) bgs with a natural hydraulic gradient of 0.0025 to 0.006. The groundwater flow direction is generally westward toward a drainage canal located immediately adjacent to the western boundary of the site. The canal generally serves as a sink for groundwater discharge, except during large storm events when the canal water elevation rises, resulting in a reversal of the hydraulic gradient. Contamination is limited to the surficial aquifer system, and DNAPL characterization activity indicated the presence of DNAPL predominantly at approximately 9.1 m (30 ft) bgs.

A pilot-scale field test of in-situ ethanol flushing was conducted at the site in August 1998 (Jawitz et al., 2000). The target area for this first flood is shown in Figure 4.1-8. The initial mass of PCE in the target area was estimated at 68 L of PCE based on a pre-remedial partitioning tracer test. The ethanol flushing demonstration removed 43 L based on mass recovered from the extraction wells, resulting in 62% removal effectiveness. This performance estimate is supported by soil core results (65% removal) and a post-remedial partitioning tracer test (63% removal). Extensive monitoring of contaminant concentrations and geochemical parameters within the source zone and downgradient plume using a conventional monitoring well network were conducted for more than 3 years following the pilot-scale ethanol flood (Mravik et al., 2003). This monitoring confirmed enhanced in-situ reductive dechlorination resulting from the residual ethanol that remained in the subsurface.

A second ethanol flood to remove additional PCE was conducted in 2004 (see Figure 4.1-8 for the target area of the second flood, located from 7.6 to 10.7 m [25 to 35 ft] bgs). This provided the opportunity to evaluate the impact of source depletion on contaminant mass flux. A total of 13 injection and recovery wells were installed to conduct the second flood. Soil samples from 7.6 to 10.7 m (25 to 35 ft) bgs were collected from cores obtained during well installation, and results were used to estimate that 11 L of PCE were present in the target zone (LFR, 2005). Ethanol flushing of the second target area during June and July, 2004 resulted in the removal of approximately 21 L of PCE, the majority of which came from one of three recovery wells (RW 202, the eastern most recovery well located between MLS1 and MLS2 as shown in Figure 4.1-8).

At the Sages site, bundled MLS wells were employed to add a vertical component to remediation and monitoring studies for three dimensional analyses. A month prior to the August 1998 ethanol flood, MLS 1-7 were installed in the source zone, each coupled to a respective recovery well (RW). Moreover, MLS locations 8 through 12 were installed at the same time to monitor the downgradient plume. MLS locations 13 and 14 were installed in mid 2004, and were used to augment the existing MLS monitoring network. During sampling, each MLS well tube was pumped and purged to 40 mL before the sample was collected. The samples were analyzed by gas chromatography for ethanol and volatile organic chemicals (VOCs). Figure 4.1-8 shows the MLS and flux well locations, as well as the general areas targeted during the first and second ethanol flooding events.

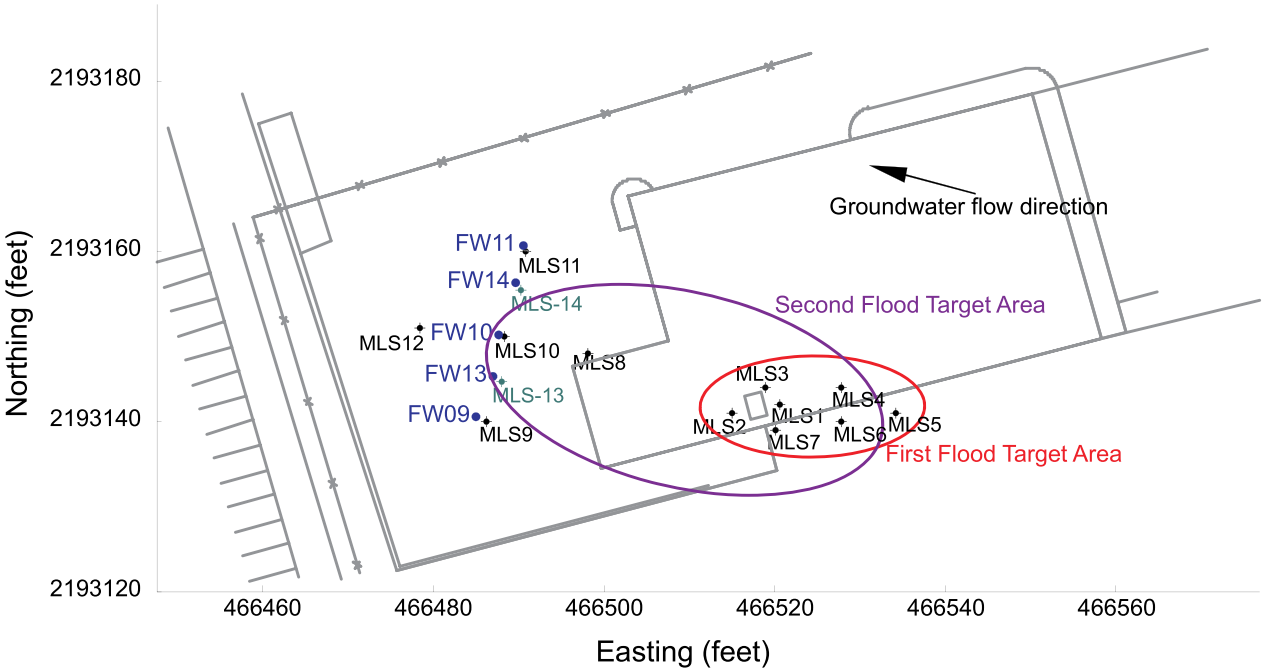

Figure 4.1-8. Multilevel sampler locations, flux well locations, and the general areas targeted during the first and second ethanol flushing events at the Sages site. Units shown are the Florida State Plane Coordinate System.

The MLS network was sampled semi-annually for the six-year period following the 1998 ethanol flood pilot test. The MLSs located orthogonal to the mean groundwater flow in the source zone (i.e., MLS-1, MLS-3, and MLS-7) are referred to as the source zone transect. The MLSs perpendicular to groundwater flow ten meters downgradient from the source zone (i.e., MLS-9, MLS-10, and MLS-11 prior to 2004, and those MLSs plus MLS-13 and MLS-14 afterwards) are designated the downgradient transect. The final MLS sampling event used in this study took place just prior to the second, full scale flushing event in June 2004.

Long term MLS monitoring was performed to assess the changes in concentration throughout the site over the stated time period. Spatial patterns of the dissolved plume emanating from the source zone are discussed as well as mass discharge estimates across the transects. The concentrations are reported as the molar sum concentration due to the initiation of microbial reductive degradation of residual PCE evidenced by increases in PCE biodegradation daughter products.

The mean molar concentration sum of each transect was calculated and then M_D was determined from the product of the site estimated Darcy flux and the cross sectional area of each transect:

$$M_D = \overline{C}_{sum} * \overline{q} * A_{xs} \quad . \tag{4.1-6}$$

The site characterization estimates for hydraulic conductivity (6 m/day) and hydraulic gradient (0.0025) were used to estimate the site Darcy flux ($\overline{q}$) of 0.015 m/day. The mean mass flux ($\overline{J}$) was calculated as the product of $\overline{C}_{sum}$ and $\overline{q}$. The mass discharge was determined from the product of the mass flux and the cross sectional area of the transect (A_{xs}) using the modified version of Guilbeault et al. (2005) and Kubert and Finkel (2006) in Equation 4.1-6.

Mravik et al., (2003) reported increases of acetate as ethanol concentrations decreased due to the microbial oxidation of ethanol. Furthermore, ethanol is non-partitioning and completely miscible, thus it will be slowly carried away by the groundwater. As ethanol was removed from the source zone by natural gradient flow and microbial degradation, daughter products of PCE dechlorination were detected.

The field test demonstrated the threshold toxicity of ethanol on the microbial population that was observed by Mravik et al. (2003) in laboratory tests with Sages core material. They reported laboratory column biodegradation of PCE when the ethanol concentration was less than 1%. In Figure 4.1.9, the ethanol and daughter/parent concentration ratios are plotted for post remedial MLS sampling six months to four years after the pilot test. In the deeper lower flow zones, less of the remedial fluids were recovered during the test. The highest concentrations of residual ethanol were found in the deepest MLS samples immediately after the flood (up to 18%). Once the ethanol concentration dropped below 1%, increases in TCE and c-DCE concentrations were observed in groundwater within the transect.

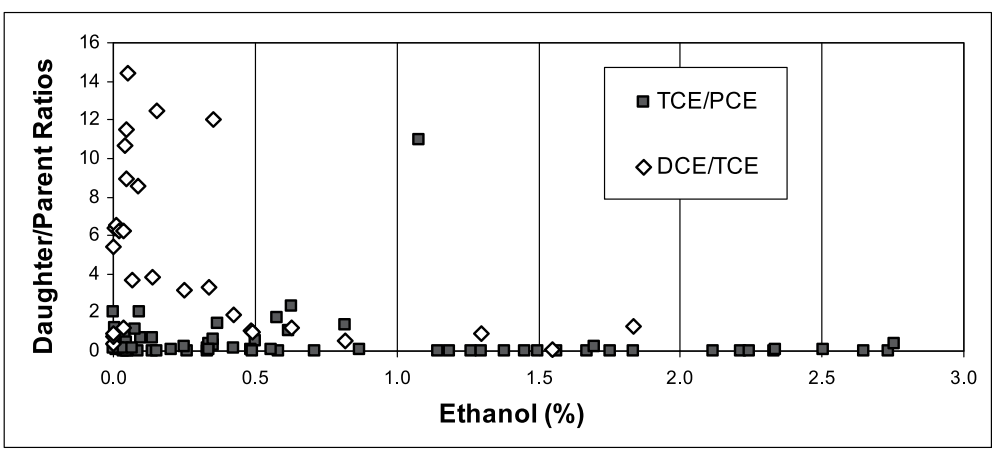

Figure 4.1-9. MLS source zone PCE/TCE and TCE/c-DCE ratios as a function of ethanol concentration in the groundwater up to four years after the 1998 pilot test (Sages site).

Source Zone Transect Concentrations. The source zone concentrations were monitored for six years after the flushing pilot test at the MLS wells. The concentrations of PCE, TCE, DCE, and VC were monitored at the source zone transect (MLS-1, MLS-3, and MLS-7).

Aside from a slight post-remedial PCE flux rebound, the site demonstrated little variability in the mean molar sum in each MLS for the first year after the flood. A slight increase in molar concentrations was detected at the source zone transect in January 1999, 5 months after the flood. By May 2000, the mean concentration molar sum began to increase significantly. In 2002, the concentrations increased markedly during the period of greatest biological activity, and then began to decrease in 2003. By June 2004, source zone molar sum concentrations decreased further to a range of 0.03-0.5 mM, lower than the initial post flushing concentration range of 0.19-0.98 mM in August 1998. Several plausible explanations for the significant decrease in source zone concentrations include, source mass depletion, aging of the source zone architecture, and decrease of microbial activity due to loss of ethanol substrate. Surfer™ was used to create contour plots of the source zone transect molar sum of chlorinated species (Figure 4.1-10). Standard kriging was applied to interpolate between measured data points. The black plus (+) marks indicate the location of each MLS sampling point.

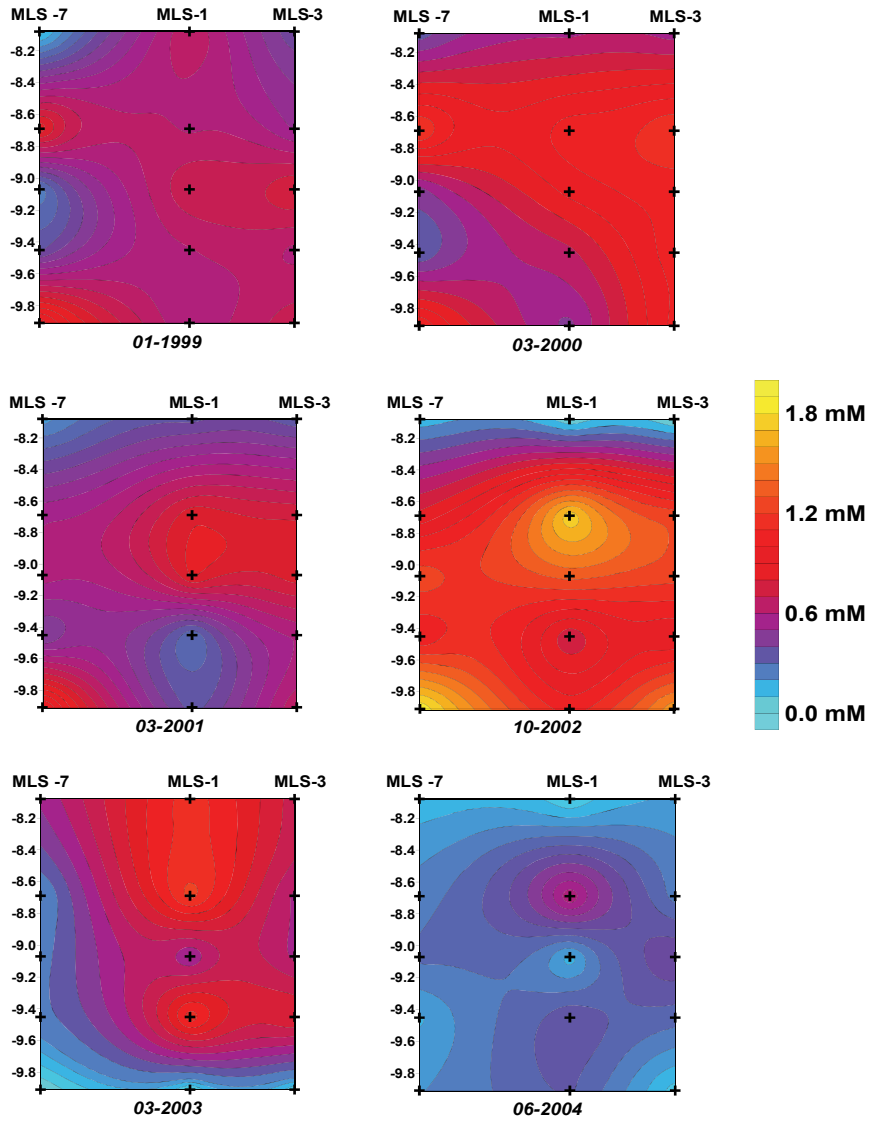

Figure 4.1-10. Sages source zone transect natural gradient concentrations for the 6-year period after the August 1998 ethanol flood. Values are millimolar sums of chlorinated ethenes (mM). Transect is MLS-7 to MLS-3, 1.49 m across, 8.08 m to 9.91 m bgs.

Source Zone Transect Mass Discharge. As aqueous PCE discharge decreased in 1999 and 2000, DCE mass flux rate increased as a result of biological dehalorespiration (Figure 4.1-11). This trend continued until 2003. In the last two years of the study period (2003 and 2004) all discharges decreased except vinyl chloride (VC), which was not detected until 2003 and 2004. Maximum and minimum mass discharge values determined in the source zone transect ranged from 1.9 to 31.1 mmol/day (0.3 to 5.2 g/day) for PCE, 0 to 2.3 mmol/day (0 to 0.3 g/day) for TCE, 0 to 36.9 mmol/day (0 to 3.6 g/day) for DCE, and 0 to 0.9 mmol/day (0 to 0.06 g/day) for VC. The site experienced a post-remedial rebound of mass discharge of PCE in the first six months after the pilot flushing test. This is likely due to the residual ethanol concentrations enhancing PCE solubility until natural gradient flow removed the majority of the ethanol. However, by the end of the first post-remedial year PCE discharge began to decrease and continued to decrease until the end of the study period. Figure 4.1-11 shows the source zone transect mass discharge over the six-year period after the 1998 ethanol flood.

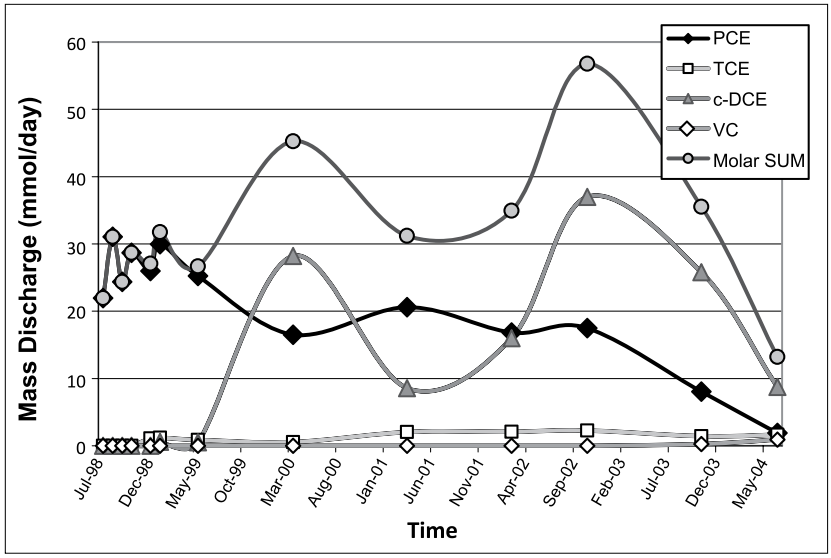

Figure 4.1-11. Sages source zone mass discharge (mmol/day) before and following the August 1998 ethanol flood.

After the initial post remedial rebound, up to 31.1 mmol/day (5.2 g/day), aqueous PCE discharge decreased to below 20 mmol/day (3.3 g/day), eighteen months after the flood event, in the March 2000 sampling event. During most of the post-remedial sampling period, the site demonstrated an increase in the total chlorinated ethene mass discharge compared to the decreasing PCE discharge. This is largely due to the formation of PCE daughter products down the biodegradation pathway which are much more soluble and have lower sorption to solids and thus can be in solution at higher total molar concentrations (Chu et al., 2004). By 2002, DCE discharge was the dominant species of the molar sum discharge indicating increased biodegradation of PCE and TCE. All chlorinated ethane mass discharges decreased in 2003 and 2004, years five and six respectively, except for the detection of low levels of VC. A paired t-test of the data demonstrated that the molar sum of concentrations at the end of study period, June 2004, were statistically different from the initial molar sum in September 1998. The total discharge reduction over the last two years of the study period may in part be due to source depletion, but is most likely a result of biosubstrate losses as ethanol was removed by groundwater flow and microbial use.

Downgradient Transect Concentrations. In addition to monitoring the source zone, the MLS transect installed downgradient of the source zone was sampled as well. The results of the downgradient control plane analysis are summarized in the Surfer™ contour plots in Figure 4.1-12. The transect consisted of MLS-9, MLS-10, and MLS-11 for the time period from 1998-2003. Two additional samplers (MLS-13 and MLS-14) were installed in 2004 in preparation for the second ethanol flood. The molar sum concentration values in the downgradient transect are slightly lower than that of the source zone transect due to dispersion, and degradation in the 10 m of aquifer between the two control planes, 1.1 mM maximum to 1.8 mM maximum respectively. Looking at the mean MLS well results, the downgradient transect recorded

relatively stable behavior for the first two post remedial-years (1999 and 2000) while recording a slight increase in the center of the transect in 2000. Throughout MLS monitoring at this transect, the higher concentrations were detected in the center of the transect at MLS-10, and in the upper region of MLS-9. In most of the transect, increases in concentrations were observed until peaking in 2002 at 1.08 mM (Figure 4.1-12). After 2002, reductions in aqueous chlorinated concentrations were observed until the end of the sampling period in 2004, concluding at 0.33 mM. These changes will be further examined through mass discharge evaluation in the next section.

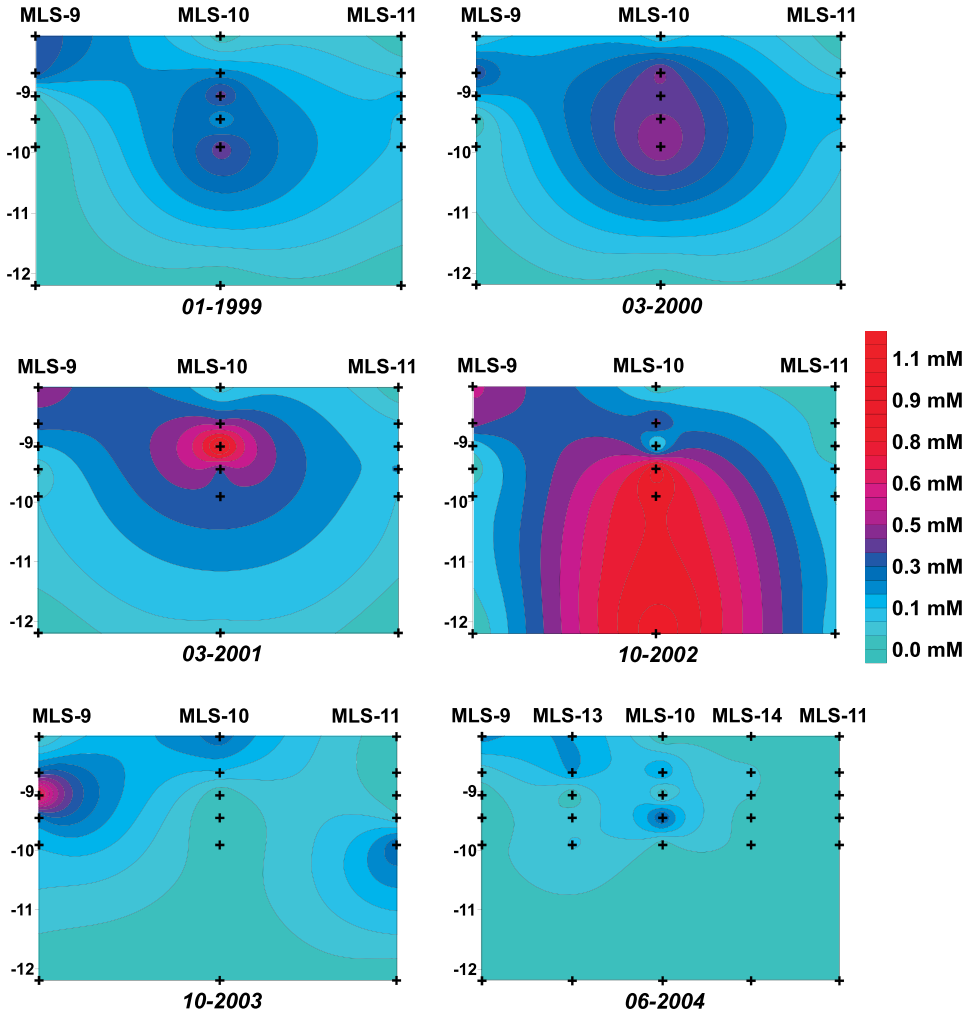

Figure 4.1-12. Sages downgradient concentration distribution for the 6-year period.

Downgradient Transect Mass Discharge. At the second control plane, chlorinated species and molar sum mass discharge were also calculated. These MLS wells were not installed prior to the pilot flood, so only an initial post remedial assessment is provided here. Figure 4.1-13 shows the chlorinated species discharge across the transect for the six-year timeframe of this project. The downgradient transect recorded some initial site flux increases in the first six months, likely site rebound, until decreases in PCE and the associated increases in DCE were observed at the end of the first post-remedial year in 1999. The PCE discharge began decreasing the most during 2001 and 2002, and accordingly the DCE and molar sum spiked markedly in this time frame. In 2003, all mass discharges began decreasing until reaching their lowest levels at the cessation of sampling in 2004.

The magnitudes of the individual chlorinated ethene mass discharges determined in the downgradient MLS transect ranged from 1.5 to 68.4 mmol/day (0.2 to 11.3 g/day) for PCE, 0 to 58.1 mmol/day (0 to 7.6 g/day) for TCE, 0 to 133.2 mmol/day (0 to 12.9 g/day) for DCE, and 0 to 1.5 mmol/day (0 to 0.09 g/day) for VC.

The patterns are comparable to the source zone transect, however the magnitude of the mass discharge is much greater. Although the concentrations were slightly lower in the downgradient transect, the cross-sectional area is much greater in the downgradient transect, and thus the mass discharge is much larger. In the last two years of the study period, the mass discharge decreased significantly, but the values were not statistically different from the initial post-remedial discharge. The observed decrease is due in part to the biodegradation of the residual source mass, but more likely due to the exhaustion of the residual ethanol as a food source for dechlorinating microbes. Another reason for the higher final flux in 2004 was the small additional PCE source mass discovered outside the pilot treatment zone. This region, just west of the pilot flood area, was treated during the full scale remediation in July 2004.

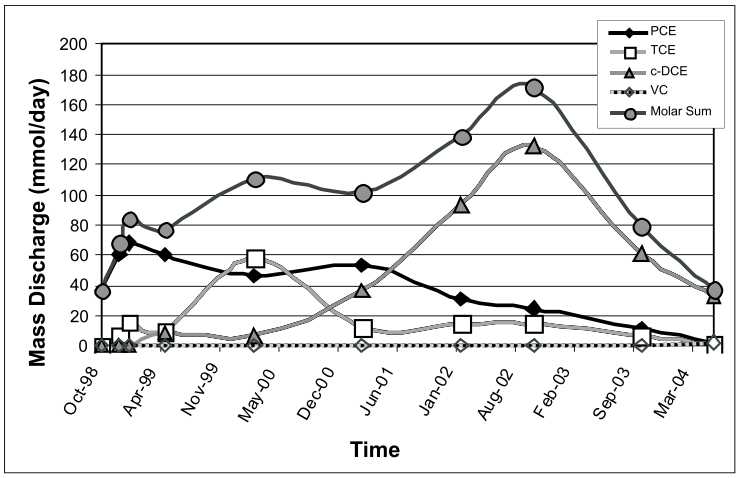

Figure 4.1-13. Sages downgradient transect mass discharge in mmol/day for the six-year period following the 1998 ethanol flushing event.

Mass Flux Based on Downgradient MLS Sampling. Pre- and post-flood mass flux was determined from MLS sampling in the downgradient control plane for the second, full scale ethanol flood in July 2004. The results are summarized in Figure 4.1-14. The second remediation was highly successful in removing the residual PCE, as it was below detection limit in the post-remedial samples. However, there must be some remaining PCE in the subsurface materials due to the presence and increases in PCE biodegradation daughter products recorded after the 2004 flood. With ethanol serving as an electron donor, indigenous microbes dechlorinated the residual PCE. PCE was present in aqueous form in the original source zone in 2007, but at a maximum of 0.08 mM. This concentration is likely easily dechlorinated in the 10 meters of aquifer between the source zone and the downgradient transect.

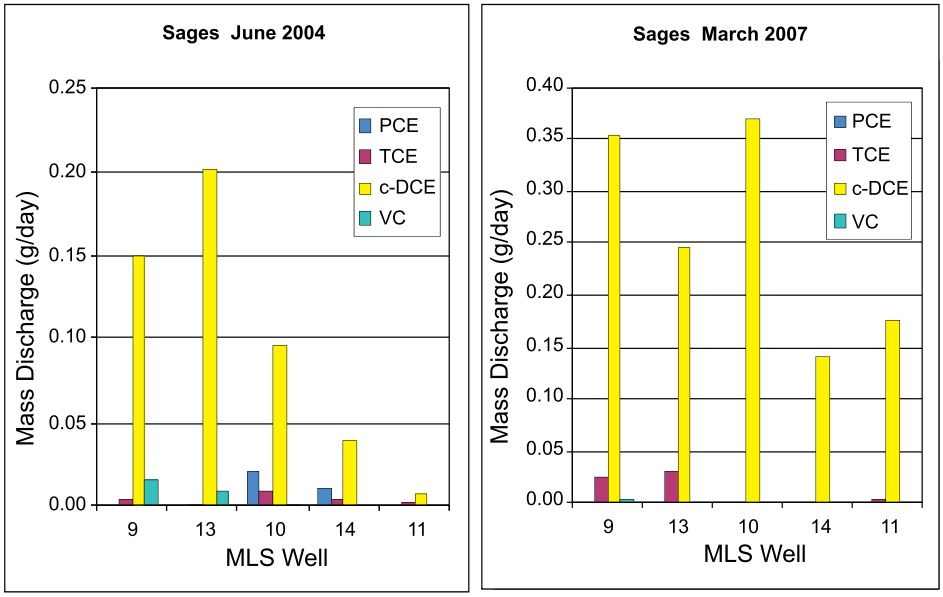

Figure 4.1-14. Pre- and post-cosolvent flood MLS mass discharge measurements in the downgradient transect at the Sages site.

Mass Flux based on Passive Flux Meter Measurements. Mass flux was measured at the downgradient transect using PFMs deployed in the 5 flux wells (FW09, FW10, FW11, FW13, and FW14 as shown in Figure 4.1-8). These wells were screened over a 3.05 m (10 ft) interval (approximately 7.62 to 10.67 m [25 to 35 ft] bgs) consistent with the MLS sampling network. This measurement was conducted in June, 2004 just prior to the second cosolvent flood. The results from this PFM deployment are summarized in Figure 4.1-15. The integrated mass discharge at the down gradient transect was 59.8 mmol/day (5.8 g/day) DCE. Other degradation products were present at significantly lower mass loads (Vinyl chloride = 7.5 mmol/day [0.47 g/day]).

The post-remediation PFM flux measurement was conducted in March, 2007. The procedures used for this measurement replicated the pre-remedial measurement. The post-remediation PFM flux data are also provided in Figure 4.1-15. The integrated mass discharge at the down gradient transect was 20.6 mmol/day (2.0 g/day) DCE. Other degradation products were present at significantly lower mass loads (Vinyl chloride = 0.64 mmol/day [0.04 g/day]). Based on these data, there was a 66% decline in DCE mass discharge at the down gradient transect.

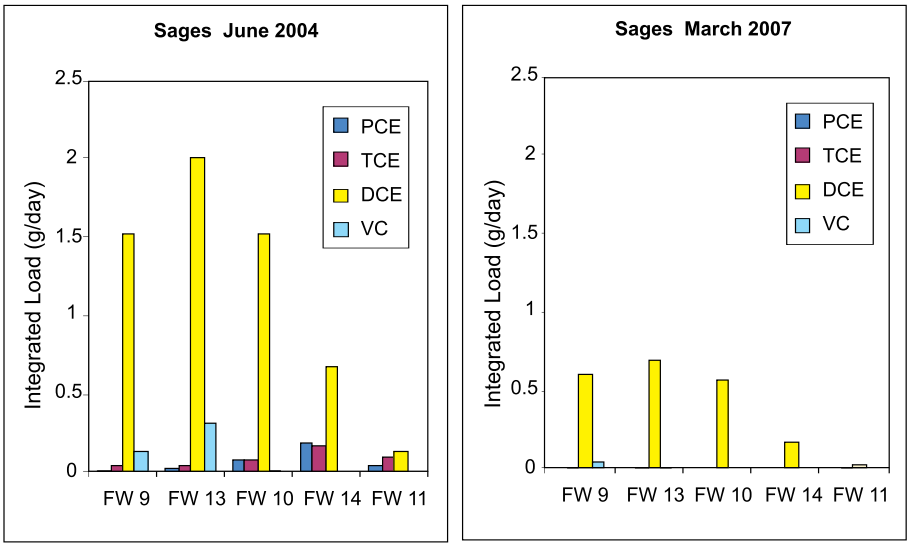

Figure 4.1-15. Pre- and post-cosolvent flood passive flux meter mass discharge measurements in the down gradient well transect at the Sages site.

Mass Flux based on Modified Integral Pump Test Measurements. Both pre- and post-remedial PFM deployments were followed by MIPTs. The pre-remedial MIPT was conducted for approximately 2.2 days, and pumping rates ranged from approximately 10 to 600 mL/min per flux well. A total of 13 samples were collected from the effluent of each pumping well over the duration of the test, and once collected, the samples were temporally stored on site in coolers until being transported to the University of Florida for GC/FID analysis. Analysis of hydraulic head data collected following PFM retrieval but prior to the start of the MIPT indicated the groundwater flow was directed away from the canal as opposed to the typical direction as shown in Figure 4.1-8. Furthermore, subsequent analysis of the hydraulic data collected during the pre-remedial MIPT suggested groundwater was flowing generally to the east rather than the west. Storm events have been noted to raise the water level in a canal located immediately to the west of the site sufficiently to temporarily reverse the groundwater flow direction. It is speculated that this may have occurred prior to the MIPT, which would account for both the head data collected prior to the start of the MIPT, and the results based on the MIPT hydraulic data. Consequently, the hydraulic data collected during the pre-remedial MIPT was only used to estimate the average hydraulic conductivity in the vicinity of the transect (1.7 m/day), and the hydraulic gradient magnitude (0.0035) and direction based on historic data was used to estimate the groundwater flux (0.6 cm/day). The compound with the highest average concentration from all wells was DCE, followed by PCE, TCE, and VC. Figure 4.1-16 summarizes the mass discharge per well based on the MIPT data. The total DCE mass discharge based on the MIPT results was 10.3 mmol/day (1.0 g/day). This value is in general agreement with the final DCE mass discharge

based on the MLS results (Figure 4.1-14), but less than the PFM results. In general however, the mass discharge spatial pattern based on the PFM and MIPT results agree, with each suggesting a decreasing trend moving from the southern to the northern end of the transect. The difference in magnitude between the PFM and MIPT results can predominantly be attributed to the difference in groundwater flux estimates. The average groundwater flux based on the PFM results was 2.6 cm/day, and the average groundwater flux based on the MIPT results was 0.6 cm/day. These groundwater flux estimates differ by a factor of 4.5, which accounts for most of the difference in DCE mass flux estimates.

The post-remedial MIPT was generally conducted in a similar manner to the pre-remedial test, with the exception that the test was conducted for a longer duration (3.7 days) in an attempt to improve the measured hydraulic response and consequently the groundwater flux estimate. Pumping rates ranged from 15 mL/min to 50 mL/min, and 16 samples were collected from each pumping well. Analysis was completed on every other sample however to minimize the laboratory workload, and inspection of the resulting concentration-time series indicated that analysis of the remaining samples was not warranted. The compound with the highest average concentration from all wells was DCE, followed by TCE and VC. No PCE was detected. The average groundwater flux based on the MIPT hydraulic data was 0.6 cm/day (directed in the westward direction). The total DCE mass discharge was 1.1 g/day based on the MIPT results, indicating no change in DCE mass discharge as a result of the second cosolvent flood. As with the pre-remedial test, the mass discharge based on the MIPT results was less than the mass discharge estimates based on the PFM results, while the general spatial distribution of fluxes was similar.

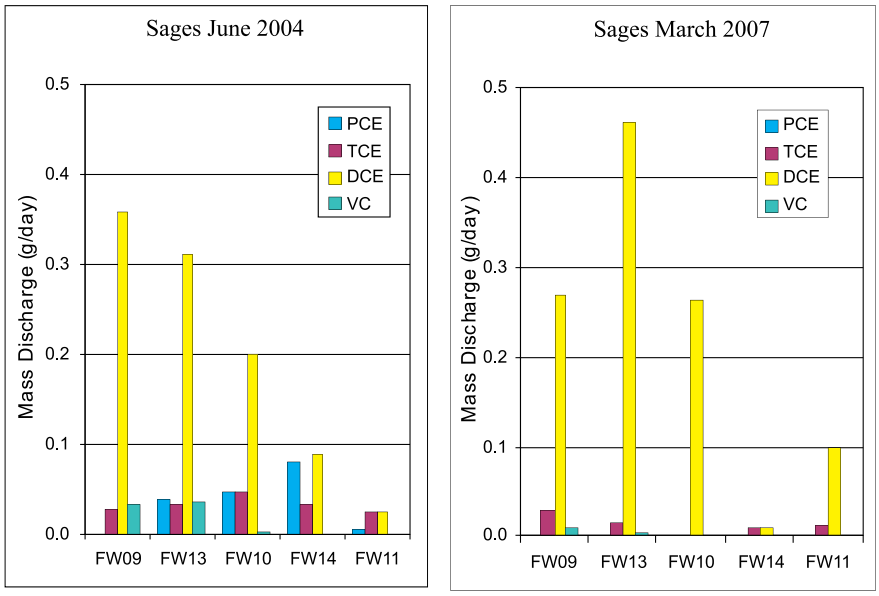

Figure 4.1-16. Pre- and post-cosolvent flood MIPT mass discharge measurements in the down gradient transect at the Sages site.

4.1.5 Borden CFB Site

The effectiveness of DNAPL source zone treatment with In-Situ Chemical Oxidation (ISCO) was evaluated using down gradient mass flux and discharge measurements. The source area consisted of DNAPL that remained in the aquifer six years after a controlled release of 50 L of a mixture of PCE, TCE and chloroform. This release is referred to as the Borden DNAPL Injection (BDI). The remaining mass was primarily PCE with an estimated total volume of 5 L. The study was conducted in the unconsolidated Borden sand aquifer with a saturated thickness of about 3.2 m. The aquifer is underlain by a regional silt and clay unit. The water table varies between 0.5 and 1.5 m below ground surface. The mass flux and discharge leaving this source area was quantified using three methods, multilevel samplers, passive flux meters and integral pump tests. Measurements were conducted shortly before the source area was assessed

using a partitioning interwell tracer test (PITT). Following the PITT the DNAPL source area was treated with permanganate. Injections of permanganate were conducted over a two month period delivering a load of oxidant to the source area. The objective of the treatment was to produce partial mass removal of the DNAPL in the source area. After a period of approximately 1.3 years the mass flux and discharge was again measured using the same protocols. This interval between treatment and post-treatment flux measurements was deemed adequate to assess flux response at a distance of 2 m down gradient of the source area given the Darcy velocity estimate of 4 cm/day.

The BDI site was instrumented heavily with multilevel samplers as part of an ongoing study to assess plume dynamics (Figure 4.1-17). The Row-6 set of multilevel samplers was selected for mass flux measurements. The initial water quality data indicated that the PCE plume was located between MLS 6-2 and MLS 6-7. Thus, fully screened wells were installed one meter down gradient of each of these multilevel samplers.

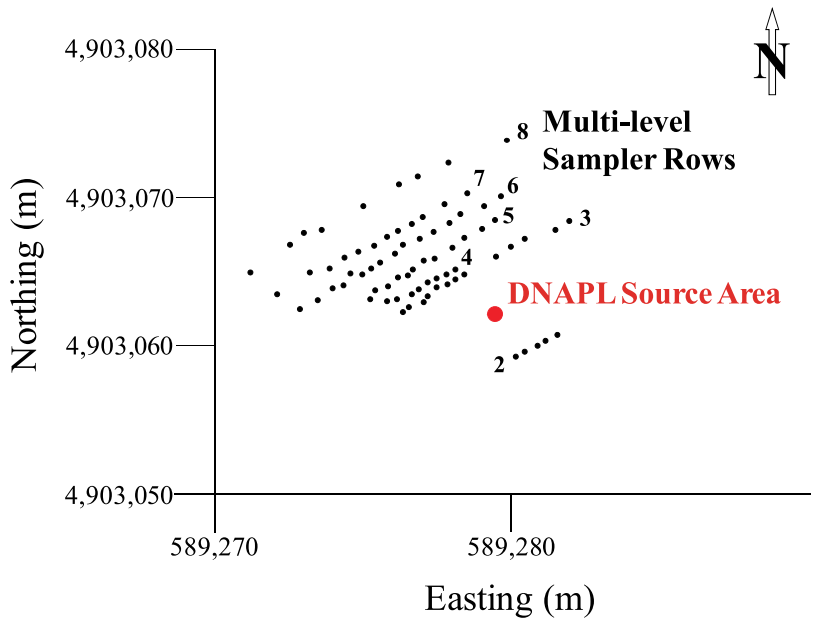

Figure 4.1-17. Borden controlled release DNAPL site instrumentation.

The resulting 8 wells were used to measure mass flux using the PFM and MIPT methods in May of 2004. The PFM data from this deployment is presented in Figure 4.1-18. It became apparent that the center of the plume had shifted to the southwest (to the left when viewed from source area in Figure 4.1-17). Based on this observation, an additional five wells were installed at one meter spacing to extend the transect for plume capture. In July of 2004 a second flux assessment was conducted using the new wells and a subset of the wells from the previous deployment. Not anticipated was the fact that the plume had shifted position back into the original set of wells selected for flux assessment. This change in flow direction was apparently the result of a transition from wet spring conditions to a lower water table position observed in the summer. This is supported by the measured groundwater elevations (0.5 m higher in May) and the measured Darcy velocities from the PFMs (4.4 cm/day in May and 2.8 cm/day in July). The higher water table in the spring tends to discharge to a ravine causing a significant ground water flow direction shift locally. Thus, it could not be confirmed that either PFM deployment sampled the entire plume width. Groundwater samples collected from all 12 wells just prior to the July 2004 flux tests were used to assist in estimating contaminant mass flux along the entire transect. These data are also provided in Figure 4.1-18. The ground water data indicates that the width of the PCE plume is similar to the width of the domain measured by the PFM deployments in July 2004 and that the concentration declines rapidly on the northeast side of the plume. Based on this information the mass integration was conducted using only the July data. Integrating the local PFM-based PCE mass flux values vertically within each well and horizontally across the transect the mass discharge of PCE was 2.2 g/day (TCE = 0.023 g/day).

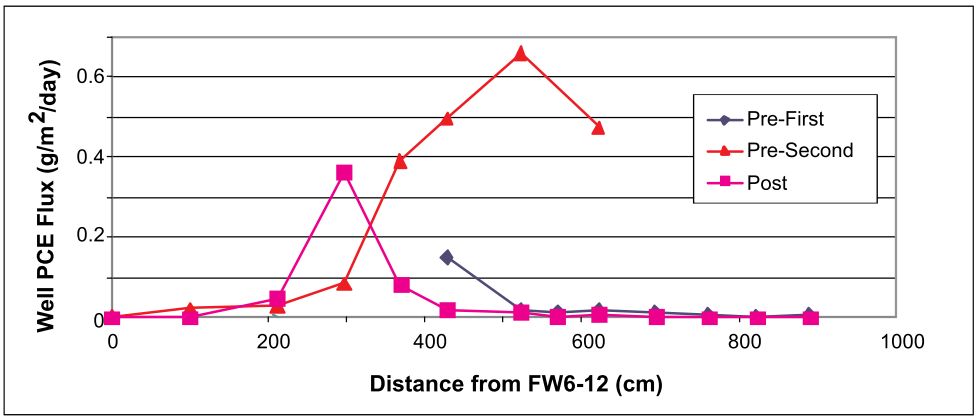

Figure 4.1-18. PCE mass flux from passive flux meters installed in wells down-gradient of row 6 at the Borden CFB site.

The results of the pre-remedial MIPT are provided in Figure 4.1-19. The values presented are average mass flux per well. The general distribution of the pre-remedial flux across the transect is consistent with that observed during the PFM deployment. The integrated pre-remedial PCE discharge across the transect was 2.2 g/day using data from both sampling events (higher value used when two values were available), which matches the value based on the PFMs.

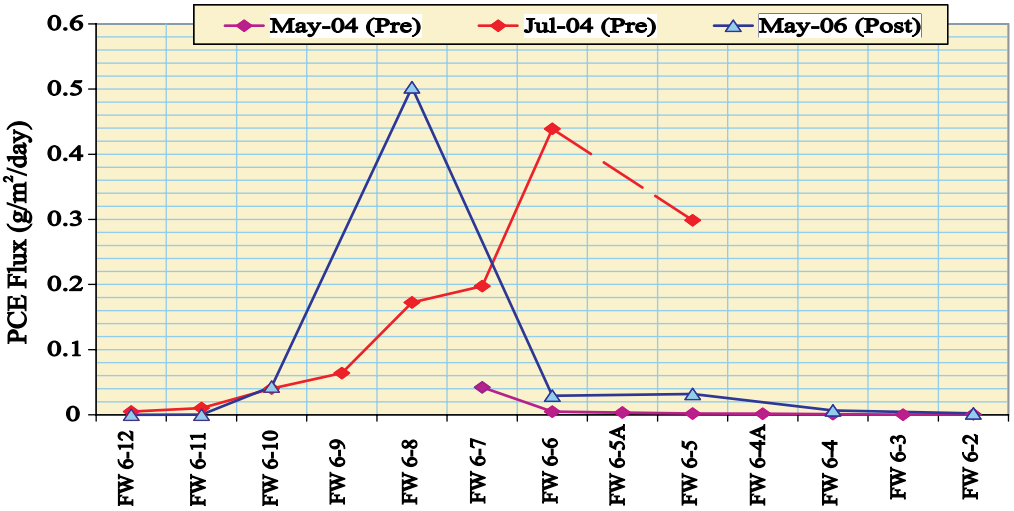

Figure 4.1-19. PCE mass flux from MIPT measurements at the Borden CFB site.

Following the pre-remedial PFM and MIPT tests, a PITT test was conducted in August 2004. The PITT used four injection wells and four extraction wells that encompassed the DNAPL source zone extending down to the Row 6 multilevel samplers. An example breakthrough curve from the PITT is provided in Figure 4.1-20. The retardation of the partitioning tracers 2-octanol and 3,5,5-trimethyl-1-hexanol are evident. Based on the measured tracer retardation and system flow rates, the estimated volume of DNAPL in the source area was about 7 L which is somewhat higher than the 5 L estimated by plume mass balance. With the previous mass discharge estimate of 2.2 g/day and the PITT-based estimate of 7 L of PCE (approximately 12 Kg) a simple zero order assumption for mass dissolution (constant discharge) indicates a period of 14 years to remove the remaining mass.

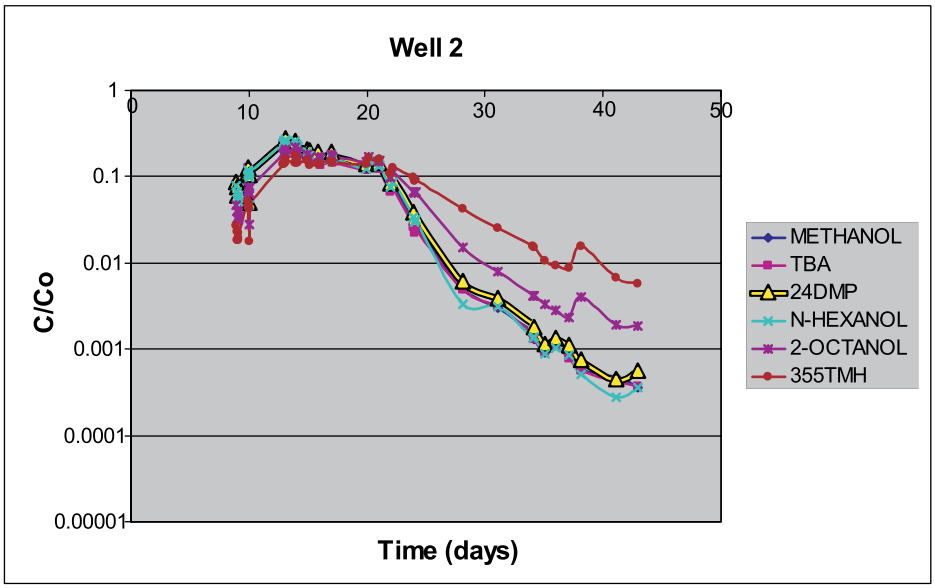

Figure 4.1-20. Example breakthrough curve for the pre-remediation partitioning tracer test at the Borden CFB site.

Following the PITT the site was treated with permanganate to oxidize the PCE in the source zone. The treatment was not intended to remove the entire source zone mass but rather some fraction of the mass to assess changes in mass flux and discharge. The partial treatment took place over several months following the PITT.

The post-remedial PFM and MIPT deployments were conducted in May 2006. During these deployments all 12 flux wells were evaluated using PFM while 8 of the wells were pumped during the MIPT. The average Darcy flux for this measurement was 4.0 cm/day based on the PFMs thus groundwater flow was similar to the first deployment conducted. The groundwater level was also comparable. The PFM derived well mass fluxes are presented in Figure 4.1-18. The maximum flux is located at well FW6-9 and is dominant at the single well. The distribution of post-remedial fluxes is likely similar to the distribution during the first PFM deployment that entirely missed the peak mass flux. The integrated PCE mass discharge across the transect was 0.54 g/day. This represents a 75% decline in PCE discharge. However, the post-remedial MIPT mass discharge estimate is substantially larger than the PFM estimate (Figure 4.1-19). The pre- and post-remedial MIPT measurements are similar. The post PCE discharge was 2.4 g/day slightly higher than the pre-remedial measurements. The differences between the MIPT and PFM data for the post measurement could be due to the interwell distribution of mass flux within the transect. The MIPT interrogates a larger volume of the formation and is more likely to identify interwell "hot spots" and thus provide a more representative measure of mass discharge.

It is estimated that the PITT removed only about 1% of the DNAPL mass and that the natural gradient dissolution would have removed approximately 8%. Thus, any significant reduction in mass discharge could be attributed to the ISCO. The quantity of mass removed would account for approximately 20 years of natural gradient dissolution assuming a first order (exponential decay) model for mass dissolution.

The PFM data can also be used to evaluate the spatial distribution of mass flux from the source zone. Two contour plots are presented (Figures 4.1-21 of the mass flux distribution along the transect with the perspective looking down gradient from the source area. Both the pre- and post-remediation distributions are fairly narrowly defined "hot spots". The pre-remediation mass flux encompasses three wells but is in a narrow vertical zone approximately 0.5 meters thick (Figure 4.1-21a). Following the ISCO a "hot spot" still remains but is lower in strength and smaller in size. This type of flux distribution data could be beneficial for targeting remedial efforts within the source zone.

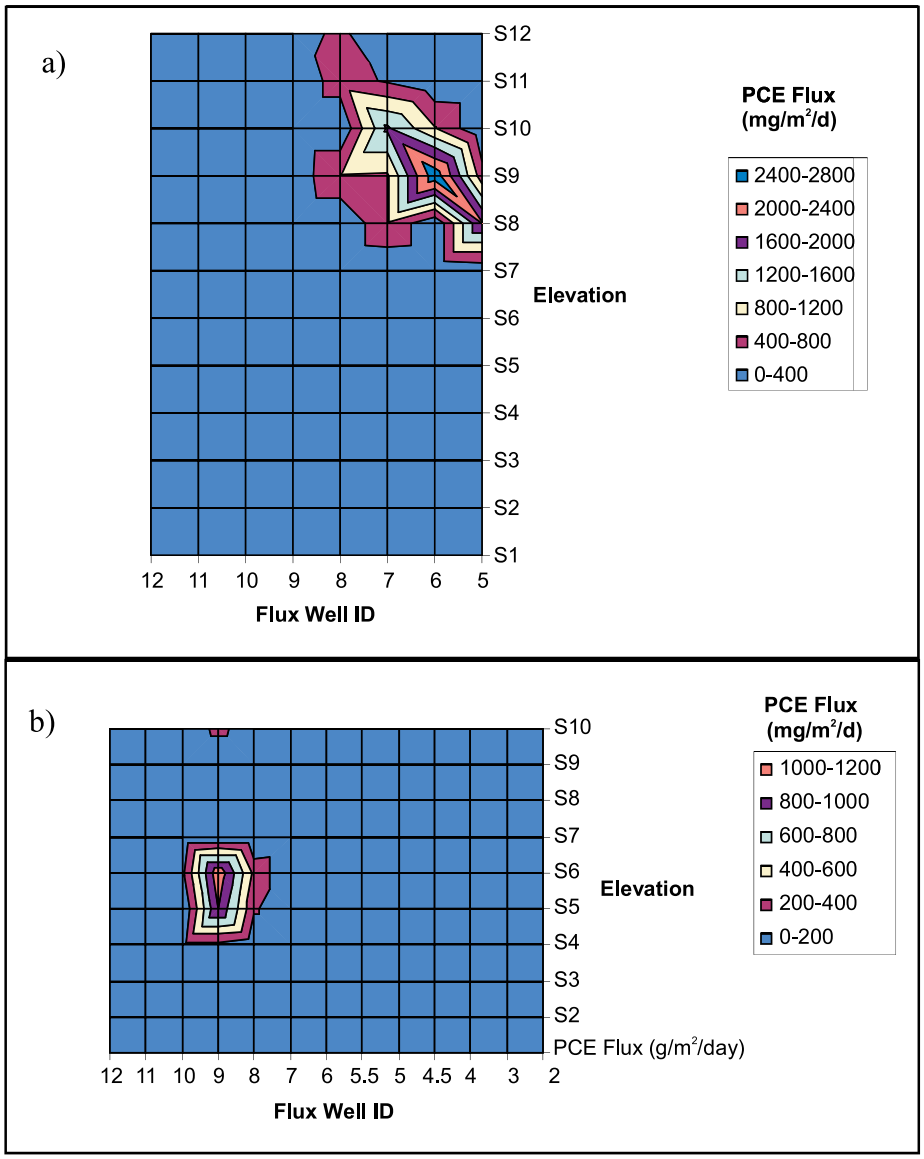

Figure 4.1-21. Pre- and post-remedial mass flux distribution of PCE in the row 6 transect at the Borden CFB site.

4.1.6 MIPT Uncertainty Analysis

To date, work published on the uncertainty of IPT measurements includes Jarsjö et al. (2005); Zeru and Schäfer (2005); Jarsjö and Bayer-Raich (2008), and Goltz et al. (2009). With the exception of Goltz et al (2009), what has been published has been developed for the IPT method as originally introduced (i.e., sequentially pumping each well at a constant rate). Goltz et al (2009) investigated the accuracy of two methods (tandem circulation wells and MIPT) to measure contaminant flux in an artificial aquifer. For the tests conducted, MIPT results underestimated the true flux by 43% to 70%. The contaminant (chloride) concentrations used in the tests were relatively uniform in both space and time, therefore it can be assumed that the error associated with the MIPT results was due to the estimate of groundwater flux rather than the interpretation of the concentration-time series. Possible explanations offered for the MIPT errors noted were well screen loss, partially-screened wells (the wells used had alternating screen and blank sections), or a failure to obtain horizontal steady-state flow. As a comparison, the tandem circulation well method was more accurate, underestimating mass flux by only 2% to 16%.

Additional investigations were conducted independently to evaluate the uncertainty associated with the modified IPT (MIPT) as described in Section 4.1.1. Uncertainty in flux measurements based on MIPTs may originate from spatial heterogeneity, a failure to meet test assumptions, or from measurement uncertainty. Assuming the former are met, the latter may be quantified using error propagation techniques and estimates of uncertainty in measurements of contaminant concentrations, water elevations, well locations, and flow rates. However, uncertainty in MIPT results due to measurement uncertainty (or measurement error) will most likely be less than uncertainty associated with a failure to meet test assumptions. Presented here are selected results of a systematic study to investigate the impact of both types of uncertainty on mass discharge measurements using the MIPT. The impact of measurement errors and modeling assumptions on estimates of the Darcy flux are first investigated, followed by an assessment of modeling assumptions related to the interpretation of the concentration-time series information.

Contaminant flux based on the MIPT is estimated from

$$J = Cq \tag{4.1-7}$$

where J is the flux ($ML^{-2}T^{-1}$), C is the concentration (ML^{-3}) estimated from the concentration time-series, and q is the groundwater flux (LT^{-1}) estimated from the hydraulic data during pumping. As a first approximation, the assumption is made that the uncertainty in the measurements of C and q are independent, and therefore the uncertainty in J as expressed by the variance, is

$$\sigma_J^2 = \sigma_c^2 q^2 + C^2 \sigma_q^2 + \sigma_c^2 \sigma_q^2 \tag{4.1-8}$$

Equation (4.1-8) can be rearranged to express the coefficient of variation of J, COV[J], as a function of the COV for q and C as Figure 4.1-22 illustrates. Two lines are shown in the graph, the blue line with diamonds represents the case where COV[q] = COV[C], and the purple line with squares represents the case where either COV[q] ≠ COV[C]=0 or COV[C] ≠ COV[q]=0. For all other cases where both COV[q] and COV[C] are > 0 but COV[q] < COV[C] or COV[C] < COV[q], COV[J] will fall between the two lines. For our analysis here the simplifying assumption has been made that C and q are independent, but it is noted that they may be correlated in certain circumstances, perhaps for example in the early stages after a spill when the high concentrations may be correlated to the high groundwater flux regions, or in an aged system after the DNAPL has been depleted, where the high concentrations may be correlated with the low conductivity regions.

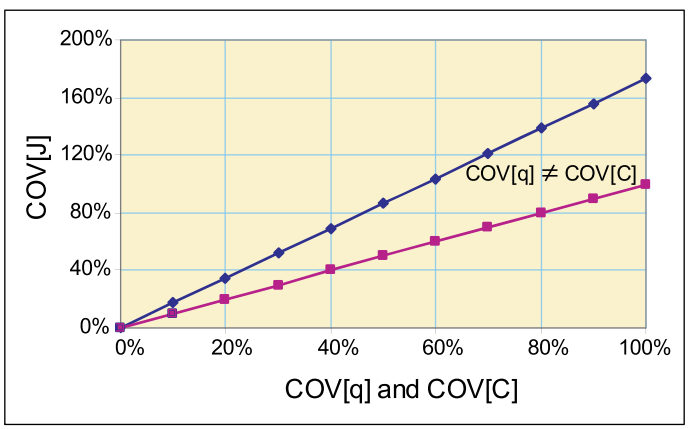

Figure 4.1-22. Covariance of J plotted as a function of the covariance for C and q assuming C and q are independent random variables. The blue line with diamonds represents the case where COV[q] = COV[C], while the purple line with squares represents either COV[q] ≠ COV[C] = 0 or COV[C] ≠ COV[q] = 0.

Uncertainty due to Measurement Uncertainty. An analysis of the uncertainty in q as estimated from the hydraulic data will first be presented. Given the use of linear regression to fit a line described by Equation 4.1-4 to the measured data, a Monte Carlo analysis was used to propagate measurement error in the independent and dependent variables. Of the measurements used to estimate groundwater flux from the MIPT (i.e., pumping rates, saturated thicknesses, inter-well distances, and water levels), water levels were considered

the most difficult to accurately and precisely measure since changes in head over relatively short distances are desired. Consequently, the analysis presented here is focused on the sensitivity of groundwater flux estimates based on the MIPT method to variability in water level measurements. The results will in turn be used with Equation (4.1-8) to estimate the sensitivity in flux estimates to groundwater flux and concentration variability.

The uncertainty associated with the change in head from a pumping well in the transect to a down gradient monitoring well is

$$\sigma^2_{\Delta h[i]} = \sigma^2_{h[obs]} + \sigma^2_{h[i]} \tag{4.1-9}$$

where $\sigma^2_{\Delta h[i]}$ is the variance in the head difference, $\sigma^2_{h[obs]}$ is the variance in the head at the observation well, and $\sigma^2_{h[i]}$ is the variance of the head at the ith pumping well. If it is assumed that the variance in any given head measurement is independent of location and independent from one another, then the variance in the head difference is $2\sigma^2_h$. Head measurements during pumping tests are typically collected using pressure transducers and data logging devices, in which case the head is calculated from the elevation of the pressure transducer plus the height of water above the pressure transducer. Assuming error in the latter can be neglected due to the fact that it is an average of a number of readings once steady state has been achieved, $\sigma^2_h = \sigma^2_{XD}$, where σ^2_{XD} is the variance of the pressure transducer elevation. The pressure transducer elevation is typically calculated as the top of casing elevation minus the sum of the distance to water below the top of casing and the height of the water above the pressure transducer. If measurement error in each of these is assumed independent, then

$$\sigma^2_{XD} = \sigma^2_{TOC} + \sigma^2_{DTW} + \sigma^2_h \tag{4.1-10}$$

And if the variance in each is assumed equal, then σ^2_{XD} =3 σ^2_h, where σ^2_h represents the variance in each of the three components that are used to estimate the pressure transducer elevation. Consequently, $\sigma^2_{\Delta h[i]}$ is equal to 6 σ^2_h. The typical precision goal associated with head measurements in groundwater field methods is on the order of 0.003 m (0.01 ft). Therefore, the impact of head measurement error ranging from 0.0003 $\leq\sigma_h\leq$ 0.03 m (0.001 $\leq\sigma_h\leq$ 0.1 ft) was investigated.

Shown in Figure 4.1-23 are the results of the Monte Carlo analysis, where the standard deviation and COV of q is shown as a function of head measurement errors. For head measurement errors less than 0.003 m (0.01 ft), COV[q] is less than 10% for distances between the transect and observation well (designated as Dx in Figure 4.1-23) of not less than 3 m. However, as the errors in head measurements increase to 0.01 m (0.03 ft) and greater, there can be significant uncertainty (≥50% COV) in the groundwater flux estimate. In practice, this can be viewed as the result of attempting to measure changes in groundwater elevation over relatively short distances, and highlights the need for accurate and precise head measurements. As the distance between the flux well transect and the down gradient observation points increases, the uncertainty due to head measurement error will decrease (i.e, compare results for Dx = 3 m versus Dx = 6 m in Figure 4.1-23). However, moving the observation point further down gradient to minimize the uncertainty due to head measurements should be balanced against increasing the test duration, the volume of water pumped, and increasing the area over which an average is estimated.

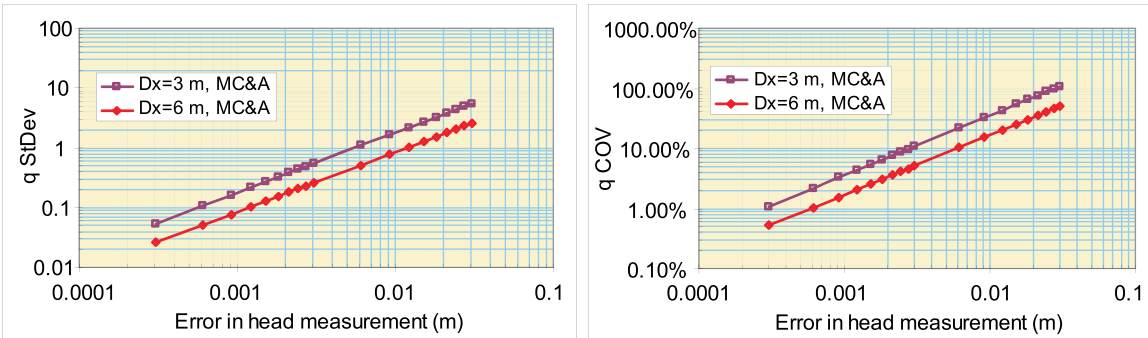

Figure 4.1-23. Standard deviation and the coefficient of variation for q as a function of uncertainty in head measurements.

Shown in Figure 4.1-24 are COV[J] as a function of head measurement uncertainty, expressed as STD[q], and COV[C] ranging from 10% to 50%. For values of σ_q generally less than 0.01 m, COV[J] is predominantly a function of COV[C]. However, for σ_q greater than 0.01 m, the impact of uncertainty in head measurements becomes more significant.

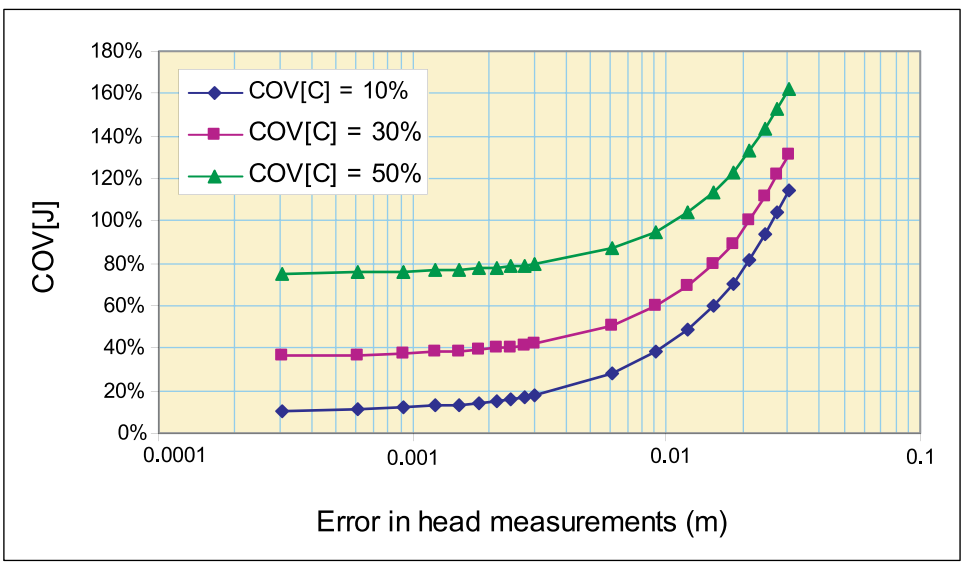

Figure 4.1-24. Covariance of J plotted as a function of the covariance for C and the standard deviation of head measurements.

Uncertainty due to Model Assumptions. The analytical equations used to estimate the groundwater flux from the MIPT data assume a homogeneous and isotropic aquifer. As such, the Darcy velocity and flux estimates are "average" values in the same manner by which a conventional pump test is considered to give an "average" estimate of hydraulic conductivity (e.g., Sánchez-Vila et al., 1999). Darcy velocities and flux estimates may either be less or greater than the true values as a result of heterogeneous, anisotropic conditions. As a means to assess the uncertainty of subsurface heterogeneous conditions on flux estimates, numerical modeling simulations using MODFLOW were conducted, and selected results are summarized below.

The modeling domain consisted of a 1000 m by 1000 m confined aquifer of thickness (B) equal to 10 m and the hydraulic conductivity (K) of 10 m/day. The head boundary conditions, consisting of no flow boundaries at y = {0, 1000} m, and constant head boundaries at x = {0, 1000} m, were set to impose a uniform flow field with a groundwater flux of 5 cm/day. Initial simulations were conducted to ensure

the domain size was sufficiently large to approximate an aquifer of infinite areal extent. A control plane transect consisting of seven pumping wells was located along the y axis. The wells in the transect were spaced 3 meters apart with the center well located at the origin. Three monitoring wells were located along the x axis, and were also spaced 3 m apart. A variable grid size was used, and the grid size in the vicinity of the wells was 0.08 m by 0.08 m. Thus the grid spacing was comparable to that of a typical two-inch monitoring well (i.e., 4 cm radius in the model versus ~2.5 cm radius for a typical monitoring well).

Two initial transient simulations under confined conditions were conducted, the first with a single pumping well at the origin and the second with all seven wells of the transect pumping. Each of these two simulations consisted of five stress periods with increasing pumping rates, Q = {1, 2.5, 5, 7.5, and 10 m^3/day}, and each stress period lasted 24 hours. Results from both simulations were analyzed using Equation 4.1-4. The resulting estimates for K and q were compared to the specified values of 10 m/day and 5 cm/day, respectively. For the first simulation with a single pumping well at the origin, the estimated values of K and q were 8.72 m/day and 4.45 cm/day, yielding percent errors of 12.8% and 10.9%, respectively. These errors are attributed to the fact that the numerical model predicts an average head over the area of the entire cell, while the analytical model predicts the head at a radius of 0.04 m. If the heads in the cells of the pumping well and the adjacent down gradient cell are averaged, and the result used as the head of the pumping well in Equation 4.1-2, then the estimated K and q (and associated errors) are 10.11 m/day (1.1%) and 5.09 cm/day (1.9%), respectively. For the sake of comparison, in the remaining analysis the head in the pumping well will be estimated as the average of the heads in the cell corresponding to the pumping well and the cell immediately down gradient. In the second simulation with all pumping wells active, the estimated K and q were 10.09 m/day (0.9 % error) and 5.02 cm/day (0.3 % error).

Two large-scale hydraulic conductivity heterogeneous patterns were investigated. The first pattern consisted of a layered hydraulic conductivity system consisting of an aquifer with three layers as depicted in Figure 4.1-25(a). Each layer was 3.33 m thick, and the geometric average hydraulic conductivity was equal to 10 m/day, and the variation in conductivity between the layers was an order of magnitude. Transient simulations with five stress periods were conducted with all seven pumping wells active. Each stress period was 24 hours, and the pumping rates for each well were 1, 2.5, 5, 7.5, and 10 m^3/day. The hydraulic conductivity of the top, middle, and bottom layers was 100, 10, and 1 m/day, respectively. For this layered system, an equivalent hydraulic conductivity is calculated using

$$\overline{K} = \sum_{i=1}^{3} \frac{B_i K_i}{B_T} \tag{4.1-11}$$

where $\overline{K}$ is the average hydraulic conductivity, B_i and K_i are the thickness and hydraulic conductivity of the ith layer, and B_T is the total thickness. Application of Equation (4.1-11) to the layered system results in an average hydraulic conductivity of 37 m/day, and with the hydraulic gradient of 0.005 imposed by the boundary conditions, the average groundwater flux is 18.5 cm/day. Results from the simulation provided estimates of K = 21.6 m/day and q = 10.7 cm/day, respectively. The percent error between these values and the average values calculated above (i.e., K = 37 m/day and q = 18.5 cm/day) were 41.6% and 42.0%, respectively, which suggests that estimation of groundwater flux based on the MIPT approach is sensitive to the vertical distribution of hydraulic conductivity.

The second heterogeneous pattern investigated consisted of the blocks as shown in Figure 4.1-25(b). The confined aquifer thickness was set equal to 10 m. The center block was 40 m wide, and the other two blocks extended over the remaining modeling domain. The hydraulic conductivity of the center block was 10 m/day, and that of the blocks on each side was 1 and 100 m/day, resulting in a geometric average K of 10 m/day and a variation in hydraulic conductivity between blocks equal to an order of magnitude. All seven pumping wells and monitoring wells were located in the center section where K = 10 m/day and q = 5 cm/day. The distance to the changes in K from the pumping wells on the ends of the transect was 11 m. The estimated K and q were 10.1 m/day and 5.0 cm/day, respectively, and the percent error relative to the true values of the center block was 1.2% and 0.6%, respectively.

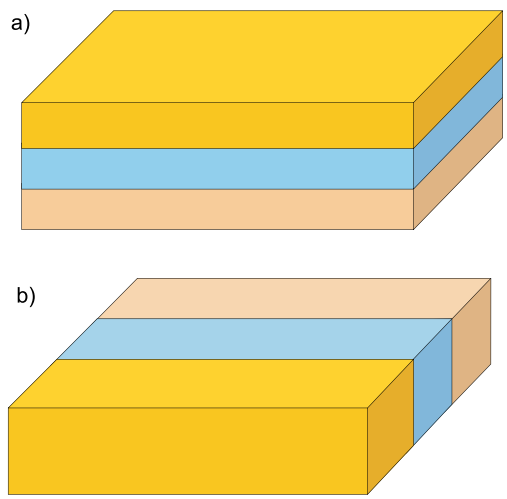

Figure 4.1-25. Layered (a) and block (b) macro-scale hydraulic conductivity patterns investigated with numeric modeling simulations.

Unconfined Simulations. Several simulations conducted for the confined aquifer were repeated using unconfined conditions to investigate how this deviation from the assumed conditions might impact the results. The constant head up-gradient boundary condition was set to a value of 10 m and the down gradient boundary condition was 5 m. The Boussinesq equation (Bear, 1979) under steady-state, no recharge conditions (i.e., $\partial/\partial x(h\,\partial h/\partial x) = 0$) was used to estimate the pre-pumping saturated thickness and groundwater flux at the control plane. The pre-pumping saturated thickness under these conditions is independent of hydraulic conductivity, and the value at the flux control plane is 7.79 m. For the first case, a single well at the origin was pumped over five stress periods (each of 24-hour duration) with increasing pumping rates, Q = {1, 2.5, 5, 7.5, and 10 m^3/day}. The unconfined aquifer consisted of a single layer of hydraulic conductivity equal to 10 m/day, the groundwater flux at the transect was therefore 4.816 cm/day. The estimated values of K and q based on the application of the MIPT to the model simulation results were 9.98 m/day and 4.93 cm/day, respectively; and the percent error between these values and the true values was 0.2% and -2.3%, respectively. A second identical simulation was conducted with the only difference being that all seven pumping wells were pumped using the same conditions previously applied to the well at the origin. The estimated values of K and q based on the application of the MIPT to this model simulation were 9.68 m/day and 4.98 cm/day, respectively. The percent error between these values and the true values was 3.2% and -3.4%, respectively.

The layered case (Figure 4.1-25a) was also repeated as unconfined simulations. Transient simulations with five stress periods of 24-hour duration were conducted with all seven pumping wells active. The pumping rates for each well were 1, 2.5, 5, 7.5, and 10 m^3/day. For the first layered pattern, the hydraulic conductivity of the top, middle, and bottom layers was 1, 10, and 100 m/day, respectively. Equation (4.1-11) was used to calculate an equivalent hydraulic conductivity for the aquifer as a whole. However, since this was an unconfined simulation, the top layer was only partially saturated, and the saturated thickness was estimated at 1.12 m (i.e., 7.79 m minus 2/3 * 10 m). The resulting equivalent hydraulic conductivity was 47.3 m/day, and the groundwater flux based on this value of K was 22.8 cm/day. Based on the application of the MIPT method to the simulation results, the estimated hydraulic conductivity and groundwater flux were 46.6 m/day and 23.0 cm/day, resulting in errors of 1.4% and -1.2%, respectively. A second, unconfined layered system was also simulated, the only difference being the hydraulic conductivity of the top, middle, and bottom layers was 100, 10, and 1 m/day, respectively. The equivalent K from this distribution and saturated thickness was 19.1 m/day, and the resulting groundwater flux was 9.2 cm/day. The estimated K and q based on the application of the MIPT to the simulation results were 25.1 m/day and 12.3 cm/day, respectively; and the resulting errors were -31.7% and -33.7%. These errors were larger than those associated with the previous simulation, and are more similar to the errors noted for

the three-layered, confined simulations. These results therefore suggest that the MIPT approach may be sensitive to the actual vertical distribution in hydraulic conductivity, rather than just vertical variation itself.

In addition to the large-scale heterogeneous patterns shown in Figure 4.1-25, a random hydraulic conductivity field with no correlation structure was used with a geometric mean hydraulic conductivity of 10 m/day, and log-transformed standard deviation of 1. Two simulations were conducted: one with the center well at the origin pumping only and another with all seven wells pumping. The pumping rates and durations applied in each case were the same as those previously used. These simulations were used to assess how well an average hydraulic conductivity and groundwater flux value could be estimated where the scale of pumping was much larger than the scale of the hydraulic conductivity heterogeneity. For the case with a single pumping well only, the estimated K and q based on the application of the MIPT to the simulation results were 5.0 m/day (49.9% error) and 2.8 cm/day (40.7% error), respectively. The errors noted were based on the mean value of the hydraulic conductivity. For the case with all wells pumping, the estimated K and q based on the application of the MIPT to the simulation results were 6.0 m/day (39.9% error) and 3.5 cm/day (26.5% error), respectively. As expected, the results with all seven wells pumping were better at predicting the average hydraulic conductivity and groundwater flux compared to the results with a single pumping well.

Comparison of Ideal and Non-ideal Capture Zones. Shown in Figure 4.1-26 are the capture zones associated with a MIPT consisting of 7 concurrently pumping wells conducted in a homogeneous, unconfined aquifer. As described earlier, the hydraulic conductivity is 10 m/day, the regional groundwater flux is 5 cm/day directed in the positive x axis, and the initial saturated thickness at the well transect is 7.8 m. At early times, the capture zones for all wells appear symmetric about the pumping well. However, at later times while the capture zone for the center well remains symmetric, the capture zones for the other wells become increasingly skewed away from the origin due to concurrent pumping. Moreover, at later times the capture zone for the two pumping wells on the ends of the transect draw water predominantly from the regions beyond the ends of the transect. While this complicates the use of the concentration-time series information to estimate the spatial distribution of the contaminant, it does help ensure the transect captures the full width of the contaminant plume. Furthermore, with the exception of the two wells on the ends of the transect, the well spacing is a good approximation to the width of the capture zone at later times.

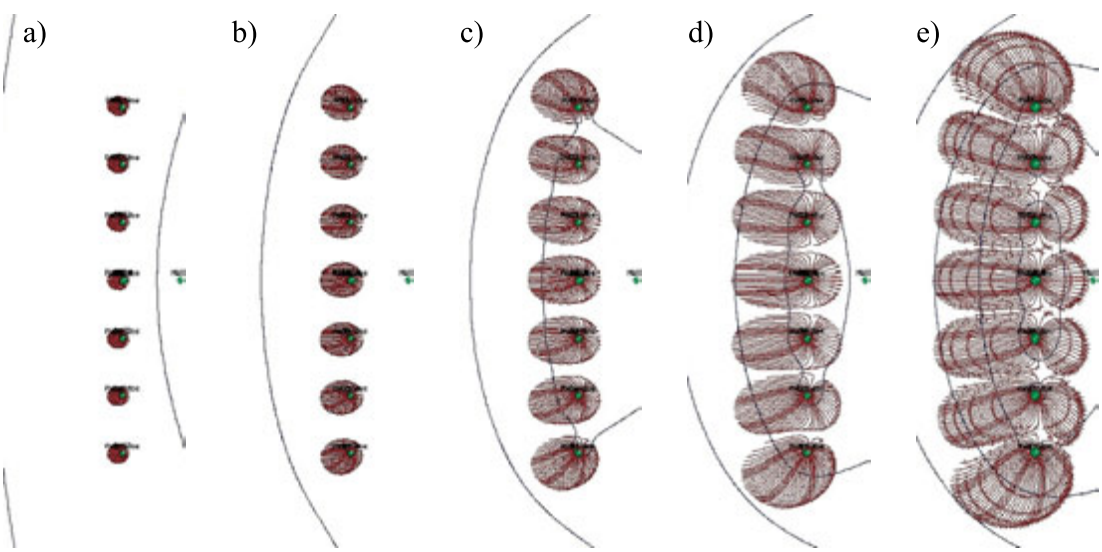

Figure 4.1-26. Capture zones for an MIPT with seven concurrent pumping wells in an unconfined aquifer with K = 10 m/day and q = 5 cm/day. Shown from left to right are the capture zones associated with the five pumping-rate steps of a) 1 m^3/day, b) 2.5 m^3/day, c) 5 m^3/day, d) 7.5 m^3/day, e) 10 m^3/day. Each step lasted 24 hours.

Shown in Figure 4.1-27 are the capture zones again associated with an MIPT consisting of 7 concurrently pumping wells conducted in an unconfined aquifer with regional groundwater flux of 5 cm/day (in the positive x-axis direction) and an initial saturated thickness at the well transect of 7.8 m. However, in this simulation the hydraulic conductivity is heterogeneous, and assumed to be an uncorrelated log-normally distributed random space function with a mean of 10 m/day and a log-transformed standard deviation of 1. Figure 4.1-28 shows the capture zone at day 5 for a second hydraulic conductivity realization from the same statistical distribution, and results from the homogeneous case and the first realization are also shown for comparison. Differences in capture zones for the heterogeneous case relative to the homogeneous case are noted by the second day (i.e., compare Figures 4.1-26b with 4.1-27b). As expected, differences are noted in the spatial distribution of the capture zones between the two realizations (compare Figure 4.1-28b with 4.1-28c). Based on the figures shown, it appears that the width of the capture zone associated with the three center wells can still be approximated by the well spacing. However, the capture zones for the two wells on each end are larger in width than the well spacing.

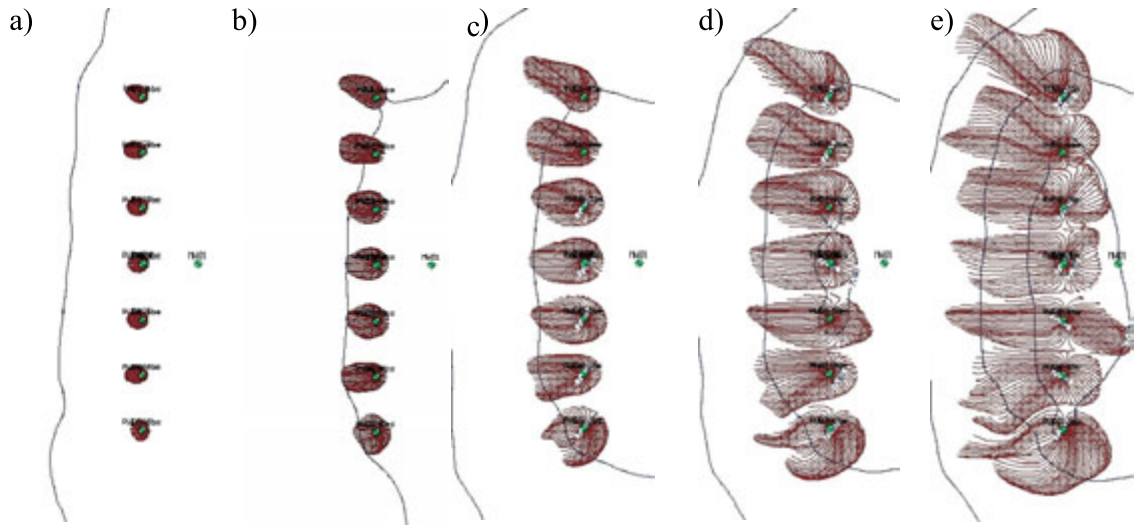

Figure 4.1-27. Capture zones for an MIPT with seven concurrent pumping wells in an unconfined aquifer with a log-normally distributed random *K* field. Shown from left to right are the capture zones associated with five pumping-rate steps of a) 1 m^3/day, b) 2.5 m^3/day, c) 5 m^3/day, d) 7.5 m^3/day, e) 10 m^3/day. Each step lasted 24 hours.

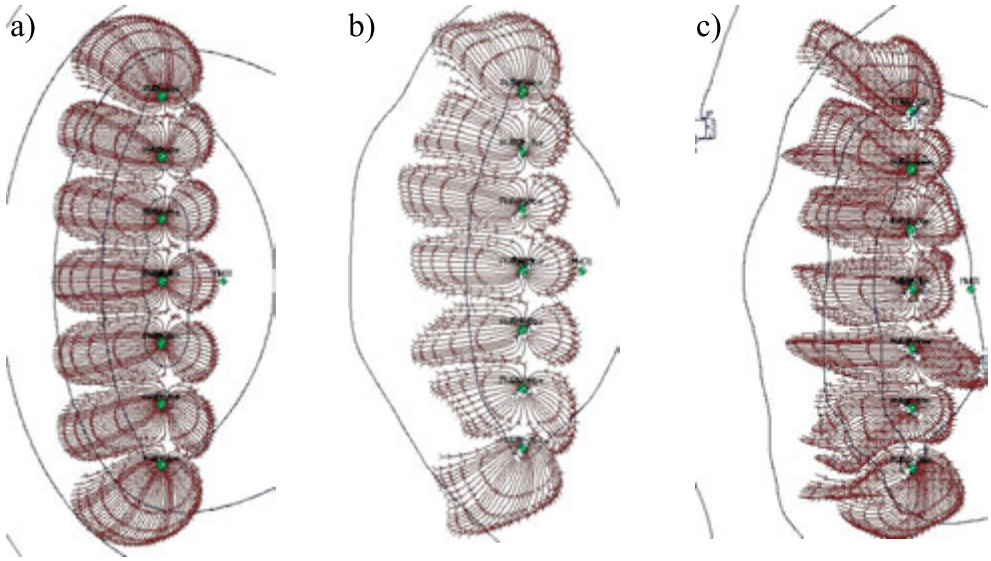

Figure 4.1-28. Comparison of capture zones with seven concurrent pumping wells for the homogeneous case (a) and heterogeneous cases: realization 1 (b) and realization 2 (c).

Uncertainty due to Concentration-Time Series Interpretations. For the MIPTs conducted at the four field sites in this SERDP project, all wells were pumped concurrently rather than sequentially as conducted in the original IPT method. Wells were pumped concurrently in our tests to minimize the disturbance to the contaminant distribution that would result from pumping each well sequentially, and to avoid the uncertainty associated with double counting mass located between adjacent wells. However, disadvantages to concurrent pumping include the development of stagnation points between wells, and a more complex flow field, which prevents the use of the Bayer-Raich et al. (2004) analytical solution. With respect to the first disadvantage, it is nonetheless possible to sample a large fraction of the space between wells, so that the general goal of the IPT (i.e., a measured response integrated over a large area) is maintained. With respect to the second disadvantage, the average spatial concentration in the capture zone of the well was estimated using the average concentration of the concentration-time series. The mass discharge was then obtained from the product of the contaminant flux and the cross-sectional flow area associated with the well transect.

An analysis of the potential uncertainty in mass discharge measurements due to the interpretation of the concentration-time series information as conducted for the MIPT was completed using a Monte Carlo analysis. The analysis consisted of two main parts: first the calculation of particles captured at a series of times associated with a particular MIPT application; and the second, the calculation of the concentration-time series by superimposing the distribution of particles captured with the contaminant plume distribution. Similar to the analysis presented by Bayer-Raich et al. (2004), the analysis conducted here assumed: (1) a two-dimensional (in the x-y plane), homogeneous and isotropic aquifer with uniform flow (directed in the positive x-axis); and (2) a mature plume such that variations in concentration across the captured zone in the x direction were assumed negligible, consequently concentration varied only in the y-direction. Furthermore, for the analysis presented here, the concentration distribution along the y-axis was described using a normal probability density function, and advection was assumed to be the predominant transport process, and dispersive transport was neglected.

A series of particles (n = 360) were released around each well, and a reverse particle tracking algorithm was used to defined the loci of particles captured at a given time. The reverse particle tracking algorithm was based on fourth-order, Runge-Kutta numerical integration with an adaptive time-step. Input variables for this calculation consisted of groundwater flux, aquifer thickness, porosity, number of wells (and well locations), pumping rates, and pumping durations. The concentration at each location was then calculated using the normal PDF (probability density function) with an assumed mean and standard deviation, and the average concentration was then calculated for all particles at a given time. The result was a concentration-

time series for each well. The code was validated by comparing the true average concentration to that estimated by applying the Bayer-Raich et al. (2004) analytical solution to the concentration-time series as produced by the code when a single pumping well was specified. Uncertainty in mass discharge estimates was then investigated by conducting a Monte Carlo analysis in which the mean and standard deviation of the normal PDF (which described the contaminant plume) were uniform random variables.

Results from a single realization are shown in Figure 4.1-29 for a case consisting of seven concurrently pumping wells spaced 3 m apart along the y axis. Pumping rates were Q = {1, 2.5, 5, 7.5, and 10} m^3/day, with each rate applied for a single day. The uniform groundwater flux was directed in the positive x-axis at a rate of 5 cm/day, the aquifer thickness was 10 m, and the porosity was 0.15. Figure 4.1-29a) shows the resulting capture zones at the end of each pumping step. The contaminant plume was centered at y = 1.5 m (midway between the third and fourth pumping well) with a maximum concentration of 20 mg/L, and a plume width defined using a standard deviation of 0.4 m (see lines in Figure 4.1-29a, which represent $\pm 3\sigma$). Figure 4.1-29b shows the concentration-time series resulting from this MIPT. For this particular case, the plume is centered midway between wells 3 and 4, which represents a more difficult case for MIPTs with concurrent pumping wells; and the plume is relatively narrow, so that concentration is only detected in wells 3 and 4. It is interesting to note in this case that while concentration continues to increase across the entire test duration in well 4, concentrations reach a peak around day 4 for well 3, and then start to decline. This can be explained by inspection of the capture zones for well 3 as shown in Figure 4.1-29a), which reveal that an increasing proportion of clean water is drawn into this well as the test progresses due to the effects of concurrent pumping. For this case the true mass discharge across the transect was 10 g/day, and the measured mass discharge based on the average concentration across the entire concentration-time series was 4.4 g/day, resulting in a percent error of 56%. Given the relative change in concentration with time (as shown in Figure 4.1-29b), another approach that could have been used is to average concentration only over the late-time portion of the concentration-time series (i.e., last day), in which case the measured mass discharge is 9.0 g/day, with a resulting percent error of only 10%.

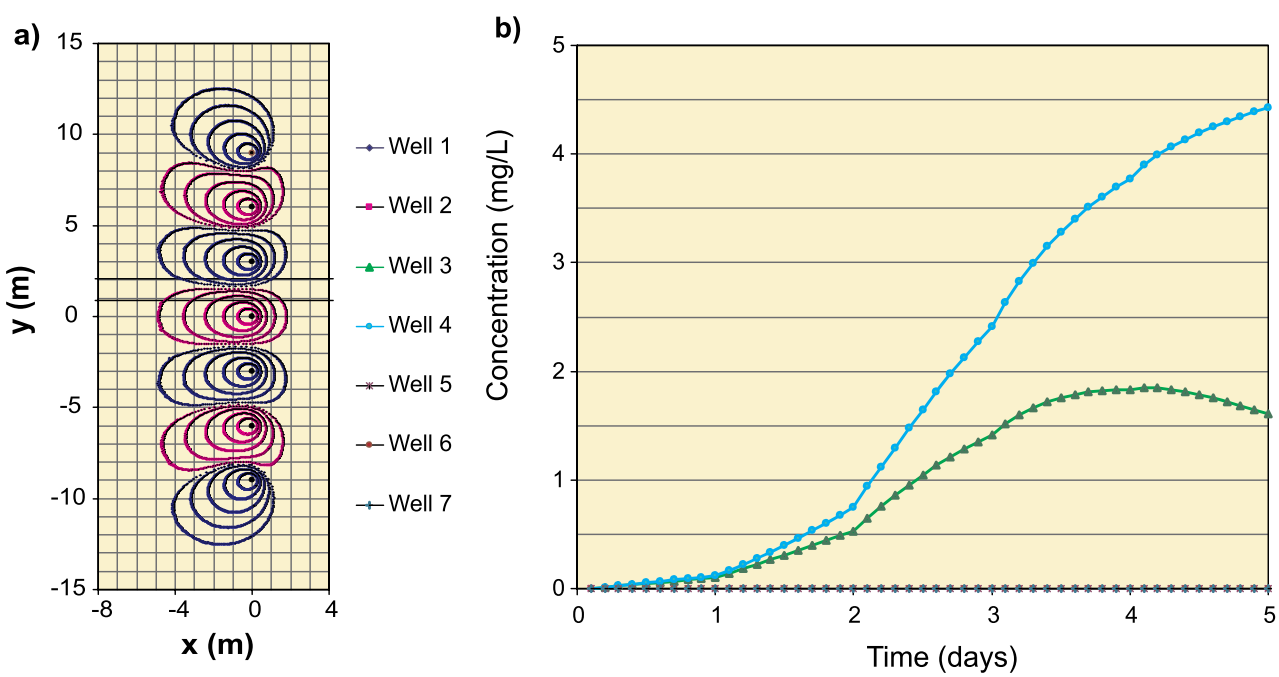

Figure 4.1-29. a) Capture zones during an MIPT consisting of seven concurrently pumping wells, and b) the resulting concentration-time series for a mature contaminant plume centered at y = 1.5 m (midway between the third and fourth pumping wells), a maximum concentration of 20 mg/L, and a plume width described by a standard deviation of 0.4 m.

Using the same aquifer parameters and MIPT details as specified in the preceding paragraph, Monte Carlo simulations with 1000 iterations were conducted in which the plume center-line varied according to a uniform random variable, with limits of $-9 \leq y \leq 9$ m. Three separate Monte Carlo simulations were completed, one each with plume standard deviations of 0.4, 0.8, and 1.2. Results are shown in Figure 4.1-30, where the average percent error (i.e., the average of the error from each realization, defined as [true $M_D - M_D$]/true M_D) is plotted as a function of the plume standard deviation. The bars in the figure indicate plus and minus one standard deviation of the calculated errors. As expected, the error decreases as the plume width increases across the transect, resulting in a more homogeneous concentration distribution. Also shown in Figure 4.1-30 is the percent error based on a point measurement technique (referred to as PM in Figure 4.1-30). The mass discharge per well using a point measurement technique was calculated as the product of the groundwater flux, cross-sectional area (aquifer thickness times well spacing), and the concentration calculated at the well. The range in errors associated with the point measurement technique is larger than the MIPT technique, especially for narrow plumes. It is also noted that while the average error for the point measurement technique is zero, there is an apparent bias of approximately 8% in the average error for the MIPT technique. Further modeling simulations (results not shown) indicated that this is predominantly due to approximating the capture zone width using the well spacing, and using the average of the concentration-time series as an estimate of the average spatial concentration in the well capture zone.

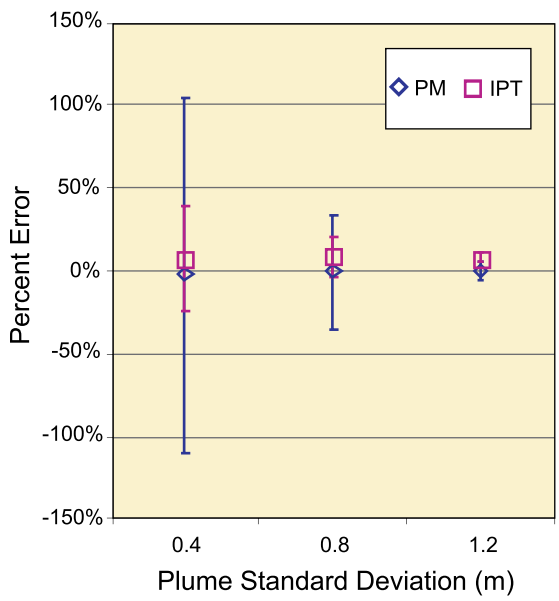

Figure 4.1-30. Results from Monte Carlo simulations where plume position is treated as a uniform random variable. Plotted in the y-axis is the average percent error in measured mass discharge relative to the true mass discharge for MIPT and point measurement techniques (PM).

In summary, modeling simulations were used to investigate the uncertainty associated with the measurement of mass discharge using the MIPT approach. Uncertainty in measurements may originate from either a failure to meet test assumptions or from measurement uncertainty. For the conditions investigated, uncertainty in Darcy flux was generally 40% or less, but was as high as 100% in some cases. Using this upper value, the resulting uncertainty in mass flux ranged from approximately 120% to 160% when the uncertainty in the average concentration ranged from 10% to 50%, respectively. Likewise, uncertainty in mass discharge estimates resulting from uncertainty in the interpretation of the concentration-time series information was also investigated. For those conditions investigated, the uncertainty in mass discharge estimates ranged from approximately 30% to 3% for narrow to broad plumes relative to the well spacing. However, results also suggested a positive bias in the average error of the MIPT measurements.

4.2 Laboratory Research

The field studies described above provide important data concerning the response to DNAPL source treatment; however, the difficulty and expense of quantifying DNAPL mass and architecture prevent an in-depth field assessment of the factors that influence this response. Thus, a series of laboratory experiments were designed to examine these factors. Bench-top experiments were conducted in two-dimensional flow chambers that served as aquifer models. The flow chambers were packed with porous media in both homogeneous and heterogeneous configurations and DNAPL was released at various locations. Relationships between contaminant architecture and mass flux were evaluated for dissolution by aqueous, surfactant, and cosolvent solutions and for mass depletion through air sparging. Light transmission visualization (LTV) methods were used to map DNAPL distribution in the flow chambers. Laboratory experiments are described in detail in the following peer-reviewed journal articles:

Light Transmission Visualization Methods:

Wang, H., X. Chen, and J.W. Jawitz (2008). Locally-calibrated light transmission visualization methods to quantify nonaqueous phase liquid dissolution dynamics in porous media. *Journal of Contaminant Hydrology* 102(1-2):28-38, doi:10.1016/j.jconhyd.2008.05.003.

Bob, M.M., M.C. Brooks, S.C. Mravik, and A.L. Wood (2008). A modified light transmission visualization method for DNAPL saturation measurements in 2-D models. *Advances in Water Resources* 31(5):727-742.

Relationship between Source Mass and Source Strength:

Fure, A.D., J.W. Jawitz, and M.D. Annable (2006). DNAPL source depletion: linking architecture and flux response. *Journal of Contaminant Hydrology* 85(3-4):118-140, doi:10.1016/j.jconhyd.2006.01.002.

Totten, C.T., M.D. Annable, J.W. Jawitz, and J.J. Delfino (2007). Fluid and porous media property effects on dense non-aqueous phase liquid migration and contaminant mass flux. *Environmental Science and Technology* 41(5):1622-1627.

Chen, X., and J.W. Jawitz (2008). Reactive tracer tests to predict DNAPL dissolution dynamics in laboratory flow chambers. *Environmental Science and Technology* 42(14):5285-5291.

Kaye, A.J., J. Cho, N.B. Basu, X. Chen, M.D. Annable, and J.W. Jawitz (2008). Laboratory investigation of flux reduction from dense non-aqueous phase liquid (DNAPL) partial source zone remediation by enhanced dissolution. *Journal of Contaminant Hydrology* 102(1-2):17-28, doi: 10.1016/j.jconhyd.2008.01.006 .

Bob, M., M.C. Brooks, S.C. Mravik, and A.L. Wood (2009). The impacts of partial remediation by sparging on down-gradient DNAPL mass discharge. (In preparation).

4.2.1 Light Transmission Visualization Methods

A limited number of techniques can be used to accurately measure DNAPL and water content in laboratory physical models (Darnault et al., 1998). Partitioning tracers, for example, have been shown to give an accurate estimate of a known volume of chlorinated solvents emplaced in a sand-packed column (Jin et al., 1995; Wilson and Mackay, 1995). A limitation of this method, however, is that the saturation obtained is typically a bulk saturation estimate and information is not obtained on the detailed distribution of saturation across the sand column. Other, non-invasive laboratory techniques that have been used to quantify fluid content in laboratory experiments include X-ray measurements (Liu et al., 1993; Rimmer et al., 1998; Tidwell and Glass, 1994), gamma ray radiation (Ostrom et al., 1998; Hopmans and Dane, 1986) and light transmission visualization (LTV; Hoa, 1981; Niemet and Selker, 2001; Tidwell and Glass, 1994; Darnault et al., 1998). Because of the limitations associated with the use of X-ray and gamma ray radiation (e.g. slow

measurements, hazard of working with high energy sources, high cost), the LTV technique has recently gained popularity (Weisbrod et al., 2003).

In this project, LTV methods were used to quantify DNAPL saturations in two-dimensional (2-D), two fluid phase systems (Wang et al., 2008; Bob et al., 2008). The methods reported here are expansions of earlier LTV methods and take into account both absorption and refraction light theories. Based on these methods, DNAPL and water saturations can rapidly be obtained point wise across sand-packed 2-D flow chambers without the need to develop calibration curves. The methods were applied to measure, for the first time, undyed DNAPL saturation in small 2-D chambers.

The extent to which light is transmitted through the flow chamber is a function of adsorption by the porous media and resident fluids and refraction at fluid/fluid and media/fluid interfaces. These adsorptive and interfacial processes can be quantified by applying Beer's and Fresnel's laws to obtain:

$$I = cI_{in}\Pi\omega_j \exp(-\Sigma d_i a_i) \tag{4.2-1a}$$

where I is the emergent light intensity, c is a constant that corrects for the difference in the point of light emission and light observation (taken to be 1 here since the light source and the experimental chamber are approximately the same distance from the detector), I_{in} is the incident light intensity, ω_j is the transmittance at the interface between phases i and i+1, a_i is the absorption coefficient of phase i, and d_i is the thickness of phase i.

For the two fluid phase (water and oil) systems used for our experiments, equation (4.2-1a) can be rewritten as:

$$I = I_{in}\omega_{pw}^{2b}\omega_{wo}^{2b(1-f_w)} \exp(-a_p d_p \delta_p - a_o d_o \delta_o) \tag{4.2-1b}$$

where ω_{pw} is the transmission factor at the sand particle-water interface, ω_{wo} is the transmission factor at the water-oil interface, b is the number of pores across the thickness of the 2-D chamber, f_w is the fraction of pores that are water-filled (water saturation), a_p is the sand particles absorption coefficient, d_p is the diameter of sand particles, δ_p is the number of sand particles across the thickness of the 2-D chamber, a_o is the dyed oil absorption coefficient, d_o is the average pore diameter, and δ_o is the number of pores that are oil-filled.

Method 1:

Five variations of the light transmission visualization (LTV) technique were tested to quantify NAPL dissolution dynamics in porous media (Wang et al., 2008). PCE was released into a two-dimensional laboratory flow chamber packed with water-saturated sand which was then sequentially flushed with a surfactant solution (2% Tween 80) until all of the PCE had been dissolved. For investigations of multiphase flow that involve visualization or imaging techniques, it is common to dye the NAPL to enhance contrast between the immiscible phases. However, the light absorption characteristics of the NAPL can change as dissolution progresses. To avoid this problem in these tests, the dye was added to the aqueous phase.

The five visualization approaches evaluated included four previously published models and a novel multiple wavelength method that has the advantage of not requiring any assumptions about the intra-pore interface structure between the various phases (sand/water/NAPL). The models evaluated were: Model 1) Beer's Law that ignores the interfacial effects of immiscible fluids; Model 2) non-wetting fluid of uniform pore size that assumes that a pore is either full of dyed aqueous phase or full of NAPL; Model 3) wetting media of uniform pore size that assumes water is wetting to sand and individual pores should be either full of dyed aqueous phase or will contain NAPL with a dyed-water film coating the sand; Model 4) two-wavelength method that allows interfacial effects to be eliminated by collecting images at two wavelengths; and Model 5) binary method where local NAPL saturations are determined by dividing the total volume of NAPL by the number of pixels that exceed a given light transmission threshold. None of the techniques used here required the use of calibration chambers.

The new multiple wavelength method (Model 4) is expected to be universally applicable to any translucent porous media containing two immiscible fluids (e.g., water-air, water-NAPL). Results from the sand-water-PCE system evaluated here showed that Model 3 (Model C of Niemet and Selker, 2001) and Model 4 (multiple wavelength model) were able to accurately quantify PCE dissolution dynamics during surfactant flushing. The average mass recoveries from these two imaging methods were about 90% during seven cycles of surfactant flushing that sequentially reduced the average NAPL saturation from 2.6×10^{-2} to 7.5×10^{-4}. Results from the three experiments (I, II, and III) are given in Table 4.2-1. Initial PCE saturation distributions are presented here for all three experiments. In Experiment III, a 2% solution of dyed Tween 80 with the same dye concentration as the resident water was displaced through the flow chamber to rapidly dissolve the NAPL. After 1 to 3 pore volumes (PVs) of Tween injection (applied PVs for each cycle are given in Table 4.2-1), the surfactant solution was displaced with 4 PVs of dyed water and images were collected to quantify the PCE distribution. This cycle of surfactant was repeated seven times until 97% of the PCE was flushed from the chamber. The PCE mass recoveries were calculated by comparing the known PCE mass to the masses obtained from LTV estimation from the four models.

Method 2:

The saturations of both dyed and undyed DNAPL were measured in a water/oil system without dying the water phase (Bob et al., 2007). To our knowledge, this is the first attempt to use light transmission visualization to quantify DNAPL in multiphase systems without the use of dyes. Different known amounts of PCE were added to a small silica sand-packed 2-D chamber that was initially saturated with water and the amount of PCE in the chamber after each addition was calculated from image analyses. In another set of experiments, known amounts of PCE were released into a larger 2-D model and air sparging experiments were carried out to remove different fractions of the PCE mass from the chamber. A GC/MS instrument that was connected to the chamber was utilized to quantify the PCE in the vapor phase leaving the chamber. In addition, a carbon column was also connected to the chamber to trap all PCE removed from the model and was analyzed to determine the mass of PCE removed.

Table 4.2-1. PCE distribution recovery, mean, and variance determined using the LTV models.

Experiment-flushing cycle	PVs[a]	Mass Recovery (%)[b]				% of PCE removed
		Model 1	Model 2	Model 3	Model 4	
I		86.2	74.6	98.2	99.3	
		84.6	69.6	94.9	99.5	
III-0		85.5	69.9	96.2	101.0	0.0
III-1	0.8	78.1	63.8	87.9	94.5	11.0
III-2	1.2	69.7	57.0	78.4	96.1	29.9
III-3	2.2	69.7	57.0	78.4	84.1	51.1
III-4	2.2	66.9	54.7	75.2	79.6	69.2
III-5	2.3	87.2	71.4	98.0	94.6	82.9
III-6	1.6	71.1	58.3	80.0	77.6	90.1
III-7	1.0	119.6	97.8	134.3	104.8	97.1
Average		81.9	67.4	92.2	93.1	
Standard deviation		15.4	12.8	17.3	9.4	

[a] *Pore volumes of 2%Tween 80 applied in each cycle*

[b] *Ratio of PCE volume estimated using LTV models and determined from effluent-based mass balance.*

The accuracy of the method was evaluated based on mass balance calculations. For the first set of experiments, the amounts of PCE calculated from image analyses were compared to the actual amounts

added and for the second set of experiments image analyses results were compared to mass balance estimates derived from effluent stream monitoring.

The LTV experimental system consisted of a 2-D flow chamber mounted on the front of a light source and a digital camera. Flow chambers were constructed of aluminum frames and 0.635 cm or 1.27 cm thick tempered glass plates and were packed with Accusand silica sands (Unimin, Le Sueur, MN). Drainage ports in the bottom of the internal aluminum frame and injection ports attached to the top allowed inflow and outflow of fluids. The large chambers used in the air sparging experiments had additional ports across the top of the chamber to direct the effluent vapors through an in-line GC/MS and into an activated carbon trap. Nominal internal dimensions of the small and large chambers were 15.24 cm by 15.24 cm by 1.4 cm and 48.26 cm by 48.26 cm by 1.4 cm, respectively. Flow chambers were packed with a range of sand fractions and media heterogeneities.

Spatial distribution of light transmitted through the flow chamber was determined by collecting digital images. The images were collected using a thermoelectrically air-cooled charge coupled device (CCD) camera (Princeton Instruments model number 7486-002). The shuttered, monochromatic camera had a 16-bit dynamic range (65585 grey levels) and 512 by 512 spatial resolution. Images were collected using either a 600 nm or a 543 nm center-wavelength, 10 nm band-pass filter (Melles Griot, Rochester, NY).

A summary of flow chamber experiments is presented in Table 4.2-2. PCE distribution within a flow chamber was ascertained by subtracting images taken with PCE present in the chamber from images taken when the chamber was fully water-saturated. Examples of these differential images for Pack A with 2 ml PCE and Pack B with 4 ml PCE are shown in Figure 4.2-1. Since light adsorption by undyed PCE and water is negligible at 600 nm, the contrast in transmitted light shown here is refraction at the water-oil interfaces. DNAPL saturation patterns estimated from these images are also shown in Figure 4.2-1

The correlation between PCE volumes calculated from image analysis and actual PCE volumes within the flow chambers is shown in Figure 4.2-2. The visualization technique provided good estimates of PCE mass for both undyed and dyed PCE.

Table 4.2-2. Summary of flow chamber experiments.

Experimental Code	Dyed PCE	Chamber Size	Incremental addition/removal	Imaging Wavelength (nm)
Pack A	No	Small	Addition	600
Pack B	No	Small	Addition	600
Pack C	Yes	Small	Addition	600
Pack D	Yes	Small	Addition	543
Pack E	Yes	Large	Removal	600
Pack F	Yes	Large	Removal	600
Pack G	Yes	Large	Removal	543

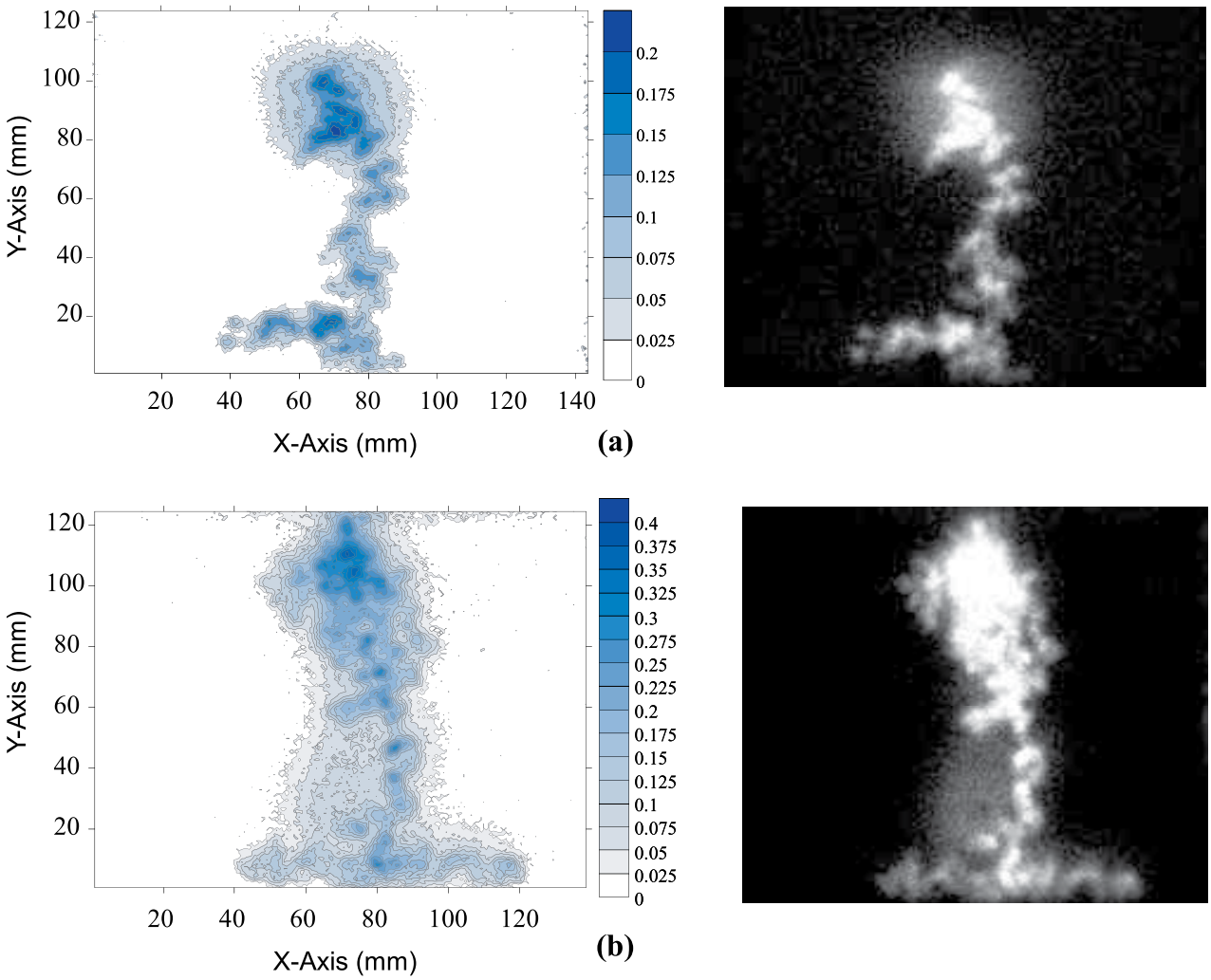

Figure 4.2-1. Distribution of PCE in porous media as determined by LTV. (a) Distribution of PCE in Pack A with 2 ml of injected PCE. (b) Distribution of PCE in Pack B with 4 ml of injected PCE (Bob et al., 2008).

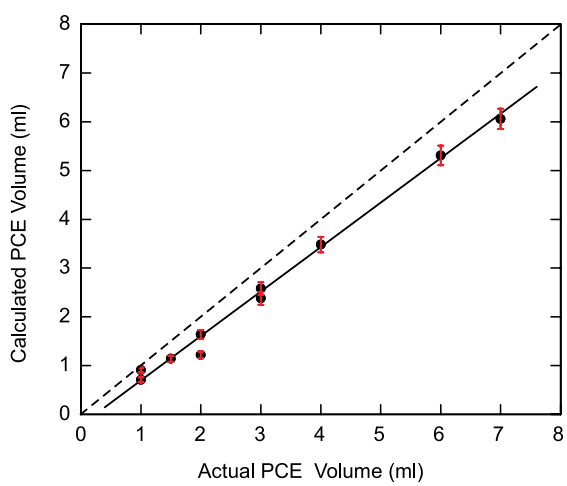

Figure 4.2-2. PCE volume calculated from image analysis versus actual PCE volume present in the model. Solid line shows the best fit and the dashed line shows the 1:1 relationship for comparison (Bob et al., 2008).

4.2.2 Relationship between Source Mass and Source Strength

Given the limitation of remedial technologies to meet acceptable water quality standards, particularly with respect to DNAPLs, the benefits of conducting costly remedial measures are unclear (EPA, 2003; NRC, 2005). A number of source-treatment benefits have been suggested, and one such benefit is a reduction in contaminant discharge from the DNAPL source area (Soga et al., 2002; Rao et al., 2002; Soga et al., 2004). If the flux which emanates from the source area is reduced by source treatment, conceptually the contaminant plume may respond in a manner which reduces the contaminant risk, such as a reduction in total plume mass or a reduction in plume spatial extent. The flux response (Figure 2.0-2) to source treatment is critical to understanding the benefits of source treatment in terms of plume response.

4.2.2.1 DNAPL source depletion: Linking architecture and flux response

The relationship between DNAPL mass reduction and contaminant mass flux was investigated experimentally in four model source zones (Fure et al., 2006). The flow cell design for the experiments featured a segmented extraction well that allowed for analysis of spatially resolved flux information. The well segments were numbered sequentially from the bottom of the flow chamber upwards (i.e. the bottom segment is referred to throughout as port 1 where the top port is referred to as port 7). This flux information was coupled with image analysis of the NAPL spatial distribution to investigate the relationship between flux and the upgradient NAPL architecture. Three experiments were conducted with 1,2-dichloroethane (DCA) and one with trichloroethene (TCE). DCA was selected for its high aqueous solubility so that the experiments could be conducted in a reasonable time frame. A summary of the experimental conditions can be found in Table 4.2-3. For brevity the four experiments will hereafter be referred to as DCA-1, DCA-2, DCA-3, and TCE-1.

A simple image analysis technique was utilized to provide semi-quantitative assessment of NAPL architecture. Reflective digital images of the flow chamber were taken at each sampling acquisition. Note that images were taken from only one side of the flow cell but compared favorably (in terms of similar NAPL distributions) with the side of the flow cell that was not imaged. The images were overlain with a finely discretized grid (grid cell size approximately 0.2 cm^2) for image processing. A binary map of the NAPL distribution was developed based on the presence (in which case the grid cell was filled black) or absence (in which case the grid cell was filled white) of NAPL in each individual grid cell. The black and white image was imported into Mathcad using an image processing function that returns matrix containing distinct numeric values for white (no NAPL) and black (NAPL) grid cells.

Table 4.2-3. Summary of experimental conditions.

	Experiment 1	**Experiment 2**	**Experiment 3**	**Experiment 4**
Name	DCA-1	TCE-1	DCA-2	DCA-3
Volume DNAPL injected (ml)	10	10	12	10
Injections	Single	Single	Double	Single
Flow chamber design	Segmented	Segmented	Segmented	In-line
Packing	Discrete layers	Discrete layers	Continuous layering	Fine gradation
Pore water velocity (cm/hr)	22.9	18.7	18.2	17.3

Trajectory integrated NAPL content, $\hat{S}$, is defined as $\hat{S} = (\hat{S}_N \eta) / \theta$ (where $\hat{S}_N$ is the trajectory average NAPL saturation, η is the porosity [$L^3 L^{-3}$], θ is the water content [$L^3 L^{-3}$]). Trajectory integrated NAPL contents were estimated by assuming horizontal flow trajectories, such that a trajectory could be represented by one row in the grid. Note that the assumption of horizontal flow trajectories is not a requirement of the streamtube model, but rather a simplification that was necessary in order to use image analysis to estimate trajectory integrated NAPL contents. A simple algorithm was used to count the number of elements in

each row of the matrix that had a numeric value corresponding to the positive identification of NAPL. This process returned an array containing the number of NAPL containing grid cells in each trajectory. By assuming a uniform saturation for each grid cell, the mass fraction in each trajectory was estimated as the number of NAPL-containing grid cells in each row divided by the total number of NAPL-containing grid cells in the domain.

Mass removal via aqueous dissolution as a function of time was determined by integrating the dissolution breakthrough curve. Mass balances for all experiments were in the range of 80-90%. Possible sources of mass balance errors include volatilization during sampling, inaccuracies in the measurement of flow, and residual NAPL remaining in the flow cell upon completion of the experiment. Fractional mass reduction (i.e., mass removal compared to initial mass) was evaluated without attempting to correct or add back in the various experimental mass losses.

An example of the flux plane response to temporal changes in the NAPL architecture is shown in Figures 4.2-3. The term 'flux plane response' is used to refer to the distribution of fluxes at the down-gradient segmented extraction well. The bar graphs plot the fraction of the total initial flux discharged from individual extraction well segments. Results are shown for six selected time steps. Also reported for each time step is the fraction of the total initial mass remaining (F_R) and the fraction of the total initial flux (F_J), where F_R is defined as the total NAPL mass in the system at a given time step divided by the total initial NAPL mass in the system at the beginning of the experiment. Likewise F_J is defined as the total flux out of all well segments at a given time step divided by the total initial flux at the beginning of the experiment. The segmented flux data is intended to be coupled with information about the up-gradient NAPL distribution to investigate the linkages between NAPL architecture and flux.

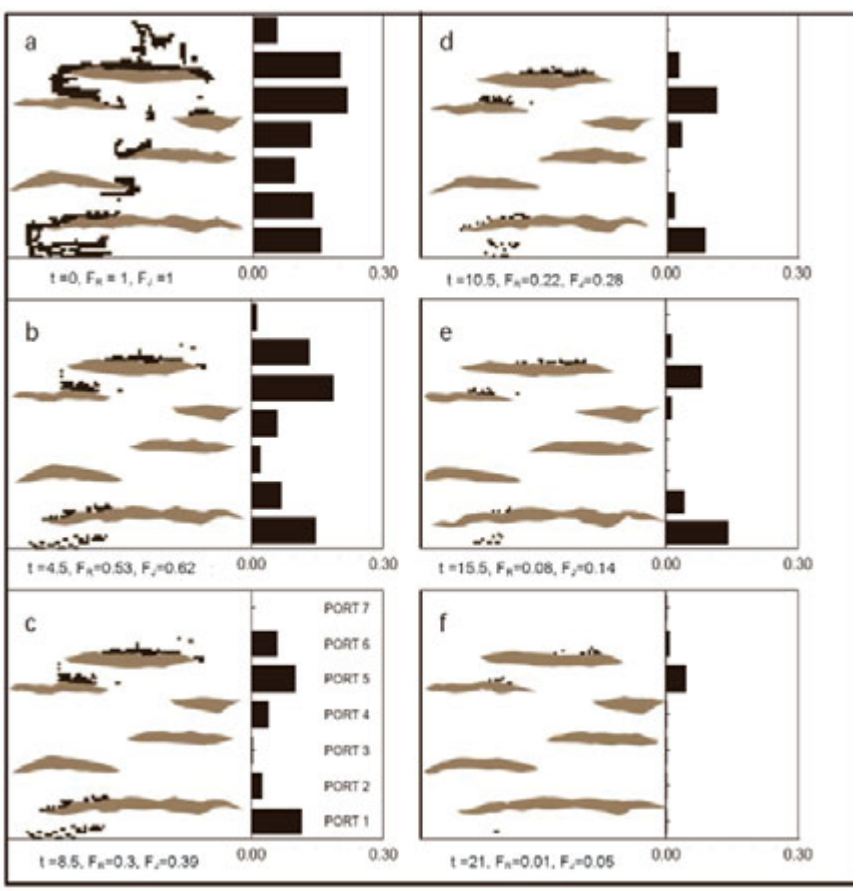

Figure 4.2-3. Flux plane response to changes in NAPL architecture for experiment DCA-1. Note that F_R is the mass fraction ((mass at time *t*)/(initial mass at *t* = 0)) and F_J is the flux fraction ((flux at time *t*)/(initial flux at t = 0)). Figures a through f show NAPL distribution and vertical flux distributions (bar graphs) at progressively longer dissolution times (Fure et al., 2006).

For discussion purposes it is useful to consider each well segment (or port) as corresponding to a bundle of streamtubes with a given distribution of trajectory integrated NAPL contents. It is also useful to recall that, based on the image analysis procedure and the definition of $\hat{S}$, an elongated NAPL morphology in the mean flow direction translates to a larger estimated trajectory integrated NAPL content, (e.g., a NAPL pool would have a much larger estimated value of $\hat{S}$ than a vertical finger).

Figure 4.2-3 indicates that reductions in flux were realized for partial reductions in mass as certain well segments showed flux decreases at earlier dissolution times than other well segments. The well segments that continued to produce mass at later dissolution times were predominantly associated with streamtube bundles characterized by larger $\hat{S}$ values (NAPL morphologies that were elongated in the mean flow direction). The well segments that were depleted of mass at earlier dissolution times were predominantly associated with streamtube bundles characterized by smaller $\hat{S}$ values (NAPL morphologies that were 'less elongated' in the mean flow direction). In summary, qualitative linkages between the flux plane response and upgradient changes in NAPL architecture indicated the important role the Lagrangian NAPL architecture played in governing dissolution dynamics in the systems studied.

Mathematical model simulations were used to further investigate the importance of Lagrangian NAPL architecture in controlling dissolution dynamics. Two simplified models, a stochastic-advective (streamtube) model and a power function model were used for this investigation. An analytical solution for flux-averaged concentration using the rate-limited streamtube model was presented by Jawitz et al., 2005 (summarized in Section 4.3.3.7):

$$C\left(t_R\right) = f_c C_s \sum_{i=1}^{n} \left[1 - \frac{\exp\left[\dfrac{k_t C_s \left(t_R - t_i\right)}{\rho_N}\right]}{\exp\left[k_t \hat{S}_i t_i\right] + \exp\left[\dfrac{k_t C_s \left(t_R - t_i\right)}{\rho_N}\right] - 1} \right] \tag{4.2-2}$$

where t is the travel time or residence time along a streamtube, t_R is total runtime, C [M L^3] is the contaminant concentration in a streamtube, C_S [M L^3] is the contaminant solubility, n is the number of streamtubes, ρ_N is the NAPL density, k_t is a mass transfer rate coefficient that is linearly related to $\hat{S}$, the trajectory integrated NAPL content, and f_c is the fraction of streamtubes that are contaminated.

If equilibrium mass transfer is assumed, Eq. (4.2-2) reduces to:

$$C\left(t_R\right) = f_c C_s \sum_{i=1}^{n} H\left(t_R - \tau_i\right) \qquad \tau = tR = t\left(1 + \frac{\rho_N \hat{S}}{C_s}\right) \tag{4.2-3}$$

where H is the Heaviside step function, R is the retardation factor, and τ is the reactive travel time which represents the combined effects of aquifer hydrodynamics and NAPL spatial distribution on NAPL dissolution (Cvetkovic et al., 1998; Jawitz et al., 2003, 2005).

The power function model used in this study relates source zone effluent concentrations to reductions in NAPL mass. The model was presented by Parker and Park (2004) and is based on the concept of an effective Damkohler number ($D_a = \kappa_{eff} L / \overline{q}$, where $\kappa_{eff}\left[T^{-1}\right]$ is the effective mass transfer coefficient, L is the source zone length in the mean flow direction, and $\overline{q}\left[LT^{-1}\right]$ is the average Darcy flux for the source zone). For brevity this model will be referred to as the Da model. The concept of the Da model is to relate the field-scale mass transfer rate coefficient to the average groundwater velocity and to the temporally changing (decreasing) global NAPL mass (Parker and Park, 2004):

$$\frac{C_{J,out}(t)}{C_s} = 1 - \exp\left[\frac{-\kappa_{eff} L}{\bar{q}}\right] \tag{4.2-4}$$

$$\kappa_{eff} = \kappa_0 \left(\frac{\bar{q}}{\bar{K}_s}\right)^{\beta_1} \left(\frac{M_S(t)}{M_{S,0}}\right)^{\beta_2} \tag{4.2-5}$$

where $C_{J,\,out}$ [ML^{-3}] is the flux averaged concentration exiting the source zone, $\bar{K}_S$ [LT^{-1}] is the average saturated hydraulic conductivity of the source zone, $M_S(t)$ is the NAPL mass in the source zone at time t, $M_{S,0}$ is the initial NAPL mass in the source zone, and κ_0 [T^{-1}], β_1, and β_2 are empirical fitting parameters. If $\beta_1 = 1$, the flux-averaged concentration exiting the source zone is independent of the mean groundwater velocity and the Da model is similar to the equilibrium streamtube model (Eq. 4.2-3).

The fraction of the total initial NAPL mass contained in each grid row (considered here as streamtubes) was estimated from image analysis of experiments DCA-1, TCE-1, and DCA-2. The fraction contaminated was converted to values of $\hat{S}$ using porosity and water content and inserted into Eqs. (4.2-2) and (4.2-3). The data were modeled under the assumption that the dissolution dynamics were primarily controlled by the $\hat{S}$ distribution. A nonreactive travel time, t, equal to the mean nonreactive travel time for the entire system was assumed for each streamtube (measured mean travel times for the three experiments were 1.2 hr for DCA-1, 1.7 hr for TCE-1, and 1.3 hr for DCA-2). The superposition of n solutions, with n being the number of trajectories from the image analysis procedure, was then used to develop the plots in Figure 4.2-4.

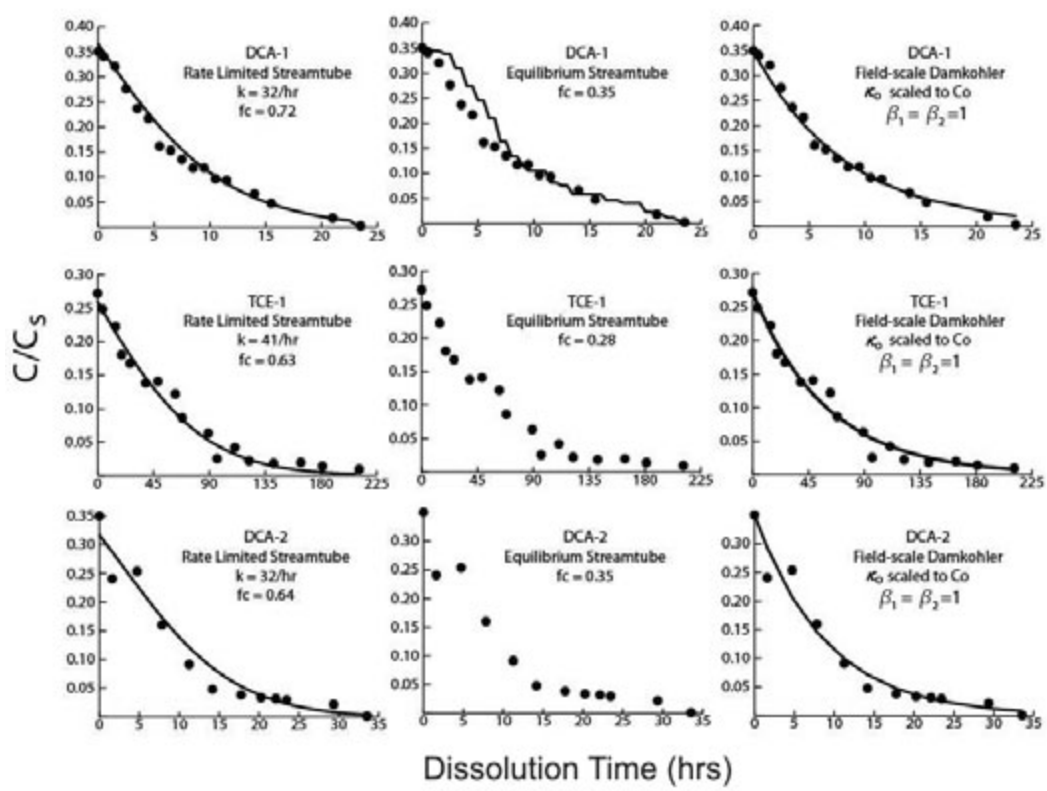

Figure 4.2-4. Comparison of the rate-limited streamtube, equilibrium streamtube, and effective Damkohler approaches for modeling source depletion from experiments DCA-1, TCE-1, and DCA-2 (Fure et al., 2006).

The nonequilibrium model required fitting one parameter (k_t) and the Da model required fitting 2 parameters (β_1, β_2). Two approaches were available for estimating f_c. In the first approach, image analysis was used to determine the fraction of streamtubes that contain NAPL. The second approach used the initial flux-averaged concentration (C_0). For example, if the initial flux averaged concentration was 50% of solubility, f_c = 0.50 could be assumed. For the equilibrium streamtube model, estimating f_c, based on the number of trajectories containing NAPL, resulted in an overestimation of C_0. Explanations for the overestimation of C_0 when using an f_c obtained from image analysis include velocities high enough to induce rate-limiting effects in the smaller trajectories and incomplete span of the NAPL across the thickness of the flow chamber in certain locations, which would result in bypass flow that was not captured in the two-dimensional image analysis technique. After estimating f_c from C_0, and using NAPL distribution information obtained from the image analysis, the equilibrium streamtube models matched the observed dissolution behavior closely (Figure 4.2-4), which supports the argument that the NAPL architecture was the primary factor controlling dissolution behavior in the systems studied. Additional processes not explicitly accounted for in the model, such as relative permeability, transverse dispersivity, and velocity variability are thought to exert a secondary influence on the dissolution behavior of the systems studied.

Although κ_0 in the Da model is treated in Parker and Park (2004) as a fitting parameter, we suggest that the physical meaning of κ_0 is similar to f_C and is primarily a measure of the fraction of streamtubes intersecting the contaminated portion of the source zone. Thus, for this application κ_0 was estimated by fitting to C_0. As shown in Figure 4.2-4, the Da model with this estimated κ_0 and $\beta_1 = \beta_2 = 1$ also provided a good fit to the data.

In summary, results indicate that in the systems studied, the relationship between DNAPL mass reduction and contaminant mass flux was primarily controlled by the NAPL architecture. A specific definition of NAPL architecture was employed where the source zone is resolved into a collection of streamtubes with spatial variability in NAPL saturation along each streamtube integrated and transformed into an effective NAPL content for each streamtube. The distribution of NAPL contents among the streamtubes (NAPL architecture) controlled dissolution dynamics. Two simplified models, a streamtube model and an effective Damkohler number model, were investigated for their ability to simulate dissolution dynamics.

4.2.2.2 Fluid and porous media property effects on dense non-aqueous phase liquid migration and contaminant mass flux

The effects of fluid and porous media properties on DNAPL migration and associated contaminant mass flux generation were evaluated in laboratory experiments (Totten et al., 2007). Relationships between DNAPL mass and solute mass flux were generated by measuring steady-state mass flux following step-wise injection of PCE into flow chambers packed with homogeneous porous media. The effects of fluid properties including density and interfacial tension (IFT), and media properties including grain size and wettability were evaluated by varying the density contrast and interfacial tension properties between PCE and water, and by varying the porous media mean grain diameter and wettability characteristics. Pertinent fluid and media properties for the experimental systems investigated are shown in Table 4.2-4. The design of the flow chamber was similar to that described by Jawitz et al. (1998), with dimensions of 14 cm by 28 cm and a pore volume of approximately 200 cm^3. Down-gradient mass flux following each incremental PCE injection was measured under steady-state water flow and after stabilization of the down-gradient PCE concentration. At each injection step, the red-dyed PCE distribution was traced from the side of the chamber to maintain a qualitative record of the PCE geometry. The experimentally measured contaminant concentrations were compared to predicted values assuming both equilibrium and rate-limited dissolution. A grid was overlain on the flow domain forming horizontal streamtubes, and the amount of DNAPL contacted in a given streamtube (or grid row) was tabulated in a manner similar to that described by Fure et al. (2006), and as summarized in the previous section. The equilibrium solute concentration was estimated as simply the product of the PCE solubility limit and the fraction of the streamtubes exposed to PCE. Rate-limited dissolution was accounted for using the modified Sherwood number (Sh') (Powers et al., 1992).

Table 4.2-4. PCE/n-decane mixture densities, media sieve and grain sizes, and best fit β values for mass loading/flux generation relationships measured in these media.

DNAPL density (g/cm^3)	US Standard Sieve No.	mean grain size (mm)	β(R^2)
1.6	20/30	0.68	0.41 (0.97)
1.6	30/40	0.48	0.54 (0.81)
1.6	40/50	0.35	0.93 (0.97)
1.6	40/60	0.32	0.26 (0.91)
1.6	50/70	0.23	0.43 (0.88)
1.4	30/40	0.48	0.66 (0.96)
1.4	40/50	0.35	0.83 (0.99)
1.1	30/40	0.48	0.88 (0.97)
1.1	40/50	0.35	1.0 (0.99)
1.0	30/40	0.48	0.92 (0.98)

PCE colored with Oil-red-O dye ($\leq 1 \times 10^{-4}$ M) was injected into the lateral center of the chamber 6.5 cm above the bottom and approximately 4 cm below the top of the sand layer. To evaluate the influence of oil/water wettability, PCE/water interfacial tension was modified by adding 0.0025, 0.005, 0.01, 0.025, 0.05 and 0.1 percent by volume of the surfactant Span 80 to PCE. Span 80 (sorbitan monooleate) was selected because of its low hydrophile/lipophile balance (HLB) value of 4.3. A low HLB surfactant was required to limit partitioning of the surfactant into the aqueous phase. The effect of surfactant concentration on PCE/water IFT was measured using a tensiometer (Tensiomat model 21, Fisher Scientific: accuracy ±0.25%).

DNAPL density was modified by using mixtures of PCE and n-decane ($\rho = 0.73$ g/cm^3). The low aqueous solubility of n-decane (0.003 mg/L) ensured limited partitioning from the non-aqueous to the aqueous phase. The IFT of the 50/50 mole fraction of PCE and n-decane mixture (52 dynes/cm) was found to be similar to that of PCE/water (47 dynes/cm), thus density was the primary property being varied in these experiments.

Experiments were conducted with DNAPL/water IFT values of 3, 13, and 47 dynes/cm (Span 80 concentrations of 0.05, 0.025, and 0 volume percent) in 30/40 sand packs. In this range of Span 80 concentrations, PCE solubility increased minimally (approximately 6%). The general pattern of DNAPL migration after initial release at the injection point was rapid migration to the base of the flow chamber followed by lateral spreading, producing a zone of residually trapped DNAPL between the injection point and the flow chamber base, and a pool across the base (Figure 4.2-5a). After each incremental release, the DNAPL distribution extent was traced and the numbers provided on the figure panels represent the cumulative number of 0.5 cm^3 PCE injections. Based on observations of the PCE distribution in the flow chamber, the extent of DNAPL lateral spreading increased slightly as IFT decreased. Pooling began by the second injection in each experiment, indicating that DNAPL vertical migration in the 30/40 sand was not significantly altered by reducing the IFT, and was therefore controlled by fluid density contrast.

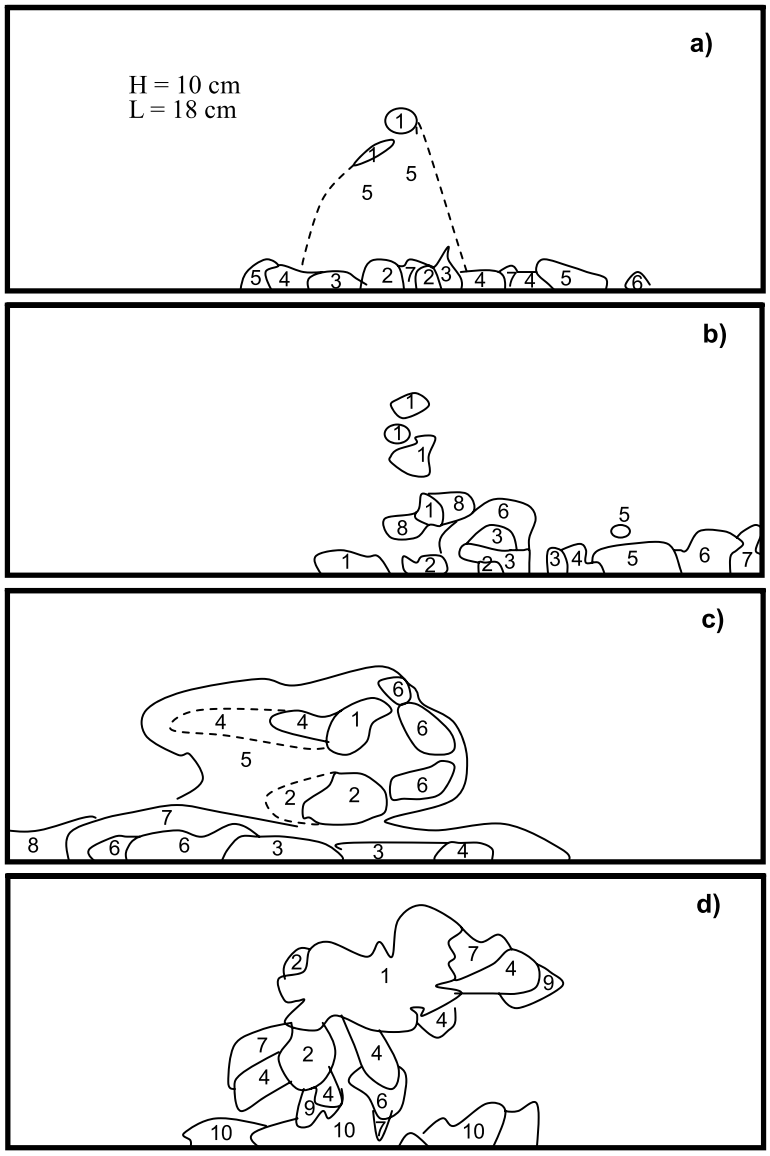

Figure 4.2-5. Tracings of observed distributions of DNAPL injected 10 cm above the flow chamber bottom in 30/40 sand with a) PCE and untreated sand, b) PCE and 50% OTS treated hydrophobic sand mixture, c) PCE and 100% hydrophobic sand, d) untreated sand and DNAPL mixture of density 1.1 g/cm^3 (Totten et al., 2007).

The mass flux generation as a function of PCE loading for these experiments is shown in Figure 4.2-6. As the IFT decreased, the effluent relative concentrations increased slightly. The maximum relative concentration appeared to be bounded by the injection point location since DNAPL did not migrate above the injection point. Because the media above the injection point (located at 0.6 of the aquifer height) was uncontaminated, the effluent relative concentration would not be expected to exceed this value (assuming DNAPL did not significantly alter the aqueous flow field).

The mass flux generation data were fit with a simple mass reduction, R_M, flux reduction R_J, power relationship $R_J = R_M^{\beta_P}$ resulting in β_P = {0.54, 0.50, 0.67} with R^2 = {0.80, 0.95, 0.98} for the 47, 13 and 3 dyne/cm systems, respectively. The entire data set was fit in Figure 4.2-6 with an average $\beta_P = 0.5$ (R^2=0.82). These results indicate that over the range of IFTs tested, relatively minor changes (β =0.5-0.67) were observed in the characteristics of the mass flux generation with PCE loading. Interfacial tensions lower than those tested here may be required to affect migration or prevent entrapment, which could significantly reduce mass flux.

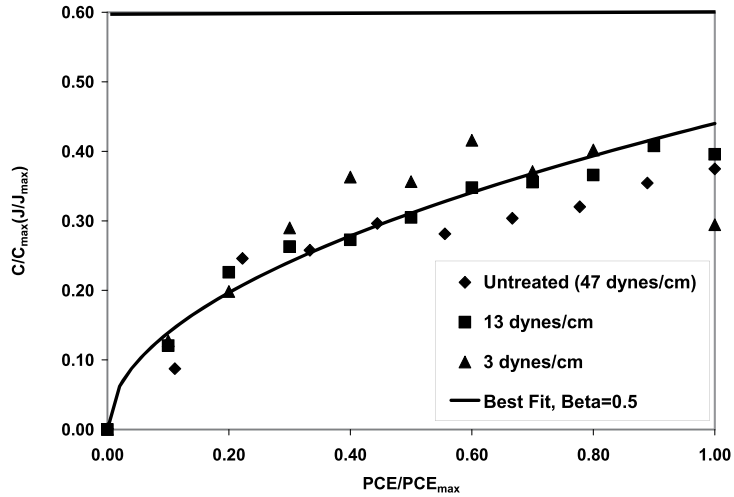

Figure 4.2-6. Fractional flux increase versus DNAPL loading for each interfacial tension value in untreated 30/40 sand (Totten et al., 2007).

Fluid density, modified using different ratios of PCE and n-decane, indicated that as density difference decreased, vertical migration was reduced and lateral migration was enhanced. This trend is illustrated in Figure 4.2-5a (pure PCE with ρ =1.6 g/cm^3) and Figure 4.2-5d (PCE and n-decane mixture with ρ = 1.1 g/cm^3). In experiments with PCE, pooling usually began by the second injection (1.0 cm^3), indicating complete vertical migration from the injection port to the bottom of the chamber. The lower density experiments required as many as nine injections (4.5 cm^3) to cause full migration from the injection port to the bottom of the experimental chamber and in the case of the ρ = 1.0 g/cm^3 experiment, no pooling occurred, indicating no full downward migration.

The PCE relative concentrations at final PCE loading were similar for all experiments, with the lower density tests generally exhibiting slightly higher values (Figure 4.2-7). These results are likely due to the observed migration of DNAPL above and below the injection port (Figure 4.2-5d), providing a larger cross sectional area exposure to flow.

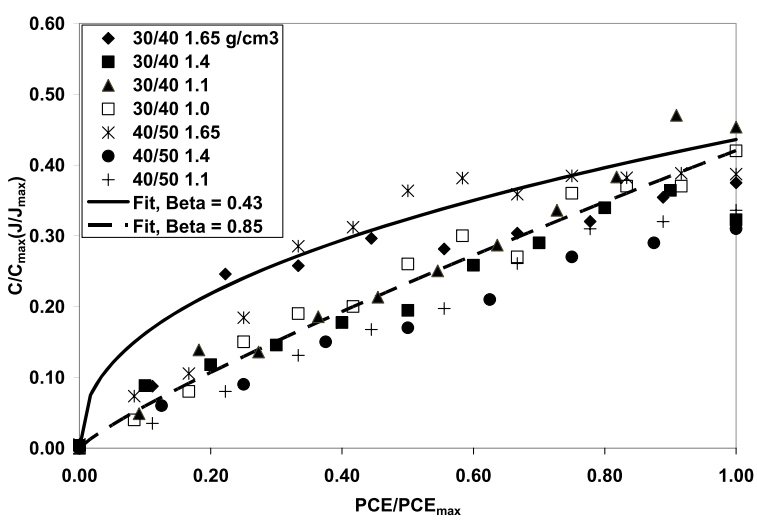

Figure 4.2-7. Fractional flux increase versus PCE loading for varying density and media (Totten et al., 2007).

The β_P values that were fit for each DNAPL density experiment are provided in Table 4.2-4. The mass loading/flux generation relationship became more linear as the density contrast decreased. The trend was particularly evident in the 30/40 sand. The shape of these curves, coupled with the DNAPL tracings, indicate that reduced vertical migration following each 0.5 cm^3 injection altered the mass flux generation relationship. Rapid downward migration, typically for higher density contrasts (i.e., pure PCE) resulted in rapid mass flux increases at low DNAPL loading when compared to the slower downward migration associated with lower fluid density contrasts. How mass becomes distributed as ganglia and pools, and how uniformly distributed those domains are, define the initial system dissolution characteristics.

The mass load and mass flux relationships measured in the laboratory experiments were compared to predictions from equilibrium and non-equilibrium dissolution models based on DNAPL contact lengths and Sherwood number correlations applied within 0.5 cm horizontal streamtubes through the flow domain. For the 20/30 sand, substantial differences were observed between the equilibrium and non-equilibrium predictions. The short length of the source zone in the groundwater flow direction may not have allowed sufficient contact time for equilibrium to have been achieved. In contrast, the longer source zones generated in the 100% hydrophobic sand (Figure 4.2-5c) were likely sufficient to achieve equilibrium. However, in both cases the measured relative concentrations were lower than those predicted, even under non-equilibrium conditions.

The model observations suggest that flow by-passing likely occurred in both experiments with the hydrophobic sand results comparing more favorably than the untreated sand. The hydrophobic media likely had less by-passing due to the more-uniform distribution of the PCE resulting from capillary wicking. The simple model applied here does capture the general shape of the flux generation mass loading relationships, suggesting that the distribution observed on the chamber wall reflects the general distribution of the DNAPL in the chamber. Application of the mass transfer correlations developed for homogeneously contaminated systems to more complex flow and contaminant distributions may be problematic given the lack of knowledge of water flow paths and DNAPL distributions within those flow paths. The predicted mass flux generation characteristics could be improved with laboratory characterization techniques that account for the DNAPL distribution across the thickness of the flow chamber (e.g., light transmission visualization techniques). While this may provide greater understanding in laboratory systems, field scale assessment may have to rely on tracer approaches to characterize these relationships.

4.2.2.3 Reactive tracer tests to predict dense non-aqueous phase liquid dissolution dynamics in laboratory flow chambers.

Reactive (i.e., partitioning) tracer tests were conducted to evaluate the relationship between contaminant mass reduction, R_M, and flux reduction, R_J in laboratory experiments with porous media contaminated with a DNAPL (Chen and Jawitz, 2008). The reduction in groundwater contaminant flux resulting from partial mass removal was obtained from cosolvent and surfactant flushing dissolution tests in laboratory flow chambers packed with heterogeneous porous media. Using the concept of streamtubes, a Lagrangian analytical solution was applied to study the contaminant dissolution. Analytical solution parameters related to aquifer hydrodynamic heterogeneities were determined from a nonreactive tracer, while those related to DNAPL spatial distribution heterogeneity were obtained from a reactive tracer. The parameter of reactive travel time variability was derived from this combination of tracers and can be used to predict the relationship between R_M and R_J.

Tetrachloroethylene (PCE) was selected as the DNAPL in this experiment. Dissolution experiments were conducted with one cosolvent flushing test (50% ethanol/water) and three surfactant flushing tests (2% Tween-80/water) to evaluate the effects of contaminant mass depletion on flux reduction. The four sets of experiments were conducted in two-dimensional flow chambers, as summarized in Table 4.2-5. The flushing solutions were selected based on their relatively high PCE solubilization capacity (~10^4 mg/L for both cosolvent and surfactant solutions) and moderate PCE-water interfacial tension (~2.4 dyn/cm for cosolvent solution and ~5.0 dyn/cm for surfactant solution respectively), which promoted PCE solubilization with minimal risk of mobilization.

Two flow chambers, similar to the design of that described by Jawitz et al. (1998), were employed in this study. The PCE was injected into the upper portion of the domain at 0.5 mL/min by a syringe pump.

Following redistribution of the injected DNAPL, approximately 10 pore volumes (PVs) of de-ionized water were displaced continuously through the flow chamber and flux-averaged PCE concentrations were measured in the effluent. Tracer tests were then conducted with methanol as the non-partitioning tracer, and 2,4-dimethyl-3pentanol (2,4DMP) n-hexanol, and 2-octanol as partitioning tracers. Approximately 9 PVs of the cosolvent solution (experiment I) and 14 PVs surfactant solution (experiment II) were continuously pumped through the chamber until either 97% of the PCE was removed or the effluent concentration was lower than the gas chromatograph (GC) detection limit. For experiments III and IV, the remedial solutions were pumped for 1 to 2 PVs and then changed back to water flushing until the PCE effluent concentration was constant, and then another 1 to 2 PVs of remedial solution were injected, again followed by water flushing. This pulsed flushing was repeated for 4 to 7 cycles. The PCE mass removal as a function of time was determined by integrating the dissolution breakthrough curves. PCE recovery rates for all experiments were in the range of 80–97%.

Table 4.2-5. Summary of the four experiments, equipment and truncated moment analysis results.

	Experiment I	**Experiment II**	**Experiment III**	**Experiment IV**
remediation solution	cosolvent	surfactant	surfactant	surfactant
flow rate (mL/min)	5.5	3.2	7.5	3.2
flushing	single	single	pulse	pulse
Pore volume (mL)	950	310	1200	305
PCE injected (mL)	11.95	11.58	8.00	9.12

Under equilibrium conditions, the flux-averaged concentration, C_J, exiting the source zone can be expressed as a function of flushing duration t_f (Jawitz et al., 2005):

$$C_J\left(t_f\right) = C_w\left(1 - f_{Q,t<t_f}\right) + C_s\left(t\right)\left(f_{Q,t<t_f} - f_{Q,c}\right) \tag{4.2-6}$$

where C_w and C_s are the solubility limits [ML^{-3}] in aqueous and flushing solution, respectively. The first term represents the fraction of the flow from stream tubes with travel time greater than the flushing duration and the second term refers to the fraction of the flow from stream tubes with travel times less than t_f but reactive travel times greater than t_f. The parameters $f_{Q,c}$ and $f_{Q,t<t_f}$ are the fraction of the flow through streamtubes that are clean and the fraction of flow through streamtubes with travel time less than the flushing duration, respectively. As shown in Appendix A of Jawitz et al. (2005), these parameters can all be determined from the moments of the t and τ distributions.

The pre-remediation source zone PCE saturation distribution for each experiment is shown in Figure 4.2-8. In experiments I and II PCE was dyed with Basic Red 94 (Sigma-Aldrich, Steinheim, Germany) and images captured with a color digital camera. In experiments III and IV, an innovative visualization method (i.e., method 1 as described in section 4.2.1) was used where the aqueous phase was dyed instead of the PCE (Wang et al., 2008). Gray scale images were captured with a 16 bit digital camera. This technique enables accurate visual quantification of the PCE distribution throughout the dissolution, whereas visualization methods that rely on dying the nonaqueous phase are limited to pre-remediation quantification (Conrad et al., 2002).

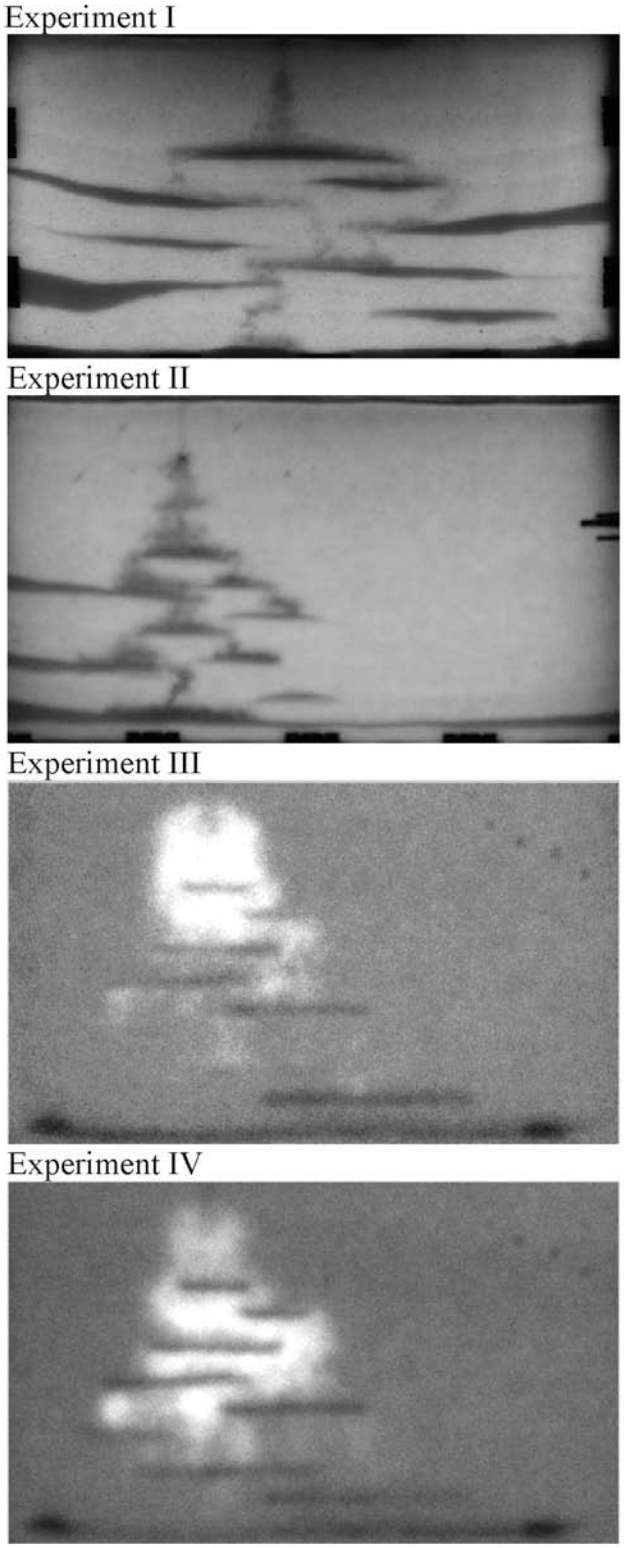

Figure 4.2-8. PCE spills before flushing. Images from experiments 1 and 2 are reflected light captured with standard digital camera and the NAPL is dyed red. Images from experiments III and IV are light transmission images captured with a CoolSnap 16-bit digital black-and-white camera (Chen and Jawitz, 2008).

Experiments I and II were conducted by continuous flushing by cosolvent and surfactant respectively. The measured dissolution breakthrough curves (BTCs) for PCE for these continuous flushing experiments are shown in Figure 4.2-9. The BTCs were predicted from the equilibrium dissolution equation 4.2-6 using the parameters obtained from the tracer tests. In the equilibrium streamtube model, the DNAPL architecture is the primary factor controlling the dissolution behavior, and other processes such as transverse dispersivity and relative permeability changes during dissolution are assumed to be negligible. The average relative errors between the model predictions and measured data for experiments I and II were 0.12 and 0.13 respectively.

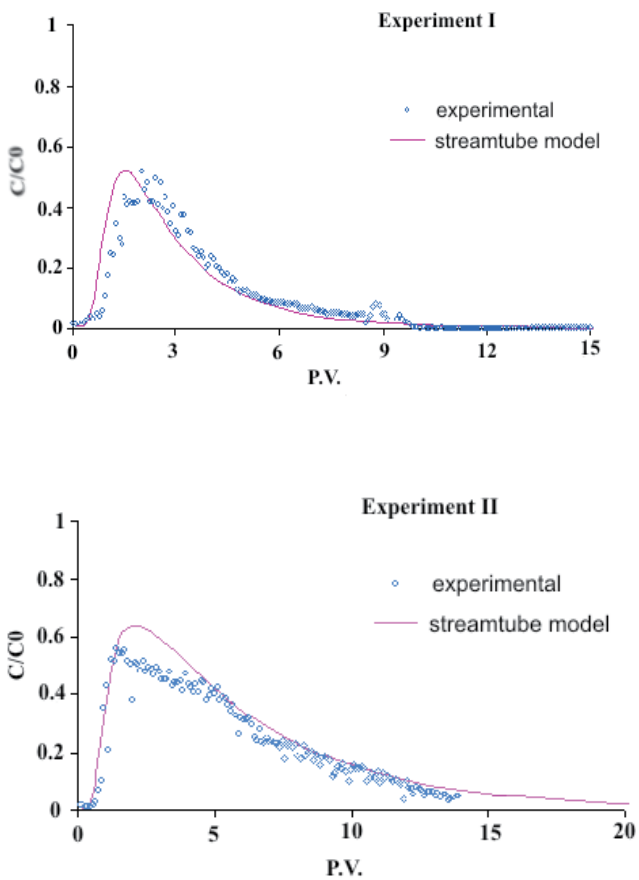

Figure 4.2-9. BTCs from surfactant flushing for Experiments I and II (Chen and Jawitz, 2008.

For the pulsed flushing experiments III and IV, the concentration of the injected surfactant solution $C_f(t)$ in equation 4.2-6 changed with time. It is difficult to simultaneously measure concentration of the surfactant and PCE by the inline GC. Assuming negligible partitioning of the surfactant into the PCE, the surfactant breakthrough curve would exhibit the same shape as the non-partitioning tracer.

The concentration of the surfactant may be expressed as:

$$C_f(t) = \frac{1}{2} erf\left(\frac{\ln t - \left(\mu_{\ln t} + \sigma_{\ln t}^2\right)}{\sqrt{2\sigma_{\ln t}}}\right) - \frac{1}{2} erf\left(\frac{\ln\left(t - t_0\right) - \left(\mu_{\ln t} + \sigma_{\ln t}^2\right)}{\sqrt{2\sigma_{\ln t}}}\right) \quad (4.2\text{-}7)$$

where $\mu_{\ln t}$ and $\sigma_{\ln t}$ were attained from non-partitioning tracer tests, and t_0 is the pulse duration of multiple flushing (PV).

Several studies have indicated that the equilibrium solubility of PCE exhibits a linear relationship with aqueous surfactant concentration (Edwards et al., 1991; Pennell et al., 1993; and Johnson and John, 1999). Batch solubility tests showed that PCE solubility increased linearly for surfactant (Tween 80) concentrations between 1000 and 40,000 mg/L. The observed linear relationship was:

$$C_s = 0.227C_f + 160 \tag{4.2-8}$$

The concentration of PCE was predicted dynamically using equations 4.2-7 and 4.2-8 (results from experiment III are shown in Figure 4.2-10). The average relative errors for experiments III and IV were 0.12 and 0.33 respectively.

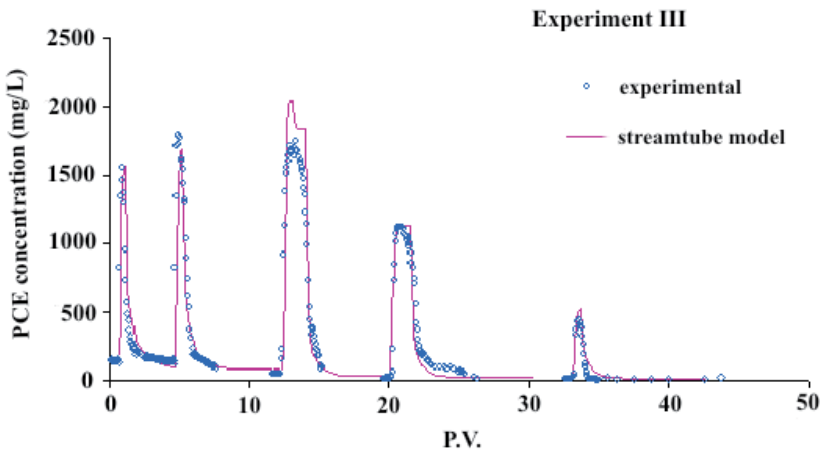

Figure 4.2-10. BTCs from surfactant flushing for Experiment III (Chen and Jawitz, 2008).

In summary, non-partitioning and partitioning tracers were applied to predict the DNAPL dissolution dynamics and mass reduction and flux reduction relationships using an equilibrium streamtube model. A single measurable parameter, reactive travel time variance, was applied to describe the overall system heterogeneity including both media heterogeneity and DNAPL architecture. Increasing the reactive travel time variance generated increased breakthrough curves spreading and shorter flushing duration to reduce DNAPL mass flux, which in turn leads to more favorable relationships between mass reduction and flux reduction.

4.2.2.4 Laboratory investigation of flux reduction from dense non-aqueous phase liquid (DNAPL) partial source zone remediation by enhanced dissolution

This study investigated the benefits of partial source zone removal using enhanced dissolution (Kaye et al., 2008). The benefits were assessed by characterizing the relationship between reductions in DNAPL mass and the corresponding reduction in contaminant mass discharge in several laboratory scale experiments. In these experiments, the effects of fluid override and underride associated with cosolvent flushing on the mass reduction (R_M) vs. flux reduction (R_J) relationship were investigated. Mass reduction and flux reduction are defined as $\left(1-\frac{M_{S,t}}{M_{S,0}}\right)$ and $\left(1-\frac{J_t}{J_0}\right)$, where $M_{S,t}$ is DNAPL mass at time t , $M_{S,0}$ is the initial DNAPL mass, J_t is contaminant mass flux at time t, and J_0 is the initial contaminant flux. Experiments were conducted using a single flushing event to remove most of the DNAPL from the system or in multiple shorter duration floods to determine the path of the R_M and R_J relationship.

Three unique cosolvent mixtures and one surfactant mixture were each tested in a two-dimensional heterogeneous aquifer model. Accounting for spatial heterogeneity of both media and DNAPL saturation is critical to the study of source zone removal. Two-dimensional flow chamber experiments allow for the emplacement of heterogeneous distributions of porous media. Tetrachloroethylene (PCE) was used as a model compound because of its ubiquity as an environmental contaminant and its relatively low aqueous solubility compared to other DNAPL contaminants. A lower-solubility DNAPL was preferred for enhanced dissolution laboratory experiments to minimize source zone depletion during water flow periods.

Eight solubilization experiments were conducted in the two-dimensional flow chambers packed with porous media and contaminated by PCE. As in previous studies, Accusand (Unimin Minnesota Corp.), a translucent porous media, was used for all of the experiments (Fure et al., 2006). The domain was packed with 20/30 sand as the main media with lenses of 40/50 sand throughout the domain. It is estimated that 90% of the flow field was in the 20/30 sand and 10% was in the 40/50.

The cosolvents used in the experiments were reagent alcohol (RA) (90.5% Ethanol, 4.5% Methanol, 5.0% Iso Propyl Alcohol) and ethyl-lactate (EL). Three different cosolvent mixtures (50% RA/50% Distilled Ionized (DI) water; 40% EL/60% DI water; and 18% RA/26% EL/56% DI water) and one surfactant mixture (2% Tween-80 by weight in DI water) were used in both single- and multiple-flushing experiments (eight experiments total). The cosolvent mixture percentages presented here are volume based. The mixtures will be referred to as 50% RA, 40% EL, Neutral Density (ND) and Surfactant (NDS) respectively. The physical and chemical properties of the mixtures are presented in Table 4.2-6. The mixtures were chosen because they have similar PCE solubilities, but significantly different densities.

Table 4.2-6. Fluid properties.

	Water	50% RA	40% EL	ND mixture	NDS
Density, ρ (g/cm^3)	1.000	0.89	1.014	1.001	1.00
Viscosity (cp),	0.895[b]	2.386[a,b]	2.238	2.369	0.9
PCE Solubility, C_{MAX} (mg/L)	150[b]	10,003	8,881	8,850	10,000

[a] Van Valkenberg, 1999

[b] Lide, D.R. and Frederikse, H.P.R., 1996

In this study two modes of injection were employed. In the single-flushing experiments (SF), each mixture was continuously flushed through the contaminated flow chamber to achieve more than 90% DNAPL mass removal. The Darcy velocity was approximately 1.3 m/d. Steady-state aqueous concentrations and mass fluxes were measured both before and after the source zone removal. After aqueous flushing, the remaining mass was recovered by enhanced dissolution to complete a mass balance. After all of the contaminant mass had been removed from the chamber, the flow characteristics were determined using a dye tracer. If the characteristics were favorable (i.e., no dead zones) PCE was injected into the media and a new experiment was started. If they were unfavorable, the chamber was taken apart, cleaned, and repacked.

In the multiple-flushing experiments (MF), the duration of each flushing episode was limited so that only a portion of the DNAPL mass was removed. The spatial distribution of the remaining DNAPL and corresponding integrated down-gradient contaminant mass flux were measured under steady-state aqueous conditions. Then, additional flushing agent was injected to further reduce the contaminant mass, and again, the steady-state aqueous contaminant mass flux was measured. This process was repeated until approximately 90% of the total mass was removed or the initial mass flux was reduced by more than 90%. The goal was to have either four or five consecutive injections that would achieve approximately 20%, 40%, 60%, 80%, and above 90% total contaminant mass removal and to measure the aqueous steady-state contaminant mass flux at each step. After the initial mass or flux was reduced by more than 90%, the remaining mass was removed and quantified to complete a mass balance.

Figures 4.2-11A B & C show the behavior of the cosolvent mixtures displacing the resident water in the chamber. These figures were created by tracing the dyed fluid front (shown as green lines in the figures). Dyed fluid fronts and DNAPL distributions were delineated by collecting digital images during the experiments. To improve resolution, a light transmission visualization (LTV) approach was used, where a light source was mounted on the back side of the flow chamber.

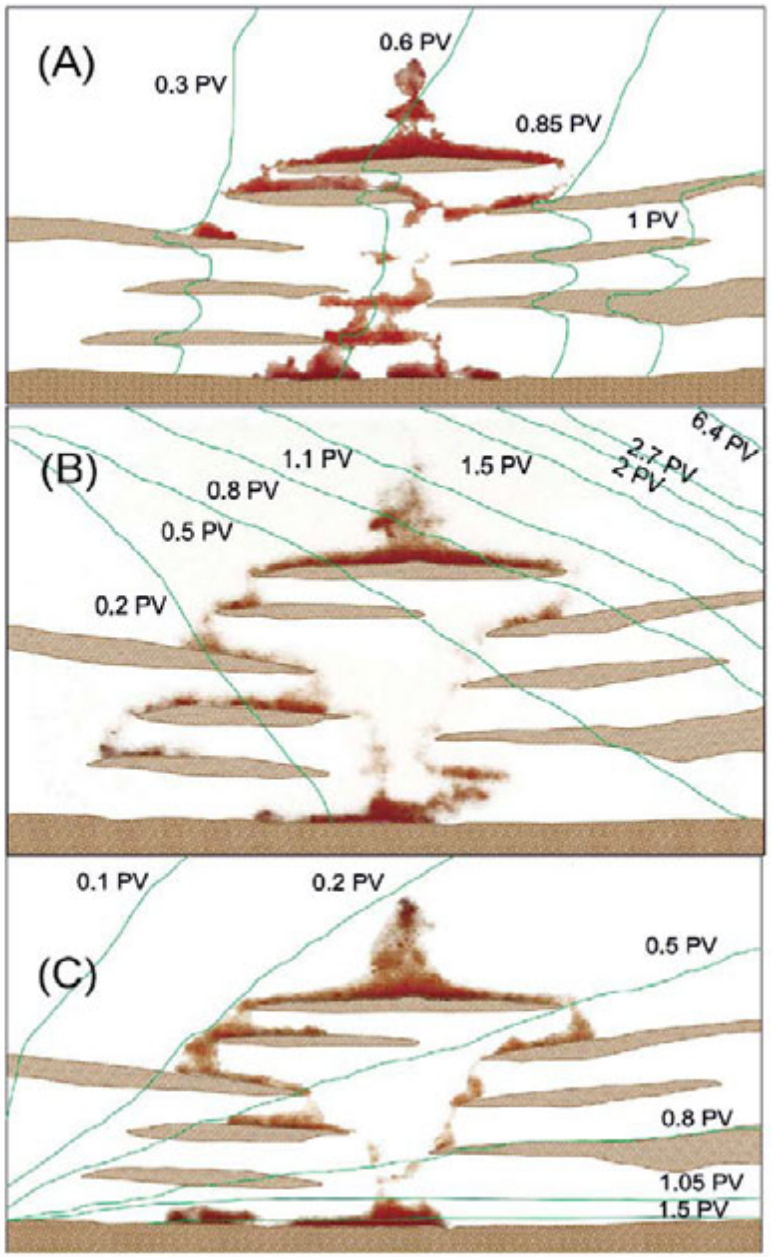

Figure 4.2-11. Displacement of resident water at different cosolvent injection volumes (PV). A) neutral density cosolvent, B) 40% EL, and C) 50% RA. The flow was from left to right at a Darcy velocity of approximately 1.3 m/d (Kaye et al., 2008).

A relatively vertical displacement front was observed for the ND solvent while significant underride and override were observed during the 40% EL and 50% RA floods, respectively. The mixing zone of the displacing front of all the mixtures was approximately 2 cm wide. The 50% RA reached the bottom of the

chamber after approximately 1.5 PVs. However, based on the effluent cosolvent concentrations, it was estimated that it did not completely displace the water at the bottom of the chamber until approximately 2 PVs had been injected. The 40% EL never completely displaced the resident water during the experiment; water remained in the top effluent corner of the chamber after almost 7 PVs of cosolvent had been injected. However, the 40% EL front reached all of the PCE contaminated areas, both residual and pooled, after only about 1.2 PVs. The angle from the horizontal of the 50% RA mixture override approached zero with continued cosolvent injection, while the angle from the horizontal made by the 40% EL mixture underride of the water stayed nearly constant from approximately 0.5 to 7 PVs.

Breakthrough curves are shown in Figure 4.2-12 for PCE and the cosolvents for the single injection flushing experiments. Visual images captured during the RA flood indicate that after injection of approximately 2.7 PVs of the cosolvent, most of the PCE mass that had been removed was from the residual portions above the lenses. Also at that point, the cosolvent had just reached the bottom of the chamber because of override (Figure 4.2-11c), and there was little change in the PCE mass in the lower portions of the chamber. However, at 3.3 PVs, the cosolvent had removed much of the residual above the bottom pool. Toward the end of the continuous injection, only pools of PCE remained above the top lens and at the bottom of the chamber. The cosolvent injected between 6.1 and 8.6 PVs removed most of the PCE above the top lens, but relatively little from the bottom pool. The lack of removal of the pool at the bottom of the chamber is due to a combination of the density override and the higher saturation of PCE in the pools.

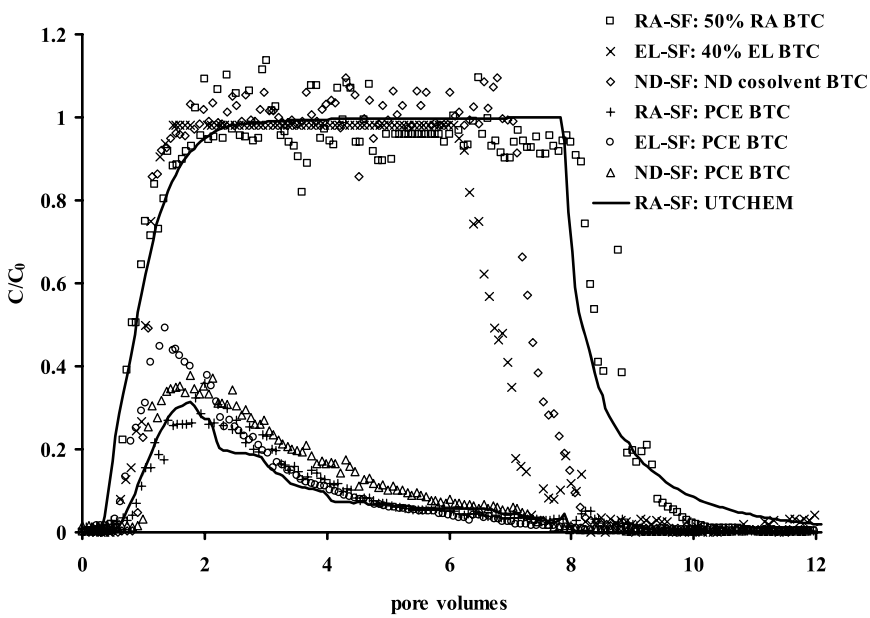

Figure 4.2-12. BTCs for all Single Flush experiments with cosolvent mixtures (Kaye et al., 2008).

Flux reduction that was based on the aqueous flushing data collected before and after the single-flush experiments yielded only a single point on a R_M vs. R_J plot (Figure 4.2-13). The multiple-flushing experiments were designed to capture more data on this curve by conducting sequential single floods, and resulted in 4 or 5 additional points on the $R_J(R_M)$ graph for each experiment. The R_J was based on the steady-state aqueous PCE concentrations measured after each flushing compared to the initial steady-state concentration.

The entire $R_J(R_M)$ path was also estimated from the SF experiments by approximating equivalent concentrations during aqueous flushing with a normalized concentration, C_N, as follows:

$$C_N = C(t)\frac{C_W}{C_{S,f}(t)} \tag{4.2-9}$$

Where $C(t)$ is the effluent PCE concentration at each time, C_W is the aqueous PCE solubility, and $C_{S,f}(t)$ is the PCE solubility in the flushing solution at each time. The latter term is a different function for each flushing agent. The estimated $R_J(R_M)$ paths of the SF experiments (designated SSA in Figure 4.2-13) all followed the same favorable trend just above the 1:1 line.

Several conclusions can be drawn from these results: 1) the experimental DNAPL architectures that were carefully constructed to be consistent between experiments resulted in similar $R_J(R_M)$ behavior, 2) partial source zone remediation using enhanced dissolution in these similarly packed systems resulted in flux reductions approximately proportional to the mass reductions, and 3) the override and underride associated with a single injection of cosolvent did not greatly influence the $R_J(R_M)$ relationship.

The RA-MF and EL-MF experiments resulted in less-favorable $R_J(R_M)$ compared to the SF experiments with the same fluids (Figure 4.2-13). The repeating override and underride associated with multiple injections of these flushing agents was the primary difference between the SF and MF experiments. The NDS-MF data support this observation as the $R_J(R_M)$ data (not shown) generally follow the SF data from all the flushing agents. Because of the stable displacement of NDC, multiple injections of this flushing agent were also expected to closely approximate the SF experiment $R_J(R_M)$ paths. However, the NDC-MF data matched the data from neither the SF nor the other MF experiments. This is likely explained by the different initial NAPL distribution in this experiment.

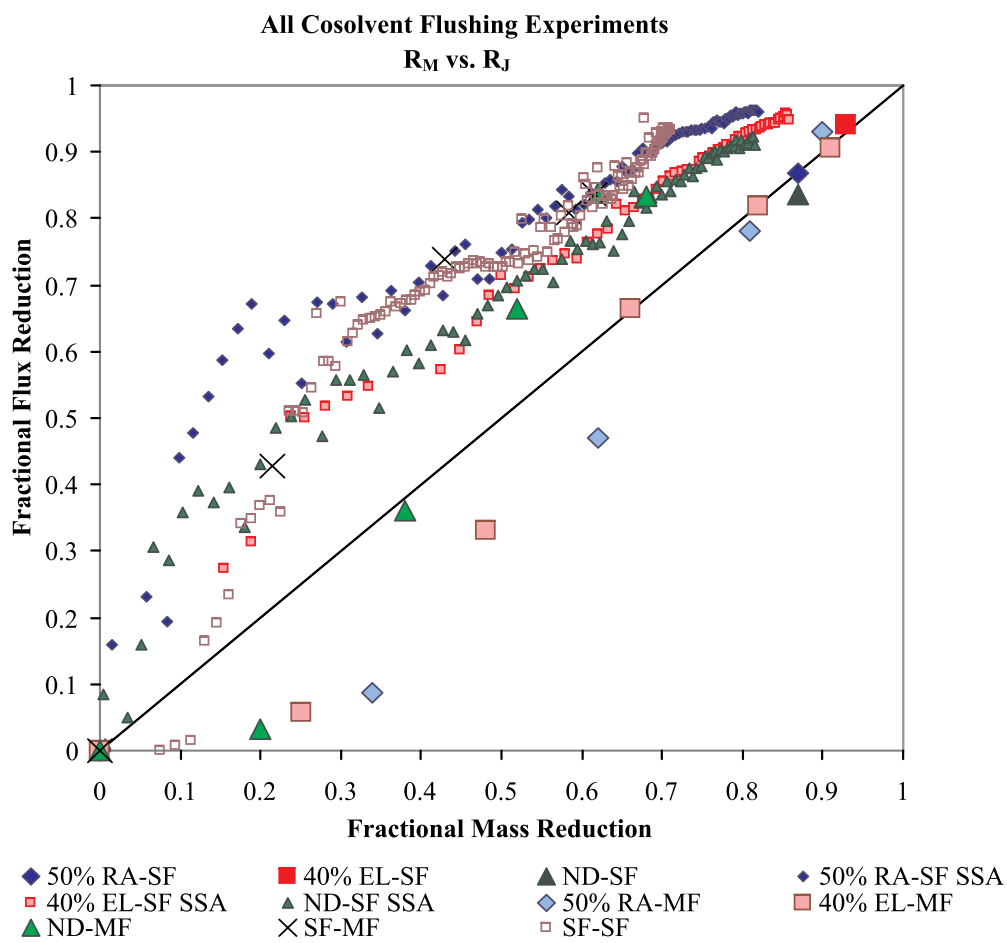

Figure 4.2-13. Aqueous based mass reduction (R_M) versus flux reduction (R_J) of the single and multiple-flushing experiments with the solubility scaled approach (SSA) path estimation of the single-flushing experiment (Kaye et al., 2008).

The R_M vs. R_J relationships of all of the single-flushing experiments were nearly identical, and in all of these experiments the initial DNAPL distributions were similar. Together, these observations indicate that the override and underride effects associated with the 50% RA and the 40% EL during miscible fluid displacement did not significantly affect the remediation performance of the agents during the single-flushing experiments. The $R_J(R_M)$ relationship of multiple injection experiments with both 50% RA and 40% EL were less favorable in the sense that there was less R_J for a given R_M than in the single injection experiments with the same flushing agent; however, the initial DNAPL architectures varied somewhat in these experiments. To eliminate the effects of different initial NAPL distributions, UTCHEM simulations were conducted for four cases (RA-SF, RA-MF, ND-SF and ND-MF) with a single initial NAPL distribution.

The ability of UTCHEM to capture the dissolution and density effects was demonstrated by simulating the RA-SF case. The DNAPL and media distribution input data for the model were created using the images from the light transmission measurements. The images were overlain with a finely discretized grid and saturation values were assigned based on the color intensity, such that the total mass of DNAPL in the domain was equal to the known mass injected. The details of the simulation domain and the fluid characteristics are presented in Table 4.2-7. The bimodal curve data presented by Hayden et al (1999) were used to estimate a bimodal curve height of 0.83. The numerical simulations used the same boundary conditions and flows as the RA-SF experiment.

The simulated ethanol and PCE breakthrough curves were in good agreement with observed laboratory data and provided confidence in the ability of the numerical simulator to capture the enhanced dissolution process and the density effects. The same DNAPL distribution was then used to simulate the RA-MF, NDC-SF, and NDC-MF cases. The results indicated that the $R_J(R_M)$ relationship was affected only slightly by the displacement fluid density differences associated with a single injection of cosolvent, and somewhat more so by the repeating override and underride associated with multiple injections but the latter effect was not as significant as that suggested by the experimental data.

Table 4.2-7. Numerical simulation input parameters.

Parameter	Value	Units
Domain Characteristics		
Grid Spacing: Δx	0.005	m
Grid Spacing: Δy	0.015	m
Grid Spacing: Δz	0.005	m
Longitudinal Dispersivity[1]	0.0017	m
Transverse Dispersivity[1]	0.00017	m
Porosity	0.383	
NAPL Saturation	0.07 – 0.25	
Fluid Characteristics: Density		
Density of water	1.0	g/cm^3
Density of PCE	1.625	g/cm^3
Density of ethanol	0.785	g/cm^3
Density of water-ethanol mixtures: linear function of density of water and ethanol		

Parameter	Value	Units
Fluid Characteristics: Viscosity		
Dynamic viscosity of water	0.895	cp
Dynamic viscosity of PCE	0.866	cp
Dynamic viscosity of water-ethanol and water-ND solvent mixture: $\delta_{mix} = (1-f_c)\delta_w e^{1.52 f_c} + 0.976 f_c e^{1.864(1-f_c)}$, where f_C is the cosolvent fraction[2]		
Fluid Characteristics: Solubility Parameters[3]		
Aqueous Solubility of PCE	150	mg/L
Maximum height of bimodal curve	0.8306	v/v
Oil concentration at Plait point	0.8554	v/v
Fluid Characteristics: Interfacial tension parameters[4]		
Interfacial tension: $IFT = IFT_0 \left(X / X_0 \right)^{k_{LF}}$, $X = \log\left(C_n^w + C_w^n + C_p^c\right)$ C_n^w is water concentration in NAPL phase (v/v), C_w^n is the NAPL concentration in the water phase, and C_p^c is the cosolvent concentration in the cosolvent poor phase		
Interfacial tension between water and PCE in absence of cosolvent, IFT_0	40	dynes/cm
Exponent describing effect of cosolvent, k_{LF}	1.98	
Mutual solubility term in absence of cosolvent, X_0	-3.82	

[1] *Dispersivity values were estimated by fitting non-reactive tracer breakthrough curves*
[2] *Coefficients determined by fitting the viscosity profile measured in the laboratory*
[3] *UTCHEM assumes that the bimodal curve is symmetrical*
[4] *Li and Fu (1992) and Liang and Falta (2008)*

4.2.2.5 The impacts of partial remediation by sparging on down-gradient DNAPL mass discharge

This study focused on assessing the impacts of DNAPL partial remediation by sparging on down-gradient mass discharge using two-dimensional (2-D) flow chambers packed with silica sands (Bob et al., 2009). The DNAPL source zone was created by adding known amounts of PCE to the chamber in two different experiments, and incremental removal of PCE mass from source zone was achieved by sparging. Following each sparging experiment, the chamber was flushed with water for a sufficient time to re-establish a steady state condition and effluent aqueous samples were collected and analyzed for dissolved PCE concentration, which was used to calculate the contaminant mass discharge. Image analysis based on LTV was employed to measure PCE saturation distribution in the chamber before and after each remediation step.

The flow chamber used in this study had nominal internal dimensions of 48.26 cm by 48.26 cm by 1.40 cm, and was constructed using a square aluminum frame (1.27 cm X 1.27 cm) and 1.27 cm thick tempered glass plates. Influent and effluent conditions were designed to essentially represent fully screened wells across the ~48 cm height of the chamber. A 6-way sampling valve was connected to the effluent line to minimize PCE

volatile losses during aqueous sample collection. In addition to the ports used to inject the PCE, the top section of the frame had four additional ports with 100-micron frits for capture of vapor phase PCE during sparging. The stainless steel tubes extending from each of these four ports were all merged into one effluent stainless steel tube line that was connected to a GC/MS instrument that was used to monitor vapor-phase PCE concentration (Fine et al., 2008). Using a tee split, this effluent line was also connected to a carbon column that captured all PCE vapor. The carbon was analyzed by extraction as a secondary check for PCE mass balance. The bottom frame had three equally-spaced ports that were used for sparging.

The chamber was packed dry with Accusand silica sands (Unimin, Le Sueur, MN). The whole model was packed with 20/30 sand to achieve a homogeneous packing for the first experiment (referred to as Pack A). For the second experiment (Pack B), a mixture of 20/30 and 40/60 sand at a ratio of 3:1 was used to achieve a homogeneous pack with a broader sand size distribution.

In both experiments, the chamber was first flushed with carbon dioxide to facilitate subsequent water saturation, then fully saturated with de-aired water and finally HPLC grade (>99.9% purity) PCE (Sigma-Aldrich Corporate, MO) dyed with Oil-Red-O (Fisher Scientific, Fair Lawn, NJ) at a concentration of 0.05 g/L was released into the chamber using a glass syringe fitted with a 20-gauge stainless steel needle. The low concentration of the dye used here is not expected to significantly alter relevant physical properties of PCE (Taylor et al., 2001). Digital images collected after PCE redistribution in the chamber are shown in Figure 4.2-14, as well as gas channels that formed during sparging experiments. Note that the mode of PCE addition was different in the two experiments. In the first experiment, 8.0 ml of the dyed PCE were added to the chamber through the top center port with the needle inserted to about 3.0 cm below the water table level. In the second experiment, PCE lateral spreading was enhanced by releasing PCE through all three top ports (3.0 ml through the center port and 2.5 ml through each of the other two ports). As before, the needle was inserted to about 3.0 cm below the water table. In both experiments, the PCE was allowed to redistribute for 72 hours and at least two LTV images were collected for each pack prior to starting the sparging experiments.

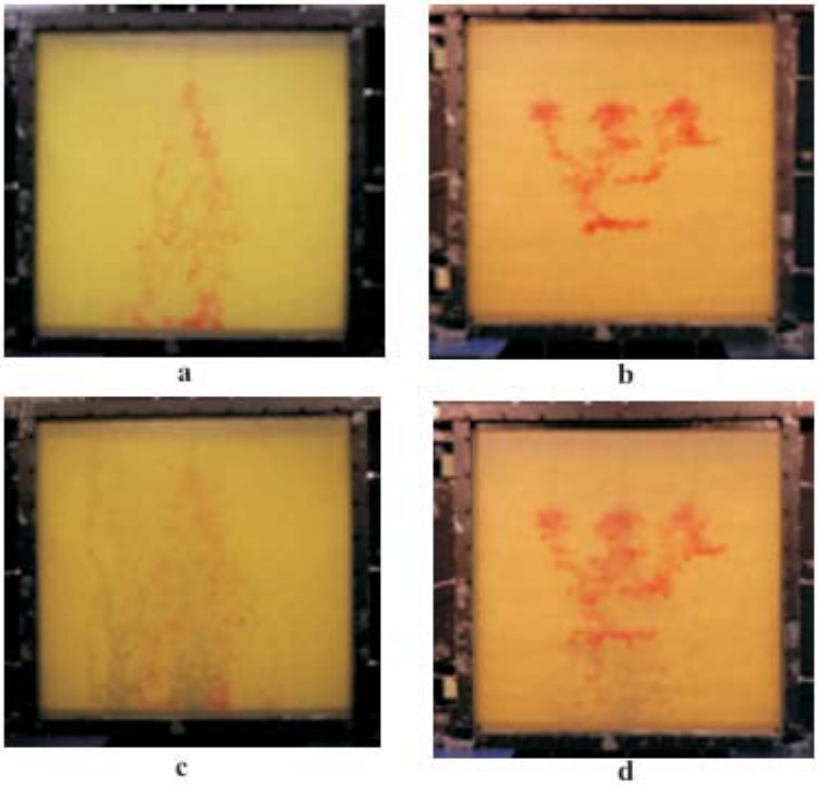

Figure 4.2-14. Digital photographs of the 2-D flow chamber: (a) and (b) show the initial distribution of PCE in Pack A and Pack B, respectively, and (c) and (d) show the sparging channels during the sparging experiments for Pack A and Pack B, respectively.

Two sparging events were conducted in the first experiment (Pack A) and four sparging events were conducted in the second experiment (Pack B). In each sparging event, a certain fraction of the PCE, as monitored by the GC/MS instrument was removed after which an aqueous flux test was conducted. The mass discharge in the presence of reduced PCE mass was then calculated and results were compared to the mass discharge in the presence of the initial PCE mass. It should be noted that CO_2, rather than air, was used in sparging to facilitate the aqueous re-saturation of the chamber. While sparging efficiency by CO_2 could be different than that by air, the performance of sparging as a remediation technique was not a major concern in this study but, as stated earlier, the focus was on the mass discharge emanating from the DNAPL source as a response to DNAPL mass reduction. The PCE saturation distribution in the chamber before and following each sparging test was measured using the modified LTV method developed by Bob et al. (2008).

The initial PCE saturation distribution in the chamber as calculated from image analyses, as well as the PCE saturation distribution following each sparging event, is shown in Figure 4.2-15 for both experiments. In this study, changes in mass flux were assessed with respect to two features of DNAPL architecture: the nature of the local scale PCE saturation and the PCE spatial distribution. With respect to the nature of the PCE saturation, an assessment was made based on whether the PCE was at or below residual saturation, in which case the PCE was considered to exist as ganglia in the pore space. Otherwise, if the PCE saturation was above the residual saturation, the PCE was considered to exist in the pore space as pools. The 12% and 15% saturation values that defined the residual saturation for pack A and B, respectively, were obtained gravimetrically from PCE residual saturation measurements conducted in a small 2-D flow chamber. The initial PCE saturation distributions indicated that PCE was present in the chamber as ganglia at or below residual saturation (≤12% for Pack A and ≤15% for Pack B) as well as pools of high saturation (>12% or 15%).

The PCE saturation distribution following the sparging events in these experiments showed that sparging can remove PCE from pooled areas as well as from areas of residual PCE saturation (see Figure 4.2-15). A summary of experimental parameters for Pack A and Pack B is given in Table 4.2-8 and experimental results are summarized in Table 4.2-9. The PCE mass removed was obtained by averaging the results of the granular activated carbon (GAC) analysis and the GC/MS. PCE mass calculations obtained from saturation values measured by the LTV method agreed quite well with GAC and GC/MS results. A detailed discussion of the LTV results and the errors associated with LTV analyses for these experiments are presented elsewhere (Bob et al., 2008). The on-line GC/MS instrument provided the advantage of monitoring how much PCE mass was removed during a given sparging event (Fine et al., 2008). Consequently, the sparging was ceased when a specified fraction of the PCE mass was removed. Total PCE mass fraction removal from Pack A and Pack B was 55% and 78%, respectively (Table 4.2-9). While these results, as well as others (Bass et al., 2000, Waduge et al., 2004) show that sparging can be an effective NAPL remediation technology, of particular interest in this study was the aqueous effluent contaminant mass discharge resulting from partial removal of the DNAPL. To assess this, the PCE mass fraction removed following each sparging event in both experiments was plotted as a function of relative mass discharge, and these data are shown in Figure 4.2-16. The steady state flux-averaged effluent PCE concentration was used to calculate the mass discharge following each sparging test, and this mass discharge was normalized to the initial mass discharge (i.e. prior to conducting the first sparging test in each experiment) to obtain the relative mass discharge.

Figure 4.2-16 shows that the removal of 55% of PCE mass in Pack A experiment resulted in 55% reduction in mass discharge but a similar mass removal in Pack B experiment resulted in very small reduction in mass discharge. Both packs were characterized by a high initial ganglia percentage of PCE distribution, but while the ganglia fraction of Pack A essentially remained the same as PCE mass was removed, the ganglia percentage in Pack B increased as PCE was removed (Table 4-2-9). This difference in mass discharge response between these two experiments highlights the importance of DNAPL architecture in controlling the down gradient mass discharge.

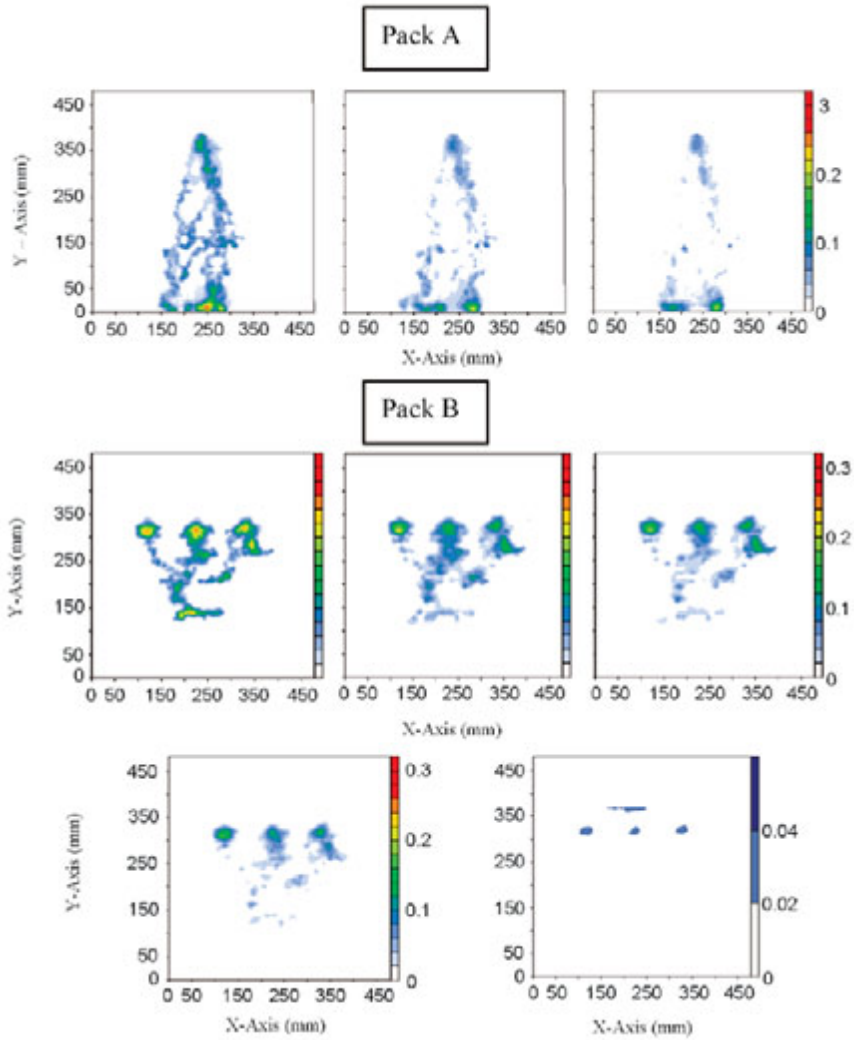

Figure 4.2-15. The initial PCE saturation distribution in the flow chamber and the saturation distribution following each sparging event. Two sparging tests were conducted in Pack A and four sparging tests were conducted in Pack B.

Table 4.2-8. Summary of PCE sparging test parameters.

Parameter	Pack A	Pack B
Porous media	20/30 Accusand	Mixture of 20/30 and 40/60 in a 3:1 ratio
Porosity, pore volume (ml)	0.311 (1026)	0.296 (931)
Volume of PCE injected (ml)	8.0	8.0
% Ganglia	85	74
Overall PCE saturation (%)	0.78	0.86
Initial flux-averaged steady-state concentration (mg/L)	61.3 ± 7.0	55.4 ± 16.2
Flux test aqueous flow rate (ml/min)	3.01 ± 0.07	3.13 ± 0.05
Initial mass discharge (mg/min)	0.189 ± 0.023	0.171 ± 0.050

Table 4.2-9. Summary of PCE sparging test results.

Parameter	First Sparging Event		Second Sparging Event		Third Sparging Event	Fourth Sparging Event
	Pack A	Pack B	Pack A	Pack B	Pack B	Pack B
Sparging rate (LPM) and duration (hours)	0.200 (5)	0.200 (5)	0.200 (4)	0.200 (3)	0.200 (9)	0.200 (9)
Total PCE removed (ml, %)	3.0 (37.5)	1.9 (23.8)	4.4 (55.0)	3.7 (46.3)	5.1 (63.8)	6.2 (77.5)
PCE present as ganglia (%)	91	94	88	93	96	100
Effluent flux-averaged concentration (mg/L)	41.7 ± 11.9	66.2 ± 14.8	25.8 ± 5.7	51.8 ± 8.0	48.3 ± 9.1	2.3 ± 0.3
Relative mass discharge (M_d / M_{d_0})	0.66 ± 0.03	1.21 ± 0.45	0.40 ± 0.10	0.95 ± 0.31	0.89 ± 0.31	0.04 ± 0.01

As more PCE mass is removed in Pack B, the mass discharge decreased significantly to 4% of the initial value indicating a 96% reduction (Figure 4.2-16). This mass reduction/mass discharge relationship where mass discharge reduction is higher than mass reduction is quite favorable. It is worth noting that the 96% reduction in mass discharge achieved in this experiment was associated with a PCE flux-averaged effluent concentration of 2.3 mg/L (see Table 4.2-9), which is significantly higher than the MCL for PCE. However, the mass discharge at this point (0.007 mg/min) was significantly smaller than the initial mass discharge. Consequently, beneficial changes in the associated plume at a real site are expected, such as a reduction in the spatial extent of the plume or the total contaminant mass in the plume. The extent to which the plume would change depends on both the magnitude of flux reduction and the natural attenuation capacity of the down gradient aquifer formation.

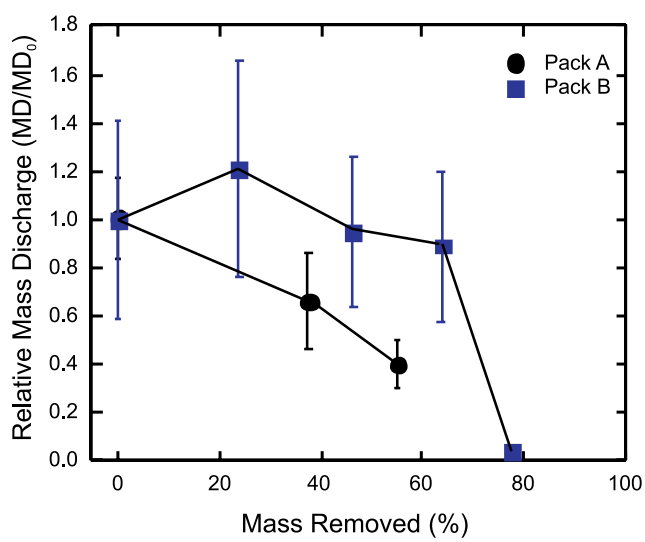

Figure 4.2-16. Relative effluent mass discharge as a function of PCE mass removed for the two experiments.

4.3 Theoretical and Modeling Research

There are three broad groups of models that have been used for the description of contaminant transport at DNAPL sites: (1) numerical models, (2) Lagrangian, or streamtube based models, and (3) analytical models. While the numerical models are based on the most detailed description of process behavior at the pore scale, they are computationally intensive and require information on spatially variable parameters like local permeability and DNAPL saturations that are difficult to characterize with reasonable accuracy using the available technologies. Though these models are generally not parameterizable at the field scale, they help in improving our understanding of the behavior of DNAPL sources and plumes.

At the other end of the spectrum are the empirical or semi-empirical analytical models that assume homogeneity of parameters and are based on several simplifying assumptions. It has been suggested that even though the "local" scale processes behind DNAPL dissolution are complex, the temporal evolution of contaminant concentrations at the source control plane can be reasonably described by these simple models. Though site-specific parameterization of these models are not yet that well established, the models, due to their computational simplicity and fast run times, serve as good tools to (1) run optimization routines for partial source and plume treatment, and (2) perform uncertainty assessments.

The Lagrangian models are the only "practical" techniques currently available for predicting site specific mass removal mass flux relationships. These models are based on estimating integrated source zone parameters using tracer tests and then using the parameters for prediction of source flux and down-gradient impacts. The ability to characterize source zones in terms of only a handful of trajectory-integrated parameters, in contrast to the potentially very large number of spatially distributed parameters required for traditional Eulerian approaches, has increased the popularity of these models over the last few years. However, tracer tests are very expensive and not yet affordable at most field sites.

The benefits of partial source zone remediation were evaluated from fundamental physical principles using each of these modeling approaches. The results of these analyses are described in detail in the following peer-reviewed journal articles and reports:

Lagrangian Models

Jawitz, J.W., A.D. Fure, G.G. Demmy, S. Berglund, and P.S.C. Rao (2005). Groundwater contaminant flux reduction resulting from nonaqueous phase liquid mass reduction. *Water Resources Research* 41(10):W10408.1-15, doi:10.1029/2004WR003825.

Wood, A.L., C.G. Enfield, F. Espinoza, M. Annable, M.C. Brooks, P.S.C. Rao, D. Sabatini and R. Knox (2005). Design of aquifer remediation systems: (2) Estimating site-specific performance and benefits of partial source removal. *Journal of Contaminant Hydrology* 81(1-4):148-166.

Coupled Source Zone and Plume Models

Falta, R.W., P.S.C. Rao, and N. Basu (2005a). Assessing the impacts of partial mass depletion in DNAPL source zones: I. Analytical modeling of source strength functions and plume response. *Journal of Contaminant Hydrology* 78(4):259-280.

Falta, R.W., N. Basu, and P.S.C. Rao (2005b). Assessing the impacts of partial mass depletion in DNAPL source zones: II. Coupling source strength functions to plume evolution. *Journal of Contaminant Hydrology* 79(1-2):45-66.

Falta, R.W. (2008). Methodology for comparing source and plume remediation alternatives. *Ground Water* 46(2):272-285.

Falta, R.W., M.B. Stacy, A.N.M Ahsanuzzaman, M. Wang, and R. Earle (2007). REMChlor Remediation Evaluation Model for Chlorinated Solvents User's Manual Version 1.0. http://www.epa.gov/ada/csmos/models/remchlor.html

Wagner, D.E., J. Huang, J.L. Heiderscheidt, and M.N. Goltz. (2009). Modeling study to quantify the benefits of groundwater contaminant source remediation. (In preparation).

Basu, N.B., A.D. Fure, and J.W. Jawitz (2008b). Simplified contaminant source depletion models as analogs of multiphase simulators. *Journal of Contaminant Hydrology* 97(3-4):87-99, doi: 10.1016/j.jconhyd.2008.01.001.

Basu, N.B., A.D. Fure, and J.W. Jawitz (2008c). Predicting DNAPL dissolution using a simplified source depletion model parameterized with partitioning tracers. *Water Resources Research* 44(7):W07414.1-13, doi:10.1029/2007WR006008.

Basu, N.B., P.S.C. Rao, R.W. Falta, M.D. Annable, J.W. Jawitz, and K. Hatfield (2008a). Temporal evolution of DNAPL source and contaminant flux distribution: impacts of source mass depletion. *Journal of Contaminant Hydrology* 95(3-4):93-109.

Falta, R.W. (2003). Modeling sub-grid block scale DNAPL pool dissolution using a dual domain approach. *Water Resources Research* 39(12):SBH 18.1-8.

Falta, R.W. (2005). Dissolved Chemical Discharge from Fractured Clay Aquitards Contaminated by DNAPLs, In: *Dynamics of Fluids in Fractured Rock*, B. Faybishenko, P.A. Witherspoon, and J. Gale, eds., Geophysical Monograph 162, American Geophysical. Union.

Falta, R.W. (2009). Monte Carlo simulations of source behavior with remediation. (In preparation).

Liang, H., and R.W. Falta (2007). Modeling field-scale cosolvent flooding for DNAPL source zone remediation. *Journal of Contaminant Hydrology* 96(1-4):1-16.

Van Antwerp, D., R.W. Falta, and J.S. Gierke (2008). Numerical simulation of field-scale contaminant mass transfer during air sparging. *Vadose Zone Journal* 7:294-304.

4.3.1 Lagrangian Models

Lagrangian models (Jawitz et al., 2005; Enfield et al., 2005; Wood et al., 2005; Basu et al., 2008b) describe the source zone as a collection of non-interacting streamtubes with hydrodynamic and DNAPL heterogeneity represented by the variations in the travel time *t* and trajectory-integrated DNAPL saturations within the streamtubes (Figure 4.3-1). These models are computationally less intensive and require fewer parameters than three-dimensional numerical models, but describe the spatial variability of source zones unlike one-dimensional flow and transport codes that assume homogeneity. The Lagrangian models assume that flow is stable and steady, advection is the dominant transport process, NAPL is immobile, and NAPL saturations are low such that dissolution does not significantly alter the properties of the flow field. These assumptions do not hold under conditions of displacement instabilities induced by buoyant or viscous forces (Jawitz et al., 1998), transient flow due to time-varying boundary conditions such as seasonal shifts in hydraulic gradients (Rivett and Feenstra, 2005), alteration of flow field due to relative permeability changes during dissolution (Geller and Hunt, 1993), and nonadvective transport of solutes with different effective diffusion coefficients (Cirpka and Kitanidis, 2000). The Lagrangian models described here were developed for dissolution-based remediation activities. There are two steps in the prediction of source depletion using Lagrangian techniques: (1) Estimation of the statistical properties of the hydrodynamic and the DNAPL distribution, and (2) Prediction of DNAPL dissolution using the estimated properties.

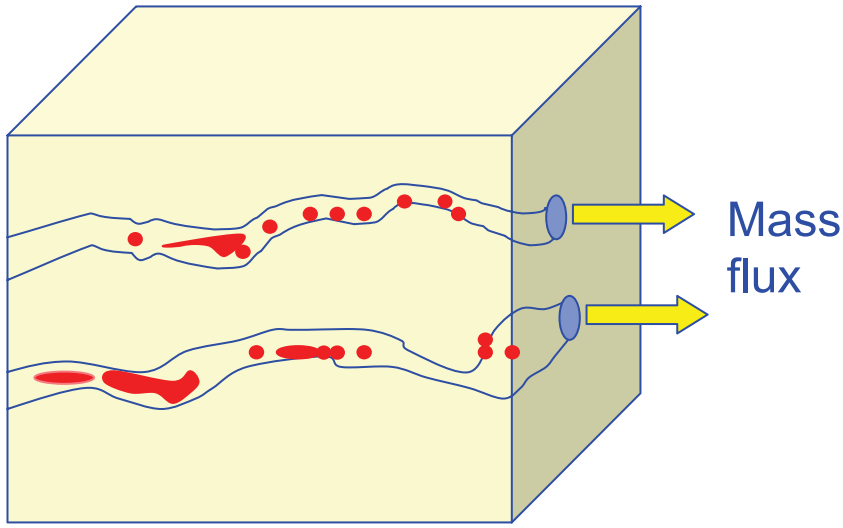

Figure 4.3-1. Lagrangian conceptualization of DNAPL source zones.

Estimation of the statistical properties of the hydrodynamic and DNAPL distribution

In the Lagarangian model, the properties of the hydrodynamic field and the DNAPL saturation distribution are described by the mean and standard deviation of the non-reactive travel time, t, and the trajectory integrated DNAPL content, $\hat{S}$ respectively.

It is important to distinguish the Lagrangian parameter $\hat{S}$ that represents an integral measure between the injection and monitoring planes from the local DNAPL content S. The NAPL content is defined as $S = S_N / (1 - S_N)$, where S_N is NAPL saturation. The mean and standard deviation of the t and $\hat{S}$ are estimated by performing non-partitioning and partitioning tracer tests under the same initial and boundary conditions as the dissolution experiment. The travel time and the NAPL contents are assumed to be lognormally distributed, and correlated ($\gamma_{\tau, \hat{S}}$ = correlation coefficient) random variables. Moreover, the flow field can be composed of multiple hydrologic units and can thus, be described by multiple lognormal distributions.

Two techniques were investigated for estimating the characteristics of the travel time and the DNAPL saturation distribution: (1) the method of moments (Jawitz et al., 2005; Basu et al., 2008b) where measured moments from tracer breakthrough curves are equated with derived moment equations to calculate the required parameters, and (2) the inverse modeling approach (Enfield et al., 2005; Wood et al., 2005) where tracer breakthrough curves are fitted to a transport model and the parameters estimated by optimization.

Method of moments: The moments of the t and $\hat{S}$ (m_1^t, m_2^t, $m_1^{\hat{S}}$, $m_2^{\hat{S}}$) distributions are estimated from the moments of the non-partitioning and partitioning tracer breakthrough curves (m_1^{np}, m_2^{np}, m_1^p, m_2^p) using the following equations (Jawitz et al., 2003)

$$m_1^{np} = m_1^t + \frac{t_0}{2} \tag{4.3-1a}$$

$$m_2^{np} = m_2^t + t_0 m_1^{np} - \frac{t_0^2}{4} \tag{4.3-1b}$$

$$m_1^p = (1-\phi) m_1^{np} + \phi \left[m_1^{np} + \Omega_N m_1^{\hat{S}} m_1^{np} \gamma - m_1^{\hat{S}} \Omega_N \frac{t_0}{2} \right] \tag{4.3-1c}$$

$$m_1^p = (1-\phi)m_2^{np} + \phi\left[\begin{array}{l}\left(1+2\Omega_N m_1^{\hat{S}}\gamma^2 + \Omega_N^2 m_2^{\hat{S}}\gamma^4\right)m_2^{np} - \\ \left(\Omega_N m_1^{\hat{S}} t_0\gamma + \Omega_N^2 m_2^{\hat{S}} t_0\gamma^2\right)m_1^{np} + \Omega_N^2 m_2^{\hat{S}}\dfrac{t_0^2}{4}\end{array}\right] \tag{4.3-1d}$$

$$m_3^p = (1-\phi)m_3^{np} + \phi\left[\begin{array}{l}\left(1+3\Omega_N m_1^{\hat{S}}\gamma^3 + 3\Omega_N^2 m_2^{\hat{S}}\gamma^6 + \Omega_N^3 m_3^{\hat{S}}\gamma^9\right)m_3^{np} - \\ \left(\begin{array}{l}\Omega_N m_1^{\hat{S}}\dfrac{t_0}{2}\gamma^2 + \Omega_N^2 m_2^{\hat{S}} t_0\gamma^4 + \Omega_N^3 m_3^{\hat{S}}\dfrac{t_0}{2} \\ +\Omega_N^2 m_2^{\hat{S}}\dfrac{t_0^2}{2}\gamma^2 + \Omega_N^3 m_3^{\hat{S}}\dfrac{t_0^2}{4}\gamma^3\end{array}\right)3m_1^{np} + \Omega_N^3 m_3^{\hat{S}}\dfrac{t_0^3}{8}\end{array}\right] \tag{4.3-1e}$$

where, Ω_N is the NAPL-water partitioning coefficient, t_0 is the solute pulse injection duration, $\phi = \left(f - \overline{S}_n\right)/\left(1-\overline{S}_n\right)$, f is the fraction of the domain that is contaminated, $\overline{S}_n$ is the average NAPL saturation for the entire spatial domain, and the correlation term $\gamma = \exp\left(\rho_{t,\hat{S}}\sigma_{\ln t}\sigma_{\ln \hat{S}}\right)$. Assuming the travel time and the DNAPL saturation distributions to be lognormal variables, the parameters of the lognormal distribution can be calculated from the estimated moments using the following equations:

$$\mu_{\ln x} = 2\ln\left(m_1^x\right) - \frac{\ln\left(m_2^x\right)}{2} \tag{4.3-2a}$$

$$\sigma_{\ln x}^2 = \ln\left(m_2^x\right) - 2\ln\left(m_1^x\right) \tag{4.3-2b}$$

where, x = t or $\hat{S}$

Inverse Modeling Approach: In the inverse modeling approach (Enfield et al., 2005; Wood et al., 2005) tracer breakthrough curves are fitted to a transport model and the parameters estimated by optimization. The variables (mean and standard deviation of the travel time and the NAPL saturation distributions of the different hydrologic units, the fraction of the domain occupied by each hydrologic unit, the contaminated fraction and the correlation coefficient) are estimated by minimizing the sum of squares logarithmic error (SSLE) using the equation:

$$SSLE = \sum_{i=1}^{p}\left(\ln\overline{C}_{p,i} - \ln\hat{C}_{p,i}\right)^2 + \sum_{j=1}^{u}\left(\ln\overline{C}_{np,i} - \ln\hat{C}_{np,i}\right)^2 \tag{4.3-3}$$

Where, $\overline{C}$ and $\hat{C}$ are the measured and estimated concentrations respectively at time t for the u or p observations; u is the number of observations for the non-partitioning tracer and p is the number of observations for the partitioning tracer.

Prediction of DNAPL source depletion behavior and mass discharge-mass flux relationships

The formulation of the DNAPL source depletion model is based on the concept of the reactive travel time, τ. The reactive travel time is defined as the time required to remove NAPL from a streamtube, under a given set of flushing conditions. This is a function of the NAPL content in the streamtube, and the travel time through the streamtube, and the solubility in the flushing solution as shown in the following equation:

$$\tau = t + \frac{M_n}{QC_S} = t + \frac{\rho_N \hat{S} L A_S \eta}{q A_S C_S} = t + Nt\hat{S} \tag{4.3-4}$$

where M_n[M] is the NAPL mass in the individual streamtube, Q is the flow rate [L^3/T], ρ_N is the NAPL density, v is the velocity in the streamtube [L/T], L is the length of the streamtube, A is the cross sectional area of the streamtube [L^2], t is the residence time or the travel time and N is the ratio of the NAPL density to the solubility (ρ_N / C_S).

For an arbitrary flushing duration t_f, all streamtubes with reactive travel times less than t_f, are clean, and contribute zero flux, while all streamtubes with $\tau > t_f$ are still contaminated. Under the equilibrium assumption, all streamtubes with $\tau > t_f$ are at solubility, and the NAPL concentration for a given streamtube i can be expressed as a function of the flushing duration T as:

$$C_i(t_f) = \begin{Bmatrix} C_W \, for \, 0 < t_f < t_i \\ C_S \, for \, t_i < t_f < \tau_i \\ 0 \, for \, \tau_i < t_f \end{Bmatrix} \tag{4.3-5}$$

The flux-averaged concentration from the source zone is calculated by adding the contribution of all the streamtubes. The distribution of streamtube travel times and the corresponding NAPL saturations are estimated using the techniques described in Jawitz et al., (2005); Enfield et al., (2005); and Wood et al., (2005). For multicomponent NAPL mixtures, equation 4.3-5 is modified using Raoult's Law (Wood et al., 2005).

Application of Lagrangian Models

The Lagrangian models were used to estimate contaminant elution curves from field pilot-scale in-situ flushing tests and results were compared to observed elution behavior (Figures 4.3-2 and 4.3-3). Parameters for the models were derived from tracer tests conducted prior to flushing. The data suggest that this modeling approach can predict dissolution behavior using nonreactive and reactive tracer travel time distributions to estimate hydrodynamic variability and NAPL distribution heterogeneity. Jawitz et al. (2005) used the combined statistics of these distributions to evaluate the relationship between contaminant mass depletion (R_M) and contaminant flux reduction (R_J) (Figure 4.3-4). The combined effects of aquifer and NAPL heterogeneities were shown to be captured in a single parameter, reactive travel time variability, which was determined to be the most important factor controlling the relationship between R_M and R_J. It was shown that as heterogeneity in aquifer properties and NAPL spatial distribution increases, less mass reduction is required to achieve a given flux reduction, although the overall source longevity increases. When rate-limited dissolution is important, the efficiency of remediation, in terms of both mass and flux reduction, is reduced. However, at many field sites the combined effects of field-scale heterogeneities and site aging will result in favorable relationships between mass reduction and flux reduction.

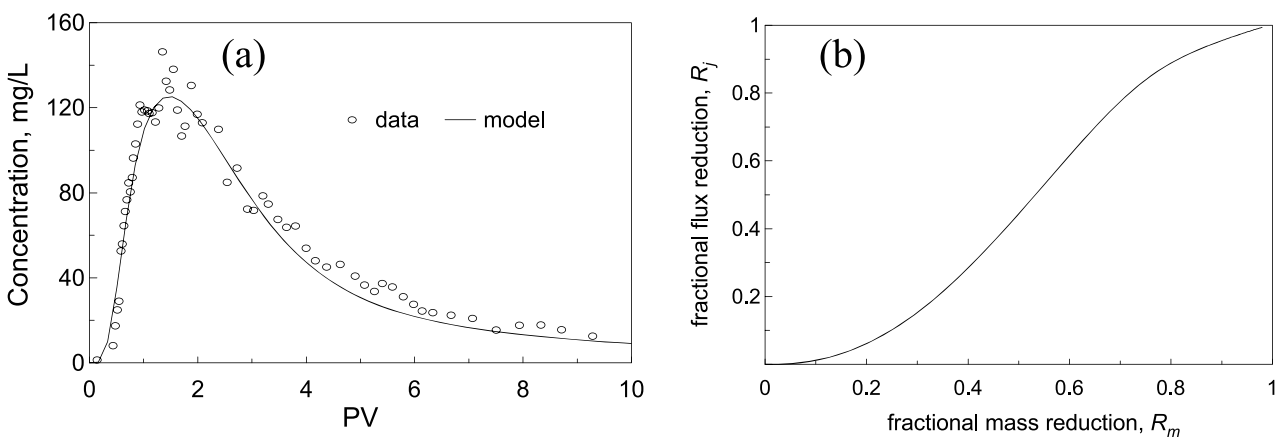

Figure 4.3-2. (a) Field dissolution data (from Jawitz et al., 1998) compared to equilibrium solution with a bimodal travel time distribution and homogeneous NAPL content. (b) R_J (R_M) based on model parameters (Jawitz et al., 2005).

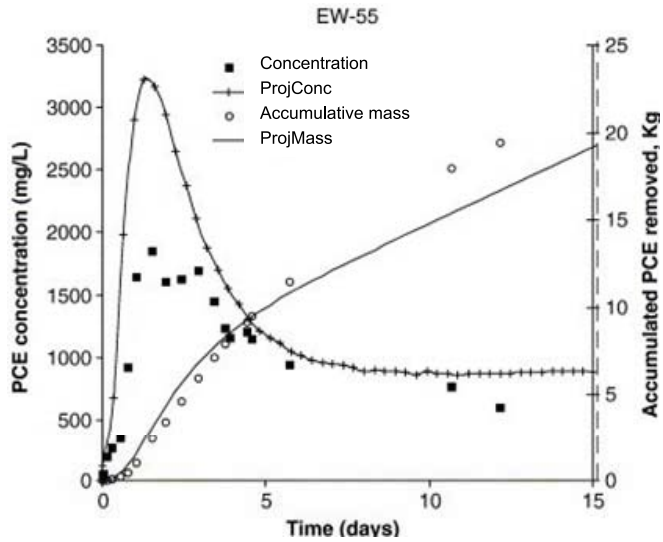

Figure 4.3-3. Measured and predicted remedial performance in a vertical circulation implementation of surfactant extraction (Wood et al., 2005).

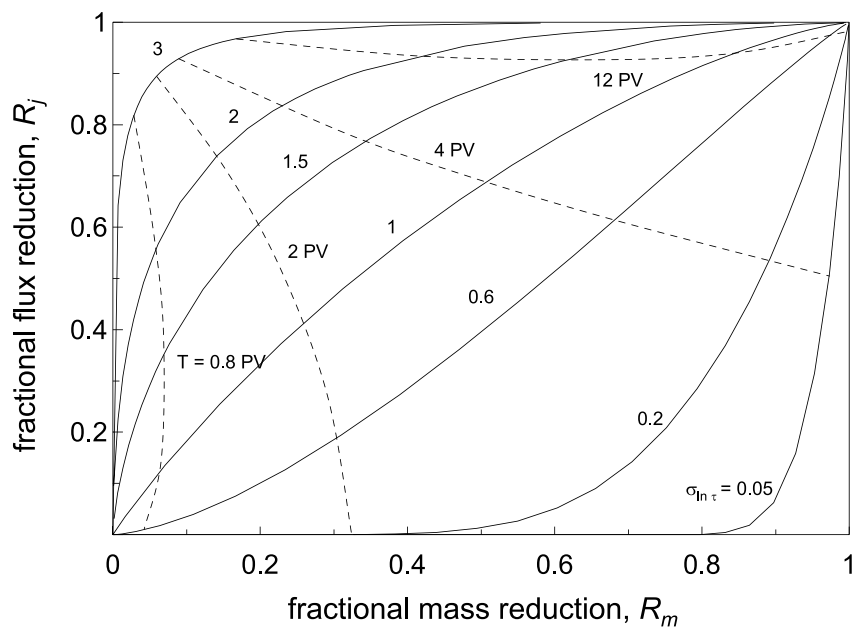

Figure 4.3-4. Solid lines are reduction in contaminant flux as a function of reduction in source zone mass for $\sigma \ln \tau = \{0.05, 0.2, 0.6, 1.0, 1.5, 2, 3\}$. Dashed lines are tie lines for flushing durations $t_f = \{0.8, 2, 4, 12\}$ pore volumes (PV). Note that N = 58 and $\mu_{\ln S} = 0.05$ (Jawitz et al., 2005).

4.3.2 Coupled Source Zone and Plume Models

Despite the sophistication of the three-dimensional and Lagrangian models, they are difficult to use at most field sites owing to financial constraints which limit the ability to obtain the necessary input data. Thus, analytical models of source behavior (Zhu and Sykes, 2004; Parker and Park, 2004; Falta et al., 2005a; Christ et al., 2006; Basu et al., 2008b) can be important decision making tools for risk assessment and remedial design. In these models, the source zone is represented by an effective homogeneous domain with the flux-averaged concentration at the source control plane ($C_J(t)$) described as a function of the mean

advective flow ($\overline{q}$, LT^{-1}) and the mean DNAPL mass ($M_S(t)$) in the domain. The source mass/source concentration relationships are coupled with simple mass balance equations to describe the time varying $C_J(t)$ as a function of the initial mass ($M_{S,0}$) and the initial flux averaged concentration ($C_{J,0}$).

The power function model (Zhu and Sykes, 2004; Falta et al., 2005a) is based on the assumption that the source mass/source discharge relationships shown in Figure 4.3-5 can be approximated by a simple power function relationship (Rao et al., 2001; Rao and Jawitz, 2003; Parker and Park, 2004; Zhu and Sykes, 2004; Falta et al., 2005a):

$$\frac{C_J(t)}{C_{J,0}} = \left[\frac{M_S(t)}{M_{S,0}}\right]^{\Gamma} \tag{4.3-6}$$

where, the exponent, Γ, determines the source discharge response to changing source mass, and generally represents site specific conditions, such as flow field heterogeneity, DNAPL distribution, and the correlation between the two. If Γ = 1, there is a 1:1 relationship (Figure 4.3-6). Values of Γ less than one produce *C vs M* curves that fall in the upper half of the graph (above the 1:1 line), while values of Γ greater than one produce *C vs M* curves that fall in the lower half of the graph. Field and laboratory data suggest that a Γ value of one is reasonable in some cases, but theoretical analyses indicate that a range of Γ values are possible, depending mainly on the correlation of the contamination distribution to the permeability field. DiFilipo and Brusseau (2008) analyzed data from a number of field studies and found that the majority of source remediations could be characterized using values of Γ between 0.5 and 2.0, though several studies had higher and lower values.

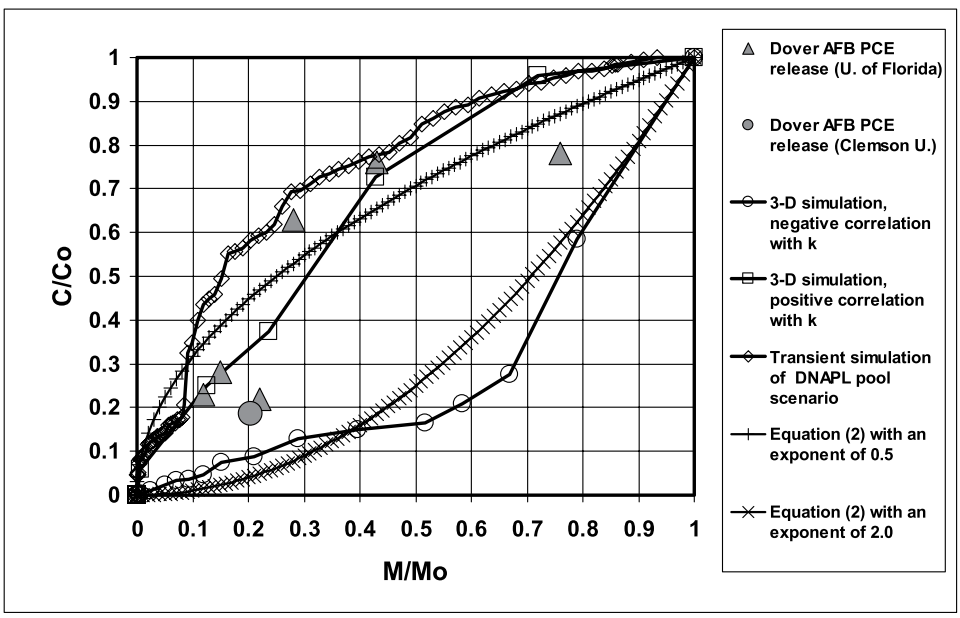

Figure 4.3-5. Source zone dissolved concentrations as a function of source zone DNAPL mass (Falta et al., 2005a).

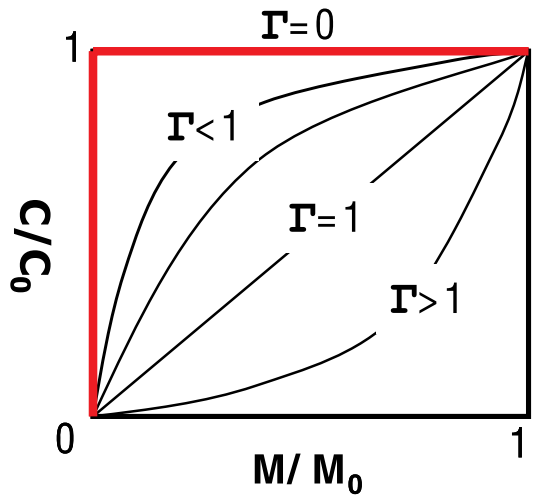

Figure 4.3-6. Power function representation of source mass/source discharge relationship (Equation 4.3-6).

4.3.2.1 Analytical expressions of source flux and mass

The power function relationship (Equation 4.3-6) can be used to describe the flux-averaged concentration at the source control plane as a function of the initial conditions using a simple mass balance technique. The contaminant discharge from a source zone is the product of the flowrate of water passing through the source zone, and the average concentration of contaminant in that water (Figure 4.3-7). Source discharge thus has units of mass per time, and is not to be confused with mass flux, which is a discharge divided by an area. If water flows through the source at a rate of $Q(t)$, and if the mass in the source zone is also subject to some form of chemical or biological first order decay, then a mass balance on the source gives:

$$\frac{dM_S}{dt} = Q(t)C_J(t) - \lambda_S M_S \tag{4.3-7}$$

where M_S is the mass remaining in the source zone with time, $C_J(t)$ is the time-dependent source dissolved concentration (flow averaged), and λ_S is the source decay rate by processes other than dissolution. Water flow through the source may be due to infiltration (above the water table) or groundwater flow (below the water table).

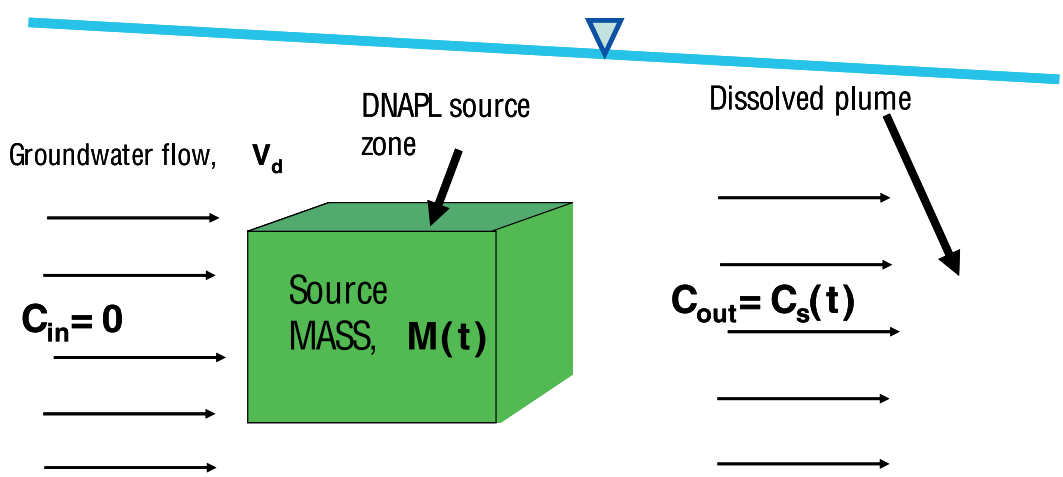

Figure 4.3-7. Conceptual model of source zone with time-dependent contaminant mass and discharge.

If the water flow rate through the source zone in Equation (4.3-7) is assumed to be constant, the power function (Equation 4.3-6) can be substituted to get:

$$\frac{dM_S}{dt} = \frac{QC_{J,0}}{M_{S,0}^{\Gamma}} M_S^{\Gamma} - \lambda_S M_S \tag{4.3-8}$$

This equation is nonlinear for Γ values other than zero and one, but it can be linearized using Bernoulli's transformation, and solved to get (Falta et al., 2005a):

$$M_S(t) = \left\{ \frac{-QC_{J,0}}{\lambda_S M_{S,0}^{\Gamma}} + \left(M_{S,0}^{1-\Gamma} + \frac{QC_{J,0}}{\lambda_S M_{S,0}^{\Gamma}} \right) e^{(\Gamma-1)\lambda_S t} \right\}^{\frac{1}{1-\Gamma}} \tag{4.3-9}$$

Using Equation (4.3-6), this leads to the time-dependent source discharge function:

$$C_{J,S}(t) = \frac{C_{J,0}}{M_{S,0}^{\Gamma}} \left\{ \frac{-QC_{J,0}}{\lambda_S M_{S,0}^{\Gamma}} + \left(M_{S,0}^{1-\Gamma} + \frac{QC_{J,0}}{\lambda_S M_{S,0}^{\Gamma}} \right) e^{(\Gamma-1)\lambda_S t} \right\}^{\frac{\Gamma}{1-\Gamma}} \tag{4.3-10}$$

Similar expressions can be derived for the case of $\lambda_S = 0$ (Parker and Park, 2004; Zhu and Sykes, 2004).

A very important special case of Equation (4.3-8) occurs when Γ = 1 and $\lambda_S = 0$. In that case, the differential equation is linear and may be integrated to get a simple exponential decay solution (Newell et al., 1996; Parker and Park, 2004; Zhu and Sykes, 2004):

$$M_S(t) = M_{S,0} e^{-\frac{QC_{J,0}}{M_{S,0}} t} \tag{4.3-11}$$

and

$$C_{J,S}(t) = C_{J,0} e^{-\frac{QC_{J,0}}{M_{S,0}} t} \tag{4.3-12}$$

Therefore, when Γ=1, both the source mass and the source discharge will decline exponentially with time. If λ_S=0, then the apparent source decay rate due to dissolution is $QC_{J,0}/M_{S,0}$, giving a source half-life of $.693M_o/(QC_o)$ (Newell and Adamson, 2005). This type of source behavior has been observed in the field at many chlorinated solvent sites (Newell and Adamson, 2005; McGuire et al., 2006; Newell et al., 2006), as well as at sites contaminated by petroleum hydrocarbons (Newell et al., 2002). The widely used EPA BIOCHLOR (Aziz et al., 2002) and BIOSCREEN (Newell et al., 1996) analytic models for natural attenuation include exponentially decaying source terms.

An important characteristic of source zones with Γ greater than or equal to one, is that theoretically the source is never completely depleted, and the source discharge is always greater than zero, even at large times. In simple terms, this happens because the rate of discharge from the source drops as fast or faster than the rate of mass depletion of the source. This type of response might be expected from a site where the DNAPL distribution was correlated with low permeability. In this case, most of the contaminant mass is trapped in low permeability zones and removing the small amount in high permeability zones will have a large effect on contaminant discharge. However, this type of source behavior also tends to lead to extensive tailing with time because the source is never completely depleted by dissolution.

When Γ<1, the source has a finite life, and the source discharge eventually is equal to zero. This type of behavior could occur when DNAPL is preferentially located in high permeability zones. In this case a given fractional reduction in source mass would produce a smaller fractional reduction in discharge. This type of source behavior leads to relatively rapid removal of the source by dissolution with little tailing.

Another useful special case occurs when Γ=0.5. This leads to a source concentration that declines as a linear function of time (Falta et al., 2005a; Newell and Adamson, 2005):

$$C_{J,S}(t) = C_{J,0} - \frac{QC_{J,0}^2}{2M_{S,0}} t \tag{4.3-13}$$

and the source completely disappears at a time of

$$t = \frac{2M_{S,0}}{QC_{J,0}} \tag{4.3-14}$$

The simplest model of source behavior is one in which Γ =0, which leads to a constant source discharge (concentration) until the source is fully depleted. This is also known as a "step function" model, and the source mass declines at a constant rate with respect to time.

The source model (Equations 4.3-9 and 4.3-10) represents source depletion by the natural process of dissolution and perhaps some other form of chemical or biological decay. This model can easily be modified to account for aggressive source remediation activities that remove a substantial fraction of the source mass over a short period of time (Falta et al., 2005a). If a source remediation effort (such as alcohol or surfactant flooding, chemical oxidation, thermal treatment, air sparging) begins at a time of t_1, and ends at a time of t_2, during which a fraction, X of the source mass is removed, the functions can be simply rescaled. Then the source mass and concentration following remediation are given by:

$$M_S(t) = \left\{ \frac{-QC_{J,2}}{\lambda_S M_{S,2}^{\Gamma}} + \left(M_{S,2}^{1-\Gamma} + \frac{QC_{J,2}}{\lambda_S M_{S,2}^{\Gamma}} \right) e^{(\Gamma-1)\lambda_S (t-t_2)} \right\}^{\frac{1}{1-\Gamma}} \tag{4.3-15}$$

$$C_J(t) = C_{J,2} \left(\frac{M_S(t)}{M_{S,2}} \right)^{\Gamma} \tag{4.3-16}$$

$$M_{S,2} = (1-X) M_{S,1} \tag{4.3-17}$$

$$C_{J,2} = C_{J,0} \left(\frac{(1-X) M_{S,1}}{M_{S,0}} \right)^{\Gamma} \tag{4.3-18}$$

where $M_{S,1}$ is the source mass at t_1, and $M_{S,2}$ is the source mass at t_2 . The change in source discharge following remediation varies as the fraction of mass remaining (1-X) raised to the power Γ . Therefore if Γ =1, a linear reduction of source discharge is expected; if Γ =2, the discharge will drop as the square of the mass fraction remaining, while if Γ =0.5, the discharge will drop as the square root of the mass fraction remaining. Examples of this type of source behavior with and without remediation are shown in Figures 4.3-8 and 4.3-9, for a case where the initial source mass is 1620 kg, with an initial source concentration of 100 mg/l, and a water flow rate of 600 m^3/yr.

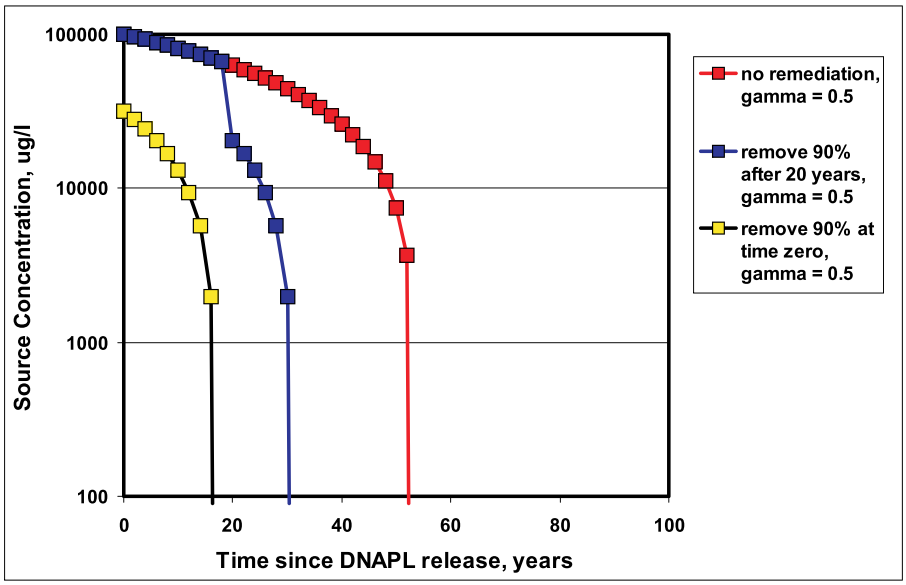

Figure 4.3-8. Source zone dissolved concentration with and without source remediation for Γ= 0.5 (Falta et al., 2005a).

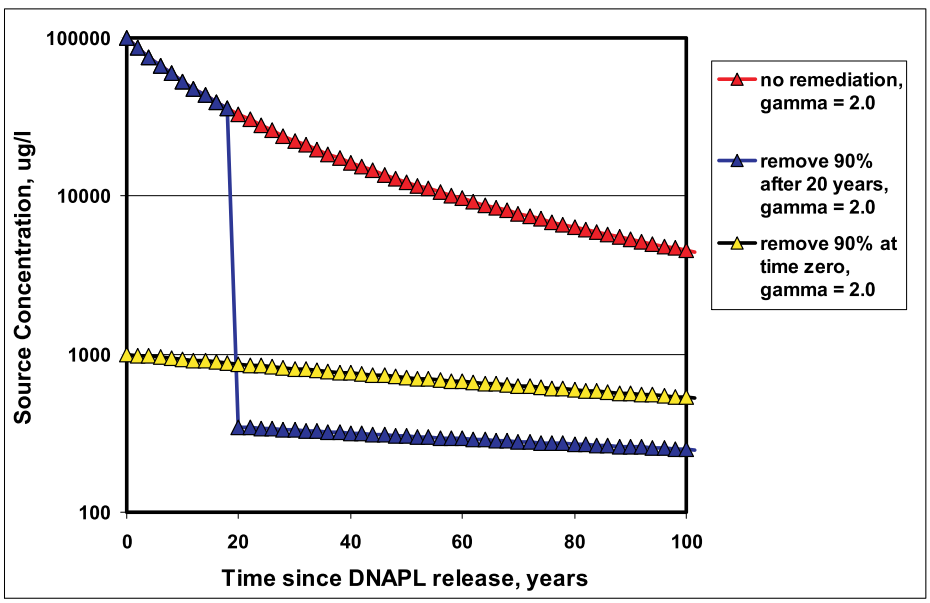

Figure 4.3-9. Source zone dissolved concentrations with and without source remediation for Γ = 2.0 (Falta et al., 2005a).

4.3.2.2 Analytical approaches including plume remediation and natural attenuation

Experience with natural attenuation as a remedy for plume management has shown that mathematical models can play an important role in the selection of remedial alternatives (Wiedemeier et al., 1999; NRC, 2000; Alvarez and Illman, 2006). In many cases, screening level simulations performed with analytical models such as BIOCHLOR (Aziz et al., 2000) or BIOSCREEN (Newell et al., 1996) are effective for demonstrating the applicability of natural attenuation. A recent study of 45 CVOC sites found that mathematical models were used at 60 percent of the sites, and that BIOCHLOR was the most frequently used model (McGuire et al., 2004). BIOCHLOR is based on a modified version of the Domenico (1987) analytical approximation for advective transport with three-dimensional dispersion. BIOCHLOR uses an

analytical transformation developed by Sun et al (1999a, b) to model the chain decay of chlorinated solvents such as PCE (PCE→TCE→DCE→VC→ethene) or TCA (TCA→DCA→CA→ethane) assuming first order reactions. The source term can be a constant concentration, or it can decay exponentially with time. BIOCHLOR, however, does not simulate source or plume remediation. These types of analytical models are also commonly used to estimate exposures for risk assessment.

An analytical approach that accounts for source remediation using the simplified source functions described above was described in Falta et al. (2005a). This model simulates simple one-dimensional advective transport of a single species with first order decay. The model was used to make several generalizations about the relationship between source remediation and plume response. One of the most significant observations was that the maximum extent of a plume is a logarithmic function of the amount of source remediation. Considering the special case where Γ is equal to one, and assuming that source remediation takes place immediately following a DNAPL release, the maximum length of a plume was shown to be

$$\frac{x_R}{x_{NR}} = 1 - \frac{\ln(1-X)}{\ln\left(\frac{C_m}{C_0}\right)} \tag{4.3-19}$$

where x_R is the maximum plume length with source remediation, x_{NR} is the maximum plume length without source remediation, X is the fraction of DNAPL source removed, C_0 is the initial source concentration, and C_m is the regulatory limit for the chemical (the concentration that defines the edge of the plume). As shown in Table 4.3-1, when the plume is defined by a very low concentration relative to the source concentration, it becomes very difficult to "shrink" a plume by source remediation alone. On the other hand, for Γ =1, source remediation efforts will reduce the future mass, concentrations, and cancer risk in a plume by an amount equal to the fraction of mass removed.

Table 4.3-1. Fraction of DNAPL source removal (X) required to reduce maximum plume length by a specified amount using Equation (4.3-19) (from Falta et al., 2005a).

	Relative maximum plume length, x_R / x_{NR}					
		0.8	*0.5*	*0.3*	*0.2*	*0.1*
$\frac{C_m}{C_0}$	10^{-1}	***.37***	***.68***	***.80***	***.84***	***.87***
	10^{-2}	***.60***	***.900***	***.960***	***.975***	***.984***
	10^{-3}	***.75***	***.968***	***.992***	***.996***	***.998***
	10^{-4}	***.84***	***.990***	***.998***	***.9994***	***.9997***
	10^{-5}	***.900***	***.997***	***.9997***	***.9999***	***.99997***

A more realistic plume model coupled to source remediation was developed in Falta et al. (2005b). This semi-analytical model uses the same source function, but the plume model simulates natural attenuation by advection with three-dimensional dispersion, and it includes first-order parent-daughter chain decay using the method of Sun et al. (1999a, b). This model was used to study the effects of immediate and delayed source remediation on the plume response. One major conclusion from this study was that source remediation was much more effective if it was conducted soon after a DNAPL release. If the source remediation is delayed, much of the contaminant mass is already in the plume, and source remediation will have little or no effect on the leading edge of the plume, and some type of plume remediation is probably required.

A major limitation of these models (Biochlor, Falta et al. (2005b)) is that they cannot simulate enhanced plume remediation, where the biogeochemical conditions are manipulated in order to increase rates of

contaminant destruction. Destruction of CVOCs in dissolved plumes can occur under natural conditions by biodegradation processes including reductive dechlorination, aerobic oxidation, anaerobic oxidation, and aerobic co-metabolism (Weidemeier et al, 1999; NRC 2000; Alvarez and Illman, 2006). It is now fairly common to engineer in-situ biodegradation systems for enhancing one or more of these processes in order to allow the plume to attenuate in a shorter distance, or to reduce plume concentrations in locations that are detached from the source. These enhancements usually involve addition of an electron donor (hydrogen, lactate, molasses or a hydrogen releasing compound) for enhancing anaerobic processes, or an electron acceptor (oxygen, air, H_2O_2 , or an oxygen releasing compound) for enhancing aerobic processes (Chapelle et al., 2003; Alvarez and Illman, 2006). In other cases, reactive barriers or basic hydraulic control through pump-and-treat are used to manage the dissolved plume. In order to simulate these processes, models need to be able to describe spatially and temporally varying reaction rates. Of the models described so far, only the BIOCHLOR model allows for two spatial zones to be defined in which the solute decay rates are different, but this is only valid if the solute concentrations in the upstream zone are at steady-state, which implies a constant source concentration in time.

Because of the above limitation, a new analytical plume model that can simulate these types of variable plume reactions, along with source remediation was developed. This model is called REMChlor for Remediation Evaluation Model for Chlorinated solvents (Falta, 2008). The key difference in REMChlor and other plume models is that the chemical reaction parameters (rates, yield coefficients) can now be arbitrary functions of both time and distance from the source. A graphical user's interface for the model was developed by the Center for Subsurface Modeling Support (CSMoS). The REMChlor model is available at http://www.epa.gov/ada/csmos/models/remchlor.html. The REMChlor analytical approach assumes a constant groundwater pore velocity of v in the x-direction, with longitudinal, transverse, and vertical dispersion. The solute can be retarded by adsorption, but the different solutes involved in coupled reactions must have the same retardation factor. These assumptions are similar to those used in previous natural attenuation plume models such as BIOCHLOR (Aziz et al., 2000; 2002), BIOSCREEN (Newell et al., 1996), LNAST (Huntley and Beckett, 2002), and the model by Falta et al. (2005b).

4.3.2.3 REMChlor model

The governing equation for the dissolved concentration of each contaminant species in the plume, C, is:

$$R\frac{\partial C}{\partial t} = -v\frac{\partial C}{\partial x} + \alpha_x v\frac{\partial^2 C}{\partial x^2} + \alpha_y v\frac{\partial^2 C}{\partial y^2} + \alpha_z v\frac{\partial^2 C}{\partial z^2} + rxn(x,t) \qquad (4.3\text{-}20)$$

Where ν is pore velocity; α_x, α_y and α_z are the longitudinal, transverse, and vertical dispersivities, respectively; R is the retardation coefficient, and $rxn(x,t)$ represents the rate of generation (+) or destruction (−) of the species due to chemical or biological reactions that are spatially and temporally variable. This plume model is coupled with the source zone mass balance given by Equation (4.3-7), using the power function relationship for the flux-averaged concentration and mass remaining in the source (C_J vs M_S) relationship [Equation (4.3-6)]. A specified flux boundary condition at x=0 ensures that the rate of discharge from the source zone is exactly equal to the rate at which contaminants enter the plume (see van Genuchten and Alves (1982)). The mass flux entering the plume is specified as:

$$\frac{Q(t)C_J(t)}{A} = \left[\eta v C(t) - \eta\alpha_x v\frac{\partial C(t)}{\partial x}\right]_{x=0} \qquad (4.3\text{-}21)$$

where $\boldsymbol{A}$ is the area over which the contaminant flux enters the groundwater flow system, $Q(t)$ is rate of groundwater flow, and η is the porosity. Outside of this area, the mass flux is zero. For sources that are located below the water table, $\boldsymbol{A}$ would be the cross-sectional area of the source zone perpendicular to the groundwater flow. For sources located above the water table, $\boldsymbol{A}$ would be the cross-sectional area at the top of the water table perpendicular to flow that was required to accommodate the infiltration rate from the source. Falta et al. (2005b) solved Equations (4.3-20) and (4.3-21) analytically for the case of first order decay reactions with constant and uniform decay rates, using a Laplace transform method, combined

with Domenico's (1987) approximation for transverse and vertical dispersion. Analytical solution of Equation (4.3-20) with variable plume reaction rates by this method would be much more difficult. Instead, a different approach is taken where the solute advection and reactions are decoupled from the longitudinal dispersion using a simple streamtube technique. Scale-dependent longitudinal dispersion is accounted for by considering a collection of streamtubes with a normally distributed pore velocity. Transverse and vertical dispersion are then simulated using Domenico's (1987) approximation.

The reactive plume model is based on a simple one-dimensional streamtube that is characterized by a constant pore velocity and solute retardation factor. Since there is only advection taking place in the streamtube, the flux boundary condition at the edge of the source zone simplifies to:

$$C(t)\big|_{x=0} = \frac{Q(t)C_J(t)}{\eta v A} \tag{4.3-22}$$

If the source is located below the water table, and $Q=\phi v A$, then the flux boundary condition is just the time-dependent source concentration,

$$C(t)\big|_{x=0} = C_J(t) \tag{4.3-23}$$

where $C_J(t)$ could be calculated, for example, by Equations (4.3-10) and (4.3-16).

One-dimensional advective transport of a solute can be represented graphically on a distance-time plot (Figure 4.3-10). Here, the time axis corresponds to the time since the contaminant was first released to the groundwater system, while the distance axis is the distance downstream from the source.

The advective front moves at a constant velocity of v/R, so that at any location, x, the front passes by at a time of $t=Rx/v$. At any time, the front is located at $x=vt/R$, and the solute concentration is always zero below this line (ahead of the front). In the absence of any plume degradation process, the concentration at any location behind the advective front can be determined from the time of solute release from the source, $t_{release}$. For a distance from the source, x, the travel time is $t_{travel}=Rx/v$. Therefore, if the total time is t, the parcel of water found at that location (x,t) was released from the source at a time of:

$$t_{release} = t - Rx/v \tag{4.3-24}$$

and the concentration at that (x,t) point would be:

$$C(x,t) = C(t_{release})\big|_{x=0} \tag{4.3-25}$$

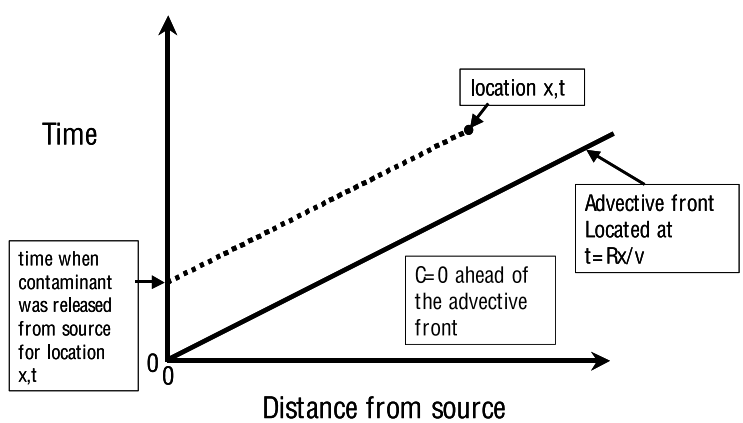

Figure 4.3-10. Distance-time plot for advective transport with a single set of reaction rates (Falta, 2008).

Plume reactions can easily be included in this advective streamtube model. As a parcel of solute is translated downstream, it is not subject to any mixing processes, so it is conceptually equivalent to a batch reaction that starts at time $t^*=0$ with an intitial condition of $C(t_{release})|_{x=0}$ and reacts for a period of time equal to the travel time to position x, $t'=Rx/v$. As an example, if the solute reaction was first order decay in the aqueous phase with a decay rate coefficient of k, then the equivalent batch reaction is:

$$R\frac{dC}{dt} = -k_d C \quad with \quad C\big|_{t'=0} = C\left(t_{release}\right)\big|_{x=0} \tag{4.3-26}$$

Then at location (x,t) behind the front, the solute concentration would be:

$$C(x,t) = C(t - Rx/v)\big|_{x=0} \exp\left(\frac{-k_d x}{v}\right) \tag{4.3-27}$$

This result is exactly the same as the Laplace transform solution to Equations (4.3-20) and (4.3-21) with zero dispersion (Falta et al., 2005a). More complicated coupled reactions can be considered using this same method, but a fundamental limitation is that all of the reacting solutes must move at the same velocity in the groundwater, so they must be assumed to have a single retardation factor, R.

The analysis can be extended to the case of time and distance dependent reaction rates by dividing the time-distance domain into distinct zones (Figure 4.3-11). Here, nine zones have been chosen to approximately represent conditions downgradient from a contaminant source over the life of a plume. The first time zone after the spill, $t < t_1$, could represent a period following the contaminant release where no manipulation of the plume has yet been attempted, a period of natural attenuation. The second time zone after the spill, $t_1 < t < t_2$ could represent a temporary period of active plume remediation (enhanced attenuation). The final time zone, $t > t_2$, could be used to represent long term conditions in the plume after manipulation of the plume ended (another period of natural attenuation).

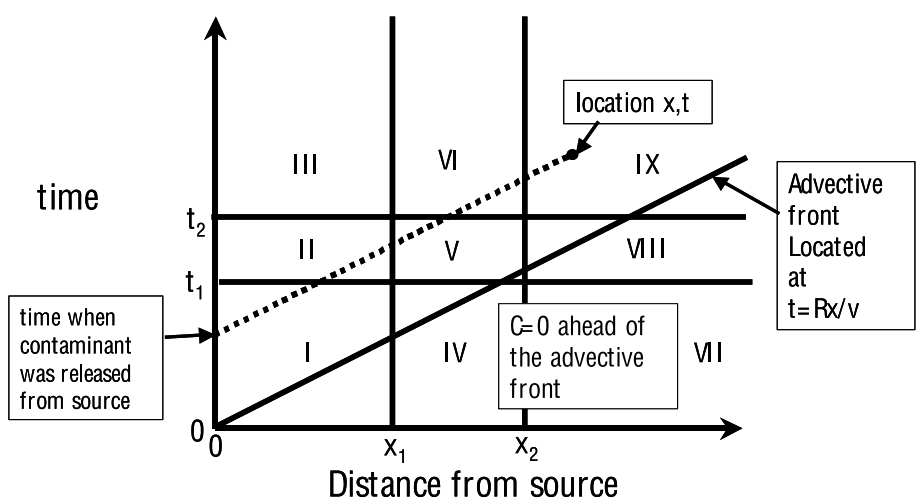

Figure 4.3-11. Distance-time plot for advective transport with multiple sets of reaction rates (Falta, 2008).

Distance from the source is similarly divided into zones so that near the source, for $x < x_1$, one set of natural or engineered biogeochemical conditions predominate, while downstream, at $x_1 < x < x_2$, another set of conditions are present. Beyond x_2, conditions might again revert back to natural background conditions.

An example of how these different plume reaction zones might be used is shown in Figure 4.3-12. Here it is assumed that there was a release of tetrachloroethylene (PCE) in 1975, but plume remediation did not begin until 2005, with a planned duration of 20 years. In the absence of any significant electron donor supply, or other enhancements, natural conditions would prevail from 1975 to 2005. The plume

remediation scheme could consist of the addition of electron donor in the first 400 m of the plume to increase the rate of reductive dechlorination of PCE and its daughter product, trichloroethylene (TCE). Because the daughter products cis-1,2-dicloroethylene (DCE) and vinyl chloride (VC) do not degrade as readily by reductive dechlorination, but they can degrade aerobically, a different reaction zone could be created from 400 to 700 m, where aerobic degradation was stimulated (Chapelle et al., 2003; Alvarez and Illman, 2006). Downgradient of this zone, conditions might revert back to their natural state.

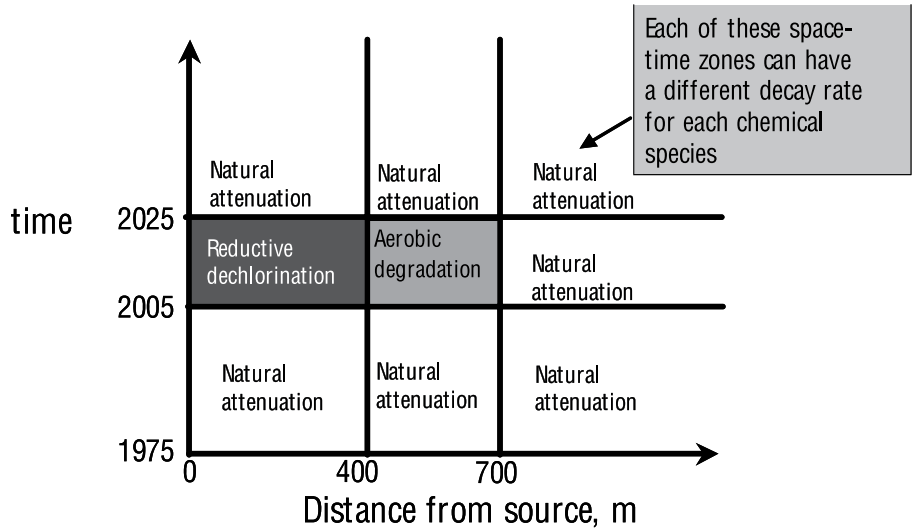

Figure 4.3-12. Hypothetical design of an enhanced plume remediation scheme with an enhanced reductive dechlorination zone for destruction of PCE and TCE and an enhanced aerobic degradation zone for destruction of DCE and VC. All other zones revert to natural background conditions (Falta, 2008).

The analytical solution for multiple reaction zones is developed using the residence time in each zone to develop the batch reaction solution for that zone. The initial conditions for the batch reaction are the final conditions from the previously encountered reaction zone. The residence times in each reaction zone are calculated using straightforward logic. For the example shown in Figure 4.3-11, the solutes that are present at location (x, t) left the source at a time, $t_{release}$ that was before t_1, so they initially encounter reaction zone (I). The residence time in zone (I) is then $t_{(\mathrm{I})} = t_1 - t_{release}$. The solutes next enter zone (II), where they remain until they cross x_1, at a time of $t_{release} + Rx_1 / v$. Therefore, the residence time in zone (II) is $t_{(\mathrm{II})} = t_{release} + Rx_1 / v - t_1$. The solutes next enter zone (V), where they remain until t_2, so the residence time in zone (V) is $t_{(\mathrm{V})} = t_2 - t_{release} - Rx_1 / v$. In this way, the residence times for each reaction zone are tabulated.

In general, solutes can pass through any of the nine reaction zones, so a total of nine reaction zone residence times are computed. For any given value of (x, t), the advective path leading to that location will cross at most five zones, so several of the zone residence times are zero. The analytical solution is constructed by sequentially performing the batch reactions in each zone that is encountered, starting with a concentration of $C(t_{release})|_{x=0}$. With the zone numbering scheme used in Figure 4.3-11, the numerical value of the reaction zone always increases with increasing travel distance.

Going back to the example of a single solute undergoing first order decay in the aqueous phase, a set of nine reaction rates are defined $(k_{(\mathrm{I})} - k_{(\mathrm{IX})})$. The solute concentration at (x, t) is then:

$$C(x,t) = C(t - Rx/v)\big|_{x=0} \exp\left\{-\sum_{n=I}^{IX} \frac{t_{(n)} k_{(n)}}{R}\right\} \tag{4.3-28}$$

A problem of significant practical interest in groundwater remediation involves simultaneous first order parent-daughter decay/production reactions. Considering a four component system, the relevant batch reaction equations for species A,B,C,D in zones (n) are:

$$R\frac{dC_{A(n)}}{dt} = -k_{A(n)}C_{A(n)} \qquad I.C. \rightarrow C_{A(n)}(0) = C_{A(n-1)} \tag{4.3-29}$$

$$R\frac{dC_{B(n)}}{dt} = y_{BA(n)}k_{A(n)}C_{A(n)} - k_{B(n)}C_{B(n)} \qquad I.C. \rightarrow C_{B(n)}(0) = C_{B(n-1)} \tag{4.3-30}$$

$$R\frac{dC_{C(n)}}{dt} = y_{CB(n)}k_{B(n)}C_{B(n)} - k_{C(n)}C_{C(n)} \qquad I.C. \rightarrow C_{C(n)}(0) = C_{C(n-1)} \tag{4.3-31}$$

$$R\frac{dC_{D(n)}}{dt} = y_{DC(n)}k_{C(n)}C_{C(n)} - k_{D(n)}C_{D(n)} \qquad I.C. \rightarrow C_{D(n)}(0) = C_{D(n-1)} \tag{4.3-32}$$

where $y_{ij(n)}$ are the yield coefficients for each parent-daughter reaction. These can also depend on distance and time if the nature of a reaction changes so that it no longer produces the same proportion of daughter product from decay of the parent (for example during aerobic degradation of DCE, little VC is produced). Equations (4.3-29 and 4.3-30) are written for reaction zone (n), and the reactions proceed for a period equal to the residence time, $t_{(n)}$, with initial conditions (*I.C.*) that are the concentrations from end of the previous reaction zone. The starting conditions for the first reaction zone are $C_{i(0)} = C_i(t - Rx / v)|_{x=0}$.

Following methods used in chemical reactor design (see, for example, Chen (1983)), the coupled reaction equations can be solved by Laplace transform methods to yield:

$$C_{A(n)} = C_{A(n-1)}f_1\left(\lambda_{A(n)}, t_{(n)}\right) \tag{4.3-33}$$

$$C_{B(n)} = C_{A(n-1)}f_2\left(\lambda_{A(n)}, \lambda_{B(n)}, y_{BA(n)}, t_{(n)}\right) + C_{B(n-1)}f_1\left(\lambda_{B(n)}, t_{(n)}\right) \tag{4.3-34}$$

$$\begin{aligned} C_{C(n)} = {} & C_{A(n-1)}f_3\left(\lambda_{A(n)}, \lambda_{B(n)}, \lambda_{C(n)}, y_{BA(n)}, y_{CB(n)}, t_{(n)}\right) \\ & + C_{B(n-1)}f_2\left(\lambda_{B(n)}, \lambda_{C(n)}, y_{BC(n)}, t_{(n)}\right) + C_{C(n-1)}f_1\left(\lambda_{C(n)}, t_{(n)}\right) \end{aligned} \tag{4.3-35}$$

$$\begin{aligned} C_{D(n)} = {} & C_{A(n-1)}f_4\left(\lambda_{A(n)}, \lambda_{B(n)}, \lambda_{C(n)}, \lambda_{D(n)}, y_{BA(n)}, y_{CB(n)}, y_{DC(n)}, t_{(n)}\right) \\ & + C_{B(n-1)}f_3\left(\lambda_{B(n)}, \lambda_{C(n)}, \lambda_{D(n)}, y_{CB(n)}, y_{DC(n)}, t_{(n)}\right) \\ & + C_{C(n-1)}f_2\left(\lambda_{C(n)}, \lambda_{D(n)}, y_{DC(n)}, t_{(n)}\right) + C_{D(n-1)}f_1\left(\lambda_{D(n)}, t_n\right) \end{aligned} \tag{4.3-36}$$

where the $\lambda_{i(n)} = k_{i(n)}/R$, and

$$f_1\left(\lambda_1, t\right) = e^{-\lambda_1 t} \tag{4.3-37}$$

$$f_2\left(\lambda_1, \lambda_2, y_{21}, t\right) = y_{21}\lambda_1\left(\frac{e^{-\lambda_1 t} - e^{-\lambda_2 t}}{\lambda_2 - \lambda_1}\right) \tag{4.3-38}$$

$$f_3\left(\lambda_1,\lambda_2,\lambda_3,y_{21},y_{32},t\right)=y_{32}\lambda_2 y_{21}\lambda_1\left(-\frac{\left(\lambda_3-\lambda_2\right)e^{-\lambda_1 t}+\left(\lambda_1-\lambda_3\right)e^{-\lambda_2 t}+\left(\lambda_2-\lambda_1\right)e^{-\lambda_3 t}}{\left(\lambda_2-\lambda_1\right)\left(\lambda_3-\lambda_2\right)\left(\lambda_1-\lambda_3\right)}\right) \tag{4.3-39}$$

$$f_4\left(\lambda_1,\lambda_2,\lambda_3,\lambda_4,y_{21},y_{32},y_{43},t\right)=\frac{y_{43}\lambda_3 y_{32}\lambda_2 y_{21}\lambda_1}{\left(\lambda_2-\lambda_1\right)\left(\lambda_4-\lambda_3\right)}\left\{\frac{e^{-\lambda_1 t}-e^{-\lambda_3 t}}{\left(\lambda_3-\lambda_1\right)}-\frac{e^{-\lambda_1 t}-e^{-\lambda_4 t}}{\left(\lambda_4-\lambda_1\right)}-\frac{e^{-\lambda_2 t}-e^{-\lambda_3 t}}{\left(\lambda_3-\lambda_2\right)}+\frac{e^{-\lambda_2 t}-e^{-\lambda_4 t}}{\left(\lambda_4-\lambda_2\right)}\right\} \tag{4.3-40}$$

These batch solutions are widely known as the Bateman equations (Bateman, 1910), originally developed to describe the decay and production of radioactive species. Here, the equations have been modified to account for variable daughter yield coefficients. These batch solutions are also equivalent to those developed by Sun et al. (1999) in their analytical transformations.

The REMChlor streamtube plume model using Equations (4.3-33)-(4.3-40) is compared with the two-zone BIOCHLOR model in Figure 4.3-13. This case assumes a constant source concentration of PCE of 1 mg/l, with a pore velocity of 100 m/yr, a retardation factor of 2, and no dispersion. Referring back to Figure 4.3-11, this test case only uses zones (I) and (IV), with steady-state conditions in zone (I). This is a special case for the new solution, which can handle fully transient conditions using all nine zones in space and time.

Over the first 500 m, PCE and TCE are allowed to degrade with first order rate constants of 0.693/yr (an aqueous half life of one year), but DCE and VC do not degrade at all in this zone. Beyond 500 m, the DCE and VC degrade with a rate constant of 0.693/yr, but the PCE and TCE do not degrade at all. The simulation time of 20 years is sufficiently long for steady-state conditions to be present in the first zone, a requirement of the BIOCHLOR model. The two solutions produce an identical result. In the first zone, PCE degrades, producing TCE, which degrades into DCE. The process stalls at DCE in this zone, and the concentration of VC is zero. Beyond 500 m, the concentrations of PCE and TCE are constant, while the DCE degrades to form VC, which also degrades.

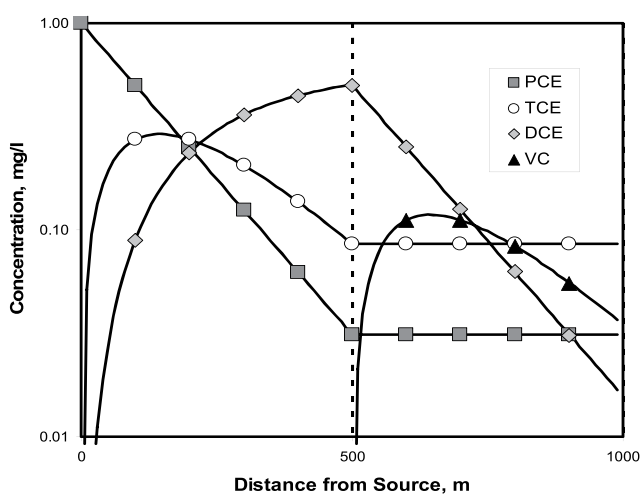

Figure 4.3-13. Comparison of the REMChlor reactive streamtube solution with BIOCHLOR for a two-zone case with steady state concentrations in the upstream zone (t = 20 years). The solid lines are computed using the REMChlor solution while the symbols are calculated using BIOCHLOR (Falta, 2008).

4.3.2.4 Cancer risk assessment

Many of the regulated groundwater contaminants and their degradation products are considered to be known or probable carcinogens by the US EPA. Cancer risk from exposure to carcinogens is quantified using the chronic daily intake (CDI) of the carcinogen (mg/kg-day) and a cancer risk slope factor (SlF) that has units of risk per mg/kg-day. The CDI is a dose rate averaged over a human lifespan, regardless of the exposure period (US EPA, 1989). The maximum exposure period, t_{ex} is usually limited to 30 years. The risk is calculated as:

$$Risk = 1 - \exp\left(-CDI \times SlF\right) \tag{4.3-41}$$

which for small risks is equivalent to (US EPA, 1989)

$$Risk = CDI \times SlF \tag{4.3-42}$$

The total carcinogenic risk, $Risk_T$, from exposure to multiple carcinogens (for example PCE, TCE, and VC) is calculated as the sum of the individual risks (US EPA, 1989)

$$Risk_T = \sum Risk_i \tag{4.3-43}$$

A major exposure route for contaminated groundwater is water from wells in the dissolved plume area. The contaminants contained in the water may be ingested directly, in drinking water, and if they are volatile, they may be inhaled as the contaminant partitions from the water into the air in the house (McKone, 1987). The cancer risk from inhalation is often as large or larger than the risk from ingestion (McKone, 1987; Williams et al., 2004).

The CDI for both ingestion (CDI_G) and inhalation (CDI_H) is computed using the well water concentration in mg/L averaged over the maximum exposure period,

$$\overline{C}_{well}(t) = \frac{1}{t_{ex}} \int_{\max(0,t-t_{ex})}^{t} C_{well}(t^*)dt^* \tag{4.3-44}$$

The lower limit in the integral restricts the exposure period to a maximum of t_{ex}. The upper limit, t, is the time since the contaminant release occurred. Once the average tap water concentration is known, the ingestion and inhalation cancer risks can be calculated using standard methods (see, for example, Maxwell et al. (1998); McKone (1987); Williams et al. (2004).

The cancer risk from water ingestion assumes a daily water intake of W_D (L/d), and a body mass of M_b (kg). Then using the standard life expectancy, t_{life}, the CDI_G is

$$CDI_G = \overline{C}_{well}\left(\frac{W_D \times t_{ex}}{M_b \times t_{life}}\right) \tag{4.3-45}$$

Typical values for W_D, M_b, and t_{life} are 2 L/d, 70 kg, and 70 years, respectively. The ingestion risk is then:

$$Risk_G = 1 - \exp\left(-CDI_G \times SlF_G\right) \tag{4.3-46}$$

where SlF_G is the oral slope factor for the carcinogen.

Calculation of the inhalation exposure requires estimation of indoor air concentrations of the carcinogen that result from water use in the house. The standard approach is to separately consider the shower stall, the bathroom, and the remainder of the house (McKone, 1987). An empirical water to gas transfer efficiency (TE) is used to relate the contaminant mass flowrate in water passing through parts of the house (shower,

bathroom, house) to the rate of mass loading in the indoor air. Based on extensive data sets collected for radon gas exposure, the *TE* for a volatile chemical is computed from the radon data with a correction for the different Henry's constant and aqueous and gaseous diffusion rates. Of these parameters, the *TE* is most sensitive to the aqueous diffusion rate, because that tends to limit the rate of mass transfer into indoor air (McKone, 1987). Typical values for *TE* are in the range of 0.3 to 0.9, depending mainly on the nature of the water use (for example a shower versus a dishwasher).

The CDI_H is computed separately for the three main compartments (shower, bathroom, house) using the average indoor air concentration of the carcinogen, $\overline{C}_a$ in units of mg/m^3 . For compartment k_c , this concentration is calculated from the average water concentraton using the tap water use rate W_{k_c} (L/hr), the TE_{k_c}, and the air exchange rate, VR_{k_c} (m^3/hr):

$$\overline{C}_{a,k_c} = \overline{C}_{well}\left(\frac{W_{k_c} \times TE_{k_c}}{VR_{k_c}}\right) \tag{4.3-47}$$

The CDI_H for each compartment (CDI_{k_c}) depends on the daily exposure time in the compartment, ET_{k_c} (hr/d), and the inhalation rate, HR (m^3/hr):

$$CDI_{H,k_c} = \overline{C}_{a,k_c}\left(\frac{ET_{k_c} \times HR \times t_{ex}}{M_b \times t_{life}}\right) \tag{4.3-48}$$

The risk from inhalation sums over the compartments

$$Risk_H = 1 - \exp\left[-\sum_{k_c} CDI_{H,k} \times SlF_H\right] \tag{4.3-49}$$

where SlF_H is the inhalation slope factor.

The lifetime excess cancer risk slope factors vary widely among different chemicals, and they are often revised or withdrawn. Conflicting values of *SlF* can be found in different sources in many instances. Table 4.3-2 lists current (as of February, 2006) recommended inhalation and oral slope factors for PCE, TCE, and VC from the California Office of Environmental Health Hazard Assessment (OEHHA, 2006).

Table 4.3-2. California cancer risk slope factors for PCE and its degradation products (OEHHA, 2006).

Chemical	Inhalation Slope Factor (mg/kg-day)$^{-1}$	Oral Slope Factor (mg/kg-day)$^{-1}$
Tetrachloroethylene (PCE)	0.021	0.540
Trichloroethylene (TCE)	0.007	0.013
Cis-1,2-Dichloroethylene (DCE)	-not a carcinogen	-not a carcinogen
Vinyl chloride (VC)	.270	0.270

4.3.2.5 Analytical/numerical approach including plume remediation and natural attenuation

An alternative approach to the analytical REMChlor Model described above is to couple the source mass/ source discharge relationship (Equation 4.3-6) to a numerical code that simulates advective/dispersive/ reactive dissolved solute transport (Equation 4.3-20). In this study, Equation 4.3-20 is utilized within the framework of the Department of Defense Groundwater Modeling System (GMS) version 5.1. GMS is employed to run the MODFLOW2000 and Reactive Transport in 3-Dimensions (RT3D) computer codes which employ the fate and transport model.

GMS uses the MODFLOW2000 computer code to model the three-dimensional steady state and transient movement of groundwater (USGS, 2000). This is accomplished using a model based on the following partial differential equation (from USGS, 2000):

$$\frac{\partial}{\partial x}\left(K_{xx}\frac{\partial h}{\partial x}\right)+\frac{\partial}{\partial y}\left(K_{yy}\frac{\partial h}{\partial y}\right)+\frac{\partial}{\partial z}\left(K_{zz}\frac{\partial h}{\partial z}\right)-q_V = SS\frac{\partial h}{\partial t} \qquad (4.3\text{-}50)$$

Where K_{xx} , K_{yy} , and K_{zz} are hydraulic conductivities along the x, y, and z-axis respectively [LT^{-1}] , h = Potentiometric head [L] , q_v is volumetric flux per unit volume [T^{-1}] , SS is specific storage of the porous material [L^{-1}] , and t is time [T] .

In this study, steady-state flow was assumed, so the potentiometric head did not change with time. In order to apply this model to determine the steady-state head field, constant head boundaries were specified. Once the boundary conditions were set, the model was run. The model uses the finite-difference method to solve the steady-state version of Equation 4.3-50 and determine the head at each cell (USGS, 2000). The heads calculated in MODFLOW are then used in the Darcy equation, along with the cell hydraulic conductivities, to determine the groundwater velocities at each cell, which are then input to the fate and transport model.

The reaction term in equation 4.3-20 (*rxn*) is a source/sink term that is used to represent the biodegradation of the chlorinated solvents. A number of models have been used to simulate chlorinated solvent biodegradation kinetics (e.g. first-order, Monod, dual-Monod). For this study, the effects of source zone remediation are simulated for a contaminated site at Dover AFB, DE, that was originally modeled by Clement et al. (2000). Following Clement et al. (2000), a first-order model was used to simulate biodegradation kinetics. Clement et al. (2000) found that the contaminant degradation at the Dover AFB site could be accurately represented by first-order kinetics in four distinct reaction zones: anaerobic zone-1, anaerobic zone-2, transition zone, and aerobic zone. The kinetic parameters used in this study are the ones used by Clement et al. (2000) and presented in Table 4.3-3 for each of the four chlorinated ethenes (PCE, TCE, DCE, and VC).

Table 4.3-3. Reaction zone degradation rates (Clement et al., 2000).

Calibrated degradation rate constants (day^{-1})

First-order rate constant	Associated contaminant	Anaerobic zone-1	Anaerobic zone-2	Transition zone	Aerobic zone
K_P (anaerobic)	PCE	3.2×10^{-4}	4.0×10^{-4}	1.0×10^{-4}	0.0
K_{T1} (anaerobic)	TCE	9.0×10^{-4}	4.5×10^{-4}	1.125×10^{-4}	0.0
K_{T2} (aerobic)	TCE	0.0	0.0	0.4×10^{-5}	1.0×10^{-5}
K_{D1} (anaerobic)	DCE	8.45×10^{-4}	6.5×10^{-4}	1.625×10^{-4}	0.0
K_{D2} (aerobic)	DCE	0.0	0.0	1.6×10^{-3}	4.0×10^{-3}
K_{V1} (anaerobic)	VC	8.0×10^{-3}	4.0×10^{-3}	1.0×10^{-3}	0.0
K_{V2} (aerobic)	VC	0.0	0.0	0.8×10^{-3}	2.0×10^{-3}
K_{E1} (anaerobic)	ETH	2.4×10^{-2}	1.2×10^{-2}	0.3×10^{-2}	0.0
K_{E2} (aerobic)	ETH	0.0	0.0	0.4×10^{-2}	1.0×10^{-2}

RT3D uses the following versions of Equation 4.3-20 to describe the fate and transport of the dissolved chlorinated compounds (from Clement, 1997):

$$\frac{\partial[PCE]}{\partial t}=\frac{\partial}{\partial x_i}\left(D_{ij}\frac{\partial[PCE]}{\partial x_j}\right)-\frac{\partial}{\partial x_i}\left(v_i[PCE]\right)-\varphi_P[PCE] \tag{4.3-51}$$

$$\frac{\partial[TCE]}{\partial t}=\frac{\partial}{\partial x_i}\left(D_{ij}\frac{\partial[TCE]}{\partial x_j}\right)-\frac{\partial}{\partial x_i}\left(v_i[TCE]\right)+Y_{T/P}\varphi_P[PCE]-\varphi_{T1}[TCE]-\varphi_{T2}[TCE] \tag{4.3-52}$$

$$\frac{\partial[DCE]}{\partial t}=\frac{\partial}{\partial x_i}\left(D_{ij}\frac{\partial[DCE]}{\partial x_j}\right)-\frac{\partial}{\partial x_i}\left(v_i[DCE]\right)+Y_{D/T}\varphi_T[TCE]-\varphi_{D1}[DCE]-\varphi_{D2}[DCE] \tag{4.3-53}$$

$$\frac{\partial[VC]}{\partial t}=\frac{\partial}{\partial x_i}\left(D_{ij}\frac{\partial[VC]}{\partial x_j}\right)-\frac{\partial}{\partial x_i}\left(v_i[VC]\right)+Y_{V/D}\varphi_{D1}[DCE]-\varphi_{V1}[VC]-\varphi_{V2}[VC] \tag{4.3-54}$$

$$\frac{\partial[ETH]}{\partial t}=\frac{\partial}{\partial x_i}\left(D_{ij}\frac{\partial[ETH]}{\partial x_j}\right)-\frac{\partial}{\partial x_i}\left(v_i[ETH]\right)+Y_{E/V}\varphi_{V1}[VC]-\varphi_{E1}[ETH]-\varphi_{E2}[ETH] \tag{4.3-55}$$

where [PCE], [TCE], [DCE], [VC], [ETH] are concentrations of PCE, TCE, DCE, VC, and ethene, respectively [ML^{-3}], φ_P, φ_{T1}, φ_{D1}, φ_{V1}, φ_{E1} are first-order anaerobic degradation rates for PCE, TCE, DCE, VC, and ethene, respectively [T^{-1}], φ_{T2}, φ_{D2}, φ_{V2}, φ_{E2} are first-order aerobic degradation rates for TCE, DCE, VC, and ethene, respectively [T^{-1}], and $Y_{T/P}$, $Y_{D/T}$, $Y_{V/D}$, $Y_{E/V}$ are chlorinated compound yield under anaerobic reductive dechlorination conditions (0.79 , 0.74 , 0.64 , and 0.45 , respectively) [MM^{-1}].

The chlorinated compound yield coefficients ($Y_{B/A}$) are used to track mass. For example, $Y_{T/P}$ = 0.79 indicates that the anaerobic reduction of 1 gram of chlorinated compound A (PCE in this instance) leads to the production of 0.79 gram of chlorinated compound B (TCE in this case). In Equations 4.3-51 through 4.3-55, sorption is assumed negligible. The concentration of PCE in the source zone was used as a boundary condition in the model. The PCE concentration was determined by the Zhu and Sykes (2004) power function, while the concentrations of TCE, DCE, VC, and ethene at the boundary were set to zero. All initial concentrations of chlorinated solutes throughout the aquifer were set to zero. The model was verified by reproducing the results obtained by Clement et al. (2000).

The relationships between source remediation and contaminant concentrations at downgradient receptors were estimated by combining the Zhu and Sykes (2004) power function model and the fate and transport model in RT3D. Figures 4.3-14 and 4.3-15 use the model developed in this study and the Dover AFB site conditions (Clement et al., 2000) to show the TCE and vinyl chloride (VC) concentration reductions, respectively, achieved at a receptor 800 meters downgradient of the source zone versus the mass reduction in the source zone.

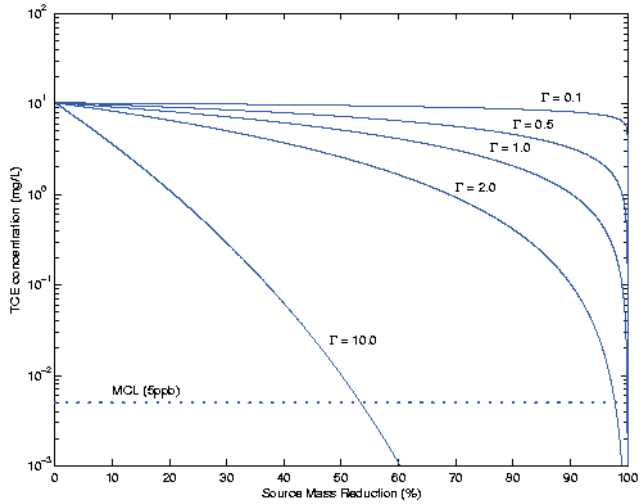

Figure 4.3-14. Steady-state TCE concentration at varying source mass reductions for a monitoring well 800 meters downgradient of the source.

These figures also show the respective maximum contaminant levels (MCLs), often used as the remediation goal, of the contaminants. The initial or maximum concentration for the PCE concentration in the source zone used in this model is 120 mg/L. Also, the percentage of source mass reduction is equal to the portion of mass removed from the source zone, defined as:

$$\%\text{Source Mass Reduction} = \frac{M_{S,0} - M_S(t)}{M_{S,0}} * 100\% \tag{4.3-56}$$

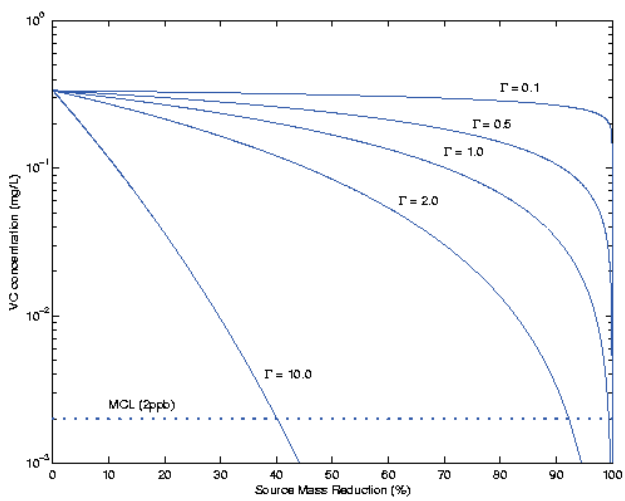

Figure 4.3-15. Steady-state vinyl chloride (VC) concentrations at varying source mass reductions for a monitoring well 800 meters downgradient of the source.

By using Figures 4.3-14 and 4.3-15, we can estimate how much source mass removal is required to achieve MCLs at a downgradient receptor. For instance, if $\Gamma = 2.0$, approximately 98% of the mass in the source zone would need to be removed to reduce TCE concentrations downgradient to MCL. Note, however, that

with 98% source-mass removal, VC concentrations at the well would be well below the MCL. Table 4.3-4 shows the approximate source mass reductions needed to attain the MCLs for the different contaminants. For the Dover AFB site, the source mass reductions necessary to accomplish the remediation goals for VC are consistently less than what is needed to achieve TCE goals and DCE goals are more easily attained than VC goals. Note also the inverse relationship between Γ and the fractional mass reduction required to achieve remedial goals.

Table 4.3-4. Percent mass reduction necessary to achieve remediation goals.

Compound	MCL (μg/L)	Γ				
		0.1	0.5	1.0	2.0	10.0
TCE	5	100.0	100.0	99.9	97.8	53.4
DCE	70	100.0	100.0	98.6	88.3	34.9
VC	2	100.0	100.0	99.4	92.3	40.1

4.3.3 Model Assessments and Applications

4.3.3.1 Simulation of laboratory and field air sparging

Comprehensive data from laboratory and field scale air sparging experiments were examined using TMVOC, a multicomponent compositional multiphase flow simulator (Van Antwerp et al., 2008; Pruess and Battistelli, 2002). Many studies have used column data to examine mass removal, but it is important to assess how accurately processes at that scale represent larger field scale processes. The laboratory and field air sparging studies simulated in this work were chosen because they have comprehensive data sets and they were designed to complement each other.

The controlled two-dimensional laboratory sparging test was simulated first. The capabilities of the local equilibrium and dual-domain mass transfer approaches for representing the observed contaminant removal rates were assessed. Using the understanding gained from simulating the controlled two-dimensional experiment, the field experiment was simulated, and the applicability of the laboratory-scale mass transfer coefficient to a field scale system was evaluated.

In a traditional numerical flow simulation, each element represents a single continuum. Within each element local equilibrium is normally assumed, in which case there is no accounting for local mass transfer limitations that may occur due to fingering of gas channels. Multiphase simulations of sparging patterns show the gradational change in averaged gas saturation outward from the injection location during air sparging (Figure 4.3-16). A more detailed representation may be that the air channel density is greater near the injection location and the air channel density decreases with distance from the sparge well. Air sparging studies have shown that channeling leaves some pore water relatively unaffected by the sparged gas (Ji et al., 1993; Elder and Benson, 1999). Contamination (NAPL or dissolved) that is isolated from the gas channels is not removed unless it diffuses through the water, into the channels. In general, kinetic interphase mass transfer needs to be incorporated into a multiphase flow and transport model to accurately simulate contaminant removal by air sparging, because it is not practical to resolve the individual gas channels in a field-scale simulation.

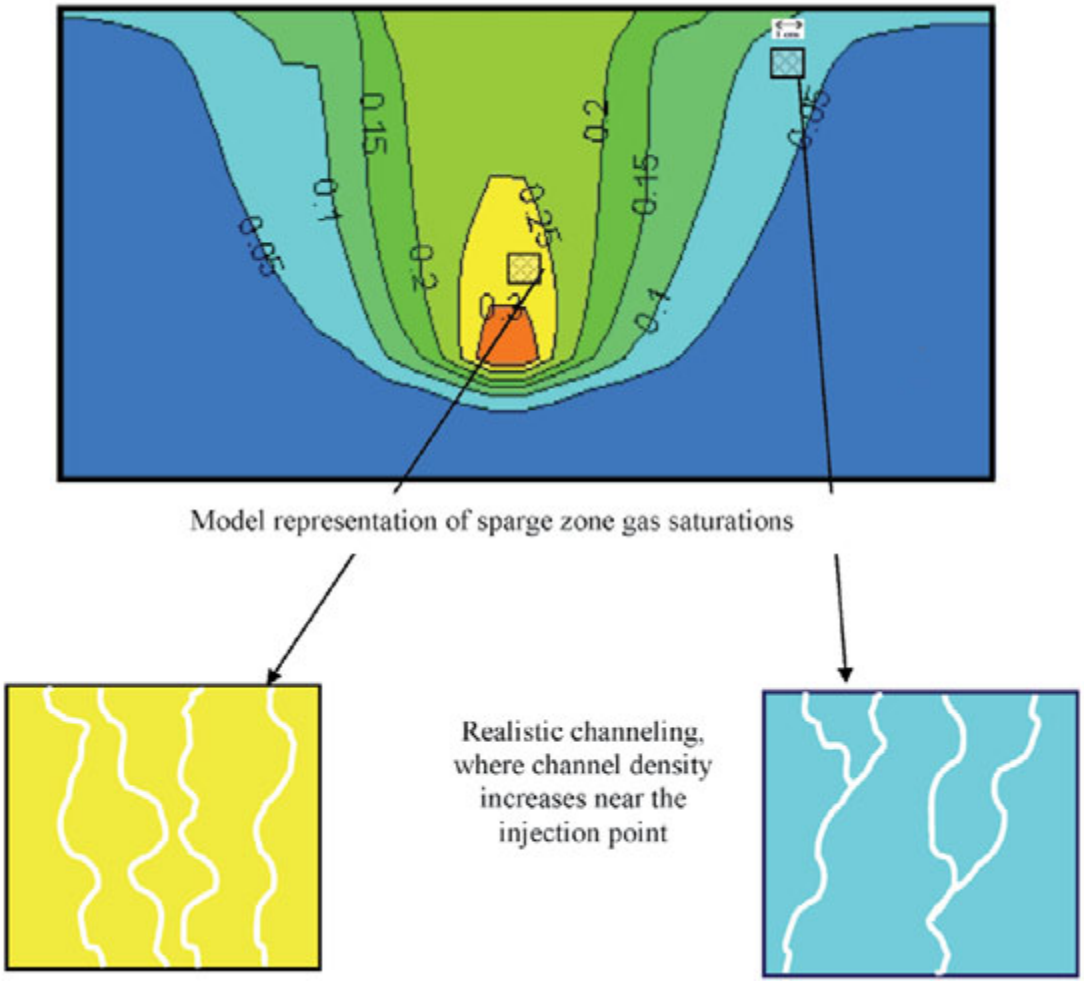

Figure 4.3-16. A simulated sparge zone in a single medium multiphase flow model versus realistic channeling that occurs in air sparging. A modeled gas saturation distribution under constant mass injection of air is on the left. Illustrations of pore scale channeling that occurs in a real system are shown on the right (Van Antwerp et al., 2008).

A dual-domain approach (Falta, 2000) was used to incorporate kinetic interphase mass transfer into the TMVOC multiphase flow code. In this approach, the 3-dimensional grid is divided into two volume fractions: one that represents coarser grained fractions of the porous media where the gas channels are created, and one that represents finer grained materials that remain nearly saturated (Figure 4.3-17). Due to capillary forces (air entry pressure), gas will tend to preferentially flow through the coarser material when both are initially water saturated. The properties of these two volumes can be chosen so that the composite media behaves like a normal porous media. The two volume fractions are locally connected one dimensionally, so that fluids and contaminant components can move between the two domains according to pressure and concentration gradients. In the present work, the fine-grained fraction tends to contain mostly water, so the mass transfer to the coarser grained fraction is limited mainly by aqueous diffusion.

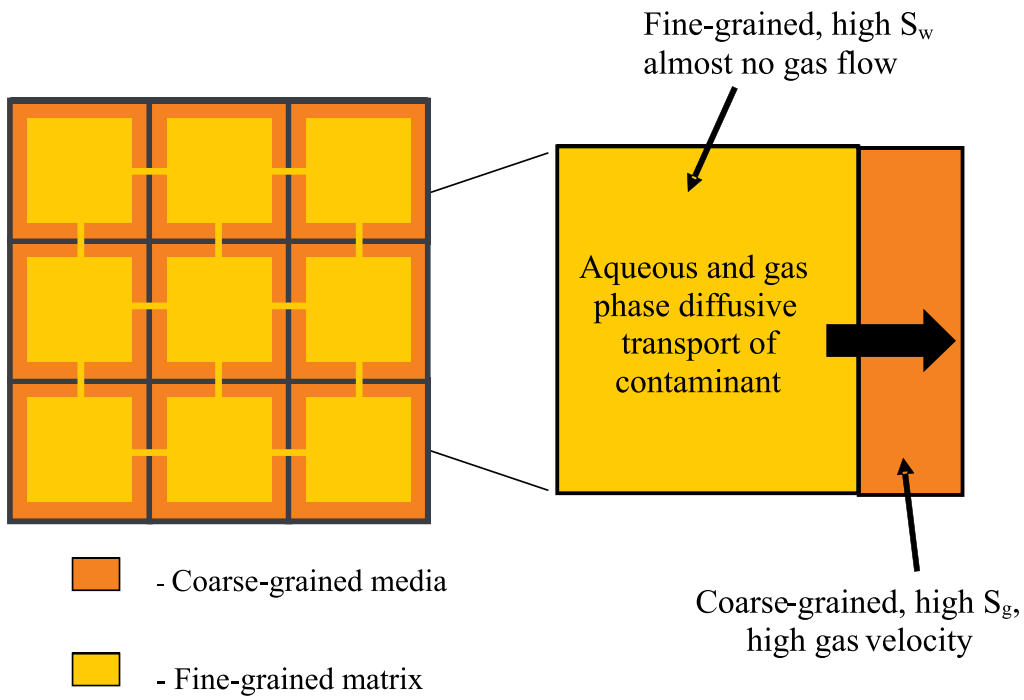

Figure 4.3-17. Schematic of connections in a dual media grid. Both media are globally connected and share a local connection. Also shown is conceptualization of dual-media processes in a grid block (Van Antwerp et al., 2008.

Air sparging was studied in a 1-m long by 0.5-m high by 4-cm thick laboratory apparatus to investigate removal rates and mobility issues of a DNAPL, PCE, during sparging in a controlled two-dimensional (2-D) configuration (Heron et al., 2002). Reported system configuration, soil properties, and sparging conditions were used as the simulation input. Chemical input parameters were obtained from published properties. The sand-water-air characteristic/permeability parameters were selected to produce a sparge zone of similar size and shape to photographs of the initial sparging period based on preliminary two-phase (air/water) simulations. No soil permeability data were available for the medium sand used in the experiment, so it was assumed to have an intrinsic permeability between 10-100 darcies, which is a typical permeability range for a medium sand. Using the initial injection rate and selected capillary parameters, the intrinsic permeability was adjusted to produce a sparge zone of similar size and shape to that appearing in photographs of the initial sparging period. These two-phase simulations showed that an intrinsic permeability of 30 darcies produced a gas plume most similar to the pictures. Model results were fit to observations of capillary rise and the formation of the sparge zone. Contaminant injection and redistribution were simulated using TMVOC along with the air sparging performance for varying injection rates, as reported in the study. Simulated PCE vapor concentrations and cumulative mass removed were compared to the experimental data.

A DNAPL source was created in the apparatus by rapidly injecting 100 ml of liquid PCE near the top of the box. Lowering and raising the water level produced a vertically smeared zone of PCE. Experimentally measured air sparging results from Heron et al. (2002) are summarized in Figure 4.3-18. The top part of Figure 4.3-18 shows the measured offgas PCE concentration (open circles) during the experiment, while the bottom part shows the cumulative mass of PCE removed (diamonds). The sparging rate was varied and included three 8-hour long pulses of air and three 1-hr pulses.

For multiphase flow problems, such as air sparging, the effects of multiple phases in the pore spaces must be considered. Generally, the relative permeabilities are assumed to be a function of the saturation in the

respective phase. More details on the capillary function and relative permeability formulation are reported in Van Antwerp et al., (2008).

In this modeling analysis of mass removal during air sparging, the two-dimensional grid consisted of 1,624 elements (28 rows high, 58 columns long) to accurately resolve the initial distribution of PCE. The element dimension perpendicular to the 2-D plane of the experiment was equal to the thickness of the apparatus. The exterior of the grid is a "no-flow" boundary. The initial water saturation and pressure distribution are assigned by assuming gravity-capillary equilibrium.

A qualitative comparison of color photographs of the initial distribution of NAPL PCE, that was dyed-red, to simulations of the NAPL redistribution patterns after injection were used to obtain the residual NAPL saturation, since it was not measured. The residual NAPL saturation, used in the three-phase relative permeability function, was adjusted until the simulated spilled PCE distribution approximately matched the distribution inferred from the pictures. Air injection in the experiment occurred at a point approximately 12-cm above the top of the silt layer. An appropriately located element was chosen to inject air at a constant rate. TMVOC allows for tabular input of time-variable injection rates, which were obtained from the experiment.

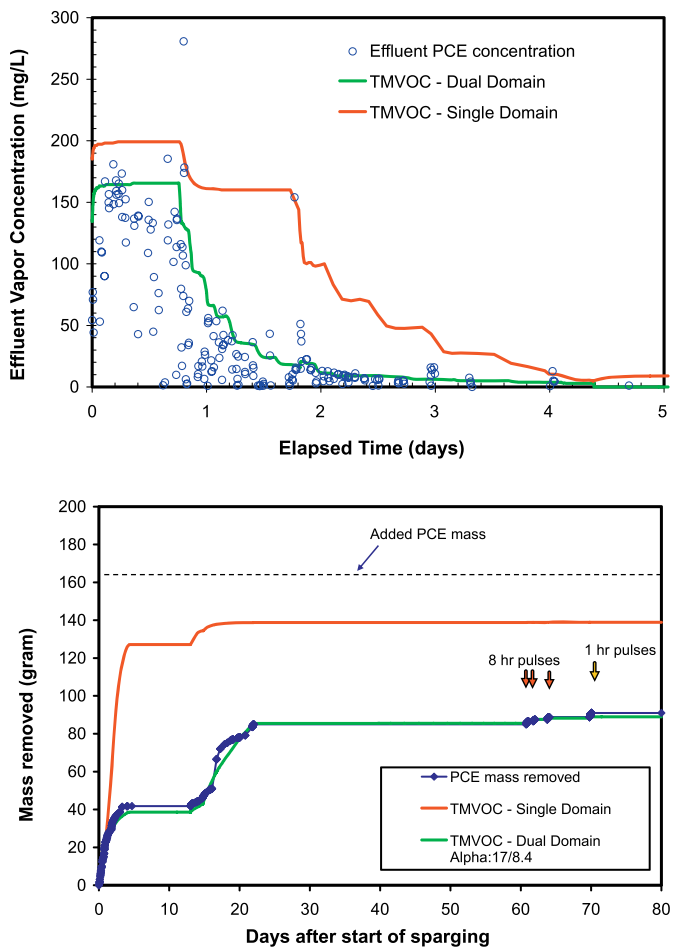

Figure 4.3-18. Results from air sparging experiments (Heron et al. 2002). The top figure (a) shows simulated effluent concentrations using single- and dual-domain approach with fine grid (28 x 58) along with the experimental data from the 2-D air sparging test. In the bottom figure (b), total mass removed as predicted by a dual-domain numerical simulation using a fine grid along with experimental mass removed from the 2-D test. The alpha ratio is representative of the capillary contrast between the coarse and fine-grained media (Van Antwerp et al., 2008).

Simulations with a single-domain local equilibrium model configuration over-predicted the contaminant mass removal rate (Figure 4.3-18). Initial concentrations predicted by the model are similar to the experimental data; however, the single-domain model is unable to resolve the rapid decrease in concentrations after one day of sparging. The over prediction of the mass removal rates for the single-domain model is even more pronounced for the cumulative mass removal calculations. Within the first 4 days the single-domain model predicts that 120 g of PCE were removed followed by the removal of an additional 20 g. In the experiment, only 90 g of PCE were actually removed. The differences in the cumulative mass removal between single domain and the experimental measurements (Figure 4.3-18) became smaller after 20 days because in the single domain simulation nearly all of the mass of PCE in the sparge zone had been removed, while in the dual-domain simulation, there was still PCE present in the sparge zone beyond 20 days.

Properties from the single medium simulation were adjusted for the two domains of the dual-domain simulation following the logic presented in Falta (2000). It was assumed that gas channels would form in approximately 20% of the sand during air sparging. A volume fraction of 20% of the original element was assigned properties of a coarse-grained media and the remaining volume fraction (80%) was assigned properties of a fine-grained media to account for zones of stagnant pore water. The volume fraction in which gas channels form cannot be readily measured, so it was a calibration variable. After adjusting the contrast in dual-domain capillary properties (α'_{gw}), the effluent concentrations from the dual-domain simulation were very similar to the laboratory data (Figure 4.3-18). As a result, the cumulative mass removal as a function of time also closely matched the experimental data.

An equivalent mass transfer value of 4.85×10^{-5} s^{-1} was calculated for this experiment, which is in the range reported by Braida and Ong (1998). This value is also close to that calculated for column studies (Falta, 2000), having the same ratio of interfacial area (A_{12}) to interfacial distance (d_2). Since this laboratory-scale study was designed to complement the field-scale study, this A_{12} / d_2 ratio was used initially for the field-scale simulation.

The next step was to use TMVOC to simulate a controlled air sparging field test. Both single- and dual-domain approaches were used in an attempt to model the observed removal rates. Only the first 57 days of operation, which included 5 operational changes (with 3 configurations and 1 shutdown), were simulated. During the second part of the test, which was not simulated, water was re-circulated in the test cell. Simulating this condition would require some code modifications to TMVOC.

This air sparging demonstration was conducted in a test cell at the Dover National Test Site (DNTS), Dover Air Force Base, Dover, Delaware. The cell was nominally 4.6-m long by 3.0-m wide by 12-m deep (15-ft by 10-ft by 40-ft). Lateral boundaries were formed by sheet piles driven through the formation and into a clay layer 12.2-m below the ground surface. This clay layer created a lower confining boundary. Investigators from Michigan Technological University performed the air sparging experiment in 1999 (Gierke et al., 2002). Constraints on the initial contaminant mass, injection/extraction flows, and the comprehensive data collection make this air sparging study well suited for testing models.

The simulation model for this site assumes homogeneous geologic conditions, however non-reactive tracer tests performed specifically in the field test cell (Falta et al., 2003) indicated zones of varying permeability, with reported horizontal permeabilities ranging from 1×10^{-11} m^2 to 8×10^{-13} m^2 (Applied Research Associates, 1996). A homogeneous model is certainly an oversimplification of the geology, but assuming a homogeneous soil system allows for the calibration aspects to be performed more straightforwardly. Furthermore, detailed knowledge of local heterogeneities is usually not available at real field sites and was not at this site. Although the laboratory system described previously was modeled as isotropic, the field site was assumed to have vertical anisotropy.

Since the injection and extraction gas flow rates were known and fixed in the simulation, the intrinsic permeability was adjusted using a preliminary multiphase flow simulation to produce air pressures in the wells similar to the measured values reported from the field. The modeled pressures were within 5% of observed pressures (25% of the observed vacuum pressure) when using an intrinsic permeability of 2×10^{-11} m^2 in the horizontal (x, y) direction and 1×10^{-11} m^2 in the vertical (z) direction.

The sparging system injected air into the lowest 1-foot interval of the well screen (11.9-m to 12.2-m bgs). A point mass injection was used to simulate the injection of 80% relative humidity air. Measured flow rates from the experiment were specified as the model input. Three different configurations were modeled during the simulated 57 days. During the experiment, combined flows through the extraction vents (33 scfm) were kept at approximately twice the rate of injection to prevent the sparge well vapors from emerging through the cell surface. These wells were also modeled using a specified mass rate of extraction based on the measured rates. The extraction wells were screened from 6.1-m to 12.2-m bgs, however, production of air occurs only from the screened interval above the saturated zone. Initially, this interval was 4.6-m but shortened as the water table mounded upward as the sparging zone developed (around 0.4-m, depending on injection/extraction well configuration).

A DNAPL source was created by injecting 107 kg of PCE into the test cell (Gierke, et al. 2002). The goal of the PCE release was to create a heterogeneously distributed, residual-NAPL contaminated zone in the lower-most 1.5 m) of the coastal sand deposits above the underlying clay layer. PCE was injected at a depth of 10.7 m bgs through 3-mm diameter injection ports distributed across the cell. Details of the resulting DNAPL structure are unknown so the PCE was emplaced in the system based on reported injection locations and volumes.

A traditional single-domain, local equilibrium model was tested based on the parameters and sinks and source described. As happened for the laboratory experiment, the field-scale, single-domain simulation over-predicted mass removal (Figure 4.3-19). The over-prediction is because subgridblock-scale mass transfer limitations are not accounted for in a single-domain approach. Simulated PCE removal (red line) for the first few days matches the experimentally derived mass removal rate fairly well, but after about 5 days the simulation results diverge from the actual measurements. The simulation predicted the total mass removal over 57 days to be approximately 65 kg, whereas the actual mass removal was 39 kg. Differences between the predicted and experimental results are likely due, in part, to the initial contaminant distribution and soil heterogeneities, and local diffusive limitations.

Properties from the single medium simulation were adjusted for the dual domains in the same manner as in the laboratory experiment simulation. The coarse grained domain was again set equal to 20% of the total volume. Again, it is unknown whether precisely 20% of the sand volume would form gas channels, but the estimate is reasonable based on Falta (2000) and the observed increase in the water table elevation. The dual-domain properties were based upon the single medium soil characteristics pertaining to the coastal sediments at the field site. A dual-domain model was run initially using the equivalent mass transfer rate (A_{12}/d_2) ratio determined for the laboratory experiment (75,000), but the model still over-predicted the PCE removal rate as shown in Figure 4.3-19 (yellow line).

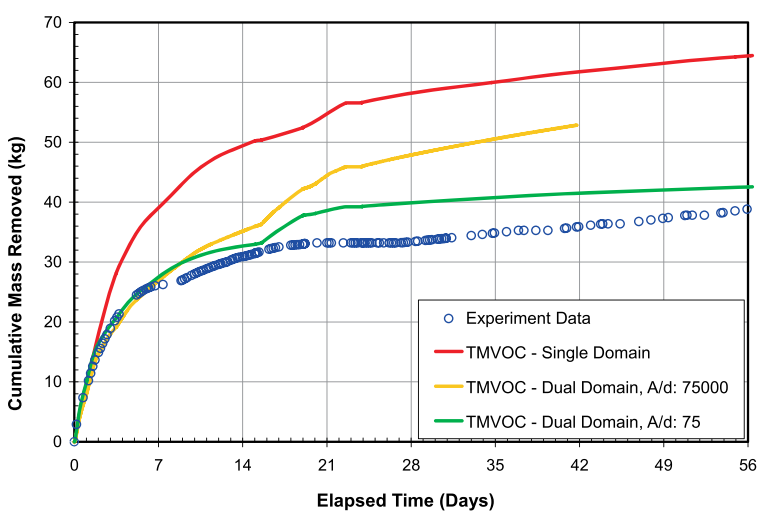

Figure 4.3-19. Total experimental mass removal and simulated removal with TMVOC using a dual-media approach with A_{12}/d_2 ratio from the laboratory-scale air sparging simulation (75,000) and the adjusted A_{12}/d_2 ratio (75) (Van Antwerp et al., 2008).

The single-domain, local-equilibrium model predicts that almost all of the contaminant within the sparge zone was removed after approximately 15 days. A three-dimensional view of the DNAPL and gas saturation distribution at 15 days shows that while the two simulation approaches predict similar overall gas flow patterns, the dual-domain model results in a slower removal of DNAPL from the sparge zone. The pooled PCE NAPL in the lower portion of the simulation remains unaffected throughout the course of both simulations.

By reducing the ratio of A_{12}/d_2 to 75 (equivalent to increasing d_2 and /or decreasing A_{12}) to reduce the effective mass transfer coefficient, a better match of the total mass removal was obtained (Figure 4.3-19, green line). Calibration of the model to the laboratory data depended on the contrast in gas saturations between the two domains, however, in calibration of the field-scale model the gas saturation contrast had a smaller effect than the A_{12}/d_2 ratio (Van Antwerp, 2006). The simulated mass removal using a dual-domain approach was similar to the actual data for the first flow configuration. At the first flow configuration change, occurring at 15 days, the model predicts a more abrupt increase in the mass removal rate than was observed. The simulated mass removed from this time forward is approximately 5 kg higher than the observed. Flow configuration 2, which begins at day 15, involves ceasing air injection into one well and doubling the flowrate at the other injection location.

In summary, a multi-phase numerical simulator was adapted to account for mass transfer limitations through a dual-domain approach. Using TMVOC as a single medium model for contaminant removal scenarios over-predicted the mass removal rates due to a local equilibrium assumption in each element. The dual-domain-model based simulation successfully matched data from the mass removal of a dense non-aqueous phase liquid for laboratory and field-scale air sparging experiments.

Although moisture characteristics of the sand used in the laboratory were unknown, the constraints of the known capillary rise, photographs of sparge zone width response to injection rate, and initial contaminant distribution provided enough information for reasonable estimation of soil parameters through model calibration. Contaminant mass removed during operational changes in air injection was accurately resolved in the dual-domain simulations, but not in single-domain simulations assuming local equilibrium. During pulsed operation in the two-dimensional experiment, the dual-domain model could accurately predict the time for concentrations to tail off after a pulse of air, although exact matches of concentrations during the pulses could not be obtained.

The A_{12}/d_2 ratio that was fitted to the laboratory data, (which is analogous to fitting a mass transfer coefficient to a system) was 1000 times larger for the field-scale air sparging demonstration. This indicates that mass transfer rates measured at a bench scale may not be applicable to field scale processes. One explanation for the difference in mass transfer coefficients may be the formation of a relatively uniform sparge zone in the two-dimensional box that is directly in contact with the NAPL PCE. In the field system there are many more heterogeneities affecting the sparge zone formation, and larger zones may be excluded from gas flow.

One drawback of this multiphase dual-domain approach to modeling mass removal in air sparging is the relatively large amount of site parameter data needed. However, as this study shows, a moderate amount of site information can still produce reasonable results if the data exists for model calibration at the field scale. Calibration of the model is important and using laboratory derived parameters may not be accurate.

4.3.3.2 Simulations of cosolvent flushing

This section presents UTCHEM simulations of a full scale field cosolvent flooding operation at a site with hydraulic control (Liang and Falta, 2007; Jawitz et al., 2000). The field effort was conducted at the former Sages Dry Cleaner site in Jacksonville, Florida. The site was contaminated by PCE with an estimated DNAPL volume of 68 liters. Approximately 34,000 liters of 95% ethanol were injected at the site during the flooding period of 3 days, followed by a 5-day water flood. The remediation effort was terminated after 8 days, and it resulted in the removal of approximately 42 L of PCE. It is believed that the remaining PCE was located in zones with limited hydrodynamic accessibility (Jawitz et al., 2000).

The numerical simulator used in this work, UTCHEM (version 9.3) was obtained from the University of Texas (Delshad et al., 1996). UTCHEM is a three dimensional, multicomponent, multiphase, compositional

surfactant flooding simulator that has been used both for environmental applications as well as enhanced oil recovery (Brown et al., 1994; Camilleri et al., 1987; Delshad et al., 1996; Freeze, et al., 1994; Liu et al., 1994; Pope and Nelson, 1978). UTCHEM uses the finite difference method with temporal discretization that is implicit in pressure and explicit in concentration (IMPES-like). UTCHEM uses a total variation diminishing (TVD) scheme that is approximately third-order in space to minimize numerical dispersion and grid-orientation effects (Datta Gupta et al., 1991; Harten, 1983; Liu et al., 1994).

To simulate cosolvent flooding and the resulting transport processes, the equilibrium phase partitioning behavior between DNAPL, water and cosolvent is of central importance. A ternary phase diagram can be used to describe the equilibrium phase partitioning behavior for surfactant flooding as well as for cosolvent flooding. A general discussion of cosolvent flooding performance based on ternary phase behavior has been presented elsewhere (Falta, 1998). In UTCHEM, the phase behavior model is based on Hand representations of the ternary phase system (Hand, 1930).

The phase behavior of the ethanol/PCE/water ternary system has been extensively studied (Hayden et al., 1999; Lunn, 1998, Lunn and Kueper, 1997; Van Valkenburg, 1999). As shown in Figure 4.3-20, the ethanol/PCE/water system exhibits the typical Type II (-) phase behavior with negative tie-line slopes. This tie line behavior indicates that the ethanol preferentially partitions into the aqueous phase rather than the DNAPL phase. An aqueous phase with a high ethanol concentration can dissolve a large amount of DNAPL, increasing the solubility by several orders of magnitude. Thus the main recovery mechanism for this phase environment is enhanced dissolution, although separate phase DNAPL mobilization is also possible at high injected alcohol concentrations (Falta, 1998).

The UTCHEM surfactant phase behavior package was fit to the ethanol/PCE/water phase behavior data of Hayden et al. (1999). The comparison of the UTCHEM representation and the experimental measurements are shown in Figure 4.3-20. It is important to recognize that the simplified Hand model used in UTCHEM may not exactly represent all parts of the ternary phase behavior. For example, in our fit of the Hayden et. al. (1999) data, we focused primarily on matching the height of the binodal curve, and the slopes of the tie lines. Because the actual curve is asymmetrical, our best fit does not perfectly match the aqueous phase composition leg of the binodal curve, so the calculated DNAPL solubilities are only approximate. It is possible to more precisely fit the aqueous phase composition leg of the binodal curve, but this tends to result in a binodal curve that is substantially higher than the laboratory data indicate.

From the phase diagram, the maximum concentration of ethanol to form a two-phase region is 0.725 (volume fraction). The PCE concentration at the plait point is 0.854 (volume fraction). These are important input parameters used to describe the phase behavior in the numerical model. As shown in Figure 4.3-20 the UTCHEM phase behavior package can reasonably account for the phase behavior of the water/ethanol/PCE system.

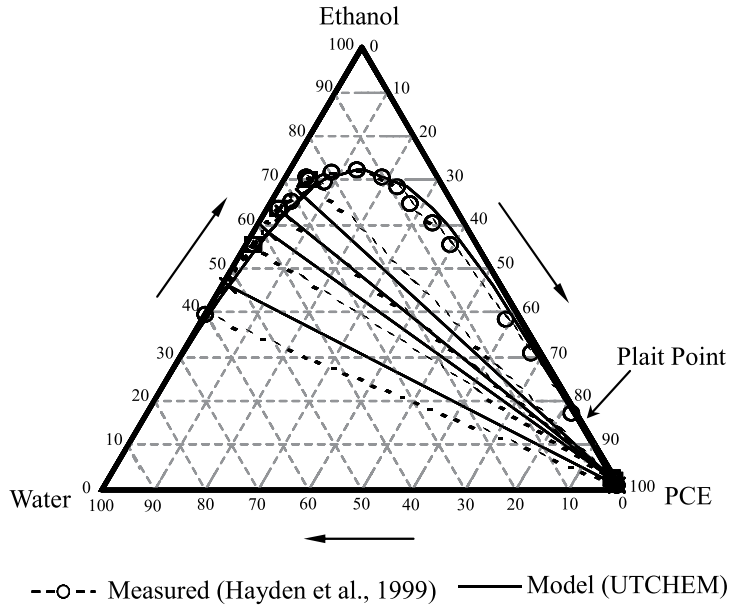

Figure 4.3-20. Modeled and measured ternary phase diagram for the system of water-ethanol-PCE (Liang and Falta, 2008).

The in-situ cosolvent flooding effort simulated here was conducted at the former Sages Dry Cleaner site in Jacksonville, Florida. The description of site background and field test operation is based on the work reported by Sillan et al. (1999) and Jawitz et al. (2000). The DNAPL source zone was characterized both before and after alcohol flooding using soil cores, groundwater samples, and interwell partitioning tracer tests (Jawitz et al., 2000). The PCE source area in plan view was approximately 7.3 m by 2.7 m (Figure 4.3-21) (Jawitz et al., 2000). The total estimated volume of PCE was 68 liters (109 kg) at the beginning of the test, equivalent to an overall average saturation of 0.004. Nine wells were used in this ethanol flooding field test, three injection wells (IWs) in the center and six recovery/hydraulic containment wells (RWs) along the perimeter of the source area (Figure 4.3-21). Approximately 34,000 liters (2 PVs) of 95% ethanol were delivered to the three injection wells during the flooding period of 3 days, followed by a 5-day water flood. The field test was terminated after 8 days, and resulted in about 42 liters (67 kg) of PCE removal.

The model domain was taken as a 24.7 m x 13.8 m x 10.7 m region discretized into 12,500 (25 x 20 x 25) cells with fine spacing in the treatment zone and coarse spacing outside the source zone (Figure 4.3-21). Constant atmospheric pressure was maintained at the top boundary. The bottom was a no flow boundary associated with a clay confining unit. The left and the right sides were constant head boundaries that match the regional gradient, with regional flow toward the west under a natural hydraulic gradient of 0.0025. The other two sides were no flow boundaries that are parallel to the regional flow direction.

Based on the positions of the well packers, the upper zone and the lower zone of each injection well were modeled as two separate wells. A total of 12 simulation wells including 6 extraction wells were used. The injection and extraction flow rates were based on the field data. The initial DNAPL saturation distribution was interpolated from soil core data and the estimated initial total DNAPL mass. Measured soil concentrations of PCE (mass fraction) at different depths were used to calculate DNAPL saturation.

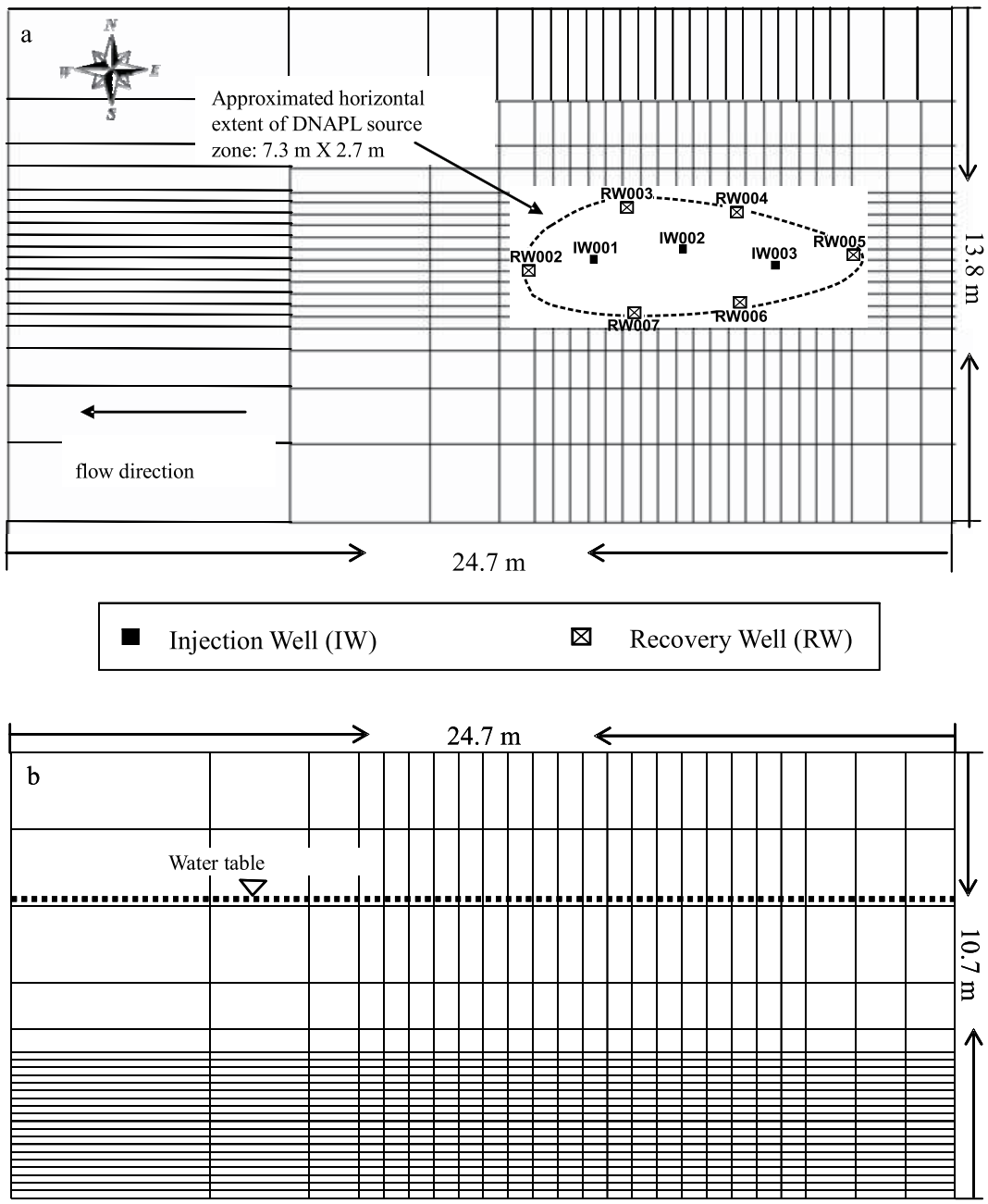

Figure 4.3-21. Plan view of model domain with the site map of well and MLS locations within the approximated DNAPL source zone at Sages (adapted from Jawitz et al. 2000) (Liang and Falta, 2008).

Three cases were considered for the Sages simulations. First, a basic model was built as a two-unit system with a simple permeability structure (referred to as the base case). To gain a better approximation to the actual permeability distribution in the field, hydraulic conductivities estimated with a borehole flow meter were used to define a layered case (referred to as the heterogeneous case). Adjustment of zones of horizontal permeability based on the field test well flow rates was also included in this heterogeneous case. Finally, the heterogeneous flow model was calibrated by adjusting initial DNAPL distribution using extraction well PCE breakthrough curves (referred to as the calibrated heterogeneous case).

The basic model was built as a two-unit system with a simple hydraulic conductivity field. The average hydraulic conductivity values from slug tests of 6.10 m/day for the upper unit (0-9 m bgs) and 3.05 m/day for the lower unit (9-10.7 m bgs) were used. An anisotropy ratio of 0.1 for vertical hydraulic conductivity to horizontal hydraulic conductivity was assumed. The overall porosity was set to 0.3. The initial DNAPL saturation distribution was interpolated based on soil core data, and distributed so that the initial total DNAPL mass was 109 kg.

Base case

Combining the flow weighted average of the six recovery wells yielded the total effluent concentrations. For this simple base case, the model overestimated total ethanol recovery at early times and underestimated PCE concentrations. However, this was a completely uncalibrated model with a very simple permeability structure.

From the simulation results of the basic model, the underestimation of ethanol effluent percentages from RW003 and RW004 suggest that the area around these two wells may be less permeable. Because of the lower permeability, RW003 and RW004 would extract a smaller amount of water from outside the target zone, thereby yielding the higher ethanol effluent percentages. On the other hand, the over predicted ethanol effluent percentages from RW006 and RW007 suggest that the formation in the vicinity of these two wells could be more permeable. Thus RW006 and RW007 would extract much more water from outside the pattern, diluting the ethanol, and yielding the lower ethanol effluent percentages. The fact that the flow rates for RW006 and RW007 were about 2~3 times greater than those for RW003 and RW004 (with the same drawdown in the well) supports this hypothesis.

Heterogeneous Case

To gain a better approximation to the actual permeability that is present in the field, hydraulic conductivities estimated with a borehole flow meter (Mravik et al., 2003) were used to condition this case. For each model layer, the harmonic mean calculated from field measurements was used to calculate the vertical hydraulic conductivity, and the weighted average was used to calculate the horizontal conductivity. If only one measurement was available for a model layer, the measurement was used for horizontal value, and an anisotropy factor of 0.1 was assumed. Both the field flow rates and the base case simulation results suggested that the area around RW006 and RW007 might be more permeable than the area around RW003 and RW004. Thus, the adjustment of horizontal permeability to make a higher permeability zone around RW006 and RW007 and a lower permeability zone around RW003 and RW004 was included in the heterogeneous case. The same initial DNAPL saturation distribution was used as in the base case.

The comparisons of simulated and field test results for PCE effluent concentrations and ethanol percentages are shown in Figure 4.3-22 for recovery wells RW002, RW003, RW004, RW005, RW006, RW007, and the total extraction fluids. For the total extraction fluids (Figure 4.3-22), the predicted overall ethanol percentages show good agreement with the field data, but the total PCE concentrations were underestimated by about a factor of two or three.

Compared to the base case, the layered heterogeneous case did a much better job of predicting the ethanol percentages, but still underestimated the PCE concentrations and the mass removal. Nevertheless, this heterogeneous model still has not been calibrated, but it used more information from the experimental site to develop a more accurate flow model.

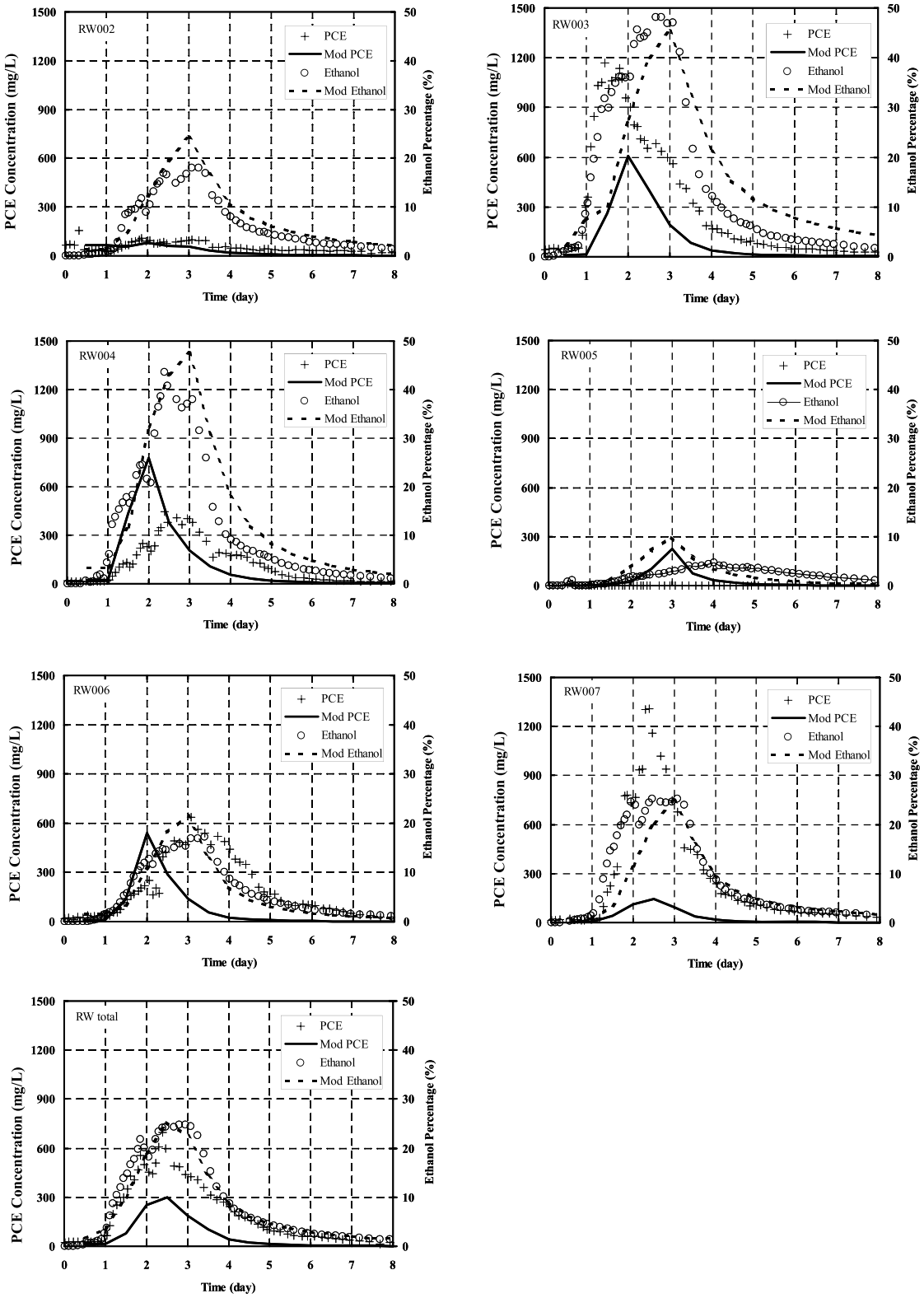

Figure 4.3-22. PCE effluent concentrations and ethanol effluent percentages for RW002, RW003, RW004, RW005, RW006, RW007, and total fluid (heterogeneous case) (Liang and Falta, 2008).

Calibrated Heterogeneous Case

Uncertainty in the initial DNAPL saturation distribution estimated from soil core data could account for the underestimation of the PCE effluent concentrations in the heterogeneous case. Since the soil core data only give PCE concentrations at a few discrete locations, it is not possible to know the details of the actual PCE distribution prior to remediation. Therefore, for this calibrated case, the initial DNAPL distribution was adjusted based on the PCE mass represented by breakthrough curves from the extraction wells. The same amount of total initial PCE mass (109 kg) was maintained for this adjusted initial DNAPL saturation distribution, and the individual soil sample concentrations are still honored. The adjusted initial DNAPL saturation distribution was used in the calibrated heterogeneous model, which used the same permeability structure as the heterogeneous case.

Only a finite number of initial DNAPL saturation distributions were tested in this calibration effort, and we acknowledge that it is possible that a better calibration could be achieved with more realizations. Furthermore, it is possible that several somewhat different initial DNAPL distributions might result in a similar overall match of the field data.

Comparisons of simulated and field test results for PCE effluent concentrations and ethanol percentages are shown in Figures 4.3-23 for recovery wells RW002, RW003, RW004, RW005, RW006, RW007, and the total extraction fluids. For the total extraction fluids (Figure 4.3-23), the predicted total ethanol percentages show good agreement with the field data, and the total PCE concentrations are close to the field data.

Compared to the results of the uncalibrated heterogeneous case, this calibrated model with a new adjusted initial DNAPL saturation distribution showed a substantially better prediction of the PCE effluent concentrations and PCE mass recovery. Unfortunately, the lack of practical field methods for characterizing DNAPL distributions makes precise well-by-well prediction of contaminant effluent concentrations difficult or impossible.

The results of a root mean squared error (RMSE) analysis for the three cases also shows this stepwise improvement of the model predictions. Compared to the base case, the RMSE on ethanol percentages for the more refined permeability model is reduced significantly from 7.4% to 3.83%. The final model, which calibrated the initial PCE distribution, shows a decrease of the RMSE on PCE concentrations from 171.9 mg/L to 72.08 mg/L.

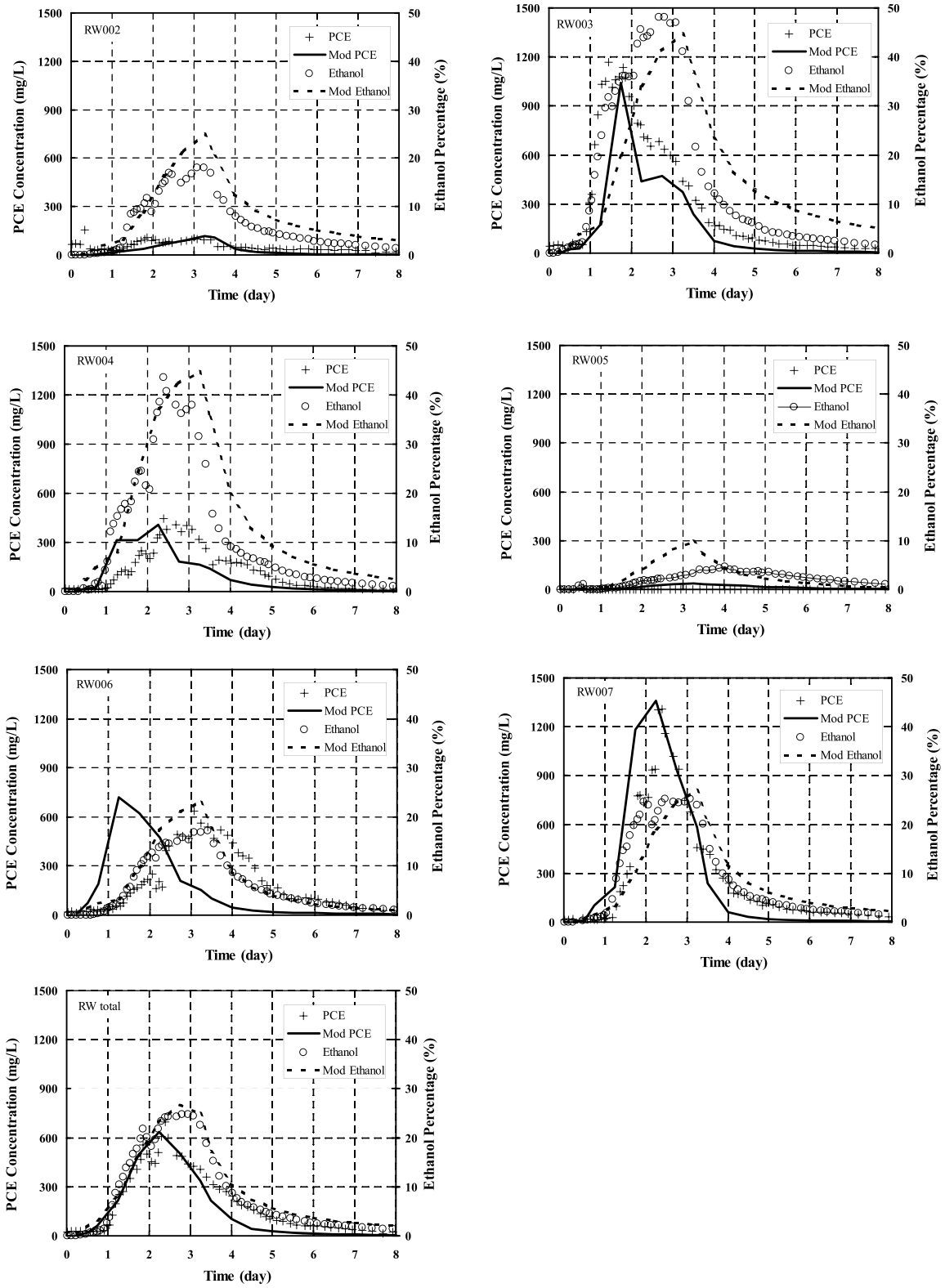

Figure 4.3-23. PCE effluent concentrations and ethanol effluent percentages for the calibrated heterogeneous case (Liang and Falta, 2008.

4.3.3.3 Dissolved chemical discharge from fractured clay

Recent experimental and theoretical studies have demonstrated that DNAPLs present in fractures in low permeability fractured porous media can dissolve and diffuse from the fractures into the matrix (Parker et al., 1994; 1997; Ross and Lu, 1999; Slough et al., 1999; Esposito and Thomson, 1999; O'Hara et al., 2000; Reynolds and Kueper, 2001; 2002; 2004; Parker et al., 2004). This relatively rapid mass transfer into the porous matrix occurs because of the sharp concentration gradients that exist after a DNAPL enters a fracture. Once the matrix has been contaminated, the contaminant can slowly diffuse back into water flowing through the fractures, leading to a long-term source of groundwater contamination. It is possible that after all of the DNAPL has been removed from a contaminated site, this dissolved mass trapped in the low permeability matrix could continue to act as a groundwater source term, perhaps for hundreds of years (Parker et al., 1997; Esposito and Thomson, 1999; Reynolds and Kueper, 2002).

Reynolds and Kueper (2002) provide some compelling analyses of the possible long-term behavior of DNAPL chemicals in fractured clays. They considered a case where 5 ml of a DNAPL were spilled into a 30 µm aperture fracture in a 3 m thick clay aquitard. Following the DNAPL release, they simulated the immediate flushing of the fracture with clean water under a gradient of 0.01. Because of the very large surface area and small volume of the fracture, the DNAPL only persists in the fracture for a few hours or days, and essentially all of it diffuses into the clay matrix, despite the clean water flush of the fracture. However, the water exiting the fracture following the clean water flush is contaminated, and a significant result of their analysis is that the chemical concentration leaving the aquitard remains above regulatory limits for 1,000 years or more under this scenario.

The purpose of this study was to explore the matrix diffusion process further, and in particular to assess the likely impact to a potable water aquifer that might underlie a contaminated aquitard (Falta, 2005). The primary scenario that will be considered here is shown in Figure 4.3-24. It is assumed that a DNAPL spill has occurred on top of a fractured clay aquitard, and that a small amount of the DNAPL has penetrated the fractures, but that no DNAPL has reached the aquifer itself. Under these conditions, it is well known that the DNAPL will disappear relatively quickly owing to matrix diffusion effects (Parker et al., 1994; 1997; Reynolds and Kueper, 2002). If a downward gradient is imposed across the aquitard (caused, for example, by groundwater pumping), then contaminated water leaving the aquitard will serve as a long-term source of groundwater contamination.

Single fracture simulations were used to examine the sensitivity of the contaminated fractured clay system to fracture flow rates and contaminant decay in the clay matrix. These simulations were performed using the T2VOC compositional multiphase flow simulator, developed at Lawrence Berkeley National Laboratory (Falta et al., 1995). The simulation grid is similar to that used by Reynolds and Kueper (2002); it explicitly discretizes a single fracture and the clay, with a very fine grid spacing (~100 µm) in the clay near the fracture. A total of 2,700 gridblocks are used in the simulation. The fracture aperture was either 30 or 100 µm, the clay was 3 m thick, with the same properties as in the Reynolds and Kueper case: a very low permeability (1.0×10^{-17} m^2), a high fraction of organic carbon (0.01), and a moderate porosity (0.3). The DNAPL is given the properties of TCE, the aqueous diffusion coefficient was set equal to 1.0×10^{-9} m^2 /s , and the tortuosity is taken to be 0.67 following Millington and Quirk (1961). The fracture apertures of 30 and 100 µm used in this study fall within the 1 to 100 µm aperture range typically reported for shallow clay deposits (Parker et al., 1994).

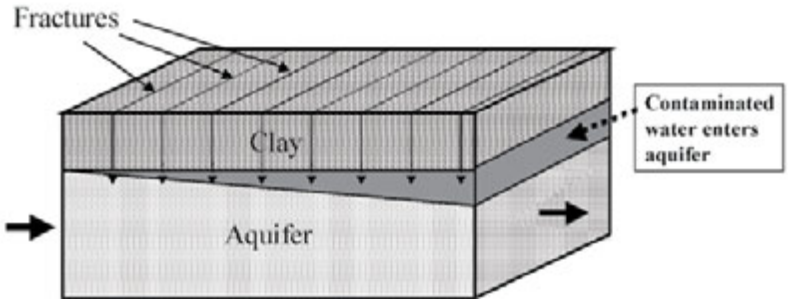

Figure 4.3-24. Conceptual view of a fractured clay aquitard. While the aquitard has a low effective hydraulic conductivity, water can flow through the fractures into the aquifer below. Contamination in the clay aquitard can then contaminate the upper part of the aquifer as shown (Falta, 2005).

To focus mainly on the long-term behavior of this TCE source, the DNAPL emplacement process is simplified somewhat compared to Reynolds and Kueper (2002). Instead of simulating a 5 ml DNAPL spill, the initial condition in these simulations is a DNAPL residual saturation of 10% or 3% throughout the fracture, depending on its aperture. This corresponds to an initial TCE mass of 13.56 g for either fracture. Because of symmetry, only half of the fracture/clay is simulated, and a no-flow outer boundary at 1.45 m corresponds to an equivalent fracture spacing of 2.9 m. The simulations each consist of two parts. In part one, the 13.56 g of TCE DNAPL is placed in the fracture with no water flow and allowed to equilibrate for a period of 20 years. Interestingly, the DNAPL phase disappears from the fracture in a few hours in this scenario, as a result of aqueous phase diffusion into the clay matrix. This is somewhat faster than Reynolds and Kueper (2002) simulated, but their DNAPL saturations in the upper part of the fracture were higher because of their DNAPL release scenario. As Reynolds and Kueper (2002) have pointed out, behavior of DNAPL in the fracture is very sensitive to the precise initial and system conditions.

Figure 4.3-25 shows the aqueous concentration of TCE in the fracture over the 20-year equilibration period. Once the DNAPL phase disappears, the concentration in the fracture shows a logarithmic decline down to a value of about 2270 µg/L, a reduction of a factor of 440, due to diffusion into the matrix. All of the initial TCE mass remains in the volume. After 20 years, a strong concentration gradient still exists in the clay, and significant dissolved concentrations have reached the model boundary at 1.45 m from the fracture.

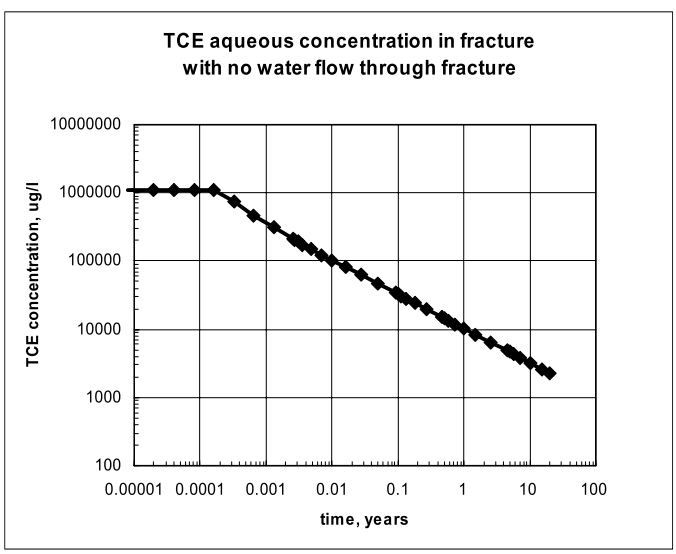

Figure 4.3-25. Simulated TCE aqueous concentration in the fracture during the 20-year equilibrium period for a 30 µm fracture with no TCE decay and a clay f_{oc} of 0.01 (Falta, 2005).

Part two of the simulation models clean water flushing of the fracture under a vertical gradient of 0.01. For 30 μm, the equivalent parallel plate permeability is 7.5 x 10^{-11} m^2, so the imposed gradient results in a Darcy velocity of 0.64 m/day, or a water flow rate of 19.2 mL/day. At 100 years, the concentration gradients in the clay have become smaller, but they are still present. For the 30 μm fracture case, after 100 years of flushing, the matrix and fracture effluent concentration (Figure 4.3-26) remains fairly high, and only about 7% of the TCE has been removed from the system. Even after 2,851 years (the end of the simulation), for the 30 μm fracture, high concentrations of the TCE remain in the system, and the fracture effluent concentration is still about 240 μg/L (Figure 4.3-26).

As noted by Reynolds and Kueper (2002), the contaminant removal by fracture flushing occurs in this case on a time scale measured in the thousands of years. However it should be recognized that this scenario did not consider any type of chemical or biological degradation of the TCE. It is not known at what rate, or by what mechanisms chlorinated solvents might degrade in a low permeability matrix, but it is plausible that some degradation could take place. To illustrate the possible importance of TCE degradation, a second simulation was run, using identical parameters, but assuming that the TCE can degrade in the aqueous phase, with a half life of 10 years. This half life is substantially longer than what is often observed in dissolved TCE plumes at field sites (Weidemeyer et al., 1999), and the production of daughter products is neglected. This simulation also uses a lower fraction of organic carbon in the clay compared to the previous simulation, 0.002 instead of 0.01. The same initial TCE mass is present in both cases. The fracture effluent from this case with TCE degradation is shown as the curve with grey diamonds in Figure 4.3-27. While the early time behavior is similar to the simulation with no degradation, a large effect is seen beginning at about 10 years. The fracture effluent concentration drops below 1 μg/L in less than 300 years in this case.

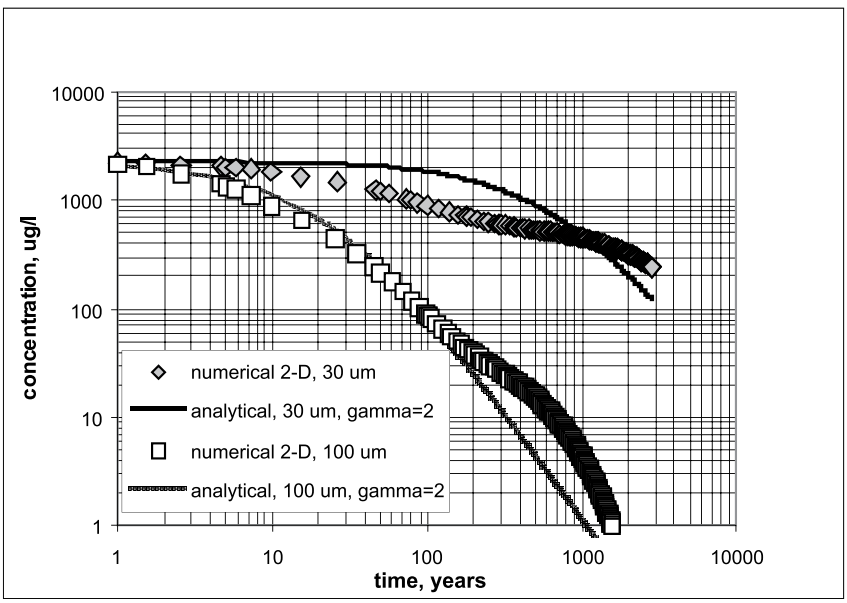

Figure 4.3-26. TCE concentration in the fracture effluent for the 30 μm and 100 μm fractures. There is no decay of TCE in the clay matrix and the f_{oc} = 0.01 (Falta, 2005).

The amount of flushing that takes place in a 30 μm fracture is relatively small because of the small area of the fracture. As the fracture aperture increases, the flow rate through the fracture increases approximately as the cube of the aperture. Thus, a 100 μm fracture (which represents the largest aperture typically found in a fractured clay) would conduct 37 times more water than a 30 μm fracture under the same gradient. A pair of simulations was performed using a 100 μm fracture aperture. The other system parameters were maintained at their previous values, and the total TCE mass initially in the fracture was the same as in the previous cases. Following the 20-year equilibration period, the fracture was flushed at a Darcy velocity of 7.1 m/day, or a flow rate of 710 mL/day, corresponding to a hydraulic gradient of 0.01. The simulated fracture effluent is shown in Figure 4.3-26 for a case with no TCE degradation (white squares), and in Figure 4.3-27 for a case with TCE degradation (white squares). Here, the larger rate of flushing leads to a

more rapid depletion of the TCE mass in the clay, and the curves begin to drop after about 1 year. Although the decline in fracture concentration is more rapid in this case than it was for the 30 μm case, the time scale for achieving regulatory limits in the fracture is still on the order of 1,000 years for the case without any TCE degradation. As would be expected, including TCE degradation speeds up this process, and the fracture concentration drops below 1 μg/L at about 150 years.

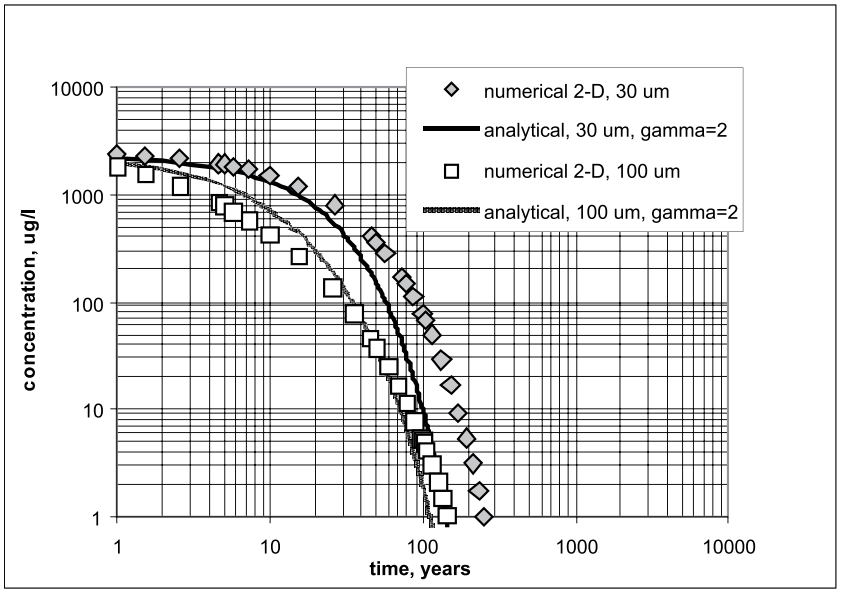

Figure 4.3-27. TCE concentration in the fracture effluent for the 30 μm and 100 μm fractures. The dissolved TCE has an aqueous phase half-life of 10 years in the clay matrix and the f_{oc} = 0.002 (Falta, 2005).

4.3.3.4 Monte Carlo simulations of source behavior with remediation

Addressing the benefit of DNAPL source remediation effort on plume response is a difficult challenge due to the intrinsic complexities and uncertainties in the process and performance of these remediation efforts (Falta et al., 2005a, Falta, 2007). Uncertainties and variability in parameters arise from hydrological and biogeochemical properties (e.g., hydraulic conductivity), from the effects of remediation (fraction of source removal, effect of source removal on discharge, rate of natural or enhanced attenuation in plume), and from the site condition and history (size and timing of contaminant releases, discharge to groundwater).

Several three-dimensional multiphase numerical models of source zone behavior that account for these parameters have been developed (see Falta et al., 1992, 1995; Delshad et al., 1996). These codes have been useful for improving the understanding of the physical and chemical processes that control the contaminant fate, transport, and removal in the source zone. These models use the deterministic approach, taking a single value for each parameter (perhaps in each gridblock), leading to a single prediction of the system response. Typically, these are selected to be "best estimates" or sometimes "worst case values". In reality, the hydrogeologic, geochemical, and process parameters used in a model are either variable, uncertain, or both variable and uncertain. The deterministic model does not reflect the nature of overall uncertainty in a simulation. The best approach to capture this inherent uncertainty is probabilistic simulation (e.g., using the Monte Carlo method), in which the uncertain parameters are represented by probability density functions (PDFs), and the result itself is also represented by a probability distribution.

Predicting the effect of the source remediation on plume behavior also has been limited by the lack of tools that explicitly link source and plume remediation (Falta et al., 2005a, Falta, 2008). A new analytical model, called REMChlor, coupling source and plume remediation, was developed to evaluate the impact of source and plume remediation at a more generic and strategic level (Falta, 2008). This transport model is not specific to any remediation technology. The contaminant source remediation is simulated as a fractional

removal at a future time; plume remediation is modeled considering decay rates of parent and daughter compounds that are variable in space and time (Falta, 2008).

In the present work, the DNAPL source function from the new analytical transport code was linked to a commercial probabilistic simulation software (GoldSim, 2007). Probabilistic simulations were conducted to evaluate the influence of the uncertainty in parameters on the effectiveness of source remediation in terms of the source discharge.

Among several commercial packages, GoldSim software (GoldSim, 2007) was chosen to perform probabilistic simulations. GoldSim is widely used in the nuclear industry for conducting performance assessment calculations. The analytical FORTRAN code for the DNAPL source function, REMChlor, was linked to GoldSim through a dynamic link library (DLL) approach. The probabilistic simulation model was developed by solving Equations (4.3-6) and (4.3-7) analytically (see Falta et al., 2005a), and using that analytical solution as the simulation model in GoldSim.

The solution of Equation (4.3-7) with the power function (Equation 4.3-6) can be used to predict the time-dependent depletion of the source zone mass by dissolution. The time-dependent mass is then used in Equation (4.3-6) to calculate the time-dependent source discharge. This model can simulate a wide range of source responses to mass loss, and it can include effects of remediation (Falta et al., 2005a).

The input variables for the current probabilistic DNAPL source model include the initial source DNAPL mass ($M_{S,0}$), the initial average source concentration ($C_{J,0}$), the exponent of the power function (Γ, gamma) relating source strength to source mass, the source decay rate by processes in addition to dissolution (λ_S), the water flow rate through the source zone (Q), and the mass fraction (X) of the source removed by a source remediation effort. All of these input variables are uncertain, but the largest uncertainty is likely to be in the power function exponent, Γ, in the initial DNAPL source mass, $M_{S,0}$, and in the fraction of source removed by remediation, X.

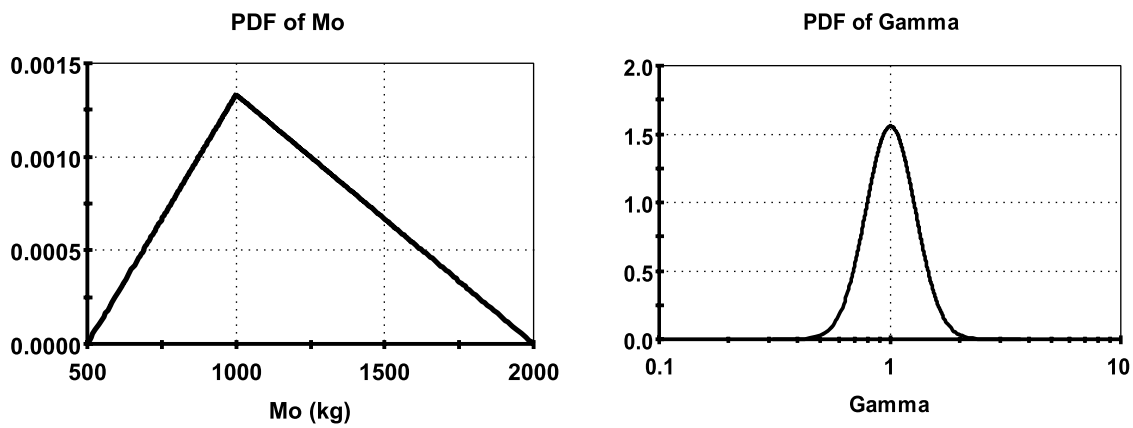

Figure 4.3-28. Two input probability distribution functions (without source remediation).

Two examples are given to illustrate the probabilistic DNAPL model. The first example is a probabilistic simulation using the DNAPL source function model, Equations (4.3-6) and (4.3-7) without any remediation effort (only natural rates of dissolution) for a hypothetical DNAPL site. The power function exponent was assumed to have a log-normal distribution with a mean value of 1, and a range between 0.5 and 2 for most values (Figure 4.3-28). The initial DNAPL source mass was treated as a stochastic variable, using a triangular PDF with a most likely value of 1000 kg, a minimum value of 500 kg, and a maximum value of 2000 kg (Figure 4.3-28). All of the other variables were held constant in this simulation (Table 4.3-5).

Table 4.3-5. Constant input parameters used in probabilistic simulation applications.

Input Parameter	Value
Averaged Initial Concentration	100 mg/L
Darcy Velocity	20 m/yr
X-section Area	30 m^2
Porosity	0.33
Source Decay Rate	0 1/yr
Time until Remediation	31 yr
Period of Remediation	0.5 yr

One thousand Monte Carlo deterministic runs were used to generate the time-dependent statistical results. Unlike a conventional deterministic simulation that only gives a single prediction of system behavior, the probabilistic simulation output shows the mean and ranges of possible system behavior (the time-dependent source concentration and mass discharge here) responding to the stochastic input variables (Γ and $M_{S,0}$). The overall source concentration (Figure 4.3-29) tends to drop gradually due to the natural dissolution, faster in the first 40 years and slower after that. Note that with an initial value of 100 mg/L, the source concentration after 100 years natural dissolution still remains at a mean value of about 1.2 mg/L.

Mass discharge leaving the source zone is linearly related to the source concentration so that it shows a similar trend as the source concentration. The initial mass discharge is 60 kg/yr and it gradually decreases to about a mean value of 0.8 kg/yr after 100 years of natural dissolution. This high source concentration and mass discharge may still result in a large dissolved plume zone.

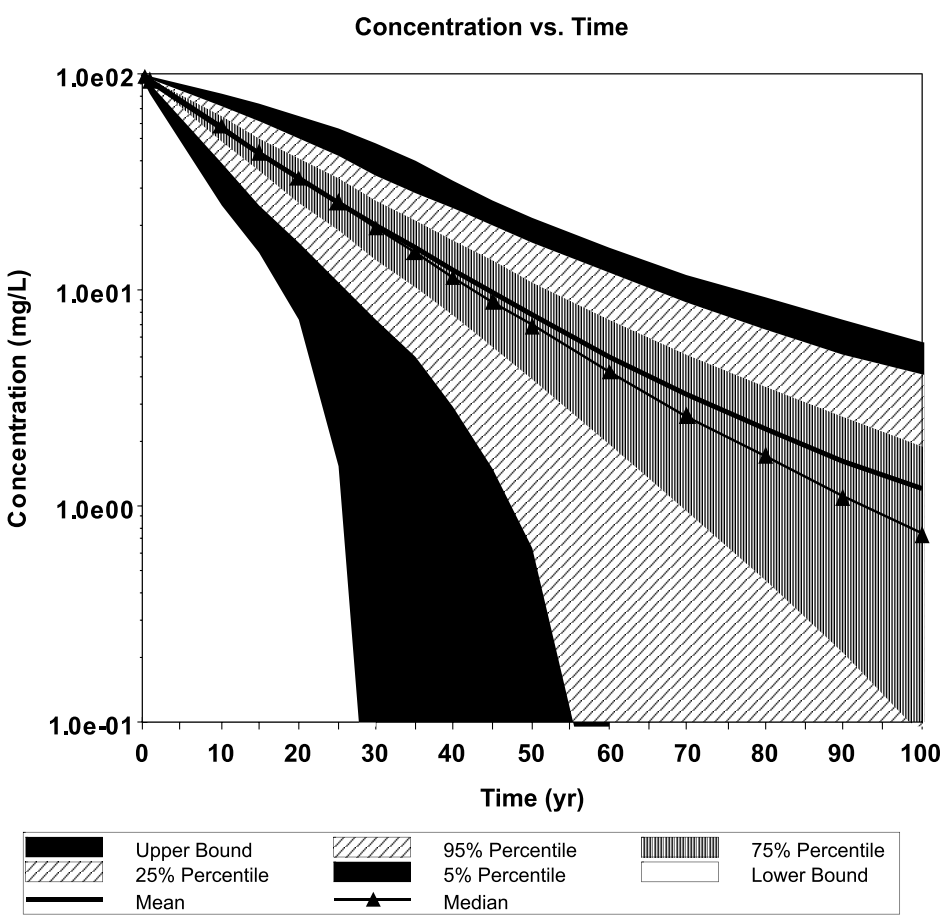

Figure 4.3-29. Probability simulation output of source concentration (without source remediation).

The second example is a probabilistic simulation using the DNAPL source function model with source remediation (see Falta et al., 2005a). Source remediation was assumed to be conducted at the 31st year after DNAPL release and lasted for a half year. In addition to two stochastic variables ($M_{S,0}$ and Γ) in the first example, the fraction of removed source mass, X, was also considered as a stochastic variable, using a triangular PDF with a most likely value of 80%, a minimum value of 60%, and a maximum value of 95% (Figure 4.3-30). All of the other variables were held constant as in the first example, and 1000 Monte Carlo deterministic runs were used to generate the time-dependent statistical results.

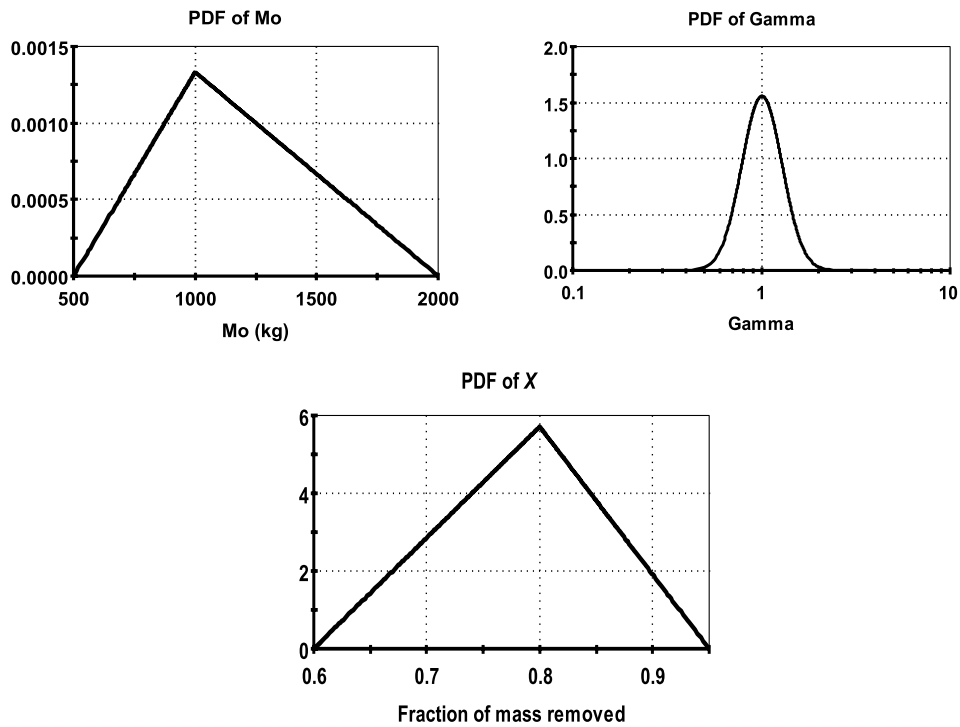

Figure 4.3-30. Three input probability distribution functions (with source remediation).

Again, the probabilistic simulation outputs show the mean and ranges of possible time-dependent source concentration and mass discharge responding to three stochastic input variables (Γ , $M_{S,0}$ and X). The overall source concentration range shows a similar gradual decrease in the first 31 years due to the natural dissolution (Figure 4.3-31). As the result of a half-year source remediation effort started at the 31st year, a sharp drop of concentration occurred in a short period of time. Following a half-year remediation effort, the mean value of the source concentration drops to 1.2 mg/L at the 53rd year and around 0.3 mg/L at the 100th year, respectively. The simulation result also indicates a decrease of uncertainty that is reflected by a narrower band of source concentration range.

Mass discharge leaving the source zone shows a similar trend as the source concentration. The mass discharge gradually drops in the first 31 years due to the natural dissolution process. A sharp drop of mass discharge then occurs in a short period of time after the source remediation effort. Following the half year remediation effort, the mean value of the mass discharge decreases to 0.8 kg/yr at the 53rd year and less than 0.2 kg/yr at the 100th year, respectively. Compared to the first example, the second example would result in a smaller dissolved plume zone due to the source remediation effort. The probabilistic simulation outputs for both examples show that the uncertainty in source concentration and discharge is increasing with increasing time.

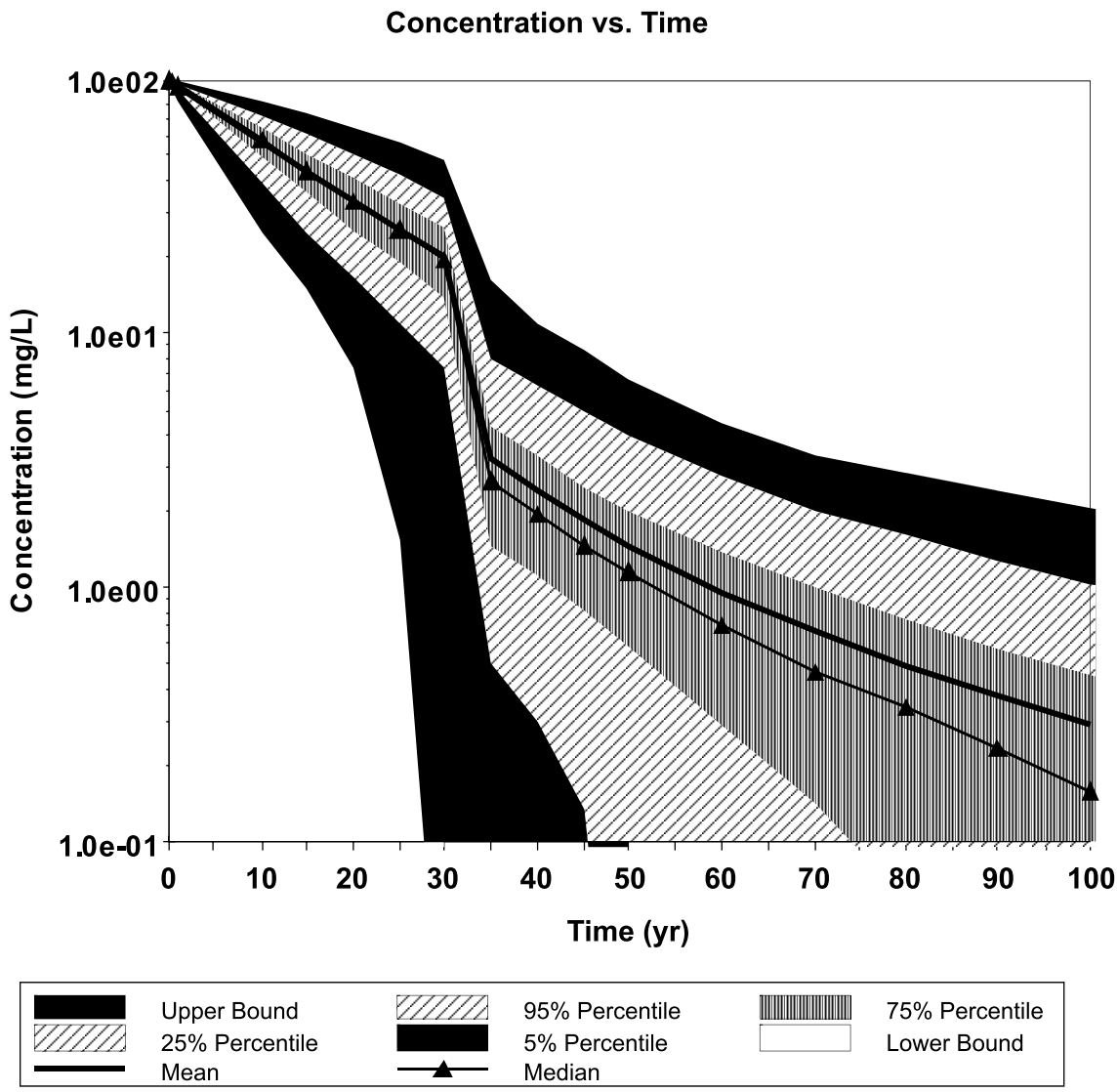

Figure 4.3-31. Probability simulation output of source concentration (with source remediation).

In summary, the GoldSim model is capable of performing the probabilistic simulation using the DNAPL source function model. It took less than a minute of computer time on a personal computer to run 1000 Monte Carlo realizations using the DNAPL source function model linked to GoldSim through a DLL approach.

Although only three stochastic input variables have been tested at this point, it is evident that this model can account for more uncertain variables, such as groundwater velocity, retardation factor, and plume decay rates. By using the full source and plume function model and considering all the uncertainties occurring during process and performance of DNAPL remediation efforts, probabilistic simulation can better predict the impact and benefit of source and plume remediation and form the basis for decisions regarding remediation alternatives.

4.3.3.5 Simplified contaminant source depletion models as analogs of multiphase simulators

Four simplified DNAPL source depletion models recently introduced in the literature are evaluated for the prediction of long-term effects of source depletion under natural gradient flow (Basu et al., 2008b). These models are simple in form (a power function equation is an example) but are shown here to serve as mathematical analogs to complex multiphase flow and transport simulators. The spill and subsequent

dissolution of DNAPLs was simulated in domains having different hydrologic characteristics (variance of the log conductivity field = 0.2, 1 and 3) using the multiphase flow and transport simulator UTCHEM. The dissolution profiles were fitted using four analytical models: the equilibrium streamtube model (ESM), the advection dispersion model (ADM), the power law model (PLM) and the Damkohler number model (DaM). All four models, though very different in their conceptualization, include two basic parameters that describe the mean DNAPL mass and the joint variability in the velocity and DNAPL distributions.

Three of the four source depletion models (ESM, ADM and PLM) can be expressed in a generalized form where the flux-averaged concentration exiting the source zone, C_J [M/L^3], can be related to a source depletion term, *SD*:

$$\frac{C_J(V_p)}{f_{c,0}C_s} = 1 - SD(V_p) \tag{4.3-57}$$

where C_s is the solubility of the DNAPL in groundwater [M/L^3], V_p is the number of pore volumes of natural flowing groundwater that have traversed the source zone, and the contaminated fraction, $f_{c,0}$, is the fraction of the streamlines initially containing DNAPL. The three models differ only in the formulation of *SD*. The DaM has a different form but simplifies to the PLM under specific conditions, as described in detail below.

The equilibrium streamtube model (ESM) is based on a Lagrangian approach where the DNAPL source zone is conceptualized as a collection of non-interacting streamtubes, with hydrodynamic and DNAPL heterogeneity represented by the variation of the travel time and DNAPL saturation among the streamtubes. Using the concept of reactive travel time, $SD(V_p)$ is equivalent to the cumulative distribution function of τ (Jawitz et al., 2005):

$$SD(V_p) = \frac{1}{2} + \frac{1}{2}\mathrm{erf}\left[\frac{\ln(V_p) - \mu_{\ln\tau}}{\sigma_{\ln\tau}\sqrt{2}}\right] \tag{4.3-58}$$

where $\mu_{\ln\tau}$ and $\sigma_{\ln\tau}$ are the mean and standard deviation of the log transformed variable $\ln\tau$. Equation (4.3-58) is appealing in that it is a compact analytical expression that can be employed in a spreadsheet type application to efficiently explore key system parameters that are frequently identified as playing a central role in the natural gradient depletion of a DNAPL source zone, including: the total DNAPL mass and the mean travel time (directly related to the first moment of $\hat{S}$ and t), the variability of the Lagrangian DNAPL architecture (related to the second moment of $\hat{S}$) and the variability of the velocity field (second moment of t). Further details of the ESM approach are presented in Jawitz et al. (2005). Here, we will use $\mu_{\ln\tau}$ and $\sigma_{\ln\tau}$ as fitting parameters to simulate the source depletion profile. Physically, $\mu_{\ln\tau}$ quantifies the mean of the combined hydrodynamic field and DNAPL architecture, while $\sigma_{\ln\tau}$ quantifies the variability of the two distributions (Jawitz et al., 2005).

Jury and Roth (1990), among others, have demonstrated the mathematical similarity of the advection dispersion equation and the lognormal travel time distribution. An alternative to representing $SD(V_p)$ as the cumulative distribution function of the lognormal variable τ would then be the dimensionless analytical solution for the advection dispersion equation (continuous injection; injection and detection in flux) given by (Kreft and Zuber, 1978):

$$SD(V_p) = \frac{1}{2}erfc\left[\sqrt{\frac{P}{4RV_p}}(R - V_p)\right] + \frac{1}{2}\exp(P)erfc\left[\sqrt{\frac{P}{4RV_p}}(R + V_p)\right] \tag{4.3-59}$$

where P is the Peclet number and R is the retardation coefficient. The Peclet number is used here in a manner analogous to $\sigma_{\ln\tau}$ in the ESM, functioning as a variability index to describe the combined effects of hydrodynamics and DNAPL architecture. The retardation factor, R , is used to describe the total mass of DNAPL in the source zone in a manner similar to $\mu_{\ln\tau}$. Note that R represents the DNAPL mass in the contaminated zone and can be converted to a total-domain retardation using f_c , as described in Jawitz et al., 2003.

Power law source depletion models have recently been presented by Zhu and Sykes (2004) and Falta et al. (2005a). The concept behind the PLM is to relate C_f to changes in DNAPL mass though an empirical variability index. Such models can be generalized as:

$$SD(V_p) = 1 - \left[\frac{M_S(V_p)}{M_{S,o}} \right]^{\beta_P} \tag{4.3-60}$$

where $M(V_p)$ is the DNAPL mass in the source zone after V_p pore volumes of flow, $M_{S,0}$ is the initial DNAPL mass in the source zone, and β_P is an empirical index that is a function of the variability of both the DNAPL distribution and the permeability field. Combining equations (4.3-57) and (4.3-60), C_J can be expressed as:

$$C_J(V_p) = f_c C_s \left[\frac{M_S(V_p)}{M_{S,o}} \right]^{\beta_P} \tag{4.3-61}$$

The parameter β_P is similar to the variability parameter $\sigma_{\ln \tau}$ in the ESM and increases with increasing domain heterogeneity (Falta et al., 2005a).

Parker and Park (2004) presented a simplified model for estimating DNAPL source zone depletion based on the concept of an effective Damkohler number *Da*:

$$\frac{C_J(V_p)}{C_s} = 1 - \exp\left[-Da\right] \tag{4.3-62}$$

Here, $Da = \kappa_{eff} L_S / \overline{q}$ where κ_{eff} [T^{-1}] is the field-scale effective mass transfer coefficient, L_s is the source zone length in the mean flow direction, and $\overline{q}$ [LT^{-1}] is the average Darcy flux for the source zone. The form of this equation is slightly different from the previous three models and thus $C_J(V_p)$ cannot be expressed in terms of $SD(V_p)$. The effective mass transfer coefficient (κ_{eff}), is related to changes in the DNAPL mass and the average groundwater velocity (Parker and Park, 2004):

$$\kappa_{eff} = \kappa_o \left(\frac{\overline{q}}{\overline{K}_s} \right)^{\beta_1} \left(\frac{M(V_p)}{M_o} \right)^{\beta_2} \tag{4.3-63}$$

where $\overline{K}_S$ [LT^{-1}] is the average saturated hydraulic conductivity of the source zone, and κ_0 [T^{-1}], β_1, and β_2 are empirical fitting parameters. The parameter β_1 describes rate limited dissolution that is neglected in the other models. For all values of β_1 except 1 the flux-averaged concentration exiting the source zone is a function of the Darcy flux, indicating that changes in contact time between the advecting groundwater and the DNAPL phase result in rate limiting effects. The "mass depletion exponent" β_2 is related to the groundwater velocity distribution, the DNAPL geometry, and the correlation between the two (Parker and Park, 2004).

The ESM, ADM, PLM, and DaM were evaluated for their ability to serve as mathematical analogs to simulations conducted using the multiphase flow and transport simulator UTCHEM (Delshad et al., 1996) over a range of hydraulic conductivity field variances ($\sigma^2_{\ln \varepsilon}$). The 2-D model domain was 30 m long (*x*-direction) and 10 m deep (*z*-direction) with 60 cells along the *x*-direction and 125 cells along the *z*-direction. The parameters used in the UTCHEM simulations were selected to represent typical values, consistent with recent numerical simulations of multiphase flow and transport. After the DNAPL spill, the dissolution process was initiated through a pair of fully-screened injection and extraction wells at the left and right boundaries. The dissolution kinetics of the DNAPL were evaluated under both equilibrium and rate-limiting conditions. The effect of non-equilibrium dissolution was implemented using a mass transfer coefficient described by the power law model of Miller et al. (1990).

DNAPL distributions are presented in Figure 4.3-32 for spills in two of the four realizations from each of the three simulation sets. Low variability in the permeability field ($\sigma^2_{\ln \varepsilon}$ = 0.2) led to relatively uniform

DNAPL architecture with the potential of greater pooling at the underlying capillary barrier (no flow boundary in the numerical simulations). As the variability of the permeability field increased, the total penetration depth decreased, leading to a DNAPL architecture that was more dominated by 'pools'. Another interesting feature is the difference in DNAPL architectures in different realizations of random fields with the same geostatistical parameters. These differences are more pronounced for domains with greater heterogeneity (Figure 4.3-32). DNAPL spill simulations are very sensitive to local permeability contrasts and thus, very different spill scenarios may sometimes be created in domains having the same $\sigma^2_{\ln \varepsilon}$.

The UTCHEM dissolution profiles were fitted using Equations (4.3-57) and (4.3-58) for the ESM, (4.3-57) and (4.3-59) for the ADM, (4.3-61) for the PLM, and (4.3-62) and (4.3-63) for the DaM. The fraction contaminated f_c in the ESM, ADM and PLM is the ratio between the initial flux-averaged concentration $C_J(V_p)$ and the aqueous solubility of the DNAPL C_s. The rate-limiting parameter β_1 in the DaM was assumed to be equal to 1 since local-scale mass transfer was not found to significantly affect the dissolution profiles. Fitting parameter values were obtained by fitting the UTCHEM simulation results to the four source depletion models using the normalized root mean square deviation (NRMSD, Jawitz et al. 2003) as the objective function for regression.

All four models (except the power function model for simulation set 1) provided reasonable fits (based on visual inspection and low NRMSD values) of the UTCHEM-generated dissolution data. For illustration, UTCHEM-generated dissolution profiles are compared to ESM, PLM and DaM fits in Figure 4.3-33. Since ADM fits were very similar to the ESM fits, they have not been shown in the figure. The good fits suggest that these simplified source depletion models can describe the dissolution behavior from DNAPL spills generated by sophisticated numerical simulators such as UTCHEM.

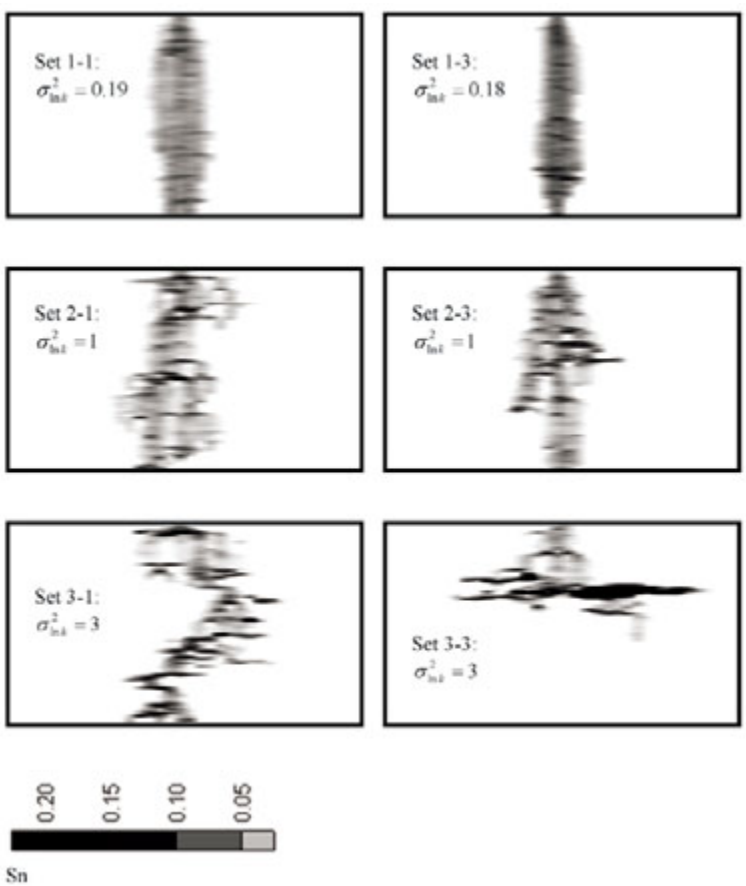

Figure 4.3-32. DNAPL spills for six representative cases. Note that $x < 7$ m and $x > 23$ m are cropped from the figures to focus on the DNAPL (Basu et al., 2008b).

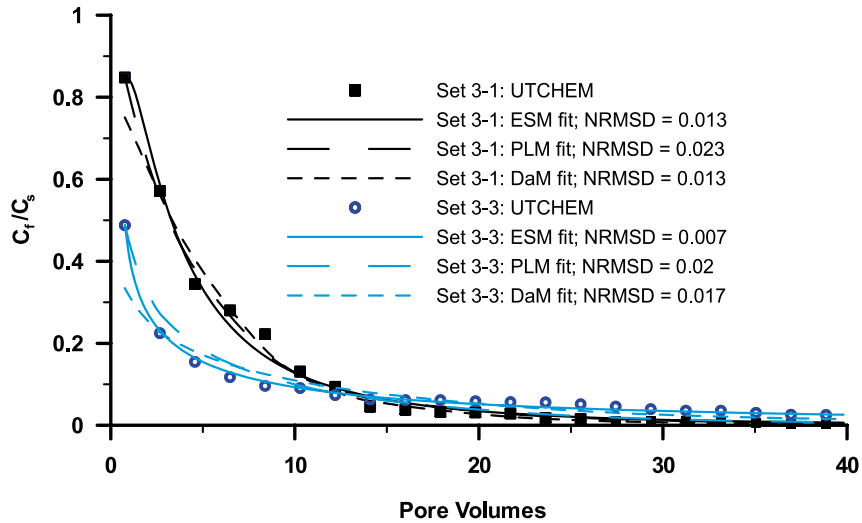

Figure 4.3-33. UTCHEM-generated dissolution profiles (symbols) and corresponding model fits for simulation realizations 3-1 and 3-3 ($\sigma^2_{\ln\varepsilon}$ =3) (Basu et al., 2008b).

The ESM, ADM and DaM fits resulted in similar NRMSD values. The ESM and ADM fits were approximately equal which is consistent with the observations made by Jury and Roth (1990) regarding the mathematical similarity of the advection dispersion equation and the lognormal distribution. The single-parameter PLM failed to capture the dissolution profile shapes as well as the other three models, especially for the low heterogeneity cases.

The dissolution profiles were integrated to examine the relationship between mass reduction $R_M(V_p)$ and flux reduction $R_J(V_p)$ (Figure 4.3-34). Flux reduction is defined as $1 - C_J(V_p)/C_J(0)$ and mass reduction is similarly defined as $1 - M_S(V_p)/M_S(0)$ where $M_S(V_p)$ is integrated from the dissolution profile. The results from the source depletion models compared well to those from UTCHEM, indicating that the simplified models not only captured the dissolution behavior, but also the integrated mass reduction–flux reduction ($R_J(R_M)$) relationships. As described by Jawitz et al. (2005), in addition to the media and DNAPL heterogeneity, the $R_J(R_M)$ relationship is also a function of the parameter λ, which is the product of the ratio of DNAPL density to its aqueous solubility C_w and the mean DNAPL content in the domain. In the present set of simulations λ is approximately equal to 5, which is close to the λ = 3 used to generate Figure 2 of Jawitz et al. (2005). Thus the R_J, (R_M) curves in Figure 4.3-34 and those presented by Jawitz et al. (2005) are similar.

The simplified models are conceptually appealing as the Eulerian point-by-point variability in permeability and DNAPL in thousands of grid blocks can be integrated into only 1, 2 or 3 parameters and yield very similar results. The models, though very different in their conceptualization, have certain basic similarities. Three of the four models (ESM, ADM and PLM) could be described by a general equation (Equation 4.3-57) with a parameter f_c describing the relationship between the DNAPL solubility and the source zone concentration at the onset of dissolution. An important difference between the ESM and the other three models is the specificity with which the velocity and DNAPL distributions are described. In the ESM, variability in velocity and DNAPL saturation along a single streamtube are integrated and transformed into an effective value (reactive travel time τ) for the individual streamtube, with the variability of this distribution controlling dissolution behavior. In the other models, the variability in velocity and DNAPL saturation is integrated not just along the individual streamtube, but into an effective parameter (P, β_P, β_2) for the entire source zone.

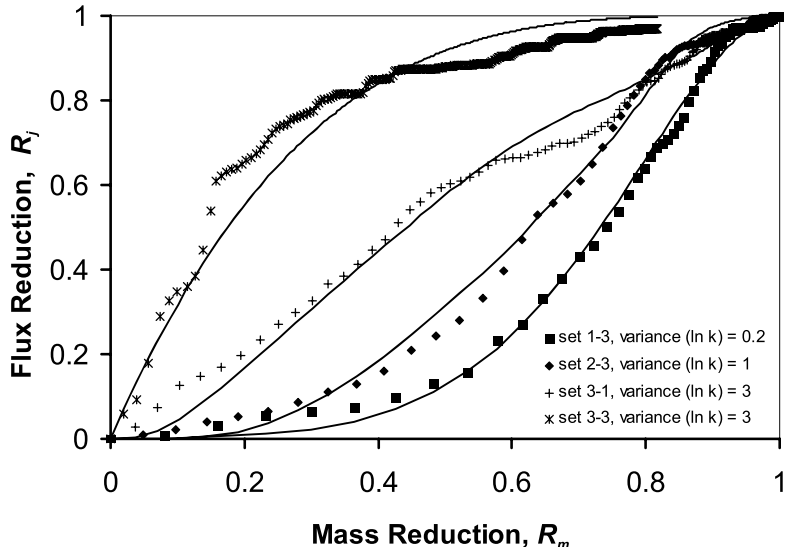

Figure 4.3-34. UTCHEM-generated mass reduction-flux reduction profiles (symbols) compared with DaM (Set 1-3), ESM (Set 2-3), ESM (Set 3-1),and PLM (Set 3-3) fits (lines) to the dissolution profile (Basu et al., 2008b).

One of the objectives of this study was to compare the four source depletion models in terms of their ability to describe UTCHEM-generated dissolution profiles. Three of the four models (ESM, ADM and DaM) resulted in similar fits. The single-parameter PLM failed to capture the dissolution behavior as well as the other three models, especially for the low-heterogeneity cases. In addition to the fitting parameters, the PLM and DaM also require information on the breakthrough curve that is integrated to calculate $M_S(V_p)/M_{S,0}$. This information is not required in the ESM and ADM.

The physical interpretations of the fitted parameters can be broadly summarized as parameters that describe the characteristics of the travel time and the DNAPL saturation distribution. In the ESM, the parameter $\sigma^2_{\ln\tau}$ describes the variability in the travel time and the DNAPL saturation distribution, while the parameter $\mu_{\ln\tau}$ describes the mean values. In the ADM, P describes the variability in the travel time and the DNAPL saturation distributions, while R describes the DNAPL mass in the contaminated zone. In PLM and DaM, the parameters β_P and β_2 describe the variability of the DNAPL saturation distribution. The parameter κ_0 in the DaM is analogous to f_c in the other three models. The DaM has a third parameter β_1 that accounts for rate limited dissolution that is neglected in the other models presented in this paper. Note that a modification of the ESM was proposed by Jawitz et al. (2005) that accounted for rate-limited effects.

The challenge now lies in estimation of the model parameters at the field scale. Parker and Park (2004) proposed that the models can be calibrated to measured source zone mass flux over time. This requires detailed flux characterization over the entire source depletion history, which is impossible at most field sites. Models calibrated for shorter time spans will not be able to capture the entire dissolution behavior. In any case, *a priori* estimation of the model parameters is preferred to requiring dependence on the measured dissolution profile.

Christ et al. (2006) proposed the use of the ganglia-to-pool (GTP) ratio for calibrating the DaM by establishing an empirical relationship between GTP and the mass transfer coefficient. However, techniques for determining the initial GTP ratio at the field scale have not yet been established. Jawitz et al. (2003, 2005) proposed the use of non-reactive and reactive tracers to describe aquifer heterogeneity and DNAPL architecture in terms of ESM parameters that could be used to forecast remedial performance. These authors presented theoretical arguments and limited field evidence in support of this approach, and Fure et al. (2006) presented laboratory data that also supported the ESM. However comprehensive validation of the ability of tracer-determined ESM parameters to predict remedial performance remains for future work.

4.3.3.6 Temporal evolution of DNAPL source and contaminant flux architecture

The objective of this study was to investigate the impact of DNAPL source mass depletion on the alteration of the contaminant flux [J (y,z,t)] distribution at the control plane (CP) (Basu et al., 2008a). Contaminant mass discharge (M_D ; local flux values integrated over the source CP) and flux distribution act as the key linkages for understanding the relationship between source mass depletion and plume dynamics (EPA, 2003). Simulation results from two separate numerical studies and CP flux monitoring data from a source depletion field study at Hill Air Force Base, Utah (Brooks et al., 2008) were used for the present analysis. Model outputs were examined to determine the temporal evolution of the population statistics (mean, variance, coefficient of variation) and the spatial structure (centroid, first and second moments and variograms) of source mass and contaminant fluxes. The associated changes in trajectory-integrated DNAPL content ($\hat{S}$) (Jawitz et al., 2005) were also investigated to link source depletion to flux changes.

Groundwater flow and contaminant transport were simulated in three-dimensional, heterogeneous, random, spatially correlated permeability ε fields with emplaced DNAPL sources. Two different sets of simulations were analyzed for this study: Set 1 was done using the numerical code ISCO3D (Zhang and Schwartz, 2000), while Set 2 was done using the code T2VOC (Falta et al., 1995). These two sets of simulations were also different in terms of flow-domain configurations, mass-transfer assumptions, and boundary conditions. Attributes of the simulated DNAPL source zones are presented in Table 4.3-6. The objective behind presenting such different scenarios was to demonstrate that the resulting observations were not a function of the assumptions of the domain characteristics or the flow and transport model used.

Table 4.3-6. Attributes of the simulated DNAPL source zones used in the numerical simulations.

Set 1: Domain 1	• Mean intrinsic permeability $\mu_\varepsilon = 9.7 \times 10^{-13}$ m^2	Case 1	• $\sigma^2_{\ln\varepsilon} = 1$
	• Domain dimensions 3 m × 0.49 m × 0.98 m (nx = 43, ny = 7; nz = 14)		• S_N and ε positively correlated $\ln(S_N) = \ln(\varepsilon) + 26.2$, (ε in m^2; $S_{N,max} = 0.15$)
	• Correlation lengths $\xi_x = 0.7$ m, $\xi_y = 0.07$ m, $\xi_z = 0.07$ m		• *DNAPL mass M* = 2.36 kg
	• Darcy flux q = 5.4 cm/day	Case 2	• $\sigma^2_{\ln\varepsilon} = 2.45$
			• S_N and ε positively correlated $\ln(S_N) = \ln(\varepsilon) + 23.6$, (ε in m^2 ; $S_{N,max} = 0.15$)
			• DNAPL mass M = 2.36 kg
		Case 3	• $\sigma^2_{\ln\varepsilon} = 1$
			• Binary distribution of S_N (S_N = 0.15 and 0.5)
			• DNAPL mass M = 12.3 kg
Set 2: Domain 2	• Mean intrinsic permeability $\mu_\varepsilon = 2 \times 10^{-12}$ m^2	Case 1	• $\sigma^2_{\ln\varepsilon} = 2.45$
	• Domain dimensions 30 m × 30 m × 15 m ($nx = ny$ = 20, nz = 25)		• S_N and ε positively correlated $\ln(S_N) = \ln(\varepsilon) + 23.2$, (ε in m^2; $S_{N,max} = 0.17$)
	• Correlation lengths $\xi_x = 30$ m, $\xi_y = 10$ m, $\xi_z = 1$ m		• DNAPL mass M = 1950 kg
	• Darcy flux q = 0.6 cm/day	Case 2	• $\sigma^2_{\ln\varepsilon} = 2.45$
			• S_N and ε negatively correlated $\ln(S) = -\ln(\varepsilon) - 31.7$, (ε in m^2 ; $S_{N,max} = 0.09$)
			• DNAPL mass M = 826 kg

Dissolution of DNAPL source mass during groundwater flow was simulated using ISCO3D (Domain 1) and T2VOC (Domain 2) codes. Simulated, time-varying DNAPL content and contaminant flux distributions at the outflow control plane during mass depletion were analyzed to study the effects of source depletion on contaminant flux (J) distribution. In addition, passive flux meter (PFM) data were used to evaluate the impact of source mass depletion on the evolution of *CP* flux distribution at operable unit 2 (OU2), Hill Air Force Base, Utah. These PFM data had horizontal and vertical resolutions of 3 m and ~25 cm, respectively.

The initial values for the mean, standard deviation and the coefficient of variation (CV) of the contaminant flux distribution (J), and the DNAPL distribution (S_N) within the domain for the simulated cases are presented in Table 4.3-7. The higher value of (CV_{S_n}) relative to CV_J is attributed to the sparse distribution of the DNAPL within the source zone, with certain regions having no DNAPL and other regions at residual saturation (see Feenstra and Cherry, 1996; Meinardus et al., 2002). An evaluation of population statistics for J and S_N distributions as a function of increasing source mass removal showed that the CV of the S_N distribution increased with time, while that of the J distribution oscillated but remained relatively constant. The relatively constant CV_J at the source *CP* is an interesting feature and was thus investigated for all five cases (Table 4.3-6). Since the initial CV_J for the domains are different, we normalized the data by plotting the relative reductions in the mean contaminant flux (R_μ) and the flux standard deviation (R_σ):

$$R_\mu = \frac{\mu_i - \mu_t}{\mu_i} \tag{4.3-64}$$

$$R_\sigma = \frac{\sigma_i - \sigma_t}{\sigma_i} \tag{4.3-65}$$

Where μ_i and σ_i are the initial mean and standard deviation of the distribution, while μ_t and σ_t are the mean and standard deviation of the distribution at time t. The results from simulations for all cases are plotted in Figure 4.3-35. All data sets indicate a 1:1 relationship between R_μ and R_σ, indicating a constant coefficient of variation. For the cases we examined, the relationship thus appears to be independent of the hydrodynamic heterogeneity as well as the correlation structure between the DNAPL and the permeability field.

Consistent with the numerical simulations, the TCE flux data from the Hill AFB field study (Brooks et al., 2008), also suggest that source mass depletion led to a proportional reduction in the mean and standard deviation of the J distribution, and thus, a temporally constant CV_J (Figure 4.3-35). However, it should be noted that to claim temporal stability based only on measurements at three points in time is difficult. Field studies are needed to characterize the complete evolution with time of the contaminant flux distribution at DNAPL source CPs.

Table 4.3-7. Coefficient of variation (CV) of the Darcy flux (q), contaminant flux (J), and the DNAPL mass (S_N) distribution.

Distribution properties	**Domain I (ISCO3D)**			**Domain II (T2VOC)**	
	Case 1	**Case 2**	**Case 3**	**Case 1**	**Case 2**
Initial CV_q	0.6	1.7	0.6	1.7	1.7
Initial CV_J	0.7	1.7	0.7	4.6	4.8
Initial CV_{Sn}	7.0	6.4	6.4	8.6	11.8

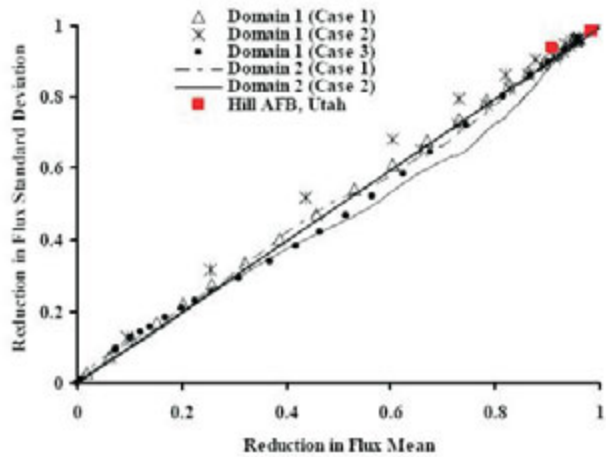

Figure 4.3-35. Relationship between the relative reductions in the mean and standard deviations of the contaminant flux (Basu et al., 2008a).

The evolution of the source distribution and the contaminant flux distribution at source CP were also investigated by examining the changes in spatial moments of S_N and J. The first normalized moments define location of the centroid, while the second centralized moments indicate the spread of the distribution about the centroid. Physically, these two parameters give an indication of the mean location of the 'hotspot' and its spatial extent. For the trajectory of the centroid, we focused on the T2VOC simulations instead of ISCO3D because (1) of the larger spatial dimensions of the flow domain, and (2) alternative DNAPL saturation distributions available based on positive or negative permeability (ε) vs. S_N correlation.

The loci of the centroid of the contaminant flux distributions are shown alongside the projection of the loci of the DNAPL distributions at the source *CP* (Figure 4.3-36). The Darcy flux (q) distribution at the same *CP* is superimposed on this plot to enable a comparison between centroids of J and up-gradient DNAPL mass. As DNAPL mass is depleted, the centroid of the DNAPL distribution shifts from the high ε to the low-ε zones because of the extended timelines required for DNAPL mass removal from those regions (Figure 4.3-36). For the positively correlated case, there was a larger amount of DNAPL mass at the bottom of the domain and thus, the centroid moves in that direction, while for the negatively correlated case, there was more DNAPL mass at the top causing the centroid to shift upwards.

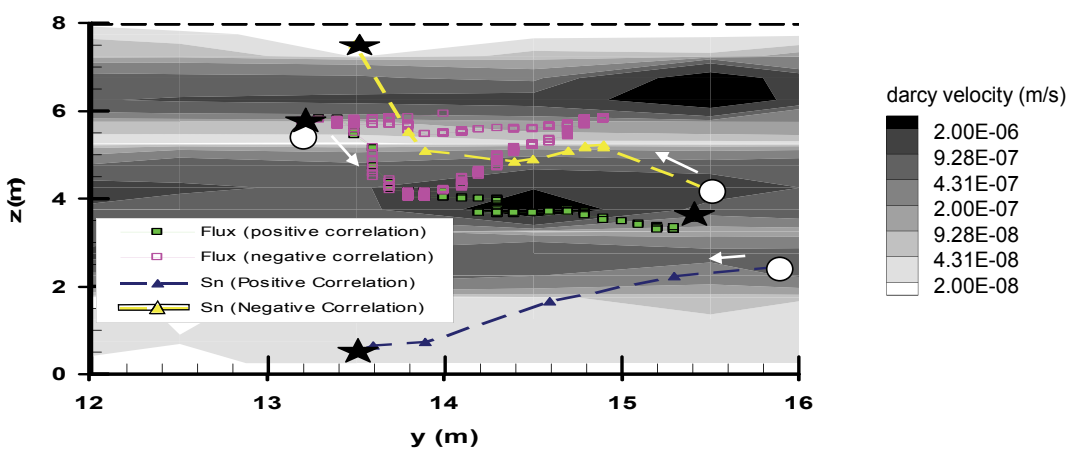

Figure 4.3-36. Locus of the Centroid of the DNAPL and contaminant flux distributions (at the source control plane) in Domain 2 (white circles indicate the initial location of the centroid and black stars denote their final location). Note that: (1) only the section of the domain below the water table is shown in the figure; (2) the initial location of the centroid of the contaminant flux distribution is the same in the positive and negative correlation cases (Basu et al., 2008a).

The second centralized spatial moments about the center of mass (σ^2_{xx} , σ^2_{yy} , σ^2_{zz}) are a measure of the spread of the S_N distribution along the x, y and z axes, respectively. Three example cases, Case 1 in Domain 1 (Figure 4.3-37a) and Cases 2 and 3 in Domain 2 (Figure 4.3-37b), are presented to show the temporal evolution of the spreads of the DNAPL and the contaminant flux distributions. The other simulations exhibited similar behavior (data not shown). These results support the previous hypotheses regarding the approximately time-invariant nature of the contaminant flux distribution. The spreads of the flux distribution were less variable in time than those of the DNAPL distribution, indicating again the greater stability of the *J* distribution (Figure 4.3-37b).

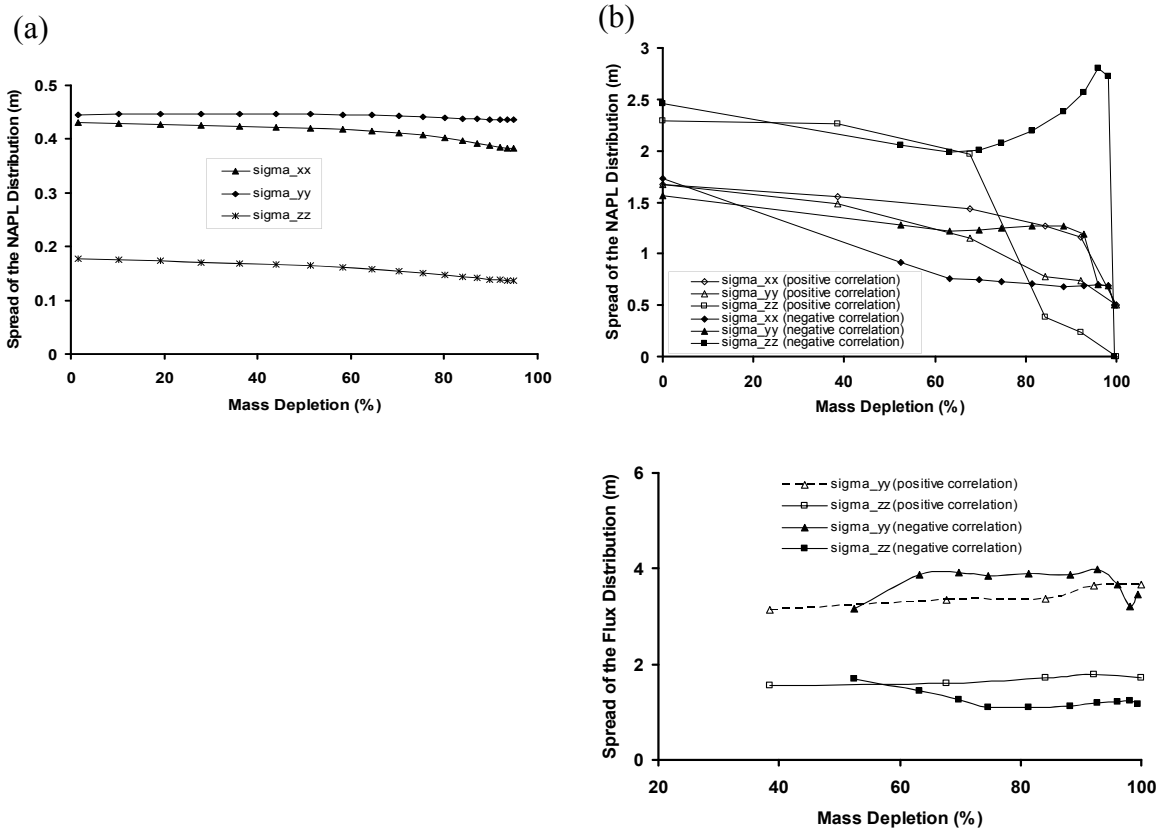

Figure 4.3-37. Spatial variance of the DNAPL and contaminant flux distributions in (a) Domain 1, Case 1 (ISCO3D), and (b) Domain 2, Cases 1 and 2 (T2VOC). Note that the spreads of the flux distributions have been plotted after flushing about one pore volume through the domain such that the fluxes at the exit control plane are reflective of the source conditions (Basu et al., 2008a).

This study shows that both the mean (μ) and the standard deviation (σ) of the contaminant flux distribution at the source *CP* decreases with source mass reduction. Moreover, μ and σ decrease proportionally, resulting in a coefficient of variation that appears to be essentially constant in time. The spatial moments of the contaminant flux distribution appear to be also essentially constant in time, indicating that – for DNAPL source zones cleaned up through in-situ flushing – the contaminant flux distribution remains stable throughout the DNAPL mass depletion process while the flux magnitude gradually fades away with time.

It should be noted, however, that these conclusions are preliminary. Rigorous investigations that account for spill scenarios, different remedial alternatives and flow configurations are required prior to generalization and subsequent application of these results. More importantly, field studies that characterize the temporal evolution of the source and flux distribution need to be conducted.

4.3.3.7 Predicting DNAPL dissolution using a simplified source depletion model parameterized with partitioning tracers

Simulations of non-partitioning and partitioning tracers were used to parameterize the equilibrium streamtube model (ESM) that predicts the dissolution dynamics of DNAPLs as a function of the Lagrangian properties of DNAPL source zones (Basu et al., 2008c). Lagrangian, or streamtube-based, approaches characterize source zones with as few as two trajectory-integrated parameters, in contrast to the potentially thousands of parameters required to describe the point-by-point variability in permeability and DNAPL in traditional Eulerian modeling approaches. The spill and subsequent dissolution of DNAPLs was simulated in two-dimensional domains having different hydrologic characteristics using the multiphase flow and transport simulator UTCHEM. Simulations were conducted with log conductivity variances $\sigma^2_{\ln\varepsilon}$ = {0.2, 1, 3} to evaluate a range of field scenarios. A set of simulations comprised of four realizations was run for each value of $\sigma^2_{\ln\varepsilon}$. Non-partitioning and partitioning tracers were used to characterize the Lagrangian properties (non-reactive travel time (t) and trajectory-integrated DNAPL content ($\hat{S}$) statistics) of DNAPL source zones, which were in turn shown to be sufficient for accurate prediction of source dissolution behavior using the ESM throughout the relatively broad range of hydraulic conductivity variances tested here.

Tracer BTCs were found to be closely matched by lognormal distributions generated using $\mu_{\ln t}$ and $\sigma_{\ln t}$ determined from the tracer moments (Figure 4.3-38.), suggesting that the assumption of log-normality for the non-reactive and reactive travel time distributions is reasonable.

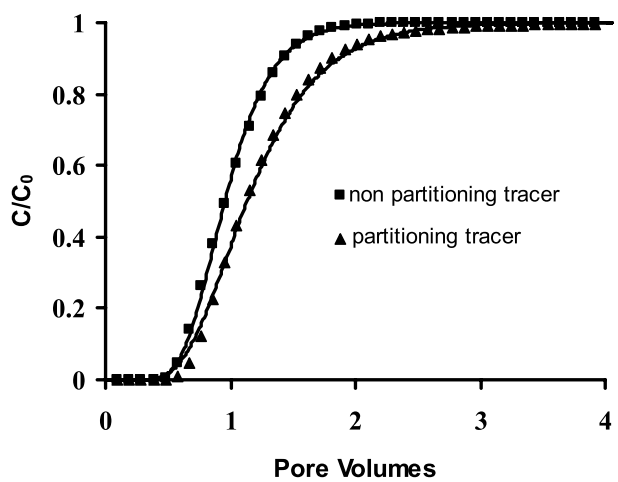

Figure 4.3-38. Non-partitioning and partitioning tracer data for simulation set 2-4. Symbols represent UTCHEM output while solid lines represent lognormal fits (Basu et al., 2008c).

The reactive travel times (distribution parameters, determined from t and $\hat{S}$ distributions ($\tau = Nt\hat{S}$, where N is the ratio of the DNAPL density to aqueous solubility)), were used to predict the DNAPL dissolution profile using the ESM. The UTCHEM-generated dissolution profile is shown along with the tracer-based ESM predicted profile for an example realization from each of the three simulation sets in Figure 4.3-39. In these simulations, $t = 0$ is defined as the time at which the contaminant peak arrives at the exit control plane (x = 30 m). The ESM accurately predicted the dissolution dynamics at the source control plane with average normalized root mean square deviation (NRMSD) values of 0.022, 0.025, and 0.027 for $\sigma^2_{\ln\varepsilon}$ = 0.2, 1, and 3, respectively.

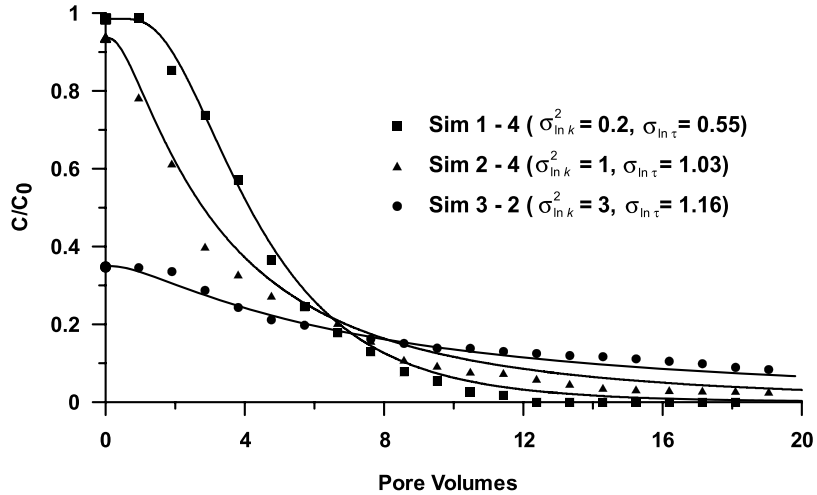

Figure 4.3-39. ESM-predicted and UTCHEM-generated dissolution profiles for simulation sets 1-4, 2-4, and 3-2. Symbols represent UTCHEM output while solid lines represent predictions (Basu et al., 2008c).

The predicted dissolution profiles were integrated to examine the relationship between mass reduction R_M and flux reduction R_J (Figure 4.3-40). Flux reduction is defined as $1 - C_J(t)/C_J(t=0)$ and mass reduction is similarly defined as $1 - M_S(t)/M_S(t=0)$ where $C_J(t)$ is the flux-averaged concentration at the exit control plane at time t, and $M_S(t)$ is DNAPL mass in the source zone at time t. The predicted mass reduction–flux reduction profiles also matched the UTCHEM-simulated behavior well, with NRMSD values varying between 0.034 ($\sigma^2_{\ln \varepsilon}$ = 0.2) and 0.054 ($\sigma^2_{\ln \varepsilon}$ = 3).

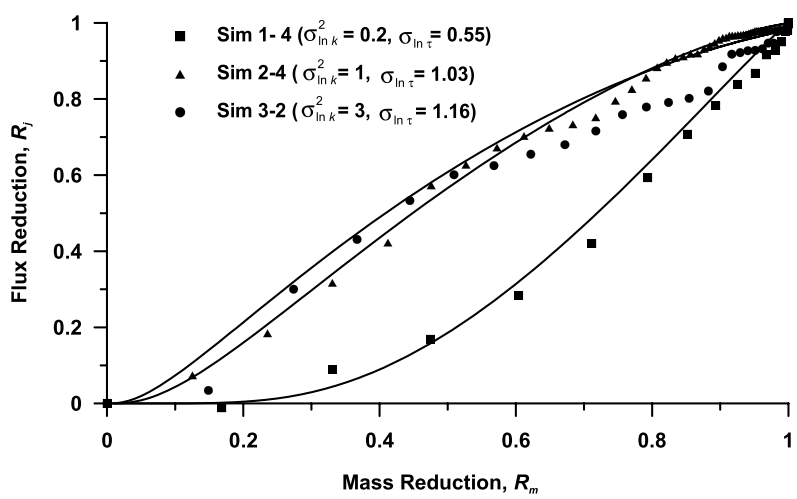

Figure 4.3-40. ESM-predicted and UTCHEM-generated mass reduction-flux reduction profiles for simulation sets 1-4, 2-4, and 3-2. Symbols represent UTCHEM output while solid lines represent predictions (Basu et al., 2008c).

Following Christ et al. (2006), the ganglia-to-pool ratio (GTP) was defined as the ratio of the DNAPL mass in cells with DNAPL saturation less than 15%, to the mass in cells with saturation greater than 15%. Based on the GTP ratio, the following up-scaled mass transfer model was proposed (Christ et al., 2006) for the prediction of flux-weighted concentration $C_f(T)$ from DNAPL source zones:

$$\frac{C_J(t)}{C_s} = 1 - \left(1 - \frac{C_J(t=0)}{C_s}\right)^{\left(\frac{M_S(t)}{M_S(t=0)}\right)^{\beta_G}} \tag{4.3-66}$$

where $\beta_G = 1.5\ GTP^{-0.26}$ and C_s is the aqueous solubility. The GTP correlation coefficient β_G was developed from simulations with GTP limited between 0.5 and 24. This model was used to predict the dissolution BTCs and the R_J (R_M) relationships for the simulations presented here; two example cases are presented in Figure 4.3-41. The model predicts a temporally constant aqueous flux for GTP equal to ∞ and was thus incapable of representing the dissolution dynamics for simulations 1-2 and 1-3 (Table 4.3-8). Within simulations where the GTP was within the prescribed range (simulation sets 2 and 3), the model proved to be a good predictor of dissolution dynamics in some cases (e.g., simulation 3-2, Figure 4.3-41); however for other cases (e.g., simulation 2-4, Figure 4.3-41) it was a relatively poor predictor of dissolution.

Table 4.3-8. Tracer-derived ESM parameters.

Simul-ation	Domain properties			Non-reactive tracer parameters		Partitioning tracer parameters		Reactive travel time distribution moments		Ganglia to pool ratio
	$\mu_{\ln \varepsilon}$	$\sigma^2_{\ln \varepsilon}$	$\overline{S}_N$	$\mu_{\ln t}$	$\sigma_{\ln t}$	$\mu_{\ln \hat{S}}$	$\sigma_{\ln \hat{S}}$	$\mu_{\ln \tau}$	$\sigma_{\ln \tau}$	
1-1	-6.85	0.19	0.00419	-0.01	0.17	-5.58	0.47	1.39	0.50	∞
1-2	-6.92	0.19	0.0033	-0.01	0.15	-5.90	0.61	1.09	0.63	∞
1-3	-6.92	0.18	0.0033	-0.01	0.17	-5.91	0.65	1.06	0.67	∞
1-4	-6.94	0.24	0.00446	-0.01	0.15	-5.55	0.55	1.44	0.55	∞
2-1	-5.62	1	0.00393	-0.06	0.33	-5.95	1.02	0.98	1.07	31.8
2-2	-5.62	1	0.00446	-0.06	0.34	-5.61	0.87	1.32	0.93	29.6
2-3	-5.62	1	0.00357	-0.08	0.40	-5.74	0.77	1.17	0.87	35.5
2-4	-5.62	1	0.00446	-0.05	0.31	-5.82	0.98	1.12	1.03	27.6
3-1	-5.62	3	0.00447	-0.15	0.54	-5.31	0.36	1.54	0.65	4.1
3-2	-5.62	3	0.00445	-0.19	0.62	-4.82	0.98	1.97	1.16	2.3
3-3	-5.62	3	0.00446	-0.20	0.63	-5.77	1.44	1.02	1.57	1.1
3-4	-5.62	3	0.00449	-0.17	0.58	-5.40	0.95	1.43	1.11	2.7

$\overline{S}_N$ = average NAPL saturation

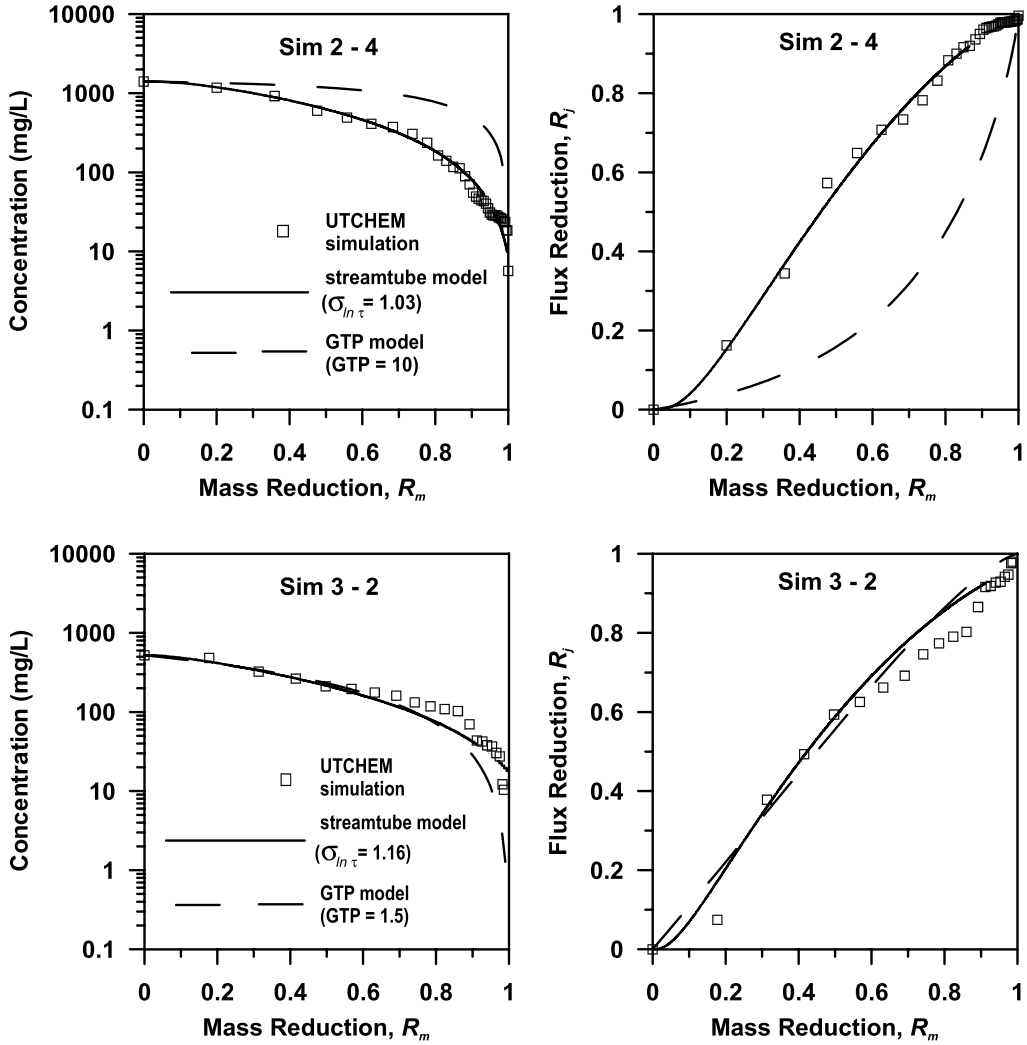

Figure 4.3-41. Comparison between the ESM and the GTP models for prediction of source dissolution behavior (Basu et al., 2008c).

Since the GTP ratio accounts for the population distribution of the NAPL but not its spatial structure, it is an incomplete descriptor of the DNAPL architecture. The Lagrangian description of the t and $\hat{S}$ distributions characterizes both the NAPL population distribution and spatial structure. No definite correlation was observed between GTP and $\sigma^2_{\ln \hat{S}}$ for the simulations presented here (Table 4.3-8). Finally, it is noted that it has not been determined how the GTP ratio would be measured at field sites (Christ et al., 2006).

In summary, the results were found to be relatively insensitive to travel time variability, suggesting that dissolution could be accurately predicted even if the travel time variance was only coarsely estimated. Estimation of the ESM parameters was also demonstrated using an approximate technique based on Eulerian data in the absence of tracer data; however determining the minimum amount of such data required remains for future work. Finally, the streamtube model was shown to be a more unique predictor of dissolution behavior than approaches based on the ganglia-to-pool model for source zone characterization.

5.0 Conclusions

The principal goal of this project was the development of tools by which to evaluate the impacts of partial DNAPL source removal. The research was based on the examination of contaminant flux responses to source zone treatment at DNAPL-contaminated sites. These field studies were supplemented with in-depth laboratory studies of the factors that control the relationship between DNAPL mass depletion and contaminant mass flux. Results from field and laboratory investigations were used to evaluate the performance of existing source remediation models and to develop new source and coupled source-plume simulators.

Results of the field, laboratory, and modeling investigations show that although response to DNAPL source treatment is dependent on a number of site specific factors (e.g., site hydrogeology, contaminant composition and architecture, remedial technology), significant contaminant flux reductions can be achieved at many sites by partial DNAPL removal. Modeling results suggest that as heterogeneity in aquifer properties and NAPL spatial distribution increases, less mass reduction is required to achieve a given flux reduction, although the overall source longevity may increase. In addition, early source treatment enhances risk reduction by decreasing contaminant discharge to the plume.

Contaminant mass flux and mass discharge data were collected before and after source treatment at four field sites. These data provide the first comprehensive field assessment of mass flux/discharge response to DNAPL source treatment. Three flux measurement techniques (transect method, passive flux meters and modified integral pump tests) were used. The MIPT employed in this study was based on published techniques and included concurrent pumping across a transect in conjunction with hydraulic head monitoring to provide a direct estimate of groundwater flux.

Mass discharge reductions of approximately 90% and 99% were observed at the Hill Air Force Base and Fort Lewis sites, respectively. Passive flux meter and MIPT test data exhibited comparable results for these sites. Less dramatic mass discharge reductions were seen at the Borden and Sages sites and significant differences were observed between measurement methods. Because the support volumes for these measurement techniques can be very different, heterogeneities in contaminant distribution and hydraulic properties could be responsible for these differences.

Relationships between contaminant architecture and mass flux were evaluated in the laboratory using 2-dimensional flow chambers. Contaminants were injected into the flow chambers to create DNAPL source zones and subsequent DNAPL mass depletion was accomplished by dissolution by aqueous, surfactant or cosolvent solutions, or by gas-phase sparging. Source strength function (relationship between DNAPL mass and contaminant mass flux) was observed to be primarily controlled by the DNAPL architecture which can be characterized by the trajectory integrated NAPL content distribution. Reactive and non-reactive tracer tests were used to estimate Lagrangian parameters (travel time and trajectory-integrated NAPL content statistics) required for predicting source dissolution behavior. These estimated parameters were used in the equilibrium streamtube model to accurately predict source dissolution.

The benefits of partial source zone remediation were evaluated from fundamental physical principles using numerical, Lagrangian and analytical approaches. Numerical models are based on the most detailed description of process behavior at the pore scale, but they are computationally intensive and require information on spatially variable parameters that are difficult to characterize with reasonable accuracy using available technologies. Though it may be difficult to calibrate these models to specific field sites, they nonetheless help improve our understanding of behavior of DNAPL sources and plumes from a process standpoint. Numerical models were used in this study to simulate laboratory and field source treatment experiments and demonstrations. Both laboratory and pilot-scale field tests of air sparging for DNAPL removal were simulated using TMVOC, a multi-component compositional multiphase flow simulator;

and a field pilot study of cosolvent flushing was simulated using UTCHEM, also a multi-component compositional multiphase flow simulator.

The Lagrangian models offer the only practical techniques currently available for predicting site specific mass removal/mass flux relationships. These models describe the source zone as a collection of non-interacting streamtubes with hydrodynamic and DNAPL heterogeneity represented by variations in travel time and trajectory-integrated DNAPL saturations within the streamtubes. Lagrangian models were used to estimate contaminant elution curves from laboratory and field pilot-scale in-situ flushing tests. Results suggest that this modeling approach can predict dissolution behavior using reactive and non-reactive travel time distributions to estimate hydrodynamic variability and NAPL distribution heterogeneity. However, as currently deployed, tracer tests that are used to characterize these travel time distributions are very expensive and may not be affordable at most field sites.

Because numerical and Lagrangian models are difficult to parameterize, analytical models of source behavior can be important decision making tools for risk assessment and remedial design. In these models, the source is represented by an effective homogeneous domain with the flux-averaged concentration at the source control plane described as a function of the mean advective flow and the mean DNAPL mass in the domain.

Predicting the effect of the source remediation on plume behavior has been limited by the lack of tools that explicitly link source and plume remediation. To address this problem, coupled source and plume models are presented. One of these models, REMChlor, was developed to evaluate the impact of source and plume remediation at a more generic and strategic level. This screening-level mass balance approach is not specific to any remediation technology. The contaminant source model is based on a power function relationship between source mass and source discharge, and it can consider partial source remediation at any time after the initial contaminant release. The source model serves as a time-dependent mass flux boundary condition to a new analytical plume model. The plume model simulates first-order sequential decay and production of several species, and the decay rates and parent/daughter yield coefficients are variable functions of time and distance.

6.0
References

Alvarez, P.J.J., and W.A. Illman (2006). *Bioremediation and Natural Attenuation*. Wiley-Interscience.

Annable, M.D., K. Hatfield, J. Cho, H. Klammler, B.L. Parker, J.A. Cherry, and P.S.C Rao (2005). Field-scale evaluation of the passive flux meter for simultaneous measurement of groundwater and contaminant fluxes. *Environmental Science and Technology* 39(18):7194-7201.

API (2003). *Groundwater Remediation Strategies Tool.* Washington, DC, 80 pp.

Applied Research Associates (1996). *Groundwater Remediation Field Laboratory. Hydrogeology Characterization and Site Development.* Dover AFB, Delaware,. 1:192.

Aziz, C.E., C.J. Newell, and J.R. Gonzales (2002). *BIOCHLOR Natural Attenuation Decision Support System Version 2.2,* User's Manual Addendum, from http://www.epa.gov/ada/download/models/biochlor22.pdf.

Aziz, C.E., C.J. Newell, J.R. Gonzales, P. Haas, T. Prabhakar, and Y. Sun (2000). *BIOCHLOR Natural Attenuation Decision Support System. User's Manual, Version 1.0,* National Risk Management Research Laboratory, U.S. EPA, Ada, OK.

Bass, D.H., N.A. Hastings, and R.A. Brown (2000). Performance of air sparging systems: a review of case studies. *Journal of Hazardous Materials* 72(2-3):101-119.

Basu, N.B., P.S.C. Rao, I. C. Poyer, M.D. Annable, and K. Hatfield (2006). Flux-based assessment at a manufacturing site contaminated with trichloroethylene. *Journal of Contaminant Hydrology* 86(1-2):105-127.

Basu, N.B., P.S.C. Rao, R.W. Falta, M.D. Annable, J.W. Jawitz, and K. Hatfield (2008a). Temporal evolution of DNAPL source and contaminant flux distribution: impacts of source mass depletion. *Journal of Contaminant Hydrology* 95(3-4):93-109.

Basu, N.B., A.D. Fure, and J.W. Jawitz (2008b). Simplified contaminant source depletion models as analogs of multiphase simulators. *Journal of Contaminant Hydrology* 97(3-4):87-99, doi: 10.1016/j.jconhyd.2008.01.001.

Basu, N.B., A.D. Fure, and J.W. Jawitz (2008c). Predicting DNAPL dissolution using a simplified source depletion model parameterized with partitioning tracers. *Water Resources Research* 44(7):W07414.1-13, doi:10.1029/2007WR006008.

Bateman, H. (1910). The solution of a system of differential equations occurring in the theory of radio-active transformations. *Proceedings of the Cambridge Philosophical Society* 15:423-527.

Bauer, S., M. Bayer-Raich, T. Holder, C. Kolesar, D. Muller, and T. Ptak (2004). Quantification of groundwater contamination in an urban area using integral pump tests. *Journal of Contaminant Hydrology* 75(3-4):183-213.

Bayer-Raich, M., J. Jarsjo, R. Liedl, T. Ptak, and G. Teutsch (2004). Average contaminant concentration and mass flow in aquifers from time-dependent pumping well data: analytical framework. *Water Resources Research* 40(8):W08303.1-10.

Bayer-Raich, M., J. Jarsjo, R. Liedl, T. Ptak, and G. Teutsch (2006). Integral pumping test analysis of linearly sorbed groundwater contaminants using multiple wells: inferring mass flows and natural attenuation rates. *Water Resources Research* 42, W08411. doi:10.1029/2005WR004244.

Bear, J. (1979). *Hydraulics of Groundwater.* McGraw Hill Book Company, New York.

Bear, J., and M. Jacobs (1965). On the movement of water injected into aquifers. *Journal of Hydrology* 3:37-57.

Beyke, G. and D. Fleming (2005). In situ thermal remediation of DNAPL and LNAPL using electrical resistance heating. *Remediation Journal* 15(3):5-22.

Bob, M.M., M.C. Brooks, S.C. Mravik, and A.L. Wood (2008). A modified light transmission visualization method for DNAPL saturation measurements in 2-D models. *Advances in Water Resources* 31(5):727-742.

Bob, M.M., M.C. Brooks, S.C. Mravik, and A.L. Wood (2009). The impacts of partial remediation by sparging on down-gradient DNAPL mass discharge. (In preparation).

Bockelmann, A., T. Ptak, and G. Teutsch (2001). An analytical quantification of mass fluxes and natural attenuation rate constants at a former gasworks site. *Journal of Contaminant Hydrology* 53(3-4):429-453.

Bockelmann, A., D. Zamfirescu, T. Ptak, P.Grathwohl, and G. Teutsch (2003). Quantification of mass fluxes and natural attenuation rates at an industrial site with a limited monitoring network: a case study. *Journal of Contaminant Hydrology* 60(1-2):97-121.

Braida, W.J. and S.K. Ong (1998). Air Sparging: Air-water mass transfer coefficients. *Water Resource Research* 34(12):3245-3254.

Broholm, K., S. Feenstra, S., and J.A. Cherry (1999). Solvent release into a sandy aquifer. 1. Overview of source distribution and dissolution behavior. *Environmental Science and Technology* 33(5):681-690.

Brooks, M.C., A.L. Wood, M.D. Annable, K. Hatfield, J. Cho, C. Holbert, P.S.C. Rao, C.G. Enfield, K. Lynch, and R.E. Smith (2008). Changes in contaminant mass discharge from DNAPL source mass depletion: Evaluation at two field sites. *Journal Contaminant Hydrology* 102(1-2):140-153.

Brown, C.L., G.A. Pope, L.M. Abriola, and K. Sepehrnoori (1994). Simulation of surfactant-enhanced aquifer remediation. *Water Resources Research* 30(11):2959-2977.

Brown, G. (2006). Using Multilevel Samplers to Assess Ethanol Flushing and Enhanced Bioremediation at Former Sages Drycleaners. M.S. Thesis, University of Florida.

Camilleri, D., A. Fil, G.A. Pope, B.A. Rouse, and K. Sepehrnoori (1987). Improvements in physical-property models used in micellar/polymer flooding. *SPE Reservoir Engineering* 2(7):433-440.

Chapelle, F.H. and P.M. Bradley (1998). Selecting remediation goals by assessing the natural attenuation capacity of groundwater systems. *Bioremediation Journal* 2(3-4):227-238.

Chapelle, F.H., B.B. Looney, and C. Sink (2004). A mass balance approach to monitored natural attenuation. In: *Remediation of Chlorinated and Recalcitrant Compounds,* A.R. Gavaskar and A.S.C. Chen (eds).

Chapelle, F.H., J.S. Widdowson, J.S. Bruner, E. Mendez, and C.C. Casey (2003). *Methodology for Estimating Times of Remediation Associated with Monitored Natural Attenuation,* U.S. Dept. of the Interior, U.S. Geological Survey; U.S. Geological Survey, Water-Resources Investigations Report 03-4057.

Chen, N.H. (1983), *Process Reactor Design,* Allyn and Bacon, Inc., Boston, MA.

Christ, J.A., C.A. Ramsburg, K.D. Pennell, and L.M. Abriola (2006). Estimating mass discharge from dense nonaqueous phase liquid source zones using upscaled mass transfer coefficients: an evaluation using multiphase numerical simulations. *Water Resources Research* 42(11):W11420.1-13.

Chu, M., P.K. Kitanidis and P.L. McCarty (2004). Possible factors controlling the effectiveness of bioenhanced dissolution of non-aqueous phase tetrachloroethene. *Advances in Water Resources* 27(6):601-615.

Cirpka, O.A. and P.K. Kitanidis (2000). Impact of biomass-decay terms on the simulation of pulsed bioremediation. *Ground Water* 38(2):254-263.

Clement, T.P. (1997). *RT3D - A Modular Computer Code for Simulating Reactive Multi-Species Transport in 3-Dimensional Groundwater Systems.* Pacific Northwest National Laboratory, Richland, WA, 59 pp.

Clement, T.P., C.D. Johnson, Y. Sun, G.M. Klecka, and C. Bartlett (2000). Natural attenuation of chlorinated ethene compounds: model development and field-scale application at the Dover site. *Journal of Contaminant Hydrology* 42(2):113-140.

Conrad, S.H., R.J. Glass, and W.J. Peplinski (2002). Bench-scale visualization of DNAPL remediation processes in analog heterogeneous aquifers: surfactant floods and in situ oxidation using permanganate. *Journal of Contaminant Hydrology* 58(1-2):13-49.

Cvetkovic, V., G. Dagan, and H. Cheng (1998). Contaminant transport in aquifers with spatially variable hydraulic and sorption properties. *Proceedings of the Royal Society of London, A. Math* 454(1976):2173-2207.

Darnault C.J., J.A. Throop, D.A. DiCarlo, A. Rimmer, T.S. Steenhuis, and J-Y. Parlange (1998). Visualization by light transmission of oil and water contents in transient two-phase flow fields. *Journal of Contaminant Hydrology* 31(3-4):337-348.

Datta-Gupta, A., G.A. Pope, K. Sepehrnoori, and M.J. King (1991). High resolution monotonic schemes for reservoir fluid flow simulation. *In Situ* 15(3):289-317.

Delshad, M., G.A. Pope, and K. Sepehrnoori (1996). A compositional simulator for modeling surfactant enhanced aquifer remediation, 1. Formulation. *Journal of Contaminant Hydrology* 23(4):303-327.

DiFilippo, E.L. and Brusseau, M.L. (2008). Relationship between mass-flux reduction and source-zone mass removal: analysis of field data. *Journal of Contaminant Hydrology* 98(1-2):22-35.

Domenico, P.A. (1987). Analytical model for multidimensional transport of a decaying contaminant species. *Journal of Hydrology* 91(1-2):49-58.

Edwards, D.A., R.G. Luthy, and Z. Liu (1991). Solubilization of polycyclic aromatic hydrocarbons in micellar nonionic surfactant solutions. *Environmental Science and Technology* 25(1):127–133.

Einarson, M.D., and D.M. Mackay (2001). Predicting impacts of groundwater contamination. *Environmental Science and Technology* 35(3):66A-73A.

Elder, C., and C. Benson (1999). Air channel formation, size, spacing, and tortuosity during air sparging. *Ground Water Monitoring and Remediation* 19(3):171-181.

Enfield, C.G., A.L. Wood, F.P. Espinoza, M.C. Brooks, M. Annable, and P.S.C. Rao (2005). Design of aquifer remediation systems: (1) Describing hydraulic structure and NAPL architecture using tracers. *Journal of Contaminant Hydrology* 81(1-4):125-147.

Esposito, S.J. and N.R. Thomson (1999). Two-phase flow and transport in a single fracture-porous medium system. *Journal of Contaminant Hydrology* 37(3-4):319-341.

Falta, R.W., K. Pruess, I. Javandel, and P.A. Witherspoon, (1992). Numerical modeling of steam injection for the removal of nonaqueous phase liquids from the subsurface, 1. Numerical formulation. *Water Resources Research,* 28(2): 451-465.

Falta, R.W. (1998). Using phase diagrams to predict the performance of cosolvent floods for NAPL remediation. *Ground Water Monitoring and Remediation* 18(3):94-102.

Falta, R.W. (2000). Numerical modeling of kinetic interphase mass transfer during air sparging using a dual-media approach. *Water Resources Research* 36(12):3391-3400.

Falta, R.W. (2003). Modeling sub-grid-block-scale dense nonaqueous phase liquid (DNAPL) pool dissolution using a dual-domain approach. *Water Resources Research* 39(12):SBH 18.1-8.

Falta, R.W. (2005). Dissolved Chemical Discharge from Fractured Clay Aquitards Contaminated by DNAPLs, In: *Dynamics of Fluids in Fractured Rock,* B. Faybishenko, P.A. Witherspoon, and J. Gale, eds., Geophysical Monograph 162, American Geophysical Union.

Falta, R.W. (2009). Monte Carlo simulations of source behavior with remediation. (In preparation).

Falta, R.W., C. Lee, S. Brame, J. Coates, and J. Myers (2003). Field Evaluation of Cosolvent-Enhanced In-Situ Remediation Cooperative Agreement CR-821992-01-0, Clemson University. 86 pp.

Falta, R.W., M.B. Stacy, A.N.M Ahsanuzzaman, M. Wang, and R. Earle (2007). REMChlor Remediation Evaluation Model for Chlorinated Solvents User's Manual Version 1.0. http://www.epa.gov/ada/csmos/models/remchlor.html

Falta, R.W. (2008). Methodology for comparing source and plume remediation alternatives. *Ground Water* 46(2):272-285.

Falta, R.W., N. Basu, and P.S.C. Rao (2005b). Assessing impacts of partial mass depletion in DNAPL source zones: II. Coupling source strength functions to plume evolution. *Journal of Contaminant Hydrology* 79(1-2):45-66.

Falta, R.W., K. Pruess, S. Finsterle, and A. Battistelli (1995). *T2VOC User's Guide.* University of California, Berkeley, CA, Lawrence Berkeley Laboratory, Earth Sciences Division, Report LBL-36400.

Falta, R.W., P.S.C. Rao, and N. Basu (2005a). Assessing the impacts of partial mass depletion in DNAPL source zones: I. Analytical modeling of source strength functions and plume response. *Journal of Contaminant Hydrology* 78(4):259-280.

Feenstra, S., J.A. Cherry, and B.L. Parker (1996). Conceptual models for the behavior of dense non-aqueous phase liquids (DNAPLS) in the subsurface. In: *Dense Chlorinated Solvents and Other DNAPLs in Groundwater: History, Behavior, and Remediation,* pp. 53-88.

Fine, D., M. Brooks, M. Bob, S. Mravik and L. Wood (2008). Continuous determination of high-vapor-phase concentrations of tetrachloroethylene using on-line mass spectrometry. *Journal of Analytical Chemistry* 80(4):1328-1335

Freeze, G.A., J.C. Fountain, and G.A. Pope (1994). Modeling the surfactant-enhanced remediation of PCE at the Borden Test Site using the UTCHEM compositional simulator. *Toxic Substances and the Hydrologic Sciences,* pp. 339-345.

Fure, A.D., J.W. Jawitz, and M.D. Annable (2006). DNAPL source depletion: linking architecture and flux response. *Journal of Contaminant Hydrology* 85(3-4):118-140.

Geller, J.T., and J.R. Hunt (1993). Mass transfer from nonaqueous phase organic liquids in water saturated porous media. *Water Resources Research* 29(4):833–845.

Gierke, J.S., D.A. Taege, D.L. Perram, and N.J. Hutzler (2002). Design Guidance for Air Sparging of Dense Nonaqueous Phase Liquids (Tetrachloroethylene, PCE) in Unconsolidated Geological Environments (Coastal Plain Aquifer): Based on the Performance Measured in a Field Test Conducted at the Groundwater Remediation Field Laboratory (GRFL), Dover National Test Site (DNTS), Dover Air Force Base (DAFB), Delaware.

GoldSim (2007). From http://www.goldsim.com/

Goltz, M.N., J. Huang, M.E. Close, M.J. Flintoft, and L. Pang (2008). Use of tandem circulation wells to measure hydraulic conductivity without groundwater extraction. *Journal of Contaminant Hydrology* 100(3-4):127-136.

Goltz, M.N., M.E. Close, H. Yoon, J. Huang, M.J. Flintoft, S. Kim, and C. Enfield (2009). Validation of two innovative methods to measure contaminant mass flux in groundwater. *Journal of Contaminant Hydrology* 106(1-2):51-61.

Guilbeault, M.A., B.L. Parker, and J.A. Cherry (2005). Mass and flux distributions from DNAPL zones in sandy aquifers. *Ground Water* 43(1):70-86.

Hand, D.B. (1930). The distribution of a consolute liquid between two immiscible liquids. *Journal of Physical Chemistry* 34:1961.

Harten, A. (1983). High resolution schemes for hyperbolic conservation lows. *SIAM Review* 25(1):1085-1090.

Hatfield, K., M.D. Annable, S. Kuhn, P.S.C. Rao, and T. Campbell (2002). A new method for quantifying contaminant flux at hazardous waste sites. In: *Groundwater Quality: Natural and Enhanced Restoration of Groundwater Pollution.* Groundwater Quality 2001 Conference, Sheffield, UK, IAHS.

Hatfield, K., M.D. Annable, J. Cho, P.S.C. Rao, and H. Klammler (2004). A direct passive method for measuring water and contaminant fluxes in porous media. *Journal of Contaminant Hydrology* 75(3-4):155-181.

Hayden, N.J., J. Diebold, and G. Noyes (1999). Phase behavior of chlorinated solvent + water + alcohol mixtures with application to alcohol flushing. *Journal of Chemical and Engineering Data* 44(5):1085-1090.

Heron, G., J.S. Gierke, B. Faulkner, S. Mravik, L. Wood, and C.G. Enfield (2002). Pulsed air sparging in aquifers contaminated with dense nonaqueous phase liquids. *Ground Water Monitoring and Remediation* 22(4):73-82.

Hoa, M. (1981). A new method allowing the measurement of rapid variations of the water content in sandy porous media. *Water Resources Research* 17(1):41-48.

Holder, T.H., G. Teutsch, T. Ptak, and R. Schwarz (1998). A new approach for source zone characterization: the Neckar Valley study. *Groundwater quality: remediation and protection.* Proceedings of the GQ'98 Conference, vol. 250. IAHS Publication, Tubingen, Germany, pp.49-55.

Hopmans J.W., and J.H. Dane (1986). Calibration of a dual-energy gamma radiation system for multiple point measurements in a soil. *Water Resources Research* 22(7):1009-1114.

Huntley, D. and G.D. Beckett (2002). Persistence of LNAPL sources: relationship between risk reduction and LNAPL recovery. *Journal of Contaminant Hydrology* 59(1-2):3-26.

Jarsjö, J. and M. Bayer-Raich (2008). Estimating plume degradation rates in aquifers: effect of propagating measurement and methodological errors. *Water Resources Research* 44:W02501, doi:10.1029/2006WR005568.

Jarsjö, J., M. Bayer-Raich, and T. Ptak (2005). Monitoring groundwater contamination and delineating source zones at industrial sites: uncertainty analyses using integral pumping tests. *Journal of Contaminant Hydrology* 79(3-4):107-134.

Jawitz, J.W., M.D. Annable, and P.S.C. Rao (1998). Miscible fluid displacement stability in unconfined porous media: two-dimensional flow experiments and simulations. *Journal of Contaminant Hydrology* 31(3-4):211-230.

Jawitz, J.W., MD. Annable, G.G. Demmy, and P.S.C. Rao (2003). Estimating non-aqueous phase liquid spatial variability using partitioning tracer higher temporal moments. *Water Resources Research* 39(7):SBH 7.1-19.

Jawitz, J.W., A.D. Fure, G.G. Demmy, S, Berglund (2005). Groundwater contaminant flux reduction resulting from nonaqueous phase liquid mass reduction. *Water Resources Research* 41(10):W10408.1-15.

Jawitz, J.W., R.K. Sillan, M.D. Annable, P.S.C. Rao, and K. Warner (2000). In-situ alcohol flushing of a DNAPL source zone at a dry cleaner site. *Environmental Science and Technology* 34(17):3722-3729.

Ji, W., A. Dahmani, D.P. Ahlfeld, J.D. Lin and E. Hill (1993). Laboratory study of air sparging: air flow visualization. *Ground Water Monitoring and Remediation* 13(4):115-126.

Jin, M., M. Delshad, V. Dwarakanath, D.C. McKinney, G.A. Pope, K. Sepehrnoori, C.E. Tilburg, and R.E. Jackson (1995). Partitioning tracer test for detection, estimation, and remediation performance assessment of subsurface nonaqueous phase liquids. *Water Resources Research* 31(5):1201-1212.

Johnson, W.P. and W.W. John (1999). PCE solubilization and mobilization by commercial humic acid. *Journal of Contaminant Hydrology* 35(4):343-362.

Jury, W.A., and K. Roth (1990). *Transfer Functions and Solute Movement Through Soil: Theory and Application.* Birkhäuser, Boston, MA.

Keely, J.F. (1982). Chemical time-series sampling. *Ground Water Monitoring Review* 2:29-38.

Keely, J.F., and F. Wolf (1983). Field applications of chemical time-series sampling. *Ground Water Monitoring Review* 3:26-33.

Klammer, H., K. Hatfield, M.D. Annable, E. Agyei, B. Parker, J.A. Cherry, and P.S.C. Rao (2007). General analytical treatment of the flow field relevant to the interpretation of passive fluxmeter measurements. *Water Resources Research* 43(4):W04407.

Kovalic, J.M. (1987). *The Clean Water Act of 1987, 2nd edition,* Water Pollution Control Federation, Alexandria, VA.

Kreft A, and A. Zuber (1978). On the physical meaning of the dispersion equation and its solutions for different initial and boundary conditions. *Chemical Engineering Science* 33:1471-1480.

Kubert, M., and M. Finkel (2006). Contaminant mass discharge estimation in groundwater based on multi-level point measurements: a numerical evaluation of expected errors. *Journal of Contaminant Hydrology* 84(1-2):55-80.

Lerner, D.N. and G. Teutsch (1995). Recommendations for level-determined sampling in wells. *Journal of Hydrology* 171(3-4):355-377.

LFR (2005). *Phase I Injection Completion Report Former Sages Dry Cleaners.* Prepared for Florida Department of Environmental Protection, Tallahassee, Florida.

Li, B. and J. Fu (1992). Interfacial tensions of two-liquid-phase ternary systems. *Journal of Chemical and Engineering Data* 37(2):172-174.

Liang, H., and R.W. Falta (2007). Modeling field-scale cosolvent flooding for DNAPL source zone remediation. *Journal of Contaminant Hydrology* 96(1-4):1-16.

Liu, J., M. Delshad, G.A. Pope and K. Sepehrnoori (1994). Application of higher order flux-limited methods in compositional simulations. *Journal of Transport in Porous Media* 16(1):1-29.

Liu Y., B. Bierck, J.S. Selker, T.S. Steenhuuis, and J-Y. Parlange (1993). High intensity x-ray and tensiometer measurements in rapidly changing preferential flow fields. *Soil Science Society of America Journal* 57:1188-1192.

Lowe, D.F., C.L. Oubre, C.H. Ward, and T.J. Simpkin (1999). *Surfactants and Cosolvents for NAPL Remediation: A Technology Practices Manual.* Lewis Publishers.

Lunn, S.R.D. (1998). *Alcohol Flooding of Porous Media Contaminated with Hazardous Immiscible Liquids.* Ph.D. Dissertation, Civil Engineering, Queen's University, Kingston, Ontario, Canada.

Lunn, S.R.D. and B.H. Kueper (1997). Removal of pooled dense, non-aqueous phase liquid from saturated porous media using upward gradient alcohol floods. *Water Resource Research* 33(10):2207-2220.

MacKay, D.M. and J.A. Cherry (1989). Groundwater contamination: pump-and-treat remediation. *Environmental Science and Technology* 23(6):630– 636.

Maxwell, R.M., S.D. Pelmulder, A.F.B. Tompson, and W.E. Kastenberg (1998). On the development of a new methodology for groundwater-driven health risk assessment. *Water Resources Research* 34(4):833-847.

McGuire, T.M., J.M. McDade, and C.J. Newell, (2006). Performance of DNAPL source depletion technologies at 59 chlorinated solvent-impacted sites. *Ground Water Monitoring and Remediation* 26(1):73-84.

McGuire, T.M., C.J. Newell, B.B. Looney, K.M. Vangelas, and C.H. Sink (2004). Historical analysis of monitored natural attenuation: a survey of 191 chlorinated solvent sites and 45 solvent plumes. *Remediation Journal* 15(1):99-112.

McKone, T.E. (1987). Human exposure to volatile organic compounds in household tap water: the indoor inhalation pathway. *Environmental Science and Technology* 21(12):1194-1201.

Meinardus, H.W., V. Dwarakanath, J. Ewing, G.J. Hirasaki, R.E. Jackson, M. Jin, J.S. Ginn, J.T. Londergan, C.A. Miller, and G.A. Pope (2002). Performance assessment of NAPL remediation in heterogeneous alluvium. *Journal of Contaminant Hydrology* 54(3-4):173-193.

Miller, C.T., M.M. Poirier-McNeill, and A.S. Mayer (1990). Dissolution of trapped nonaqueous phase liquids: mass transfer characteristics. *Water Resources Research* 26:2783-2796.

Millington, R.J., and J.P. Quirk (1961). Permeability of porous solids. *Transactions of the Faraday Society* 57:1200-1207.

Mravik, S.C., G.W. Sewell, and A.L. Wood (2000). Cosolvent-based source remediation approaches. In: *Remediation of Chlorinated and Recalcitrant Compounds: Physical and Thermal Technologies,* pp. 269-276.

Mravik, S.C., R.K. Sillan, A.L. Wood, and G.W. Sewell (2003). Field evaluation of the solvent extraction residual biotreatment technology. *Environmental Science and Technology* 37(21):5040-5049.

Newell, C., R.K. McLeod, and J.R. Gonzales (1996*). BIOSCREEN Natural Attenuation Decision Support System User's Manual, Version 1.3,* U.S. Environmental Protection Agency, National Risk Management Research Laboratory.

Newell, C.J., H.S. Rifai, J.T. Wilson, J.A. Connor, J.J. Aziz, and M.P. Suarez (2002). *Calculation and Use of First-Order Rate Constants for Monitored Natural Attenuation Studies,* U.S. EPA Remedial Technology Fact Sheet. U. S. Environmental Protection Agency.

Newell, C.J. and D.T. Adamson (2005). Planning-level source decay models to evaluate impact of source depletion on remediation time frame. *Remediation Journal* 15(4):27-47.

Newell, C.J., I. Cowie, T.M. McGuire, and W. McNab (2006). Multi-year temporal changes in chlorinated solvent concentrations at 23 MNA sites. *Journal of Environmental Engineering* 132(6):653-663.

Niemet M.R., and J.S. Selker (2001). A new method for quantification of liquid saturation in 2-D translucent porous media systems using light transmission. *Advances in Water Resources* 24(6):651-666.

NRC (2000). *Natural Attenuation for Groundwater Remediation,* National Research Council, National Academy Press, Washington, DC, 274 pp.

NRC (2005). *Contaminants in the Subsurface Source Zone Assessment and Remediation*. Committee on Source Removal of Contaminants in the Subsurface. The National Academies Press. Washington, DC, 372 pp.

O'Hara, S.K., B.L. Parker, P.R. Jorgensen, and J.A. Cherry (2000). Trichloroethene DNAPL flow and mass distribution in naturally fractured clay: evidence of aperture variability. *Water Resources Research* 36(1):135-147.

OEHHA (2006). Cancer Potency Information, California Office of Environmental Health Hazard Assessment, http://www.oehha.ca.gov/risk/ChemicalDB/index.asp.

Ostrom M., C. Hofstee, H. Dane, and R.J. Lenhard (1998). Single-source gamma radiation procedures for improved calibration measurements in porous media. *Soil Science* 163(8):646-656.

Parker, B.L., J.A. Cherry, and S.W. Chapman (2004). Field study of TCE diffusion profiles below DNAPL to assess aquitard integrity. *Journal of Contaminant Hydrology* 74(1-4):197-230.

Parker, B.L., R.W. Gillham, and J.A. Cherry (1994). Diffusive disappearance of immiscible-phase organic liquids in fractured geologic media. *Ground Water* 32(5):805-820.

Parker, B.L., D.B. McWhorter, and J.A. Cherry (1997). Diffusive loss of non-aqueous phase organic solvents from idealized fracture networks in geologic media. *Ground Water* 35(6):1077-1088.

Parker, J.C. and E. Park (2004). Modeling field-scale dense nonaqueous phase liquid dissolution kinetics in heterogeneous aquifers. *Water Resources Research* 40(W05109):1-12.

Pennell, K.D., L.M. Abriola, and W.J.Weber, Jr. (1993). Surfactant enhanced solubilization of residual dodecane in soil columns. 2. Mathematical modeling. *Environmental Science and Technology* 27(12):2341-2351.

Pickens, J.F., J.A. Cherry, G.E. Grisak, W.F. Merrittand, and B.A. Risto (1978). A multilevel device for ground-water sampling and piezometric monitoring. *Ground Water* 16(5):322-327.

Pope, G.A., and R.C. Nelson (1978). A chemical flooding compositional simulator. *Society of Petroleum Engineers Journal* 18(5):339-354.

Powell, T., G. Smith, J. Sturza, K. Lynch, and M. Truex (2007). New advancements for in situ treatment using electrical resistance heating. *Remediation Journal* 17(2):51-70.

Powers, S.E., L.M. Abriola, and W.J. Weber (1992). An experimental investigation of nonaqueous phase liquid dissolution in saturated subsurface systems: steady-state mass-transfer rates. *Water Resources Research* 28(10):2691-2705.

Pruess, K. and A. Battistelli (2002). *TMVOC, a Numerical Simulator for Three-Phase Non-Isothermal Flows of Multicomponent Hydrocarbon Mixtures in Saturated-Unsaturated Heterogeneous Media,* Lawrence Berkeley National Laboratory, Berkeley, CA, Report LBNL-49375.

Rao, P.S.C., M.D. Annable, and H. Kim (2000). NAPL source zone characterization and remediation technology performance assessment: recent developments and applications of tracer techniques. *Journal of Contaminant Hydrology* 45(1-2):63-78.

Rao, P.S.C., J.W. Jawitz, C.G. Enfield, R.W. Falta Jr, M.D. Annable, and A.L. Wood (2002). Technology integration for contaminated site remediation: cleanup goals and performance criteria. In: *Groundwater Quality: Natural and Enhanced Restoration of Groundwater Pollution.* Proceedings of the Groundwater Quality 2001 Conference, Sheffield, UK, June 2001, pp. 571-578.

Rao, P.S.C. and J.W. Jawitz (2003). Comment on ''Steady-state mass transfer from single-component dense non-aqueous phase liquids in uniform flow fields'' by T.C. Sale and D.B. McWhorter. *Water Resources Research* 39(3):1068.

Reynolds, D.A. and B.H. Kueper (2001). Multiphase flow and transport in fractured clay/sand sequences. *Journal of Contaminant Hydrology* 51(1-2):41-62.

Reynolds, D.A. and B.H. Kueper (2002). Numerical examination of the factors controlling DNAPL migration through a single fracture. *Ground Water* 40(4):368-377.

Reynolds, D.A. and B. H. Kueper (2004). Multiphase flow and transport through fractured heterogeneous porous media. *Journal of Contaminant Hydrology* 71(1-4):89-110.

Rimmer A., D.A. DiCarlo, T.S. Steenhuis, B. Bierck, D. Durnford and J-Y. Parlange (1998). Rapid fluid content measurement method for fingered flow in an oil-water-sand system using synchrotron x-rays. *Journal of Contaminant Hydrology* 31(3-4):315-334.

Rivett, M.O. and S. Feenstra (2005). Dissolution of an emplaced source of DNAPL in a natural aquifer setting. *Environmental Science and Technology* 39(2):447-455.

Rivett, M.O., S. Feenstra, and J.A. Cherry (2001). A controlled field experiment on groundwater contamination by a multicomponent DNAPL: creation of the emplaced-source and overview of dissolved plume development. *Journal of Contaminant Hydrology* 49(1-2):111-149.

Ross, B. and N. Lu (1999). Dynamics of DNAPL penetration into fractured porous media. *Ground Water* 37(1):140-147.

Sale, T.C., and D.B. McWhorter (2001). Steady state mass transfer from single-component dense nonaqueous phase liquids in uniform flow fields. *Water Resources Research* 37(2):393-404.

Sánchez-Vila, X., P.M. Meier, and J. Carrera (1999). Pumping tests in heterogeneous aquifers: an analytical study of what can be obtained from their interpretation using Jacob's method. *Water Resources Research* 35(4):943-952.

Schwarz, R., T. Ptak, T. Holder, and G. Teutsch (1998). Groundwater risk assessment at contaminated sites: a new investigation approach. In: *Groundwater Quality: Remediation and Protection.* GQ'98 Conference, Tübingen, Germany, IAHS Publication No. 250.

Schwille, J.F. (1988). *Dense Chlorinated Solvents in Porous and Fractured Media, Model Experiments.* Lewis Publishers, Chelsea, MI.

Sillan, R.K., M.D.Annable, and P.S.C. Rao (1997). *In-situ Cosolvent Flushing for Enhanced Solubilization of a Complex NAPL: Comprehensive Field-Scale Evaluation,* Draft Final Report. University of Florida, Gainesville, FL.

Sillan, R.K., M.D. Annable, and P.S.C. Rao (1999). *Evaluation of In-Situ DNAPL Remediation and Innovative Site Characterization Techniques.* Florida Center for Solid and Hazardous Waste Management, Gainesville, FL.

Slough, K.J., E.A. Sudicky, P.A. Forsyth (1999). Numerical simulation of multiphase flow and phase partitioning in discretely fractured geologic media. *Journal of Contaminant Hydrology* 40(2):107-136.

Soga, K., J. Page, and N. Gowers (2002). NAPL source zone remediation – mass flux approach. In: *Environmental Geotechnics*. Fourth International Congress on Environmental Geotechnics (4th ICEG), Rio de Janeiro, Brazil, 2:1069-1081.

Soga, K., J.W. Page, and T.H. Illangasekare (2004). A review of NAPL source zone remediation efficiency and the mass flux approach. *Journal of Hazardous Materials* 110(1-3):13-27.

Sun, Y., J.N. Petersen, and T.P. Clement. (1999a). Analytical solutions for multiple species reactive transport in multiple dimensions. *Journal of Contaminant Hydrology* 35(4):429-440.

Sun, Y., J.N. Petersen, T.P. Clement, and R.S. Skeen (1999b). Development of analytical solutions for multi-species transport with serial and parallel reactions. *Water Resources Research* 35(1):185-190.

Suter, G.W. (1993). *Ecological Risk Assessment.* Lewis Publishers, Chelsea, MI, 643 pp.

Thermal Remediation Services, Inc. (2005). *Final NAPL Area 1 Completion Report.* In Situ Thermal Remediation (Electrical Resistance Heating) East Gate Disposal Yard. Ft. Lewis, WA.

Tidwell V.C., and R.G. Glass (1994). X-ray and visible light transmission for laboratory measurement of two dimensional saturation fields in thin-slab systems. *Water Resources Research* 30(11):2873-2882.

Totten, C.T., M.D. Annable, J.W. Jawitz, and J.J. Delfino (2007). Fluid and porous media property effects on dense non-aqueous phase liquid migration and contaminant mass flux. *Environmental Science and Technology* 41(5):1622-1627.

U.S. ACE (2002). *Field Investigation Report, Phase II Remediation Investigation.* East Gate Disposal Yard, Fort Lewis, WA, DSERTS No. FTLE-67.

U.S. EPA (2003). *In-situ Thermal Treatment of Chlorinated Solvents: Fundamentals and Field Applications,* U.S. Environmental Protection Agency, Office of Solid Waste and Emergency Response, Office of Superfund Remediation, Technology Innovation Office, Washington DC. EPA 542-R-04-010. http://www.epa.gov/tio/download/remed/epa542r04010.pdf

U.S. EPA. (1989). Risk Assessment Guidance for Superfund, Volume 1, Part A. Office of Emergency and Remedial Response, Washington, D.C. EPA/540/1-89/002. http://www.epa.gov/oswer/riskassessment/ragsa/index.htm

U.S.G.S. (2000). *MODFLOW-2000, The U.S. Geological Survey Modular Ground-Water Model,* User Guide to Modularization Concepts and the Ground-Water Flow Process. U.S.G.S. Open File Report 00-92, 121 pp.

URS Corporation (URS) and INTERA (2003). *Final Panel 1 and Panel 5 Surfactant Enhanced Aquifer Remediation (SEAR) Report, Operable Unit 2, Hill Air Force Base, Utah.* Prepared for the Air Force Center for Environmental Excellence and the Environmental Management Division, Hill Air Force Base, Utah.

VanAntwerp, D. (2006). *Using a Dual-Media Approach to Model Air Sparging Mass Transfer,* Clemson University.

VanAntwerp, D., R.W. Falta, and J.S. Gierke (2008). Numerical simulation of field scale contaminant mass transfer during air sparging. *Vadose Zone Journal* 7:294-304.

van Genuchten, M.T. and W.J. Alves (1982). *Analytical Solutions of the One-Dimensional Convective-Dispersive Solute Transport Equation,* U.S. Department of Agriculture, Technical Bulletin No. 1661, 151 pp.

van Valkenburg, M.E. (1999). *Solubilization and Mobilization of Perchloroethylene by Cosolvents in Porous Media.* Ph.D. Dissertation, Environmental Engineering Sciences, University of Florida. Gainesville, FL.

Waduge, W.A.; Soga, K. and Kawabata, J. (2004). Effect of DNAPL entrapment conditions on air sparging remediation efficiency. *Journal of Hazardous Materials* 110(1-3):173-183

Wagner, D.E., J. Huang, J.L. Heiderscheidt, and M.N. Goltz. (2009). Modeling study to quantify the benefits of groundwater contaminant source remediation. (In preparation).

Wang, H., X. Chen, and J.W. Jawitz (2008). Locally calibrated light transmission visualization methods to quantify nonaqueous phase liquid mass in porous media. *Journal of Contaminant Hydrology* 102(1-2):29-38.

Weidemeier, T.D., H.S. Rifai, C.J. Newell, and J.T.Wilson (1999). *Natural Attenuation of Fuels and Chlorinated Solvents in the Subsurface.* John Wiley and Sons, Inc., New York, NY, 632 pp.

Weidemeier, T.H., M.S. Swanson, D.E. Moutoux, E.K. Gordon, J.T. Wilson, B.H. Wilson, D.H. Kampbell, P.E. Haas, R.N. Miller, J.E. Hansen, and F.H. Chapelle (1998). *Technical Protocol for Evaluating Natural Attenuation of Chlorinated Solvents in Ground Water.* EPA 600/R-98/128, 248 pp.

Weisbrod N., M. Niemet, and J.S. Selker (2003). Light transmission technique for the evaluation of colloidal transport and dynamics in porous media. *Environmental Science and Technology* 37(16):3694-3700.

Widdowson, M.A., S. Shearer, R.G. Andersen, and J.T. Novak (2005). Remediation of polycyclic aromatic hydrocarbon compounds in groundwater using poplar trees. *Environmental Science and Technology* 39(6):1598-1605.

Williams, P.R.D., L. Benton, and P.J. Sheehan (2004). The risk of MTBE relative to other VOCs in public drinking water in California. *Risk Analysis* 24(3):621-634.

Wilson R.D., and M.D. Mackay (1995). Direct detection of residual non-aqueous phase liquid in the saturated zone using SF6 as a partitioning tracer. *Environmental Science and Technology* 29(5):1255-1258.

Wood, A.L., and C.G. Enfield (1999). *In Situ Enhanced Source Removal.* EPA/600/C-99/002.

Wood, A.L., C.G. Enfield, F.P. Espinoza, M. Annable, M.C. Brooks, P.S.C. Rao, D. Sabatini, and R. Knox (2005). Design of aquifer remediation systems: (2) Estimating site-specific performance and benefits of partial source removal. *Journal of Contaminant Hydrology* 81(1-4):148-166.

Zeru, A., and G. Schäfer (2005). Analysis of groundwater contamination using concentration–time series recorded during an integral pumping test: bias introduced by strong concentration gradients within the plume. *Journal of Contaminant Hydrology* 81(1-4):106-124.

Zhang, H., and F.W. Schwartz (2000). Simulating the in situ oxidative treatment of chlorinated compounds by potassium permanganate. *Water Resources Research* 36(10):3031-3042.

Zhang, Y.K., I.A. Khan, X.H. Chen and R.F. Spalding (2006). Transport and degradation of ethanol in groundwater. *Journal of Contaminant Hydrology* 82(3):183-194.

Zhu, J., and J. F. Sykes (2004). Simple screening models of NAPL dissolution in the subsurface. *Journal of Contaminant Hydrology* 72(1-4):245-258.

7.0
Appendix A
List of Technical Publications

Peer-Reviewed Papers:

Basu, N.B., A.D. Fure, and J.W. Jawitz (2008), Simplified contaminant source depletion models as analogs of multiphase simulators, *Journal of Contaminant Hydrology* 97(3-4):87-99 doi: 10.1016/j.jconhyd.2008.01.001.

Basu, N.B., A.D. Fure, and J.W. Jawitz (2008). Predicting DNAPL dissolution using a simplified source depletion model parameterized with partitioning tracers, *Water Resources Research,* 44:W07414, doi:10.1029/2007WR006008.

Basu, N.B., P.S.C. Rao, R.W. Falta, M.D. Annable, J.W. Jawitz, and K. Hatfield (2008). Temporal evolution of DNAPL source and contaminant flux distribution: impacts of source mass depletion, *Journal of Contaminant Hydrology,* 95(3-4):93-109.

Bob, M., M. Brooks, L. Wood, T. Lee, and C. Enfield (2008). A modified light transmission visualization method for DNAPL saturation measurements in 2-D models. *Advances in Water Resources Journal* 31(5):727-742.

Brooks, M.C., A.L. Wood, M.D. Annable, K. Hatfield, J. Cho, C. Holbert, P.S.C. Rao, C.G. Enfield, K. Lynch, and R.E. Smith. (2008). Changes in contaminant mass discharge from DNAPL source mass depletion: evaluation at two field sites. *Journal Contaminant Hydrology* 102(1-2):140-153, doi:10.1016/j.jconhyd.2008.05.008.

Chen, X., and J.W. Jawitz, (2008). Reactive tracer tests to predict DNAPL dissolution dynamics in laboratory flow chambers. *Environmental Science & Technology* 42(14):5285-5291.

Cho, J., M.D. Annable, and P.S.C. Rao (2003). Residual alcohol influence on NAPL saturation estimates based on partitioning tracers. *Environmental Science & Technology,* 37(8):1639-1644.

Falta, R.W. (2003). A dual domain approach for modeling subgridblock scale DNAPL pool dissolution. *Water Resources Research* 39(12):SBH 18-1-8.

Falta, R.W. (2008), Methodology for comparing source and plume remediation alternatives. *Ground Water* 46(2):272-285.

Falta, R.W., N. Basu and P.S.C. Rao (2005). Assessing the impacts of partial mass depletion in DNAPL source zones: II. Coupling source strength functions to plume evolution. *Journal of Contaminant Hydrology* 79(1-2):45-66.

Falta, R.W., P.S.C. Rao and N. Basu (2005). Assessing the impacts of partial mass depletion in DNAPL source zones: I. Analytical modeling of source strength functions and plume response. *Journal of Contaminant Hydrology* 78(4):259-280.

Fine, D., M. Brooks, M. Bob, S. Mravik and L. Wood (2008). Continuous determination of high-vapor-phase concentrations of tetrachloroethylene using on-line mass spectrometry. *Journal of Analytical Chemistry* 80(4):1328-1335.

Fure, A.D., J.W. Jawitz, and M.D. Annable (2006). DNAPL source depletion: linking architecture and flux response. *Journal of Contaminant Hydrology* 85(3-4):118-140.

Goltz, M.N., M.E. Close, H. Yoon, J. Huang, M.J. Flintoft, S.J. Kim, and C.G. Enfield (2009). Validation of two innovative methods to measure contaminant mass flux in groundwater, *Journal of Contaminant Hydrology* 106(1-2):51-61.

Goltz, M.N., S. Kim, H. Yoon, and J. Park (2007). Review of groundwater contaminant mass flux measurement. *Environmental Engineering Research* 12(4):176-193.

Goltz, M.N.; J. Huang, M.E. Close, M.J. Flintoft, and L. Pang (2008). Use of tandem circulation wells to measure hydraulic conductivity without groundwater extraction. *Journal of Contaminant Hydrology* 100(3-4):127-136.

Jawitz, J.W., A.D. Fure, G.G. Demmy, S. Berglund, and P.S.C. Rao (2005). Groundwater contaminant flux reduction resulting from nonaqueous phase liquid mass reduction. *Water Resources Research.* 41(10):W10408.1-15.

Kaye, A.J., J. Cho, N.B. Basu, X. Chen, M.D. Annable, and J.W. Jawitz (2008). Laboratory investigation of flux reduction from dense non-aqueous phase liquid (DNAPL) partial source zone remediation by enhanced dissolution. *Journal of Contaminant Hydrology* 102(1-2):17-28, doi: 10.1016/j.jconhyd.2008.01.006 .

Liang, H., and R.W. Falta (2008). modeling field-scale cosolvent flooding for DNAPL source zone remediation. *Journal of Contaminant Hydrology,* 96(1-4):1-16.

Rao, P.S.C. and J.W. Jawitz (2003). Comment on "Steady state mass transfer from single-component dense nonaqueous phase liquids in uniform flow fields" by T.C. Sale and D.B. McWhorter. *Water Resources Research* 39(3):1068.

Totten, C.T., M.D. Annable, J.W. Jawitz, and J.J. Delfino (2006). Fluid and porous media property effects on dense non-aqueous phase liquid migration and contaminant mass flux, *Environmental Science & Technology* 41(5):1622-1627.

VanAntwerp, D., R.W. Falta, and J.S. Gierke (2008). Numerical simulation of field scale contaminant mass transfer during air sparging, *Vadose Zone Journal,* 7:294-304.

Wang, H., X. Chen, and J.W. Jawitz (2008). Locally calibrated light transmission visualization methods to quantify nonaqueous phase liquid dissolution dynamics in porous media. *Journal of Contaminant Hydrology* 102(1-2)29-38, doi:10.1016/j.jconhyd.2008.05.003.

Wood, A.L., C.G. Enfield, F. Espinoza, M. Annable, M.C. Brooks, P.S.C. Rao, D. Sabatini and R. Knox (2005). Design of aquifer remediation systems: (2) Estimating site-specific performance and benefits of partial source removal *Journal of Contaminant Hydrology* 81(1-4):148-166.

Wood, R.C., J. Huang and M.N. Goltz (2006). Modeling chlorinated solvent bioremediation using hydrogen release compound (HRC). *Remediation Journal* 10(3):129-141.

Zhang, C., H. Yoon, C.J. Werth, A.J. Valocchi, M.B. Basu, and J.W. Jawitz (2008). Evaluation of simplified mass transfer models to simulate the impacts of source zone architecture on nonaqueous phase liquid dissolution in heterogeneous porous media. *Journal of Contaminant Hydrology* 102(1-2):49-60, doi:10.1016/j.jconhyd.2008.05.007.

Zhang, R. A.L. Wood, C.G. Enfield and S-W. Jeong (2003). Stochastical analysis of surfactant-enhanced remediation of denser-than-water nonaqueous phase liquid (DNAPL)-contaminated soils. *Journal of Environmental Quality* 32(3):957-965.

Technical Reports:

Basu, N. (2006). *Flux Based Site Assessment and Design of an Integrated Remediation System.* Ph.D. Dissertation, Purdue University.

Brown, G. (2006). *Using Multilevel Samplers to Assess Ethanol Flushing and Enhanced Bioremediation at Former Sages Drycleaners*. M.S. Thesis, University of Florida.

Bulsara, N. (2004*). The Occurrence of the Lead Scavengers Ethylene Dibromide and 1,2-Dichloroethane in Groundwater from Leaking Gasoline Underground Storage Tanks with a Case Study in South Carolina.* M.S. Thesis, Clemson University.

Falta, R.W. and M.B. Stacy (2008). *REMChlor - Remediation Evaluation Model for Chlorinated Solvents.* http://www.epa.gov/ada/csmos/models.html.

Fure, A.D. (2005*). Relationships Between Mass and Flux in DNAPL Source Zones.* Ph.D. Dissertation. University of Florida.

Kavanaugh, M. and P.S.C. Rao, eds. (2003). *The DNAPL Remediation Challenge: Is There a Case for Source Depletion?* EPA/600/R-03/143.

Kaye, A. (2006). *Laboratory Investigation of Dense Non-Aqueous Phase Liquid (DNAPL) Partial Source Zone Remediation Using Cosolvents.* M.S. Thesis, University of Florida.

Kim, S.J. (2005). *Validation of an Innovative Groundwater Contaminant Flux Measurement Method.* M.S. Thesis, AFIT/GES/ENV/05M-02, School of Engineering and Management, Air Force Institute of Technology.

Lee, J. (2006). *Development and Assessment of Surfactant Modified Sorbents to Measure Inorganic and Organic Contaminant Fluxes Using Passive Flux Meter*. Ph.D. Dissertation, Purdue University.

Liang, H. (2005). *Multiphase Flow Modeling of Field Scale Cosolvent Flooding for DNAPL Remediation.* M.S. Thesis, University of Clemson.

Totten, C. (2006). *Effect of Porous Media and Fluid Properties on Dense Non-Aqueous Phase Liquid Migration and Dilution Mass Flux.* PhD Dissertation, University of Florida.

VanAntwerp, D. (2006). *Using a Dual-Media Approach to Model Air Sparging Mass Transfer.* M.S. thesis, Clemson University.

Wagner, D.E. (2006). *Modeling Study to Quantify the Benefits of Groundwater Contaminant Source Remediation.* M.S. Thesis, AFIT/GES/ENV/06M-07, School of Engineering and Management, Air Force Institute of Technology.

Wheeldon, J.G. (2008). *An Evaluation of Current Mass Flux Measurement Practices and Implementation Guide.* M.S. Thesis, AFIT/GEM/ENV/08M-23, School of Engineering and Management, Air Force Institute of Technology.

Wood, R.C. (2005). *Modeling Application of Hydrogen Release Compound to Effect In Situ Bioremediation of Chlorinated Solvent-Contaminated Groundwater.* M.S. Thesis, AFIT/GEM/ENV/05M-14, School of Engineering and Management, Air Force Institute of Technology.

Yoon, H. (2006). *Validation of Methods to Measure Mass Flux of a Groundwater Contaminant.* M.S. Thesis, AFIT/GES/ENV/06M-08, School of Engineering and Management, Air Force Institute of Technology.

Conference Proceedings:

Brown, G.H., M.D. Annable, J. Cho, H. Kim (2005). Surfactant enhanced air sparging in Borden sand. Bringing Groundwater Quality Research to the Watershed Scale (*Proceedings of GQ2004*, the 4th International Groundwater Quality Conference, held at Waterloo, Canada, July 2004). IAHS Publ. 297, pp. 418-425.

Falta, R.W. (2003). Modeling subgridblock scale DNAPL pool dissolution using a dual domain approach. In: *Proceedings TOUGH Symposium,* Lawrence Berkeley National Laboratory, Berkeley, CA. May 12-14.

Published Technical Abstracts:

Annable, M.D. (2003). Flux based site characterization and remedial performance assessment. SERDP Annual Technical Symposium, Washington, DC, December 2-4.

Annable, M.D., M.C. Brooks, C.G. Enfield, R.W. Falta, M.N. Goltz, J.W. Jawitz, P.S.C. Rao, and A.L. Wood (2006). Field and laboratory evaluation of DNAPL remedial performance. Partners in Environmental Technology Technical Symposium and Workshop, Washington, DC, November 28-30.

Basu, N.B., A.D. Fure, and J.W. Jawitz (2006). Prediction of down-gradient impacts of DNAPL source depletion using tracer techniques. Fall Meeting of the American Geophysical Union, *EOS Transactions* AGU, 87(52), Fall Supplement, Abstract H23G-04, San Francisco, CA, December 11-15.

Bob, M., M.C. Brooks, T.R. Lee, C.G. Enfield, and A.L. Wood (2004). Saturation measurements of immiscible fluids in 2-D static systems: validation by light transmission visualization, American Geophysical Union Fall Meeting, San Francisco, CA, December 13-17.

Bob, M.M, A.L.Wood and T.R. Lee (2004). The impact of partial DNAPL source zone remediation. Fourth International Conference on Remediation of Chlorinated and Recalcitrant Compounds, Monterey, CA, May 24-27.

Bob, M.M, M.C. Brooks, S.C. Mravik and A.L. Wood (2007). An experimental assessment of the impacts of partial DNAPL source zone depletion using sparging as a remediation technology. Second International Conference on DNAPL: Characterization and Remediation, Niagara Falls, NY, September 24-28.

Bob, M.M, M.C. Brooks, S.C. Mravik and A.L. Wood (2007). A modified light transmission visualization method for DNAPL saturation measurements in 2-D models. The 2007 AGU Fall Meeting, San Francisco, CA, December 10-14.

Brooks, M.C., C.G. Enfield, M.D. Annable, and A.L. Wood (2004). Field measurements of contaminant flux by integral pumping tests, American Geophysical Union Fall Meeting, San Francisco, CA, December 13-17.

Brooks, M.C., C.G. Enfield, M.D. Annable, and A.L. Wood (2004). Field measurements of pre- and post-remedial contaminant flux by integral pumping tests, SERDP/ESTCP Partners in Environmental Technology Symposium, Washington DC, November 30-December 2.

Brooks, M.C. and A.L. Wood (2005). Measurement and use of contaminant flux as an assessment tool for DNAPL remedial performance. NIEHS Web Seminar, August 10.

Brown, G.H., M.D. Annable, and H. Kim (2004). Design of a surfactant enhanced air sparging field test. Groundwater Quality 2004, 4th International Conference, Waterloo, July 19-22.

Chen, X., H. Wang, and J.W. Jawitz (2006). Comparison of tracers and image analysis for characterizing DNAPL spatial distribution and the effects of mass removal on contaminant flux reduction. Fall Meeting of the American Geophysical Union, *EOS Transactions* AGU, 87(52), Fall Supplement, Abstract H11C-1264, San Francisco, CA, December 11-15.

Espinoza, F., A.L. Wood, M.C. Brooks, and C.G. Enfield (2004). Using tracers to describe NAPL heterogeneity, American Geophysical Union Fall Meeting, San Francisco, CA, December 13-17.

Falta, R. (2004). Contaminant discharge from fractured clays contaminated with DNAPL. Proceedings of the Second International Symposium, Dynamics of Fluids in Fractured Rock, Berkeley, CA, February 10-12.

Falta, R.W. (2004). The relationship between partial contaminant source zone remediation and groundwater plume attenuation. Spring Meeting of the American Geophysical Union, abstract in *EOS Transactions,* AGU, 85(17), Montreal, Canada, May 17-21.

Falta, R.W. (2005). Assessing the benefit of radiological source remediation efforts in terms of groundwater plume attenuation. Poster presented at the 50th Annual Meeting of the Health Physics Society, American Conference of Radiological Safety, Spokane, WA, July 10-14.

Falta, R.W. (2005). Impact of DNAPL source remediation on dissolved plumes. Invited talk presented at the Theis Conference, National Ground Water Association, Sedona, AZ January 14-17.

Falta, R.W. (2005). The relationship between partial DNAPL source zone remediation and groundwater plume attenuation. Presented at the 6th Environmental Technology Symposium and Workshop, U.S. Army Environmental Center, Portland, OR, March 14-16.

Falta, R.W. (2006). Impacts of DNAPL source zone treatment: experimental and modeling assessment of benefits of partial source removal. SERDP/ESTCP DNAPL Source Zone Workshop, Baltimore, MD, March 7-9.

Falta, R.W. (2006). REMChlor – Remediation evaluation model for chlorinated solvent sites. 18th Annual National Tanks Conference, U.S. Environmental Protection Agency, Memphis, TN, March 20-22.

Falta, R.W., P.S.C. Rao, N. Basu, A.L. Wood, C. Enfield, M. Annable, J. Jawitz and M. Goltz (2004). Analytical assessment of the impacts of partial mass depletion in DNAPL source zones. SERDP/ESTCP Partners in Environmental Technology Symposium, Washington, DC, November 29–December 2.

Fure, A.D., J.W. Jawitz, and M.D. Annable (2004). Designing flushing-based remediation systems for maximum reduction in contaminant mass discharge, *EOS Transactions,* AGU, 85(46), Fall Meeting Supplement, Abstract H42A-05. December 13-16.

Fure, A.D., J.W. Jawitz, and M.D. Annable (2004). Relationship between NAPL mass reduction and contaminant source strength: laboratory experiments. Groundwater Quality 2004, 4th International Conference, Waterloo, July 19-22.

Fure, A.D., J.W. Jawitz and M.D. Annable (2003). NAPL mass reduction effects on contaminant source strength: laboratory experiments. American Geophysical Union Fall Meeting, San Francisco, CA, December 8-11.

Goltz, M. (2003). Impact of source treatment. AFIT Remediation Project Manager Briefing. Wright-Patterson AFB, April.

Goltz, M.N. (2007). Groundwater contaminant mass flux measurement methods, Stanford Hydrogeology Seminar Series, Stanford, CA, November 7.

Goltz, M.N. (2007). Modeling and measuring the benefits of a groundwater contaminant source remediation, Yonsei University, Seoul, Korea, June 21.

Goltz, M.N. (2007). Modeling and measuring the benefits of remediating a groundwater contamination source. Hanyang University, Seoul, Korea, June 20.

Goltz, M.N., J. Huang, D.E. Wagner, and J.L. Heiderscheidt (2006). Modeling the benefits of groundwater contaminant source remediation. 2006 Western Pacific Geophysics Meeting, Beijing, China, July 24-27.

Goltz, M.N., J. Huang, D.E. Wagner, and J.L. Heiderscheidt (2006). Modeling the benefits of groundwater contaminant source remediation. Partners in Environmental Technology Technical Symposium and Workshop, Washington, DC, November 28-30.

Jawitz, J., M. Annable, M. Brooks, C. Enfield, R. Falta, M. Goltz, S. Rao, and L. Wood (2005). Impacts of DNAPL source treatment on contaminant mass flux. SERDP Annual Technical Symposium, Washington, DC, November 29-December 1.

Jawitz, J.W. (2003). Benefits of partial removal of NAPL source zones and measurement of solute fluxes. United States Department of Agriculture Western Regional Project W-82 Regional Project Meeting, Tucson, AZ, January 9-10.

Jawitz, J.W. (2003). The relationship between mass reduction and flux reduction for NAPL source zones. 225th American Chemical Society National Meeting, Division of Environmental Chemistry, New Orleans, LA, March 23-28.

Jawitz, J.W. (2004). Effects of contaminated site age on dissolution dynamics. *EOS Transactions,* AGU, 85(46), Fall Meeting Supplement, Abstract H31A-0369, December 13-16.

Jawitz, J.W. (2004). Groundwater contaminant flux reduction resulting from contaminant mass reduction. Gordon Research Conference: Modeling Flow and Transport in Permeable Porous Media, The Queens College, Oxford, UK, July 11-16.

Jawitz, J.W. (2004). Groundwater contaminant flux reduction resulting from contaminant mass reduction. Groundwater Quality 2004, 4th International Conference, Waterloo, July 19-22.

Jawitz, J.W. (2006). DNAPL source zone characterization and remedial performance assessment, U.S. EPA National Remedial Project Manager Training Conference, New Orleans, LA, June 19-22.

Jawitz, J.W., N. Basu, and X. Chen (2007). Prediction of down-gradient impacts of DNAPL source depletion using tracer techniques: Laboratory and modeling validation. *EOS Transactions.* AGU, 88(23), Joint Assembly Supplement, Abstract H22C-03, Acapulco, Mexico, May 22-25.

Jawitz, J.W., N. Basu, X. Chen, and A. Fure (2006). Tracer techniques for characterization of aquifer and contaminant heterogeneity, and remedial performance prediction in a Lagrangian framework. Geological Society of America Annual Meeting and Exposition, Philadelphia, PA, October 22-25.

Jawitz, J.W., X. Chen, and N.B. Basu (2007). Reactive tracer techniques for predicting DNAPL mass depletion and flux reduction. Groundwater Quality 2007: 5th International Conference, Fremantle, Australia, December 2-7.

Jawitz, J.W. and P.S.C. Rao (2003). Influence of aquifer heterogeneity on the mass reduction/flux reduction relationship for NAPL source zones. Joint Meeting of the European Geophysical Union and the American Geophysical Union, Abstract EAE03-A-07882, HS5-1MO2O-005, Nice, France, April 7-11.

Rao, P.S.C. (2003). DNAPL source remediation: what is the case for partial source depletion? NRC Committee Meeting, Irvine, CA, August 19.

Totten, C.T., M.D. Annable, J.W. Jawitz, and J.J. Delfino (2004). Influence of media and fluid properties on NAPL residual geometry and contaminant mass flux, *EOS Transactions.* AGU, 85(46), Fall Meeting Supplement, Abstract H42A-03, December 13-16.

VanAntwerp, D., and R.W. Falta (2006). Modeling kinetic interphase mass transfer during field scale air sparging operations with a dual domain approach. TOUGH Symposium 2006, Berkeley, CA, May 15-17.

Wang, H., X. Chen, and J.W. Jawitz (2006). Visualization methods to quantify DNAPL dynamics in chemical remediation. Fall Meeting of the American Geophysical Union, *EOS Transactions* AGU, 87(52), Fall Supplement, Abstract H11C-1267, San Francisco, CA, December 11-15.

Wood, A.L. (2003). DNAPL source remediation: assessment of state of the science and practice. EPA Science Council, Ada, OK, October 21.

Wood, A.L. (2003). Impacts of DNAPL source remediation on source strength. SERDP Annual Technical Symposium, Washington, DC, December 2-4.

Wood, A.L. (2003). Need and benefits of source control. ORD/HSRC Meeting. Cincinnati, OH, August 26.

Wood, A.L. (2005). DNAPL source remediation research. DOE Performance Monitoring Workshop, Butte, MT, June 21-23.

Wood, A.L., M.D. Annable, J.W. Jawitz, C.G. Enfield, R.W. Falta, M.N. Goltz and P.S.C. Rao (2004). Impact of DNAPL source treatment on contaminant mass flux. Third International Conference on Remediation of Chlorinated and Recalcitrant Compounds. Monterey, CA, May 24-27.

Wood, A.L. and C.G. Enfield (2003). Performance monitoring and forecasting. U.S. EPA Technical Support Project Semi-Annual Meeting, Seattle, WA, April 21-25.

Wood, A.L. and M.C. Brooks (2005). DNAPL source remediation research. Ground Water Forum Meeting, Phoenix, AZ, May 24.

Wood, A.L. and M.C. Brooks (2007). Flux-based site management. U.S. EPA Ground Water Forum, Las Vegas, NV, November 8.

Wood, R.C., J. Huang, C.A. Bleckmann, and M.N. Goltz (2005). Modeling in situ bioremediation of chlorinated solvent-contaminated groundwater using HRC(r). Eighth International In Situ and On-site Bioremediation Symposium, Baltimore MD, June 6-9.

Yoon, H., M.E. Close, J. Huang, M.C. Brooks, A.L. Wood, J. Bright, and M.N. Goltz (2006). Validation of mass flux measurement methods in an artificial aquifer. Fifth International Conference on Remediation of Chlorinated and Recalcitrant Compounds, Monterey, CA, May 22-25.

Book Chapters:

Annable M.D. (2008). Mass flux as a remedial performance metric at NAPL contaminated sites. In: *Methods and Techniques for Cleaning-up Contaminated Sites.* M.D. Annable, M. Teodorescu, P. Hlavinek and L. Diels (eds). NATO Science for Peace and Security Series–C, pp. 177-186.

Brooks, M.C. and A.L. Wood (2006). The measurement and use of contaminant flux for performance assessment of DNAPL remediation. In: *Remediation of Hazardous Waste in the Subsurface: Bridging Flask and Field.* C.J. Clark II and A.S. Lindner (eds.). ACS Symposium Series 940. American Chemical Society, Washington, DC, pp. 211-220.

Falta, R.W. (2005). Dissolved chemical discharge from fractured clay aquitards contaminated by DNAPLS. In: *Dynamics of Fluids in Fractured Rock,* B. Faybeshenko (ed). Geophysical Monograph Series Volume 162, American Geophysical Union.

United States
Environmental Protection
Agency

PRESORTED STANDARD
POSTAGE & FEES PAID
EPA
PERMIT NO. G-35

Office of Research and Development (8101R)
Washington, DC 20460

Official Business
Penalty for Private Use
$300

Recycled/Recyclable
Printed with vegetable-based ink on
paper that contains a minimum of
50% post-consumer fiber content
processed chlorine free

EPA 600/R-09/036 Impacts of DNAPL Source Treatment: Experimental and Modeling Assessment of the Benefits of Partial DNAPL Source Removal